

Integrated Condition Assessment of Subway Networks
Using Computer Vision and Nondestructive Evaluation Techniques

Thikra Dawood

A Thesis
In the Department
of
Building, Civil, and Environmental Engineering

Presented in Partial Fulfillment of the Requirements
For the Degree of
Doctor of Philosophy (Building Engineering) at
Concordia University
Montreal, Quebec, Canada

November 2017
© Thikra Dawood, 2017

**CONCORDIA UNIVERSITY
SCHOOL OF GRADUATE STUDIES**

This is to certify that the thesis prepared

By: **Thikra Dawood**

Entitled: **Integrated Condition Assessment of Subway Networks Using
Computer Vision and Nondestructive Evaluation Techniques**

and submitted in partial fulfillment of the requirements for the degree of

DOCTOR OF PHILOSOPHY (Building Engineering)

Complies with the regulations of the University and meets the accepted standards with respect to originality and quality.

Signed by the final Examining committee:

_____	Chair
Dr. M. Kazemi Zanjani	
_____	External Examiner
Dr. M. Lu	
_____	External to Program
Dr. A. Hammad	
_____	Examiner
Dr. O. Moselhi	
_____	Examiner
Dr. A. Bagchi	
_____	Thesis Supervisor
Dr. T. Zayed	
_____	Thesis Supervisor
Dr. Z. Zhu	

Approved by:

Dr. F. Haghigat, Graduate Program Director

January 23, 2018

Dr. A. Asif, Dean, Faculty of Engineering and Computer Science

ABSTRACT

Integrated Condition Assessment of Subway Networks Using Computer Vision and Nondestructive Evaluation Techniques

Thikra Dawood, Ph.D.

Concordia University, 2017

Subway networks play a key role in the smart mobility of millions of commuters in major metropolises. The facilities of these networks constantly deteriorate, which may compromise the integrity and durability of concrete structures. The ASCE 2017 Report Card revealed that the condition of public transit infrastructure in the U.S. is rated D-; hence a rehabilitation backlog of \$90 billion is estimated to improve transit status to good conditions. Moreover, the Canadian Urban Transit Association (CUTA) reported 56.6 billion CAD in infrastructure needs for the period 2014-2018. The inspection and assessment of metro structures are predominantly conducted on the basis of Visual Inspection (VI) techniques, which are known to be time-consuming, costly, and qualitative in nature. The ultimate goal of this research is to develop an integrated condition assessment model for subway networks based on image processing, Artificial Intelligence (AI), and Non-Destructive Evaluation (NDE) techniques. Multiple image processing algorithms are created to enhance the crucial clues associated with RGB images and detect surface distresses. A complementary scheme is structured to channel the resulted information to Artificial Neural Networks (ANNs) and Regression Analysis (RA) techniques. The ANN model comprises sequential processors that automatically detect and quantify moisture marks (MM) defects. The RA model predicts spalling/scaling depth and simulates the de-facto scene by developing a hybrid algorithm and interactive 3D presentation. In addition, a comparative analysis is performed to select the most appropriate NDE technique for subway inspection. This technique is applied to probe the structure and measure the subsurface defects. Also, a novel model for the detection of

air voids and water voids is proposed. The Fuzzy Inference System (FIS), Adaptive Neuro-Fuzzy Inference System (ANFIS), and Monte Carlo Simulation (MCS) are streamlined through successive operations to create the integrated condition assessment model. To exemplify and validate the proposed methodology, a myriad of images and profiles are collected from Montréal Metro systems. The results ascertain the efficacy of the developed detection algorithms. The attained recall, precision, and accuracy for MM detection algorithm are 93.2%, 96.1%, and 91.5% respectively. Whereas for spalling detection algorithm, are 91.7%, 94.8%, and 89.3% respectively. The mean and standard deviation of error percentage in MM region extraction are 12.2% and 7.9% respectively. While for spalling region extraction, they account for 11% and 7.1% respectively. Subsequent to selecting the Ground Penetrating Radar (GPR) for subway inspection, attenuation maps are generated by both the amplitude analysis and image-based analysis. Thus, the deteriorated zones and corrosiveness indices for subway elements are automatically computed. The ANN and RA models are validated versus statistical tests and key performance metrics that indicated the average validity of 96% and 93% respectively. The air/water voids model is validated through coring samples, camera images, infrared thermography and 3D laser scanning techniques. The validation outcomes reflected a strong correlation between the different results. A sensitivity analysis is conducted showing the influence of the studied subway elements on the overall subway condition. The element condition index using neuro-fuzzy technique indicated different conditions in Montréal subway systems, ranging from sound concrete to very poor, represented by 74.8 and 35.1 respectively. The fuzzy consolidator extrapolated the subway condition index of 61.6, which reveals a fair condition for Montréal Metro network. This research developed an automated tool, expected to improve the quality of decision making, as it can assist transportation agencies in identifying critical deficiencies, and by focusing constrained funding on most deserving assets.

Dedicated To

My beloved husband "Louay"

My precious daughter "Ruad"

My adorable son "Yazan"

ACKNOWLEDGEMENTS

I would like to express my profound gratitude and special appreciation to my supervisors, Dr. Tarek Zayed and Dr. Zhenhua Zhu, for their constructive guidance, great dedication, professional attitude, and valuable advice. I am particularly indebted to them for their constant faith in my research work and for allowing me to grow as a researcher. It would have been impossible to accomplish this thesis without their indispensable support and encouragements.

I would like to extend my heartfelt gratitude to Dr. Osama Moselhi for his inspirational insights and mentorship. His continuous encouragement, help, and support will always be appreciated. I would also like to thank my examining committee members; Dr. Amin Hammad, Dr. Ashutosh Bagchi and Dr. Ming Lu. Their brilliant comments and suggestions offered a considerable momentum to the quality of my work.

I am greatly thankful to Mr. Dominic Chaussée, Senior Engineer at the Société de Transport de Montréal (STM) for his outstanding collaboration in facilitating my data collection. Also, much gratitude goes to Mr. Philippe Desmarais and Mr. Antonio Léautaud for providing the technical support in Montréal subway network. My special thanks are due to Mr. Alex Tarussov, President of Radex Detection Inc.

for his in-kind contributions to the research, by participating in the data collection and providing the required GPR equipment.

My sincere thanks go to my colleagues who helped me in the data collection of this research; Mohammed Abdul Rahman, Mohammed Alsharqawi, and Laith El-Khateeb. It was a pleasure working and sharing with you the fruitful thoughts and discussions. Also, I am grateful to all my friends and colleagues in the Construction Automation Lab for the friendly and professional environment that we were sharing along the years. I would also like to acknowledge the University Communication Services (UCS) at Concordia University for shedding a light on my research, publish it in the media, and help reinforcing Concordia's position among the universities.

No words could ever express my deepest love and appreciation to my beloved husband Louay, my daughter Ruaa, and my son Yazan for their unconditional love. I owe you all the precious moments that I spent away from you to accomplish this work. Your enthusiasm to see this work coming to light was a huge motivator. You are the most important people in my world and to you I dedicate this thesis.

TABLE OF CONTENTS

LIST OF FIGURES	xii
LIST OF TABLES	xvii
LIST OF ABBREVIATIONS	xix
CHAPTER 1: INTRODUCTION.....	1
1.1 Problem Statement and Research Motivation	1
1.2 Research Objectives	2
1.3 Research Methodology.....	3
1.4 Structure of the Thesis.....	5
CHAPTER 2: LITERATURE REVIEW.....	7
2.1 Existing Assessment Models of Subway Networks	7
2.2 Concrete Degradation and Deterioration Mechanisms.....	11
2.2.1 Concrete Degradation.....	11
2.2.2 Subway Deterioration Mechanisms	13
2.3 Previous Subway Assessment Models	18
2.4 Automated Defect Detection and Assessment Models	23
2.5 Modelling Techniques used in the Research	25
2.5.1 Image Processing Techniques	25
2.5.2 Artificial Neural Networks (ANNs)	29
2.5.3 Regression Analysis (RA)	31
2.5.4 Fuzzy Set Theory and Fuzzy Inference System (FIS)	33
2.5.5 Neuro-Fuzzy Technique	35
2.5.6 Monte Carlo Simulation (MCS)	37
2.5.7 Non-Destructive Evaluation (NDE) Techniques for Subway Structures	38
2.6 Gaps in the Body of Knowledge versus Potentials	43

CHAPTER 3: RESEARCH METHODOLOGY	46
3.1 Overall Research Methodology	46
3.2 Surface Defect-Based Assessment Model	48
3.2.1 Image Acquisition.....	48
3.2.2 Image Preprocessing.....	52
3.2.3 Machine Learning-Based Processing	62
3.2.4 Condition Assessment of Surface Defects	70
3.3 Selection of the Most Appropriate NDE Technology	73
3.3.1 Advantages and Disadvantages of Different NDE Technologies	74
3.3.2 Comparison of NDE Technologies versus Selection Criteria	74
3.4 Subsurface Defect-Based Assessment Model	77
3.4.1 Profiles Acquisition	77
3.4.2 Data Analysis.....	78
3.4.3 Data Processing	81
3.4.4 Condition Assessment of Subsurface Defects	82
3.5 Integrated Defect-Based Condition Assessment Model	83
3.5.1 Defect Condition Assessment using Simulation	86
3.5.2 Fuzzy-Based Condition Index	88
3.5.3 Element Condition Index using Neuro-Fuzzy	90
3.5.4 Integrated Subway Condition Index	94
CHAPTER 4: DATA COLLECTION	97
4.1 Preliminary Data Collection	97
4.2 Key Indicators in Data Collection	101
4.2.1 Key Indicators in Surface Data Collection	101
4.2.2 Key Indicators in Subsurface Data Collection	103

CHAPTER 5: MODEL DEVELOPMENT AND IMPLEMENTATION	108
5.1 Moisture Marks Model	108
5.1.1 Preprocessing of Moisture Marks	108
5.1.2 ANN Model for Moisture Marks Recognition	111
5.1.3 Moisture Marks (MM) Model Validation	116
5.2 Spalling Model	122
5.2.1 Preprocessing of Spalling using Hybrid Algorithm	122
5.2.2 Regression Model for Spalling Quantification	124
5.2.3 Spalling (SP) Model Validation	128
5.3 Scaling Model.....	131
5.3.1 Preprocessing of Scaling	131
5.4 Cracks Model	133
5.4.1 Preprocessing of Cracks	133
5.4.2 Cracks Recognition.....	135
5.5 Subsurface Data Analysis.....	138
5.5.1 Mapping using Amplitude Analysis	138
5.5.2 Mapping using Image-Based Analysis (IBA)	148
5.6 Evaluation of Surface and Subsurface Defects	163
5.7 Integrated Defect-Based Condition Assessment Model.....	175
5.7.1 Defect Condition Assessment using Simulation	175
5.7.2 Fuzzy-Based Condition Index	180
5.7.3 Element Condition Index using Neuro-Fuzzy	182
5.7.4 Integrated Subway Condition Index	188
5.7.5 Sensitivity Analysis	190
CHAPTER 6: AUTOMATED TOOL.....	193

6.1 MATLAB Coding for Surface Defects	194
6.1.1 Unique Properties of Moisture Marks and Algorithm Coding	194
6.1.2 Scaling Algorithm Coding.....	197
6.1.3 Cracks Algorithm Coding.....	197
6.1.4 Regression Analysis for Spalling Quantification	199
6.2 Subsurface Defects Software Application.....	200
6.3 Integrated Assessment Software Application.....	203
CHAPTER 7: CONCLUSIONS AND RECOMMENDATIONS	208
7.1 Summary and Conclusions	208
7.2 Research Contributions	211
7.3 Research Limitations.....	212
7.4 Recommendations for Future Work	213
7.4.1 Current Research Enhancement Areas	213
7.4.2 Future Research Extension Areas.....	214
REFERENCES.....	216
APPENDIX A: DATA COLLECTION AND VALIDATION IMAGES IN MONTRÉAL SUBWAY NETWORK.....	236
APPENDIX B: PLANS OF THE SELECTED SYSTEMS IN MONTRÉAL NETWORK	244

LIST OF FIGURES

Figure 2.1 Ridership in the Major North American Cities (Adapted from APTA 2016)	7
Figure 2.2 Concrete Degradation in Different Montréal Metro Stations (a) Water Overflow and Moisture Marks; (b) Wide Cracks in Stairs Structure; (c) Corrosion and Delamination in Concrete Floor Slab	11
Figure 2.3 Phases of Chloride-Induced Corrosion (Arndt et al. 2010).....	12
Figure 2.4 Different Surface Defects in Subway Networks (Dawood et al. 2015 _a)	13
Figure 2.5 Carbonation-Initiated Corrosion (Adapted from Penttala 2009).....	17
Figure 2.6 Gray-level Image and its Matrix.....	26
Figure 2.7 MLP Neural Network (Dawood et al. 2017 _b).....	30
Figure 2.8 ANFIS Architecture.....	36
Figure 2.9 Sugeno Fuzzy Model Reasoning Mechanism	37
Figure 2.10 NDE Methods for Subway Networks	39
Figure 2.11 GPR Principles (Hugenschmidt and Mastrangelo 2006).....	41
Figure 3.1 Overall Model Flowchart.....	47
Figure 3.2 Overall Flowchart for Surface Defects Condition Assessment	49
Figure 3.3 Image Acquisition Phase	50
Figure 3.4 Defects Prioritization and Related Attributes	50
Figure 3.5 Image Preprocessing Phase	53
Figure 3.6 Moisture Marks Detection Algorithm (Dawood et al. 2017 _b).....	54
Figure 3.7 Spalling Detection Algorithm (Dawood et al. 2017 _a)	56
Figure 3.8 Scaling Detection Algorithm Flowchart.....	60
Figure 3.9 Cracks Detection Algorithm.....	62
Figure 3.10 Moisture Marks Model Development via ANN	64
Figure 3.11 ANN Training and Fitting Stage (Dawood et al. 2017 _b).....	66
Figure 3.12 Quantifying Moisture Marks Distress (Dawood et al. 2017 _b).....	66
Figure 3.13 Quantifying Spalling/Scaling Distress (Dawood et al. 2017 _b).....	67
Figure 3.14 Regression Model Overview	69
Figure 3.15 Cracks Processing and Recognition Scheme	70
Figure 3.16 NDE Technology Selection Flowchart.....	73
Figure 3.17 Overall Flowchart for Subsurface Defects Condition Assessment	77

Figure 3.18 Profiles Acquisition Phase.....	78
Figure 3.19 Amplitude Analysis of Rebar Reflections	79
Figure 3.20 Image-Based Analysis Flowchart.....	80
Figure 3.21 Example of the IBA Software	80
Figure 3.22 Amplitude Attenuation Map	81
Figure 3.23 Image-Based Corrosiveness Map	82
Figure 3.24 Integrated Condition Assessment Scheme	85
Figure 3.25 Crystal Ball Model Framework.....	87
Figure 3.26 Types of Inspection Results.....	89
Figure 3.27 Neuro-Fuzzy Prediction Model	91
Figure 3.28 Fuzzy Consolidation Model Structure	95
Figure 4.1 Subway Network Hierarchy	97
Figure 4.2 Selected Stations and Tunnels in Montréal Subway	100
Figure 4.3 Canon EOS Rebel XS and its Telephoto (Canon 2015)	101
Figure 4.4 Image Acquisition Process in a Montréal Subway Tunnel (Dawood et al. 2017 _a) ...	102
Figure 4.5 Various Defects in Montréal Subway Network (a) Cracks and Moisture Marks; (b) Spalling; (c) Scaling.....	103
Figure 4.6 Tunnel Plan and Scanning Paths	104
Figure 4.7 Profiles Acquisition Process in a Montréal Subway Tunnel	106
Figure 4.8 GPR Profiles Samples (a) inter St. Laurent and Place-Des-Arts Tunnel using 900 MHz Antenna; (b) in Vendôme Station using SS-MINI Antenna	106
Figure 5.1 Three Planes of Moisture Marks Image (Dawood et al. 2015 _b).....	109
Figure 5.2 Moisture Marks Edge Detection (Dawood et al. 2017 _b)	110
Figure 5.3 Morphological Operations (a) Image Dilation; (B) Image Holes Filling (Dawood et al. 2017 _b).....	110
Figure 5.4 Defect Detection (a) Image Noise Cleaning; (b) Mask Overlay (Dawood et al. 2017 _b)	111
Figure 5.5 ANN Architecture (Mathworks 2013) (Dawood et al. 2017 _b)	112
Figure 5.6 ANN Datasets and Their Matrices.....	113
Figure 5.7 ANN Validation Scheme (a) Validation Performance; (b) Training State; (c) Error Histogram.....	114

Figure 5.8 ANN Samples Results (a) MSE and R2 Results; (b) Regression Analysis Scheme .	115
Figure 5.9 Three False Positive Results (a) Upper Slab Scaling; (b) Wall Spalling (Dawood et al. 2017 _b).....	118
Figure 5.10 Samples of True Positive Results (a) Before Preprocessing; (b) After Preprocessing with Parameters; Threshold 0.2, Sigma 5, Disk Diameter 30, Opacity 0.7	119
Figure 5.11 Intermediate Results of Preprocessing with Parameters; Threshold 0.2, Sigma 5, Disk Diameter 30, Opacity 0.7.....	120
Figure 5.12 Three Planes of Spalling Image.....	122
Figure 5.13 Filtering in the Spatial Domain (a) Gray-Level Image; (b) Image Thresholding; (c) Image Histogram.....	123
Figure 5.14 Filtering in the Frequency Domain (a) Gaussian Blur 3D Filter; (b) Color Transformer Filter; (c) Smart Filter (Dawood et al. 2017 _a).....	123
Figure 5.15 Defect Detection (a) Image Calibration; (b) Shape Extraction (Dawood et al. 2017 _a).....	124
Figure 5.16 Spalling 3D Model (a) Schematic Representation of Spalling Depth; (b) Interactive 3D Surface Plot; (c) Defect Profile (Dawood et al. 2017 _a).....	125
Figure 5.17 Fitted Regression Models (Dawood et al. 2017 _a).....	126
Figure 5.18 Residual Analysis Scheme (Dawood et al. 2017 _a)	128
Figure 5.19 Three False Positive Results (Dawood et al. 2017 _a).....	130
Figure 5.20 Exploring the Color Space.....	132
Figure 5.21 Scaling Binary Transformation (a) Gray-Level Image; (b) Image Thresholding; (c) Image Histogram.....	132
Figure 5.22 Filtering Scaling Defect (a) Processing with Maximum Entropy; (b) Scaling Detection.....	133
Figure 5.23 Converting the RGB Image to Grayscale Image	133
Figure 5.24 Crack Edge Detection.....	134
Figure 5.25 Morphological Operations (a) Image Dilation; (b) Image Hole Filling	135
Figure 5.26 Crack Detection.....	135
Figure 5.27 Image Calibration (a) Setting Image Scale; (b) Crack Segments	136
Figure 5.28 Sample of Crack Width Measurements	137

Figure 5.29 Data Processing using Amplitude Analysis (a) Raw Profile; (b) Edited Profile; (c) Gain Application; (d) Migration and Rebar Picking.....	139
Figure 5.30 Condition States using Amplitude Analysis.....	141
Figure 5.31 Attenuation Maps of (a) VSS; (b) SPTW; (c) SPTS	143
Figure 5.32 Attenuation Maps of Outremont Station (a) OSW1; (b) OSW2; (c) OSS.....	144
Figure 5.33 Amplitude Clustering for Six Datasets (a) VSS; (b) SPTW; (c) SPTS; (d) OSW1; (e) OSW2; (f) OSS	146
Figure 5.34 Corrosiveness Indices for Six Datasets (a) VSS; (b) SPTW; (c) SPTS; (d) OSW1; (e) OSW2; (f) OSS	147
Figure 5.35 Deterioration Maps of (a) VSS; (b) SPTW; (c) SPTS.....	151
Figure 5.36 Deterioration Maps of Outremont Station (a) OSW1; (b) OSW2; (c) OSS	152
Figure 5.37 IBA Model in Non-Reinforced Concrete	154
Figure 5.38 IBA Framework for Air/Water Voids Identification.....	155
Figure 5.39 Sample of Scanned GPR Profiles in FPTV	157
Figure 5.40 Deterioration Map of FPTV	159
Figure 5.41 Correlation between GPR-IBA and Camera Images in FPTV	160
Figure 5.42 Coring Locations	161
Figure 5.43 Comparison between Various NDE Techniques (a) Laser-Based Thermal Ortho-Photo (Al Lafi et al. 2017); (b) GPR-IBA Deterioration Map.....	164
Figure 5.44 Salt on Stairs in a Montréal Subway Station.....	172
Figure 5.45 Probability Distribution Analysis of MM in FPTV (a) Statistics and Comparison Chart; (b) Best Fit Distribution.....	176
Figure 5.46 MM Condition Index Chart.....	177
Figure 5.47 Inputs and Output Membership Functions (a) MM; (b) SP; (c) SC; (d) CR; (e) CO; (f) AV; (g) WV; (h) CI.....	181
Figure 5.48 Inputs MFs of the Selected Network (a) MM; (b) SP; (c) SC; (d) CR; (e) CO; (f) AV; (g) WV	186
Figure 5.49 3D Surface Presentations (a) MM and SP Versus CI; (b) CR and CO Versus CI; (c) AV and WV Versus CI.....	187
Figure 5.50 Fuzzy Consolidation Model Configuration.....	189
Figure 5.51 Fuzzy Estimator for Subway Condition Index	190

Figure 5.52 Sensitivity Analysis using Spider Chart	192
Figure 6.1 Workflow of the Automation Process	193
Figure 6.2 Curve Fitting Tool in MATLAB®	199
Figure 6.3 Spalling Depth Calculation Sheet.....	200
Figure 6.4 Sample of RADAN® Processing Sheet	201
Figure 6.5 Sample of RADxpert® Processing Sheet.....	202
Figure 6.6 Sample of Crystal Ball Excel Spreadsheet	203
Figure 6.7 Sample of Simulation Statistics.....	204
Figure 6.8 Sample Fuzzy Rules Configuration.....	205
Figure 6.9 Sample of ANFIS Optimization Scheme (a) Data Training; (b) Data Testing; (c) Data Checking	206
Figure 6.10 Consolidation Model Demonstration.....	207

LIST OF TABLES

Table 2.1 Condition Assessment of Major Subway Transit Authorities	9
Table 2.2 Problem Priorities in Transit Infrastructure (Russell and Gilmore 1997).....	14
Table 3.1 Moisture Marks (MM) Condition Ratings	71
Table 3.2 Spalling (SP) Condition Ratings	71
Table 3.3 Scaling (SC) Condition Ratings	72
Table 3.4 Cracks (CR) Condition Ratings	72
Table 3.5 Advantages and Disadvantages of Various NDE Technologies for Subway Evaluation	75
Table 3.6 Evaluation and Selection of NDE Method.....	76
Table 3.7 Corrosion (CO) Condition Ratings	83
Table 3.8 Air Voids (AV) and Water Voids (WV) Condition Ratings.....	83
Table 3.9 Integrated Condition Index	84
Table 4.1 Montréal Metro Preliminary Visits	99
Table 4.2 Subsurface System Scanning Related Data	107
Table 5.1 Detection Performance Evaluation (Dawood et al. 2017 _b).....	117
Table 5.2 Model Validation Results (Dawood et al. 2017 _b).....	121
Table 5.3 Statistical Diagnostic Tests (Dawood et al. 2017 _a).....	127
Table 5.4 Detection Performance Evaluation (Dawood et al. 2017 _a).....	129
Table 5.5 Model Validation Results (Dawood et al. 2017 _a).....	131
Table 5.6 Definition of Various RC States using IBA.....	150
Table 5.7 Definition of Various Non-RC States using IBA	158
Table 5.8 Coring Samples and their Properties.....	162
Table 5.9 Condition Indices of FPTV	165
Table 5.10 Condition Indices of VSS	167
Table 5.11 Condition Indices of OSW1	169
Table 5.12 Condition Indices of OSW2	170
Table 5.13 Condition Indices of OSS	170
Table 5.14 Condition Indices of SPTW	173
Table 5.15 Condition Indices of SPTS.....	174

Table 5.16 Condition Indices of Defects	178
Table 5.17 Sample of Entry Data	182
Table 5.18 Comparison of Multi Networks Results	184
Table 5.19 Predicted Condition Indices for Subway Elements	188

LIST OF ABBREVIATIONS

AD	Anderson-Darling
Adj R ²	Adjusted R-square
AHP	Analytic Hierarchy Process
AI	Artificial Intelligence
AIP	Average Invalidity Percent
ANFIS	Adaptive Neuro-Fuzzy Inference System
ANN	Artificial Neural Network
ANP	Analytic Network Process
APTA	American Public Transportation Association
ASCE	American Society of Civil Engineering
AV	Air Voids
AVP	Average Validity Percent
BART	San Francisco Bay Area Rapid Transit
BIM	Building Information Modeling
Cal Train	California Train Transit
CI	Condition Index
CIRC	Canadian Infrastructure Report Card
CO	Corrosion
CR	Cracks
CTA	Chicago Transit Authority
CUTA	Canadian Urban Transit Association
2D	Two-Dimensional
3D	Three-Dimensional
4D	Four-Dimensional
5D	Five-Dimensional
DFT	Discrete Fourier Transform

EM	Electro-Magnetic
ER	Electrical Resistivity
FDTD	Finite Difference Time Domain
FIS	Fuzzy Inference System
FMCS	Fuzzy Monte Carlo Simulation
FPTV	Frontenac and Papineau Tunnel Vault
FTA	Federal Transit Administration
GA	Genetic Algorithm
GPR	Ground Penetrating Radar
GPS	Global Positioning System
HC	Hardened Concrete
HCP	Half-Cell Potential
HVAC	Heating, Ventilation, and Air Conditioning
IBA	Image-Based Analysis
IDFT	Inverse Discrete Fourier Transform
IE	Impact Echo
IP	Image Processing
IR	Infrared
KPI	Key Performance Indicator
KS	Kolmogorov-Smirnov
MAE	Mean Absolute Error
MAUT	Multi-Attribute Utility Theory
MCI	Metro Condition Index
MCS	Monte Carlo Simulation
MF	Membership Function
MLP	Multi-Layer Perceptron
MM	Moisture Marks

MRPPI	Maintenance and Rehabilitation Planning for Public Infrastructure
MSE	Mean Squared Error
MSR	Multi-Scale Retinex
MSRP	Model for Station Rehabilitation Planning
MTA	Mass Transit Administration
MTA NYCT	Metropolitan Transit Authority-New York City Transit
MTR	Mass Transit Railway of Hong Kong
MTRC	Mass Transit Railway Corporation of Hong Kong
NDE	Non-Destructive Evaluation
NMAE	Normalized Mean Absolute Error
NRMSE	Normalized Root Mean Squared Error
NYCT	New York City Transit
OOI	Object Of Interest
OSIM	Ontario Structure Inspection Manual
OSS	Outremont Station Slab
OSW1	Outremont Station Wall #1
OSW2	Outremont Station Wall #2
PH	Potential of Hydrogen
PROMETHEE	Preference Ranking Organization Method of Enrichment Evaluation
RA	Regression Analysis
RABIT	Robotics Assisted Bridge Inspection Tool
RATP	Paris Rapid Transit Authority
RC	Reinforced Concrete
RGB	Red, Green, and Blue
RMSE	Root Mean Squared Error
ROI	Region Of Interest
SASW	Spectral Analysis of Surface Waves

SC	Scaling
SCI	Subway Condition Index
SDI	Station Diagnosis Index
SHRP	Strategic Highway Research Program
SP	Spalling
SPTS	St. Laurent and Place-Des-Arts Tunnel Slab
SPTW	St. Laurent and Place-Des-Arts Tunnel Wall
SSDI	Subway Station Diagnosis Index
SSE	Sum of Squares Due to Error
STM	Société de Transport de Montréal
SUPER	SUBway PERformance
TOMIE	Tunnel Operations, Maintenance, Inspection, and Evaluation Manual
UPV	Ultrasonic Pulse Velocity
USB	Universal Serial Bus
USW	Ultrasonic Surface Waves
VI	Visual Inspection
VSS	Vendôme Station Slab
WMATA	Washington Metropolitan Transit Authority
WV	Water Voids

CHAPTER 1: INTRODUCTION

1.1 Problem Statement and Research Motivation

The competitiveness among metropolitan cities hinges on their capability to build up a robust public transit system. Subway networks have always been an integral part of transit infrastructure and a vital constituent of the urban fabric. They play a key role in catalyzing sustainable economic development. In 2009, transit-based industries boosted Quebec's economy by 1.1 billion CAD in added value, which accounts for 14,110 jobs per year (Public transit 2010). The facilities in subway infrastructure are subjected to severe environmental conditions and constant heavy loads, which undermine their serviceability. According to the ASCE 2017 Report Card, the condition of public transit infrastructure in the U.S. is rated D-; therefore, the Federal Transit Administration (FTA) estimated a rehabilitation backlog of \$90 billion required to improve transit status to good conditions (ASCE 2017). Furthermore, the major large cities in the world have several tunnels running under rivers. Leakage of water or infiltration has been considered the most serious problem and the main cause of concrete degradation. Five transit agencies in the United States along with the Société de Transport de Montréal (STM) in Canada have reported that water leakage is the most significant structural issue and been classified as the first priority among other problems (Russell and Gilmore 1997; Chaussée 2012). A huge amount of water infiltration through subway systems may accelerate the deterioration mechanisms and subsequently causes the closure of their facilities; as occurred in Montréal Metro's Yellow Line due to water leakage, which ceased the use of the line for 25 weekends. The structural defects facing transit authorities are derived from water intrusion, among others are corrosion of reinforcing steel bars, spalling, water voids, etc. Therefore, providing cutting-edge serviceability through periodic structural inspection and assessment is crucial in keeping the subway network operational and avoiding catastrophic

incidents; such as the collapse of concrete infrastructure, which brings about numerous fatalities and injuries, as well as the loss of wealth and businesses.

Recent inspection techniques require specialized inspectors to frequently travel to the targeted subway system and visually evaluate the structure's deterioration level. While these techniques can deliver substantial inspection information (ACI 2008), they are known to be costly, labor-intensive, and error-prone. They have inherent shortcomings in recognizing the structural integrity and quantifying the severity of distress as some parts of the structure are inaccessible to inspectors. Therefore many distresses are not diagnosed until they progress and become serious.

The topic of subway assessment has been tackled by many researchers whose studies were subjective and relied on inspection data, or focused on measuring only surface flaws, and failed in evaluating the whole subway network. Some models required a vast amount of data to be implemented, while others could not be validated due to the insufficiency of data. Therefore, the current state-of-the-practice is unreliable in estimating the severity of defects. This accentuates the need for computer vision-based detection and quantification scheme, which automates the current practice and provides coherent outcomes. This scheme incorporates multiple algorithms and computational approaches to visual data in order to develop an integrated framework for the detection and evaluation of distresses. It endeavors to bridge the gaps pertaining to the current practice and to ameliorate the existing level of defects' assessment in subway networks.

1.2 Research Objectives

The major goal of this research is to develop an integrated condition assessment model for subway networks using computer vision and Non-Destructive Evaluation (NDE) techniques. The integrated model builds on the fusion of image processing, artificial intelligence (AI), and NDE techniques. To achieve this goal, the following sub-objectives are defined:

1. Identify and study the surface and subsurface defects of subway components.
2. Develop a surface defect-based assessment model.
3. Perform a comparative analysis of the appropriateness of different NDE technologies for subway networks.
4. Develop a subsurface defect-based assessment model.
5. Develop an integrated defect-based condition assessment model.
6. Automate the developed framework.

1.3 Research Methodology

A comprehensive methodology of this research is elaborated in chapter 3. The following steps may briefly introduce the entire research methodology:

Step 1: Literature review

A comprehensive state-of-the-art literature review is conducted; including current practices of subway transit models, concrete deterioration mechanisms, previous efforts related to the condition assessment of subway networks. In addition, several cutting-edge techniques are reviewed including but are not limited to, image processing, Artificial Neural Networks (ANNs), Regression Analysis (RA), Fuzzy Inference System (FIS), Adaptive Neuro-Fuzzy Inference System (ANFIS), and the currently applied Non-Destructive Evaluation (NDE) technologies.

Step 2: Surface defect-based assessment model

This step aims at developing an automated assessment tool for subway networks based on image processing and machine vision algorithms. This model comprises four main phases namely; image acquisition, image preprocessing, machine learning-based processing, and condition assessment of surface defects. Successive filtering operations are performed on the images, such as filtering

in the spatial domain, and filtering in the frequency domain. A hybrid algorithm is proposed and a 3D model of a de facto distress is created in the detection stage. Then Artificial Intelligence (AI) techniques, e.g., ANNs and RA are leveraged to evaluate the defects in the recognition stage.

Step 3: Selection of the most appropriate NDE technique

Subsequent to studying NDE fundamentals in the literature review, the research proceeds with a comparative analysis to identify and select the most applicable NDE technique for subway inspection. First, the advantages and limitations of several NDE technologies are investigated. To be followed by establishing a set of selection criteria and comparing each NDE technique against the criteria. Finally, the most suitable NDE technique for subway inspection is selected.

Step 4: Subsurface defect-based assessment model

The selected NDE technique from the preceding step is utilized to develop the subsurface defect-based assessment model, which encompasses four main phases namely; Profile acquisition, data interpretation, data processing, and condition assessment of subsurface defects. After collecting subsurface data, the amplitude analysis and image-based analysis techniques are incorporated to interpret and process the data. Consequently, maps that reveal the subsurface deterioration of the facility are generated automatically.

Step 5: Integrated defect-based condition assessment model

In this step, a unified system that combines the surface defect-based assessment model and the subsurface defect-based assessment model is proposed. The system commences by calculating the defects condition indices for each element. Later, a fuzzy logic control engine is created on the basis of experts' knowledge. In order to optimize the results, a neuro-fuzzy model is developed to predict the element's condition index. Then, the subway's condition index is computed.

Step 6: Develop an automated tool for the proposed models

Eventually, an automated tool is created to facilitate the implementation of the model. The automated tool consists of two parts; the first pertains to image processing algorithms and defects detection coding, while the second part displays calculation sheets and visual demonstration of different data mining and machine vision process.

1.4 Structure of the Thesis

This thesis is comprised of seven chapters, the organization of which is as follows:

Chapter 1

Highlights the problem statement and research motivation. Then, it introduces the research objectives, brief methodology description, and research organization.

Chapter 2

Compiles a comprehensive literature review of the evaluation models accomplished by subways authorities worldwide, concrete degradation and deterioration mechanisms, as well as, previous subway research endeavors and automated assessment models. A thorough explanation is provided for the various image processing, pattern recognition, and nondestructive evaluation techniques.

Chapter 3

Provides a detailed description of the proposed methodology, which involves three stages and entails developing three main models. Multiple algorithms and a proliferation of processing techniques are presented. A comparative analysis is also performed in this chapter to select the most appropriate NDE technology for subway inspection.

Chapter 4

Demonstrates data acquisition and collection procedures for both surface defect-based assessment model and subsurface defect-based assessment model. Further, it presents the different key

indicators in the data collection process.

Chapter 5

The key idea of the research methodology is elaborated in the model development and implementation. Validation and correlation of the results are illustrated consecutively. Moreover, data interpretation and deterioration maps are generated for real case studies in Montréal subway network.

Chapter 6

Presents the automated tool for the developed model, which entails the algorithms syntheses and visualization of the calculation schemes.

Chapter 7

Draws relevant conclusions by highlighting the current research contributions, as well as, its limitations and future work enhancements.

CHAPTER 2: LITERATURE REVIEW

2.1 Existing Assessment Models of Subway Networks

In major metropolitan areas, people incorporate various aspects of the city living, one of these crucial aspects is the mobility and commuting. Statistics show that the number of passengers choosing the subway system for their daily travel is on the rise. According to the American Public Transportation Association (APTA) fourth quarter report (APTA 2016), in New York City, around 2.8 billion trips took place in 2016, while in the case of Montréal, that number reached 354 million trips. Toronto recorded around 303 million trips, Chicago 239 million, Washington D.C. 234 million, Boston 172 million, and Vancouver 137 million trips. The report also revealed that transit ridership demonstrated an ascending trend in North America in the last decade and this trend is expected to continue (APTA 2016). Furthermore, The Federal Transit Administration (FTA) reported that transit ridership had increased 26 percent in the last 20 years (NTD/FTA 2017). Figure 2.1 presents the subway ridership in some of the major North American cities.

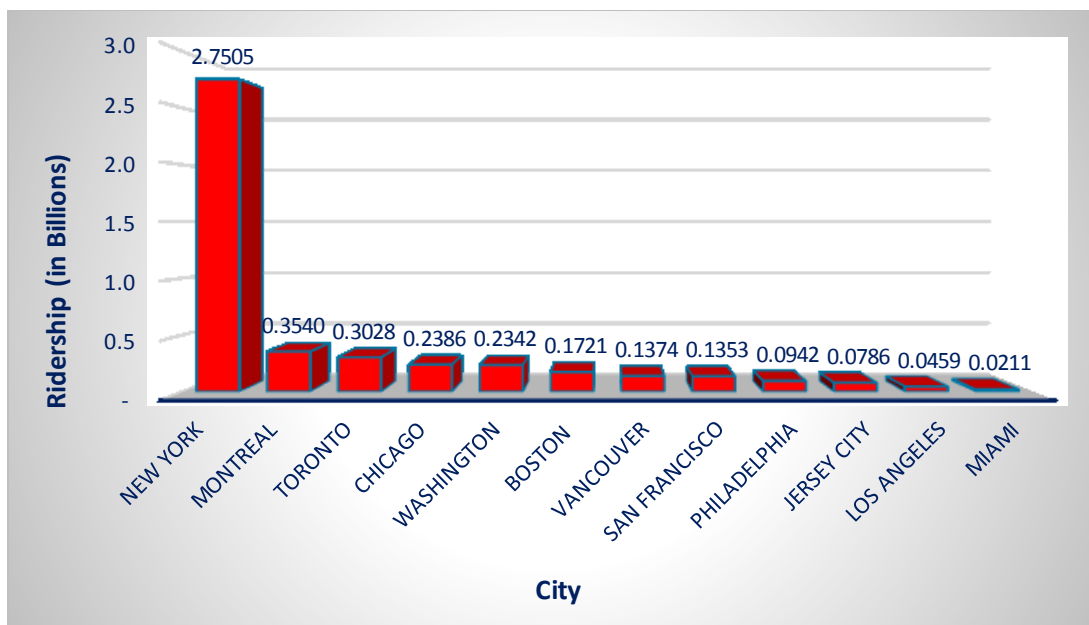


Figure 2.1 Ridership in the Major North American Cities (Adapted from APTA 2016)

The increasing demand on subway networks will participate in the deterioration of the structure; this is becoming more significant as the systems continue to age. Moreover, these networks are in constant heavy use as they are exposed to heavy loading frequency. They are also subjected to an aggressive and severe environment, where the tunnel systems are huge and dark. These factors may increase the deterioration rates to be higher than anticipated.

The deterioration of subway networks presented significant challenges for public transit authorities and forced them to perform good asset management practices. The purpose of these practices is to maintain aging and obsolete facilities, amid the economic downturn that has caused huge cuts in their funding and increased the backlog of repair and rehabilitation. Table 2.1 presents the major existing subway transit authorities and their strategies for the condition assessment and rehabilitation of subway assets. Furthermore, the table shows the different criteria considered by these authorities during the evaluation process. From this table, it is shown that the Société de Transport de Montréal (STM) has implemented three programs named Réno-Stations I, Réno-Stations II and Berri Project in order to renovate some of the stations in Montréal subway network (STM 2011). Although the assessment of structural deterioration under these programs was carried out by expert visual inspectors at the component level and based on a 1 – 5 scale, no comprehensive models for the structural performance of stations or subway network were considered.

A different model was implemented by the Transit Authority of New York City named the Point Allocation System. Each station was evaluated according to different criteria after allocating points to each criterion. The prioritization for rehabilitation was determined by the summation of the allocated points for each station (Abu-Mallouh 1999). While this model considered the structural conditions of the stations, it was limited to stations and not the whole network; it also failed in describing the deterioration levels in these stations.

Table 2.1 Condition Assessment of Major Subway Transit Authorities

Subway Transit Authority	Year Opened	System Length (Km)	No. of Stations	No. of Lines	Evaluation/ Rehabilitation Program	Criteria Considered in the Evaluation
Société de Transport de Montréal (STM)	1966	69.2	68	4	Réno-Stations I Réno-Stations II Berri Project	Physical condition of subway elements Performance condition of subway elements
Metropolitan Transit Authority- New York City Transit (MTA NYCT)	1904	373	468	24	Point Allocation System	Structural conditions Daily usage Automatic fare control Intermodal American Disabled Agreement Developer funding potential Felonies Terminal station Security of outside funding Point of interest
California Train Transit (Cal Train)	1864	124.6	32	1	Station Evaluation Model	Accessibility of the station Location of the station and amenities Parking availability Connectivity with transportation modes Appearance and cleanliness Structural condition Information services Ticket vending machines Safety and Security
Washington Metropolitan Transit Authority (WMATA)	1976	188	91	6	Key Performance Indicator (KPI)	Customer satisfaction Customer injury rate Rail fleet reliability Escalator system availability Elevator system availability Employee injury Crime rate
London Transit	1863	402	270	11	Key Performance Indicator (KPI)	Cleanliness Information Services On-trains information, station services Safety and security Train services Staff
Paris Rapid Transit Authority (RATP)	1900	214	303	16	ELECTRE III Decision Support Model	Platform users Transit passengers Coordination of works Maintenance of wall and roof tiles Visual aspect of the station Level of discomfort Environment
Mass Transit Railway- Hong Kong (MTR)	1910	218.2	84	10	Key Performance Indicator (KPI)	Growth and learning Customer Internal processes Safety and security Financial performance Environmental performance

Another model was applied by California Train Transit, which is the Station Evaluation Model. Stations were evaluated according to several criteria, the weighted average of the criteria was calculated, then stations were ranked from excellent (1) - poor (5) (Abu-Mallouh 1999). This model had a similar limitation as the previous one since it failed in considering the entire network and in developing a deterioration model.

Key Performance Indicator (KPI) is the evaluation model used by three different authorities, Washington Metropolitan Transit Authority (WMATA), London Transit, and Mass Transit Railway of Hong Kong (MTR). KPI measures the performance of a station with respect to several criteria set by the authority, as shown in the table. In the case of Washington Metropolitan Transit Authority (WMATA), KPI represented a percentage of the most accomplished activities over planned (WMATA 2013). This methodology emphasized on many different elements; however, no indexes for building performance of the whole network were produced. On the other hand, KPI of London Underground represented the overall weighted average of 23 measures evaluated by the customers according to the determined criteria (Abu-Mallouh 1999). There is a drawback to the London Transit KPI method, that it did not develop a deterioration model. The KPI of Mass Transit Railway of Hong Kong (MTR) was not different from the two above mentioned KPIs since it did not generate any index or model for the network. This assessment program mainly used 36 key performance indicators, which measured the performance of metro network through the six categories shown in the table; it also used the benchmarking process to compare the performances of Hong Kong Metro network and the metro networks of 14 large cities in the world (MTR 2012). Another effort was made by the Paris Rapid Transit Authority (RATP) to rank the stations that should be renovated. The “ELECTRE III” decision support model and software was utilized in the

ranking process by considering the criteria listed in Table 2.1 (Roy et al. 1986). This model does not represent a deterioration model of the Paris subway network as well.

2.2 Concrete Degradation and Deterioration Mechanisms

2.2.1 Concrete Degradation

In the construction industry, concrete is considered one of the most versatile materials. This is due to its longevity, especially if the structure is well-built and appropriately maintained. However, several factors affect the structural integrity and thus the performance of the structure. Such factors include but are not limited to, harsh environmental conditions, chemical pollution, external loading, insufficient material selection, unskilled workers, and disastrous natural events. Subsequently, various deterioration mechanisms may act instantaneously, and the synergic consequences may cause the degradation and deterioration of the facility. Concrete degradation may be featured as an internal, external, or combined distresses. These distresses participate not only in degrading the structure aesthetically but in hindering its functionality (Jain and Bhattacharjee 2012). Figure 2.2 shows concrete degradation in various Montréal subway systems.

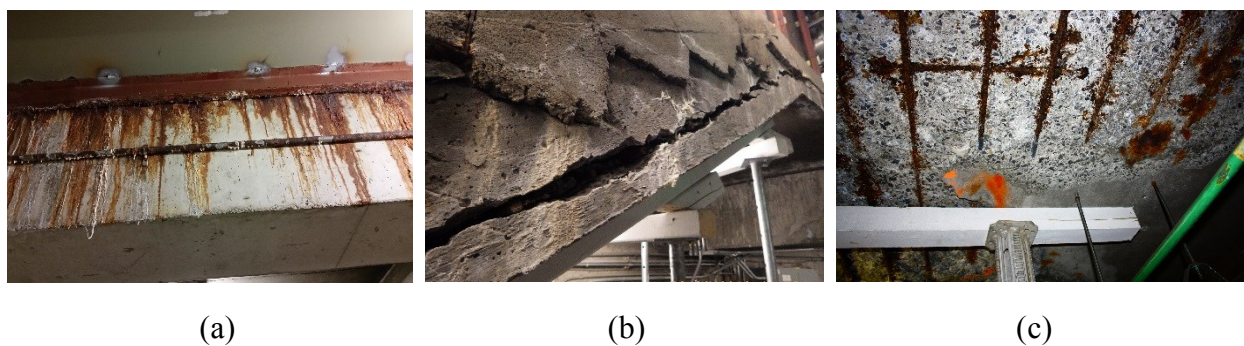


Figure 2.2 Concrete Degradation in Different Montréal Metro Stations (a) Water Overflow and Moisture Marks; (b) Wide Cracks in Stairs Structure; (c) Corrosion and Delamination in Concrete Floor Slab

Some defects such as the cracks may exist in a newly-constructed Reinforced Concrete (RC) structure even if the facility is not exposed to any loading frequency. This is due to substandard construction practices, i.e., excess water to cement ratio, rapid curing, and drying stage under high temperatures. Such practices may cause the concrete to shrink, which is the main cause of cracking. These early-developed cracks in concrete may widen and worsen later on after the facility is subjected to different loading severity. Additionally, the concrete distress is more accelerated by the environmental conditions such as water intrusion, de-icing salt, corrosion of steel reinforcement, and freeze and thaw cycles, which eventually lead to the spalling of concrete due to the buildup of tensile stresses (Rhim 2001; Gucunski et al. 2010). Figure 2.3 illustrates the previously explained process in nine phases.

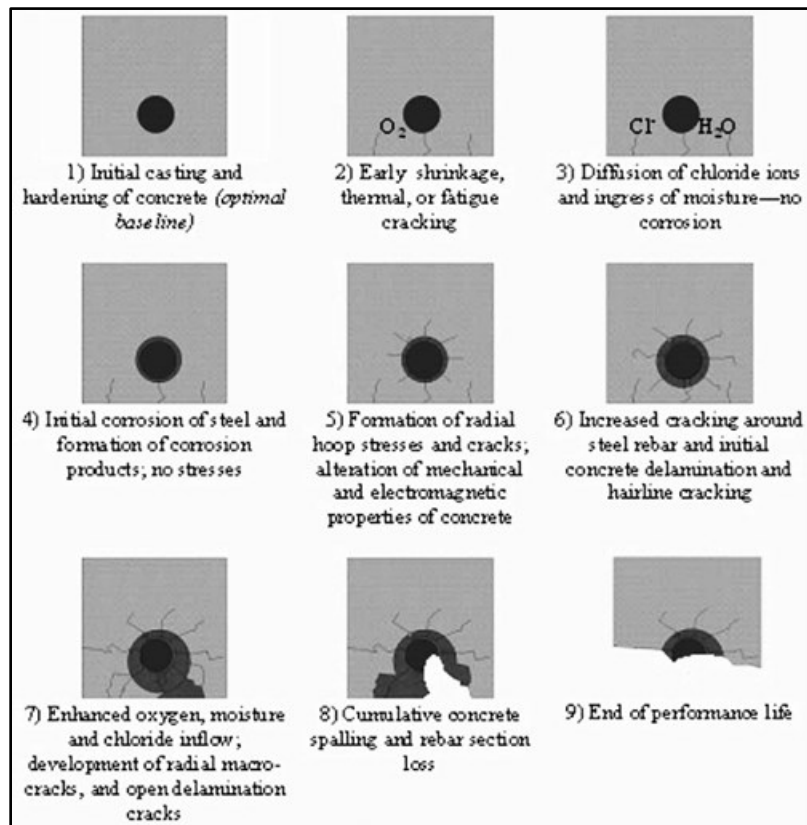


Figure 2.3 Phases of Chloride-Induced Corrosion (Arndt et al. 2010)

2.2.2 Subway Deterioration Mechanisms

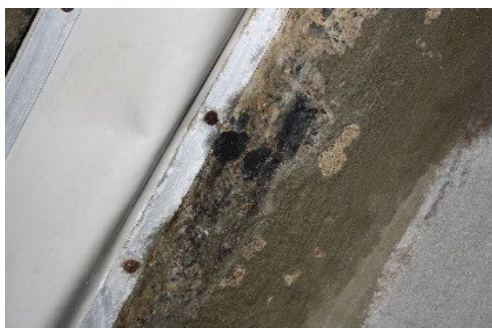
Subway networks are subjected to severe environmental conditions, as well as constant heavy loads, which increase the deterioration mechanisms of their components. Various types of deterioration mechanisms may develop on or sub the surfaces of concrete subway elements during their service life. Some of these distresses are superficial, which cause no major threat to the structural integrity or public safety, such as hairline (minor) cracks or concrete scaling. But some of them impose potential internal stresses, which might damage the structure and lead to the loss of concrete bond over the rebar layer of what's known as delamination. Defects may develop on the surfaces or sub surfaces of RC structures. Surface distresses include moisture marks, spalling, cracks, etc. While subsurface distresses include delamination and reinforcement corrosion. Examples of surface defects are shown in Figure 2.4.



(a) Cracks on Lower Slab



(b) Moisture Marks on Upper Slab



(c) Scaling on Upper Slab



(d) Spalling on Lower Slab

Figure 2.4 Different Surface Defects in Subway Networks (Dawood et al. 2015_a)

Water Leakage

Major large cities in the world have several tunnels running under rivers, as in the case of the Société de Transport de Montréal (STM), and the Metropolitan Transit Authority-New York City Transit (MTA NYCT). Leakage of water or infiltration has been considered the most serious problem and the main cause of concrete degradation. Five transit agencies in the United States along with the STM in Canada have reported that water leakage is the most significant structural issue, and it has been classified as the first priority among other problems (Russell and Gilmore 1997; Chaussée 2012) as shown in Table 2.2.

Table 2.2 Problem Priorities in Transit Infrastructure (Russell and Gilmore 1997)

Transit Agency	Priority #1	Priority #2	Priority #3
MTA of Maryland	Tunnel Leaks	Concrete Cracking	Concrete Spalling
BART	Tunnel Leaks	Concrete Cracking	Steel Corrosion
CTA	Tunnel Leaks	Concrete Cracking	Delamination
MTRC	Tunnel Leaks	Concrete Spalling	Concrete Cracking
NYCT	Tunnel Leaks	Subway Drainage	Concrete Spalling

A huge amount of water leakage in a subway system accelerates the deterioration rate and subsequently causes the closure of its facilities, as what happened in Montréal Metro's Yellow Line that passes under the St-Laurence River. Water infiltration through concrete structure ceased the use of the line for 25 weekends. Other structural defects facing transit authorities are derived from water intrusion, among others are moisture marks, cracking, spalling, corrosion of reinforcing steel bars, and delamination.

Moisture Marks

Moisture marks also known as wet areas are formed by water ingress through thin cracks in concrete. When the water reaches the concrete surface, it evaporates leaving white deposits of salty exudations. Although moisture marks distress is not regarded as a structural problem, a regular inspection and monitoring of the structure are required because it may indicate the volume of water intrusion through concrete. Hence, if this amount exceeds a certain limit, it may give a warranting signal of a serious deterioration or damage in the facility.

Spalling

Spalling takes place when a chunk of concrete on the surface breaks away. This defect is initiated as the stress in concrete surpasses the design capacity, generating long and wide cracks within the concrete. As the deterioration mechanism develops, it will cause structural disintegration that may eventually result in a loss of a piece of concrete. Spalling affects the aged concrete and could be caused by many reasons, such as the corrosion of steel bars. As the oxidized layer is formed and become greater in size, it will exert an expansive force on the adjacent concrete causing it to detach and break away. Also, spalling could be caused by concrete aggregates that absorb excessive moisture. The expansion and contraction of this moisture during the freeze-thaw cycles will cause the concrete to bulge and thoroughly results in a loss of a piece of concrete (Kabir 2008).

Scaling

Scaling occurs when portions of the concrete surface layer or mortar peel away. This deterioration mechanism happens because of the intrusion of salts from de-icing chemicals into concrete, which will release large magnitude thermal strains. Consequently, the layer may manifest flaking and become detached when the generated stresses are greater than the tensile strength that keeps the layer attached to the substrate (Mindess and Young 1981; Pigeon and Pleau 1995).

Scaling might affect large areas of concrete infrastructure, or its effect might be limited to isolated locations where air voids or water voids exist near the surface. It might not even be shown until other factors like passing vehicles breakdown the separated layer into fragments (Kabir 2008).

Cracking

Cracks in underground facilities may develop due to the environmental conditions such as water leakage, or human-made conditions such as impact forces caused by pile drilling from neighboring construction, or as a result of continuous vibration caused by moving trains on rail tracks. Although this vibration is considered minor in its magnitude, it might cause tensile or compressive stresses in the walls and other subway components, leading to the immediate destruction of mechanical equipment (Delatte et al. 2003). Cracks monitoring and maintenance present substantial challenges for engineers and subway authorities as they may affect the structural integrity and permit more water leakage, thus damaging tunnel liners.

Steel Corrosion

Corrosion of rebars in RC structures has always been considered the major problem that triggers several subsequent distresses, especially after some timespan. Actually, in newly-constructed RC structures, reinforcing steel bars are wrapped in an alkaline cement coating, which is acting as a passive oxide film that surrounds the steel bars, thus protecting them from corrosion. The passivity

property of the film could be preserved if the PH levels are maintained above 9. Nevertheless, as the structure ages, passivity is destroyed, and corrosion starts to activate due to two major factors: carbonation, and chloride contamination (Penttala 2009). Figure 2.5 illustrates the initiation of rebar corrosion caused by carbonation.

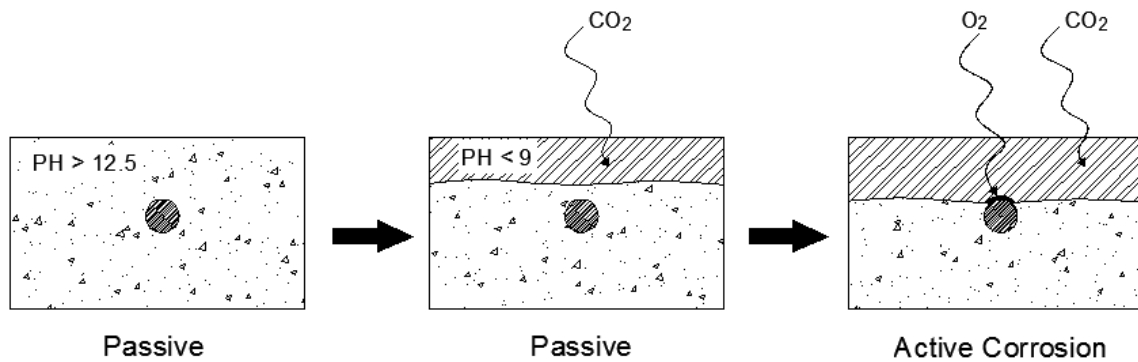


Figure 2.5 Carbonation-Initiated Corrosion (Adapted from Penttala 2009)

If the hygrometric conditions of the structure are stable, the depth of the carbonation layer from the concrete surface could be calculated according to Equation (2.1). Where, x is the carbonation depth in (mm), k is the carbonation coefficient in ($\text{mm}/\text{year}^{0.5}$), and t is the exposure time in (years) (Penttala 2009).

$$x = k \times \sqrt{t} \quad (2.1)$$

Air Voids

In hardened concrete (HC), an air void is a spherical or irregularly shaped air bubble that exceeds 1 mm in dimension and is contained in the cement paste. The physical aspects of voids such as shape, size, frequency, type, and spacing, are of great importance as they control several concrete properties, i.e., compressive strength, resistance to the chemical attack on the rebars, and resistance to freezing and thawing damage. Generally, air void percentage is specified upon designing the mixture. It is recommended that a large number of very small air voids are produced in the paste

so that proper air distribution is created through shortening the distance between air voids. Hence, protecting the paste from freezing and thawing cycles. A ratio of air void volume to paste volume that surpasses a specific limit may generate channel ways for the infiltration of water and the penetration of harmful substances, which may in turn, weaken the HC and affect its integrity. The compressive strength of concrete is lowered by around 5% for each excessive air void content. On the other hand, the decrease of spacing between air voids will participate in the protection of concrete against damage caused by freezing and thawing mechanisms (FHWA 1997).

Water Voids

Water void is an irregular shaped pocket whose dimension surpasses 1mm. The form, location, and interior surface of water void indicate that it is generated by water. These voids encompassed water when the concrete is unhardened. Consequently, water is trapped and prohibited from rising to the surface as a result of paste hardening or the existence of mixture aggregates. The unusually large amount of water voids found in fresh concrete indicates a defect caused either by craftsmanship or concrete mixture proportions. In subway networks, water voids are found behind concrete liners as a result of water infiltration through the soil. Leakage of water or infiltration is considered the most serious problem and the main cause of concrete degradation, especially in subway networks constructed under rivers. A huge amount of water leakage through soil accelerates the deterioration rate because of the high concentration of water between the rock and concrete as in the case of Montréal subway network.

2.3 Previous Subway Assessment Models

Condition assessment of an asset is the procedure with which the nature and level of the physical degradation are identified and documented; this might also include listing the details of any repair work and the related costs (Brandt and Rasmussen 2002). Therefore, a historical record of the

asset's health will be established (Hammad et al. 2003), which may provide essential inputs for future maintenance planning or risk assessment. It can determine the hidden causes of visible defects before the problem will progress to a significant level of severity.

Many endeavors have been made previously to assess the condition of subway systems. Semaan (2006) developed a condition assessment model known as "SSDI" to diagnose and assess the conditions of subway stations. This model has defined functional criteria and applied the Analytic Hierarchy Process (AHP) in order to calculate their weights. Then, the Preference Ranking Organization Method of Enrichment Evaluation (PROMETHEE) was used to find the aggregation of weights and scores. And finally, Station Diagnosis Index (SDI) was calculated using the Multi-Attribute Utility Theory (MAUT), and a condition scale for the evaluation of each station was proposed. This model was applied later on Montréal Metro stations. As described by the author, the model was developed only for stations and cannot be applied for tunnels, auxiliary structures or the entire network. The SSDI model is a diagnostic model, thus it does not evaluate the station's structural deterioration over time. Also, this framework was capable of assessing surface defects based on visual inspection reports. Therefore, the severity of defects was not investigated.

Subsequently, another model, which is called the "SUPER model" was proposed by Semaan (2011) to assess the performance of subway network. First, the subway network was broken down into its components. Second, the physical and functional performances of each component in the network were assessed and integrated into one performance index using the AHP and MAUT theory. Third, Performance prediction curves for all the components in the network were constructed using a Weibull reliability function. And finally, the series-parallel system technique was leveraged to evaluate the performance of various systems, lines, and the whole network. This model was implemented in the Montréal subway network. Although this was the first attempt to

evaluate the condition of subway networks, it was characterized as subjective since it relied on visual inspection reports in assessing the structural performance of subways. Moreover, it did not provide a comprehensive model that considers both the visible and hidden defects.

Kepaptsoglou et al. (2012) presented a model to evaluate the functional condition of subway stations; this model was applied to Athens Metro systems. Several criteria and sub-criteria were allocated to every station. The AHP and Fuzzy AHP techniques were utilized to rank the sub-criteria according to their significance to the station's operational phase. The sub-criteria were weighted and evaluated on a scale of 0-5 by Athens Transit Authority. Then, their scores were aggregated with the use of MAUT to get the Metro Condition Index (MCI). This model was developed solely for the condition assessment of subway stations. Hence, it failed in evaluating the whole network. Although criteria weights were determined on the basis of expert opinions, this research lacked the objectivity in quantifying and estimating the severity of defects.

In order to enhance the previous model and attain the interdependencies among its criteria, Gkountis and Zayed (2013) applied the Analytic Network Process (ANP) and used the same 0-5 scale. Then, the additive MAUT was implemented to acquire the station's condition index. However, this model had the same limitations as the previous one in spite of utilizing the ANP technique to augment its accuracy.

Abu-Mallouh (1999) developed a "Model for Station Rehabilitation Planning" so-called "MSRP" in an effort to improve the "Point Allocation Model" implemented by the MTA NYCT. The MSRP considered the same functional and social criteria used by New York Transit Authority. The Analytic Hierarchy Process (AHP) technique was applied to obtain weights for the stations. For rehabilitation planning, a powerful optimization technique (Integer Programming) was used to allocate budget for the stations. The weights and budget allocation were later utilized to prioritize

stations for rehabilitation. In fact, the MSRP is a budget allocation model rather than a condition assessment or a deterioration model, and it is only limited to the evaluation of stations. Furthermore, it did not use real collected data for the validation process.

Another model “Maintenance and Rehabilitation Planning for Public Infrastructure” namely “MRPPI” was proposed by Farran (2006) and implemented in the Montréal subway stations. This methodology considered life-cycle cost analysis of the structural elements in concrete infrastructure. It applied Markov Chains theory to evaluate the deterioration of the elements and utilized transition probability matrices as input variables to the model. Consequently, Genetic Algorithm (GA) optimization technique was employed to minimize the life-cycle cost after establishing a series of intervention actions. Several drawbacks were noticed in the MRPPI model, such as it is not an integrated model since it was applied to solely one component of the metro station (slab). Besides, it required a huge amount of data that make it impractical to be applied in the rehabilitation planning process.

A network design model was generated by Derrible and Kennedy (2010) and implemented on Toronto Metro system. This schematic model was developed by computing three major factors including coverage, directness, and connectivity. Numerous variables were investigated in the computing process, including covered area, ridership, possible transfer options, and a number of lines. The objective of this study was to improve the efficiency and ridership of Toronto Metro network by assessing its performance, as well as, comparing it to other subway networks. Despite the attempt of the researcher to evaluate the subway on a network level, the study did not deliver a condition assessment model that tackles the structural performance of subway networks.

Marzouk and Abdel Aty (2012) created a Building Information Modeling framework for the maintenance of subway infrastructure using BIM. Various asset management indicators were

included in the body of this research, such as the structural integrity, mechanical systems, HVAC systems, electrical system, and user-related indicators. The model aimed at offering a solid background by proposing BIM flowchart that considers the indicators as prepared inputs to a comprehensive BIM/Asset management model. However, their system was ambiguous in describing the proposed indicators, and it didn't consider any distresses or deterioration options in subway structures.

Abouhamad (2014) developed a risk-based asset management framework for subway networks. The study has proposed two main models namely; fuzzy risk index model and risk-based budget allocation model. In the first main model, the risk was evaluated using three sub-models; the probability of failure, consequences of failure, and criticality index. The probability of failure for several structural components was evaluated based on inspection reports and Weibull reliability function. Consequences of failure were evaluated through seven attributes, including revenue loss, replacement/repair cost, user traffic frequency, interruption rate, service continuation, ease of providing an alternative, and time to repair. Consequently, criticality index was computed using seven criteria, including a number of lines, number of exits, recreational locations, vital locations, residence locations, intermodal station, and end station. And finally, the second main model was proposed, which is a budget allocation model. It delivered recommendations to prioritize stations for rehabilitation action and applied two sets of variables, the risk index components and decision variables represented by cost, time, and percentage improvement. This model was subjective due to its reliance on the expert's judgments and feedback. In addition, as the author mentioned, it might not guarantee the coherence to in-depth analysis. Also, the model needs to be validated using an extensive and real-life dataset.

2.4 Automated Defect Detection and Assessment Models

Computer vision-based techniques have gained a lot of momentum during the last two decades, which can be seen in their multiple applications in the industry as well as in academia. These techniques are specifically applied for the detection and evaluation of distresses in civil infrastructure. In this regard, the mainstream of research pertains to the field of bridges, La et al. (2014) presented a crack detection and mapping algorithm for bridge deck data collected via a robotic system. Adhikari et al. (2013_a) proposed a model for crack quantification in bridges supported by artificial neural networks and 3D visualization models. Abudayyeh et al. (2004) developed an automated bridge inspection system based on imaging data and integrated with the Bridge Management Systems PONTIS.

Further progress has been achieved in the field of computer vision, especially when it's complemented with various nondestructive evaluation technologies. Examples of such studies can be found in the pavement defect inspection; Li et al. (2016_b) designed an integrated framework for the detection and measurement of potholes on the basis of 2D images and Ground Penetrating Radar (GPR) data. Yu and Salari (2011) introduced a laser-based detector and classifier for pavement defect inspection. Koch and Brilakis (2011) presented a pothole detection method that involved image thresholding, morphological thinning, elliptic regression, and texture extraction.

The remainder of the research extends through a proliferation of applications in water pipes, wastewater, road tunnels, and civil structures in general. Atef et al. (2015) utilized a multi-tier technology to locate water pipes and detect leaks based on the image processing of captured Infrared (IR) and GPR images. Guo et al. (2009) presented a condition assessment approach of wastewater systems grounded in visual pattern recognition techniques. Yu et al. (2006) devised a system for inspecting and measuring tunnel cracks, the system comprised of a mobile robot and a

crack processor. Zhu (2011) retrieved critical structural defects from images and utilized multiple computational mechanics for column recognition and rehabilitation of civil infrastructure. Jahanshahi et al. (2013) incorporated depth perception, image processing, and pattern recognition for the purpose of crack detection and quantification. Hutchinson and Chen (2006) proposed a statistical procedure for the detection of cracks through utilizing Bayesian Decision Theory.

The majority of these studies relied on identifying the unique properties of defects in developing their models. For example, German et al. (2012) considered four visual appearances in the automatic detection of spalled regions on concrete columns. Such features include: 1) an extremely textured region; 2) ribbed texture on the surface of exposed rebars; 3) rebars' distinguished color; and 4) rebar's width should be proportionally less than column's width/height ratio. In a study to detect pavement potholes, Koch and Brilakis (2011) determined three distinctive visual features, including: 1) one or more shadows should be comprised in the pothole area; 2) pothole shape is presumed to be elliptical; and 3) pothole texture is much coarser than the surrounding pavement area. Jahanshahi and Masri (2011) proposed a crack detection approach for civil structures by extracting five features, namely; eccentricity, area, solidity, compactness, and correlation coefficient. The aforementioned efforts indicate that there still remain gaps in the body of knowledge since the majority of automated models in Reinforced Concrete (RC) structures have focused on the detection and evaluation of cracks and potholes. However, little research work has been accomplished in the context of other surface defects such as moisture marks, scaling, and spalling.

In this respect, Adhikari et al. (2013_b) simulated on-site visual inspection by creating a 3D model of a de facto bridge, followed by overlaying 2D digital images on the developed model to get the bridge condition index. German et al. (2012) retrieved the major properties of spalled regions on

concrete columns subsequent to detecting the defect in an attempt to assess the safety of post-earthquake buildings. First, the images were thresholded by means of a local entropy-based algorithm. Second, the spalling depth and length were evaluated using global adaptive thresholding algorithm. Third, template matching and morphological operations were performed. Nevertheless, these two studies did not address accurately how the geometrical measurements of defect were computed. Thus it was unclear how to evaluate the severity of spalling defect. On the other hand, there is a scarcity of research regarding the automatic detection and evaluation of scaling and moisture marks defects in civil infrastructure.

2.5 Modelling Techniques used in the Research

In this research, multiple techniques are applied to achieve its ultimate objectives. Such techniques include but are not limited to; Image Processing (IP), Artificial Neural Networks (ANNs), Regression Analysis (RA), Fuzzy Inference System (FIS), Adaptive Neuro-Fuzzy Inference System (ANFIS), Monte Carlo Simulation (MCS), and Non-Destructive Evaluation (NDE) techniques.

2.5.1 Image Processing Techniques

Digital image processing refers to those techniques whereby image features are extracted for the purpose of measuring and quantifying discrete objects in the image. In general, image processing is used to enhance the quality of the image by removing the noise within the image frame. Proper processing is a significant step in preparing the images to be used for specific purposes, such as machine learning and data mining.

These techniques utilize the images as inputs and outputs in the process. The term “image” could be defined as a two dimensional (2D) function $f(x, y)$, where f denotes the gray-level or intensity of the image at a spatial coordinate point (x, y) that corresponds to each pixel in the image

(Gonzalez and Woods 2008). The image is formed when a light reflected from an object is captured by an optical device (i.e., camera), thereby a 2D representation of the image is formed on the image plane (Looney 1997). Generally, the images are either gray-level images or color images. A gray-level image is a black-and-white image that has one matrix only, and the elements of the matrix represent pixels' intensity values. Figure 2.6 shows the matrix of a gray-level image. The color image is an RGB image that is formed of three planes: red, green, and blue; each plane has its own matrix. Normally, RGB images are converted to gray-level images to facilitate image enhancement and detection processes. RGB images are commonly used in image processing and computer visual applications. (Pratt 1978; Smith 1978).

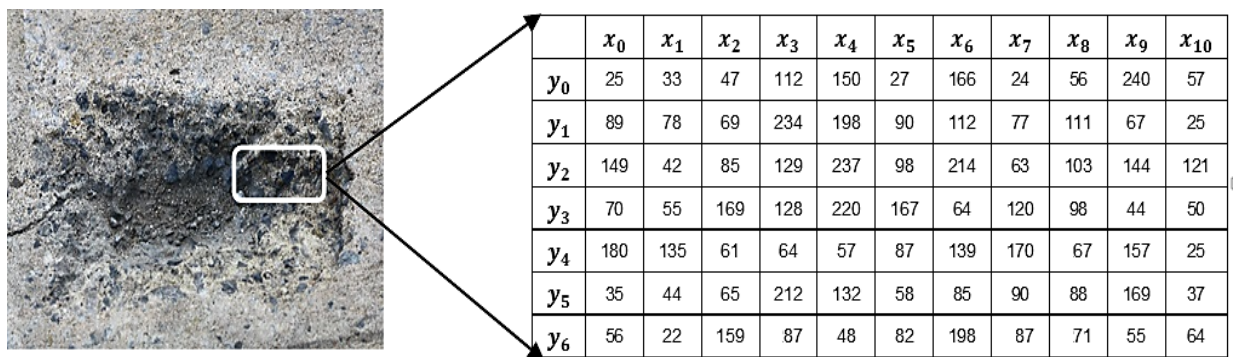


Figure 2.6 Gray-level Image and its Matrix

2.5.1.1 Image Preprocessing in the Spatial Domain

Spatial filters are used to enhance image quality by suppressing some image frequencies while permitting others to pass. For each pixel, filter functions are applied to calculate a new value based on its neighboring pixels' values. The output of this process is dependent on the size and type of kernel utilized in the filter. Generally, there are two types of spatial filters: 1) Low-pass filters, 2) Median filters.

Low-pass filtering minimizes image deviations by computing the averages of neighboring values, thus suppressing high frequencies and allowing low frequencies to pass. This process will result in smoothing the grayscale image, and it is proportional to the kernel's size. Whereas, median filtering smooths the image by replacing center pixel values with the computed median values of the neighboring pixels while it preserves edge pixel values bigger than the kernel size.

Image segmentation is one of the most significant methods in spatial preprocessing. It's the subdivision of an image into regions or objects. Grayscale thresholding is the fastest and most applicable method worldwide in segmenting image features (Gonzalez and Wintz, 1987). Through thresholding, the object of interest (OOI) is separated from the background of the image. This could be conducted by selecting an intensity level value T provided that all other image pixels having $f(x, y) > T$ will be classified as object pixels (Russ and Woods 1995; Weeks 1996). The goal of thresholding is to reduce the multiple gray-levels of the image into two gray-levels (i.e., black and white). This process is known as binary transformation, accordingly matrix elements of a binary image will have either zero or one value.

The selection of the best threshold value of a gray-scale image is associated with histogram equalization. Several image processing operations in the spatial domain depend on histogram manipulation, mainly for image enhancement, segmentation, and compression (Gonzalez and Woods 2008). Usually, selecting the value T is a trial-and-error method that takes into consideration human intervention to decide if this technique has extracted the necessary object attributes (Russ and Woods 1995). Histogram equalization technique is performed to automatically enhance the contrast of the grayscale image for the purpose of generating a new image with equal brightness levels. The contrast becomes bigger as brightness values are closer to the histogram maxima and vice versa (Rosenfeld and Kak 1982).

2.5.2.2 Image Preprocessing in the Frequency Domain

Filtering in the frequency domain involves adjusting the Fourier transform of an image, followed by calculating the inverse transform to produce the output image. Therefore, for a digital image $f(x, y)$, of size $M \times N$, the filtering will be in the form of Equation (2.2) (Gonzalez and Woods 2008).

$$g(x, y) = \mathfrak{F}^{-1}[H(u, v)F(u, v)] \quad (2.2)$$

Where, \mathfrak{F}^{-1} is the Inverse Discrete Fourier Transform (IDFT), $F(u, v)$ is the Discrete Fourier Transform (DFT) of the original image, $f(x, y)$, $H(u, v)$ are filter transfer functions, and $g(x, y)$ is the processed (filtered) image.

Generally, frequency filters are used for smoothing (blurring) and sharpening purposes. Smoothing is accomplished by utilizing low-pass filters that attenuate the high-frequency modules of Fourier transform. There are three categories of low-pass filters: 1) Ideal low-pass filters, 2) Butterworth low-pass filters, 3) Gaussian low-pass filters. These categories vary from very smooth as in the Gaussian filter to very sharp as in the Ideal filter, while Butterworth filter signifies a transition between the smoothness of the Gaussian filter and the sharpness of the Ideal filter. On the other hand, sharpening is achieved by applying high-pass filters that attenuate the low-frequency modules without affecting high-frequency data in the Fourier transform. Also, three categories of high-pass filters are considered: 1) Ideal high-pass filters, 2) Butterworth high-pass filters, 3) Gaussian high-pass filters. As discussed above, the categories of high-pass filters cover the same range between the smoothness of the Gaussian filter and sharpness of the Ideal filter (Gonzalez and Woods 2008).

The Gaussian low-pass filter is one of the most widely-used filters in computer vision. This blurring technique reduces the high-frequency components of the image, and the process is

accomplished using a convolution kernel or a weighed kernel. The Gaussian blur algorithm might be slow as its processing time depends on the image size and the kernel size. It uses convolution with a Gaussian function to smooth and enhance image structures, and it's built on the hypothesis that higher weights are given to pixels closer to the image frame rather than pixels inside the image, and higher weights to pixels at the corners rather than non-corner pixels in the image frame. Therefore, when a convolution operation is conducted with a very large blurring radius, edge pixels and specifically corner pixels will dominate the mapped result (image J).

2.5.2 Artificial Neural Networks (ANNs)

Artificial neural networks are considered one of the most popular supervised learning techniques that can recognize the pattern between input and output datasets (Momeni et al. 2015). ANNs have been designed on the basis of the human nervous system, as they mimic the function of the human brain in processing the information and they are very fault tolerant systems (Patterson, 1996; Tsoukalas and Uhrig (1997). Therefore, many researchers have been inspired to study and explore their computational capacities, specifically to identify and measure the extent of damages in structures. Dawood et al. (2017_b) incorporated image processing and ANNs to detect and recognize moisture marks defects in subway networks. Kilic and Unluturk (2014) applied the backpropagation neural networks to classify GPR profiles and detect moisture ingress in bridges. Adhikari et al. (2013_a) proposed a model for crack quantification in bridges supported by artificial neural networks and 3D visualization models. Zhu (2011) retrieved critical damage attributes from images and employed multiple computational mechanics including ANNs for column recognition and rapid infrastructure assessment. A multi-layer perceptron ANNs were leveraged by Kabir (2008) to classify thermographic, color, and grayscale imagery in an effort to assess the ANN efficiency in identifying concrete defects. Al-Barqawi and Zayed (2006) integrated Analytic

Hierarchy Process (AHP) and ANN to evaluate the condition and predict the performance of water mains. Xu and Humar (2006) developed a method to calculate a modal energy-based damage index, then estimated the severity of damages in a girder bridge based on ANNs.

In recent years, several ANN models have been developed and applied in different scientific fields; however, the Multi-Layer Perceptron (MLP) is considered the most powerful system (Sarle 1994). Usually, the multi-layer perceptron has three layers, input, hidden, and output layer as represented in Figure 2.7. Each layer includes a number of neurons that are connected to the neurons of the neighboring layer through connections. These connections have weights that are multiplied by the inputs of the preceding layer, followed by summing up the result with a bias value to obtain the net value (Moselhi et al. 1991).

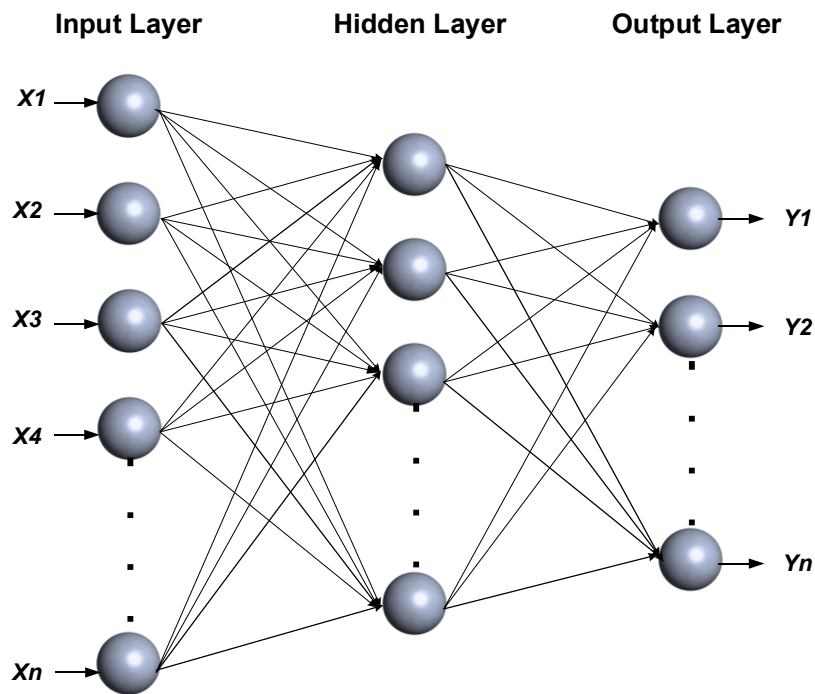


Figure 2.7 MLP Neural Network (Dawood et al. 2017_b)

Therefore, for a d -dimensional feature vector, the neuron has $d+1$ inputs, and the 0^{th} input, which functions as a bias of the neuron, has a value of 1 and a related weight of w_0 . The output of the

neuron, which is called the *net*, is computed by summing up its weighted input values and then multiplying the result by the activation function f according to Equations (2.3) and (2.4) respectively (Polikar 2006).

$$net = \sum_{i=0}^d w_{ji} x_i = \mathbf{x} \cdot \mathbf{w}^T + w_0 \quad (2.3)$$

$$y = f(net) \quad (2.4)$$

2.5.3 Regression Analysis (RA)

Regression analysis is a statistical approach that analyzes and models the relationships between two or more variables to predict the response variables from predictor variables. The simplest form of this relationship is a linear regression model that is postulated in Equation (2.5) (Chatterjee and Hadi 2012):

$$Y_i = \beta_0 + \beta_1 X_i + \varepsilon_i \quad (2.5)$$

Where, Y_i is the response variable in the i th trial, β_0 and β_1 are the model regression coefficients, X_i is the predictor variable in the i th trial, and ε_i is the random disturbance or error.

In the case when there is more than one predictor variable, the model is called a multiple regression and the generic form of this relation is expressed in Equation (2.6) (Kutner et al. 2005):

$$Y_i = \beta_0 + \beta_1 X_{i1} + \beta_2 X_{i2} + \dots + \beta_{p-1} X_{i,p-1} + \varepsilon_i \quad (2.6)$$

Normally, the values of the regression coefficients $\beta_0, \beta_1, \beta_2$, etc. in Equation (2.6) are unknown and must be estimated from related data. Since there exist no prior information about the proper predictor variables and the form of regression relationship (e.g., linear or curvilinear), it is of utmost importance to analyze the data in order to develop an appropriate regression model.

There exist several methods to check the forms of linearity by observing the curvatures in different plots, such as looking at the scatterplot of residuals as opposed to the fitted values. Moreover, checking the scatterplot of residuals against each predictor. If the scatterplot proposes a curvilinear relationship, it means this is a polynomial regression model. The mathematical definition of this model is presented in Equation (2.7) (Kutner et al. 2003):

$$Y_i = \beta_0 + \beta_1 X_{i1} + \beta_2 X_{i1}^2 + \cdots + \beta_h X_{i1}^h + \varepsilon_i \quad (2.7)$$

Where, h is the degree of the polynomial equation, and the relationship is called quadratic when $h = 2$, cubic when $h = 3$, quartic when $h = 4$, and so forth. Although the polynomial regression fits a non-linear relationship between the response variable and Predictor variable, it is recognized a linear regression model.

Dawood et al. (2016, 2017_a) developed an automated framework to detect and quantify spalling distress in subway infrastructure by fusing a hybrid algorithm and regression analysis. Senouci et al. (2014) leveraged a regression modeling technique and ANNs to predict the failure cause of oil pipelines. Kim et al. (2013) estimated the construction cost of school building projects grounded in three techniques, i.e., regression analysis, ANNs, and support vector machine. Cheng et al. (2012) studied the effect of the three safety management practices on a combined project performance using hierarchical regression analysis. Hwang (2009) predicted the changes in construction costs via the development of two dynamic regression models. Wang et al. (2009) presented five multiple regression models to predict the annual break rates of water mains. Chughtai and Zayed (2007) assessed the operational condition of sewers through a multiple regression model. Koo and Ariaratnam (2006) evaluated the severity of damage in an underground pipe using logistic regression.

2.5.4 Fuzzy Set Theory and Fuzzy Inference System (FIS)

Infrastructure assessment results have inherently certain degrees of vagueness and uncertainty. The fuzziness may appear due to the vagueness in the linguistic form of defining the severity of defect, imprecision of surveying conditions, and so forth. One of the best techniques for dealing with these kinds of problems is the application of Fuzzy Set Theory. This theory is capable of overcoming the limitations of imprecision, imperfection, vagueness, and uncertainty of data. Thus, it may translate the severity level of a structure to condition rating (Rajani et al. 2006), and it enables modeling the expertise in more precision, more human-like way.

Fuzzy Set Theory was first introduced by Zadeh in 1965. The theory is based on assigning a membership function (MF) to the vague set of objects. Each membership defines the degree an object belongs to a fuzzy set, and it covers a range between 0 and 1. Various forms of membership functions (MFs) could be assigned to different sets. Among the most popular forms are; triangular, trapezoidal, Gaussian, bell, and Sigmoid (Jang et al. 1997). A triangular MF of one dimension is determined by three parameters $\{a, b, c\}$ with, $a < b < c$ define the x coordinates of the three corners of the implicit triangular MF. This MF is characterized in Equation (2.8).

$$\text{Triangle } (x; a, b, c) = \begin{cases} 0, & x \leq a \\ \frac{x-a}{b-a}, & a \leq x \leq b \\ \frac{c-x}{c-b}, & b \leq x \leq c \\ 0, & c \leq x \end{cases} \quad (2.8)$$

A trapezoidal MF of one dimension is determined by four parameters $\{a, b, c, d\}$ with, $a < b \leq c < d$ define the x coordinates of the four corners of the implicit trapezoidal MF. The form of this MF is expressed in Equation (2.9).

$$\text{Trapezoid}(x; a, b, c, d) = \begin{cases} 0, & x \leq a \\ \frac{x-a}{b-a}, & a \leq x \leq b \\ 1, & b \leq x \leq c \\ \frac{d-x}{d-c}, & c \leq x \leq d \\ 0, & d \leq x \end{cases} \quad (2.9)$$

A Gaussian MF of one dimension is determined by two parameters $\{c, \sigma\}$, as c denotes the MF's center, and σ denotes the MF's width. Equation (2.10) describes the parameters of this MF.

$$\text{Gaussian}(x; c, \sigma) = e^{-\frac{1}{2}\left(\frac{x-c}{\sigma}\right)^2} \quad (2.10)$$

A bell membership function of one dimension is determined by three parameters $\{a, b, c\}$, where b is usually positive. In the condition b is negative, the MF takes the upside-down shape bell. Equation (2.11) models the form of this MF.

$$\text{Bell}(x; a, b, c) = \frac{1}{1 + \left|\frac{x-c}{a}\right|^{2b}} \quad (2.11)$$

A sigmoidal membership function of one dimension is determined by two parameters $\{a, c\}$, where a controls the slope at the edge point $x = c$. This MF is defined mathematically in Equation (2.12).

$$\text{Sig}(x; a, c) = \frac{1}{1 + \exp[-a(x-c)]} \quad (2.12)$$

The concepts of Fuzzy Set Theory formed the basis to develop a new computation framework so-called The Fuzzy Inference System (FIS). The framework encompasses a set of fuzzy rules that are defined by membership functions (MFs). The fuzzy inference engine evaluates the rules and maps input variables to output variables. The most commonly utilized FIS is the Mamdani

technique, which is grounded in expert knowledge, as a more intuitive manner in describing the human cognitive approach. The Mamdani fuzzy inference technique could be summarized in the following steps (Esragh and Mamdani 1981):

1. Fuzzification of input variables.
2. Fuzzy reasoning and rule evaluation.
3. Aggregation of fuzzy outputs.
4. De-fuzzification.

2.5.5 Neuro-Fuzzy Technique

Several construction management types of research require applying the ANN technique to infer outputs from the inputs based on training the network. However, some problems involve fuzzy input and output datasets. Therefore, the ANNs and fuzzy logic are fused to customize one platform of what is called the neuro-fuzzy technique. The Sugeno type neuro-Fuzzy estimator is known as Adaptive Neuro-Fuzzy Inference System (ANFIS) and was first presented by Jang (1993). The hybrid learning scheme of ANFIS relies on generating a Fuzzy Inference System (FIS) that includes input and output fuzzy sets, defining the fuzzy membership function for each, creating the rule knowledge base, and determining how the process is carried out (McNeill and Thro 1994). The ANFIS works similarly to artificial neural networks (ANNs) as it learns the pattern between the stipulated input and output datasets, then it computes the MFs that are tailored to input/output datasets. As input and output variables are loaded to the ANFIS structure, the ANFIS toolbox starts constructing an FIS along with membership parameters. Such parameters are tuned by using only a back propagation method or by combining this method with a least squares algorithm system. Parameters tuning allows for the learning and modeling process of the fuzzy estimator from the data entry (Mathworks 2013). Among the advantages of using ANFIS

framework is that it facilitates the modeling process and it circumvents the need to expert knowledge (Sengur 2008). Jang (1996) presented the graphical representation of ANFIS structure, as well as, a first-order Sugeno fuzzy model with two fuzzy if-then rules as demonstrated in Figure 2.8 and Figure 2.9. Figure 2.8 shows a computation scheme to predict one output out of two inputs to the ANFIS machine. The inputs x and y are loaded to ANFIS that is constructed of five layers. Figure 2.9 depicts the reasoning mechanisms of the following fuzzy rules:

Rule 1: If x is J_1 and y is K_1 then $f_1 = p_1x + q_1y + r_1$

Rule 2: If x is J_2 and y is K_2 then $f_2 = p_2x + q_2y + r_2$

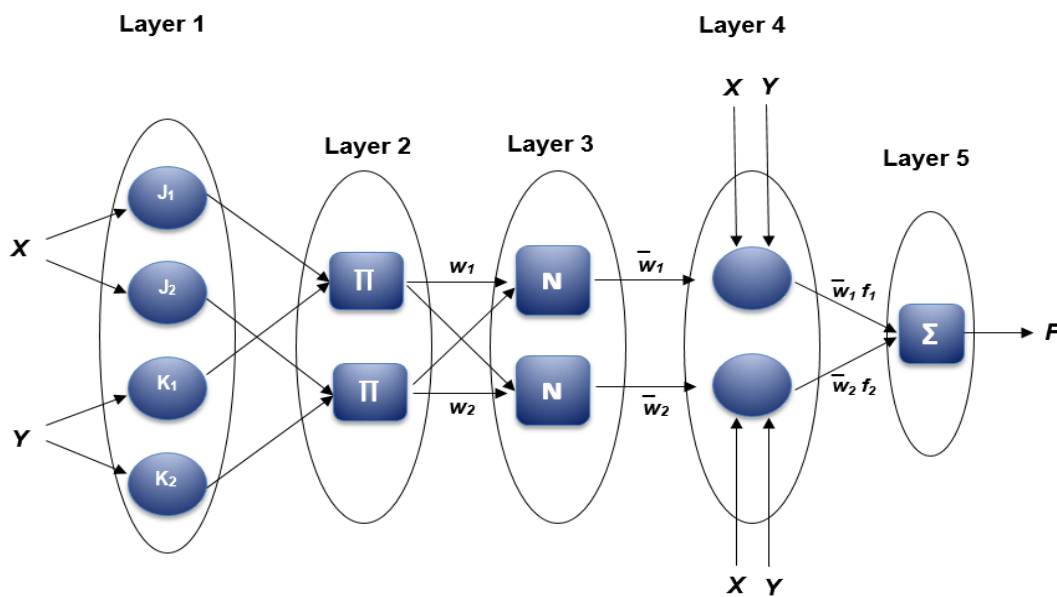


Figure 2.8 ANFIS Architecture

A wide range of neuro-fuzzy applications could be found in the literature review. Parvizsedghy and Zayed (2015) developed a model to predict the consequence of failure for oil and gas pipelines supported by the neuro-fuzzy technique. Zayed and Mahmoud (2014) leveraged the neuro-fuzzy approach to predict the productivity of horizontal directional drilling. Ebrat and Ghodsi (2014) designed an ANFIS model to assess the risk of construction projects. Yu and Skibniewski (2010)

integrated ANFIS with cost estimation concepts for mining estimation knowledge from residential construction projects. Sengur (2008) utilized the ANFIS in conjunction with wavelet transform to improve image classification. Sinha and Fieguth (2006) classified the defects of buried pipes on the basis of training a neuro-fuzzy network.

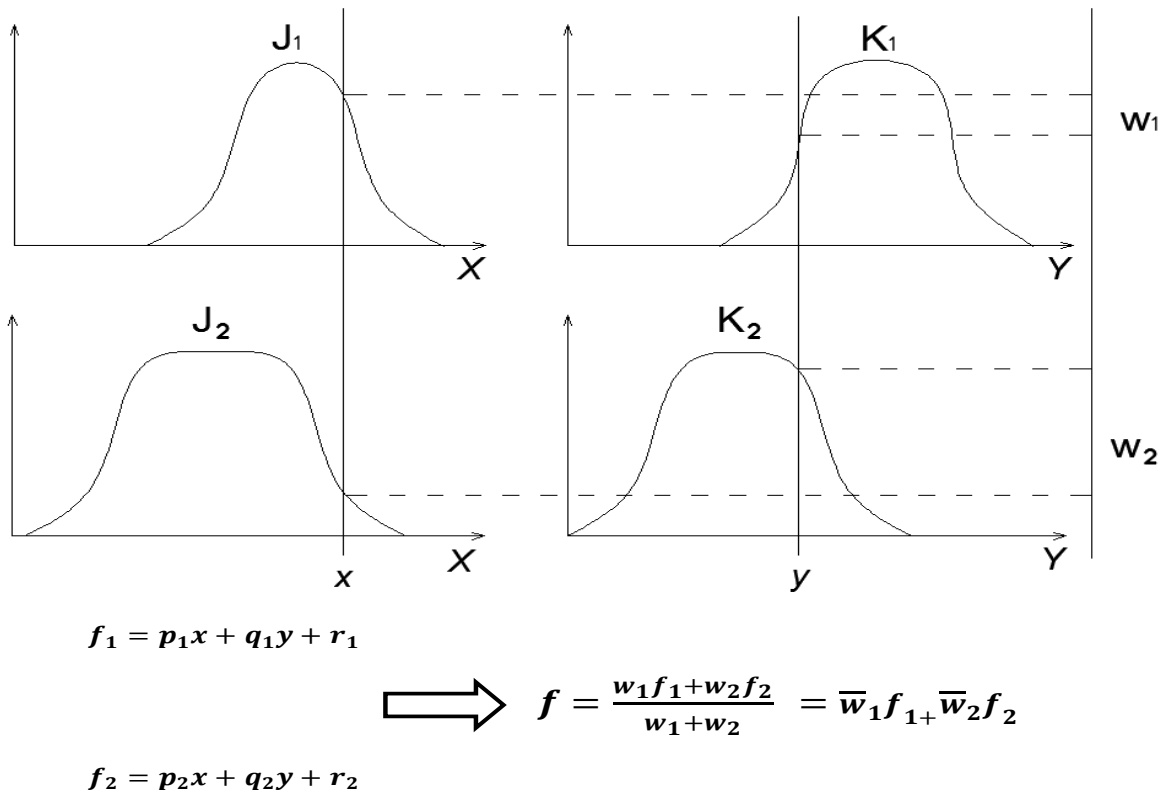


Figure 2.9 Sugeno Fuzzy Model Reasoning Mechanism

2.5.6 Monte Carlo Simulation (MCS)

Monte Carlo techniques involve a wide-range of computational algorithms that are mainly used to address the deterministic problems; specifically when the problems tend to follow a probabilistic pattern. These techniques apply repeated random sampling and multiple iterations to obtain the optimized solution. They are conducive to tackling any problem especially when it is hard to be solved with alternative methods. Monte Carlo Simulation (MCS) could be applied to attain a proliferation of objectives such as forecasting, optimization, and numerical integration. In the

space and oil domain, Monte Carlo-based models for the prediction of failure, cost overruns, and schedule overruns proved to be superior to human perception or other soft approaches (Hubbard and Samuelson 2009). Other applications were found in the construction management; Montaser et al. (2012) estimated the productivity of earthmoving operations through incorporating GPS data and MCS. Barraza (2011) utilized the MCS to propose a stochastic allocation method for the estimation and allocation of project time contingency. Sadeghi et al. (2010) constructed a Fuzzy Monte Carlo Simulation (FMCS) framework to analyze the risk in construction projects. Abu Dabous et al. (2008) integrated the fuzzy logic concept and MCS to create a condition rating system for bridge decks. Barraza and Bueno (2007) addressed the uncertainty of project activities as part of the proposed method for cost contingency management via MCS.

Generally, Monte Carlo Simulation involves the following steps:

1. Model identification and inputs definition.
2. Parameters definition (e.g., mean, standard deviation) for each element in the model.
3. Random data designation.
4. Deterministic computation and inputs simulation.
5. Results aggregation and outputs analysis.

2.5.7 Non-Destructive Evaluation (NDE) Techniques for Subway Structures

NDE term refers to the methods used to test and evaluate the condition of a material or an object without causing damage or altering its state. Delatte et al. (2003) divided the NDE techniques in subway structures into two categories, based on the inspection speed of these methods. The first category includes the NDE techniques for rapid inspection, where the application of these methods involves no interruption of service in a subway system. The second category includes the NDE techniques for detailed inspection, where their application requires shutting train traffic. Each of

these categories includes numerous technologies as presented in Figure 2.10. It is worth noting that visual inspection is also considered a nondestructive method. However, the term NDE in this thesis refers to all the nondestructive evaluation techniques excluding the visual inspection method.

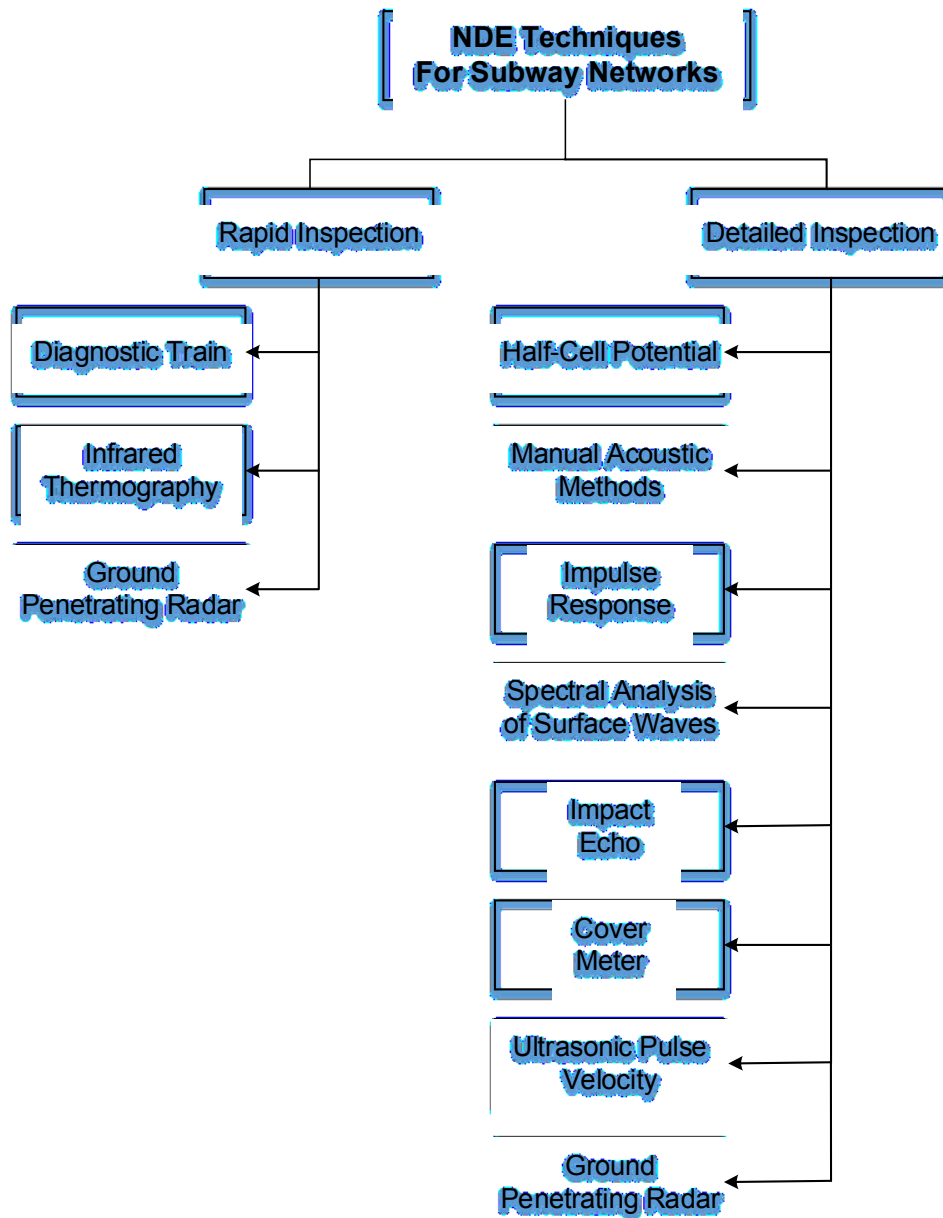


Figure 2.10 NDE Methods for Subway Networks

Non Destructive Evaluation (NDE) techniques have demonstrated to be useful for concrete surface evaluation. Accordingly, numerous studies were conducted due to their versatile applications and efficacy. Kim et al. (2015) proposed a framework to assess the dimensional and surface quality of precast concrete elements on the basis of BIM and 3D laser scanning. In a study SHRP 2 (2013), as part of Strategic Highway Research Program, infrared thermography was characterized as one of the top technologies used for detecting surface anomalies and delaminations in concrete bridge decks. Ham et al. (2017) characterized the microcrack damage in concrete by developing a contactless ultrasonic surface wave method. Shah et al. (2013) investigated the micro and macro level of defects in concrete by computing linear and non-linear Ultrasonic Pulse Velocity (UPV) factors. Dilek (2006) utilized the UPV, Young's modulus of elasticity, and concrete air permeability to assess the severity of concrete damage.

Scott et al. (2003) used Impact Echo (IE) testing in conjunction with Fast Fourier Transform analysis to determine the location of distress, crack or discontinuity, and depth of component. Electrical Resistivity (ER) technique was performed by Lataste et al. (2003) to classify the damage in concrete, especially to quantify the crack width and depth. Consequently, the authors concluded that the extracted information from ER and acoustic method could be fused to yield precise diagnosis for the structure. A multi-spectral image analysis approach was presented by Valença et al. (2013) to automatically assess concrete damages and delineate the deteriorated zones. Sadowski (2015) presented a methodology to recognize the values of pull-off adhesion between the layers of concrete. His methodology was based on three NDE techniques (3D laser scanning, acoustic impulse response, impact-echo) and ANNs.

2.5.7.1 Ground Penetrating Radar (GPR)

GPR is a geophysical method, based on the propagation behavior of Electro-Magnetic (EM) waves. A GPR system for concrete inspection generally consists of a central unit (computer), pulse generator, transmitting and receiving antennae, and video monitor as depicted in Figure 2.11. GPR could be equipped with two antennae so-called a bi-static antenna, one for transmission and the other for receiving, or it might be equipped with one antenna that both transmits and receives and is called a mono-static antenna.

As the GPR is dragged over the structure, the pulses are emitted by the antenna and transmitted through different layers of materials. Accordingly, part of the wave reflects back when it strikes the interface between two layers with different dielectric constants (ϵ), and the remaining energy is absorbed. The subsurface conditions are evaluated by analyzing the GPR profiles that include the time delays and amplitudes of reflected signals (Chen and Wimsatt 2010; Hamrouche et al. 2011).

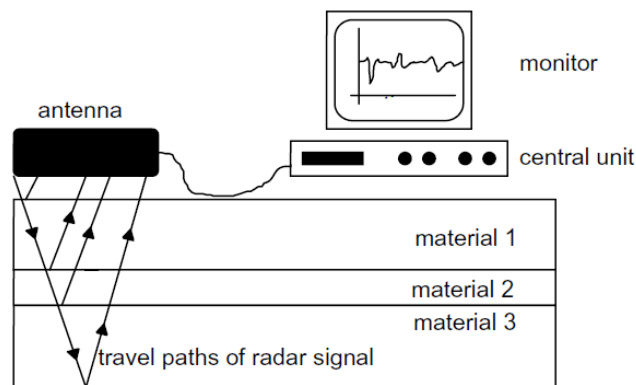


Figure 2.11 GPR Principles (Hugenschmidt and Mastrangelo 2006)

GPR is used for the condition assessment of several concrete structures such as highways, bridge decks, parking lots, foundation systems, retaining walls, tilt wall panels and sidewalks. For those structures, it is appropriate to use a highly portable radar system with a ground-coupled, mono-

static antenna. However, for particular projects, such as road condition evaluation, an air-launched (horn) antenna is usually used (Gehrig et al. 2004).

Numerous GPR condition assessment systems and methods have been developed to assess the Reinforced Concrete (RC) infrastructure. In this regard, Wiwatrojanagul et al. (2017) proposed a novel method to determine the locations of rebars in RC structures and measure the cover thickness by utilizing GPR data. Senin and Hamid (2016) developed two nonlinear regression models to estimate the moisture and chloride content in an RC slab. Their models were compared to GPR amplitude attenuation data of the slab, which showed good correlation results. Hoegh et al. (2015) characterized the air void variation in asphalt concrete via an air-coupled GPR antenna. Consequently, a dielectric map was generated. For bridge deck structures; Le et al. (2017) incorporated an autonomous robotic system with the machine intelligence and pattern recognition techniques for effective condition assessment of bridge decks. Their system was equipped with a digital camera, GPR, and Electrical Resistivity (ER) for data collection on concrete bridge decks. Martino et al. (2016) proposed a method to quantify bridge deck corrosion, by multiplying the mean and skewness of rebar attenuation signals of several bridge decks, then comparing multiplication results to corrosion values measured by Half-Cell Potential (HCP) method. Dinh et al. (2015) clustered the GPR amplitude data into categories to assess the condition of concrete bridge decks. Their model was implemented and compared to the output of other NDE technologies, which revealed reasonable results. Gucunski et al. (2015) designed a Robotics Assisted Bridge Inspection Tool (RABIT) comprised of Electrical Resistivity (ER), Impact Echo (IE), Ground-Penetrating Radar (GPR), and Ultrasonic Surface Waves (USW) techniques. Gucunski et al. later utilized this fully autonomous tool to assess the delamination and quality of concrete in bridge decks. In the context of pavements, Li et al. (2016_b) devised a pothole detector

for concrete pavements after creating a complementary processing of image and GPR data. In another study, Li et al. (2016_a) proved the accuracy of GPR technique to evaluate the thickness of concrete pavements. Their method fused the results of three NDE techniques, i.e., GPR, Ultrasonic Surface Waves (USW), and Impact Echo (IE). For tunnels, Prego et al. (2016) conducted a study to assess the capability of GPR to inspect railway tunnels, specifically during the early stages of construction. The results demonstrated the appropriateness of GPR to assess the condition of concrete linings in the tunnels.

Many researchers studied data interpretation of GPR technology (Martino et al. 2014; Gucunski et al. 2013; La et al. 2013; Barnes et al. 2008; Parrillo et al. 2006). Generally, data interpretation methods fall into two categories: amplitude (numerical) analysis method, and image-based analysis (IBA) method. Amplitude analysis was the focus of research during the past years, while IBA of GPR data still requires a lot of investigation. A functional mapping procedure based on GPR image analysis was only developed in the recent years (Tarussov et al. 2013). Dawood et al. (2015_d) proposed two approaches for the corrosiveness assessment of concrete bridge decks. Temurcan et al. (2016) summarized the corrosion mapping procedure of concrete bridge decks based on GPR-IBA. Abouhamad et al. (2017) established a systematic framework of GPR-IBA after discussing various scenarios of signal attenuation. This study concluded that GPR-IBA uses the full information content in a GPR profile, most of which is overlooked by the numerical analysis. Also, GPR-IBA eliminates the discrepancies of numerical analysis by considering the corrosion-related and the non-corrosion-related factors.

2.6 Gaps in the Body of Knowledge versus Potentials

There have been several efforts to address the condition assessment of subway systems. However, the literature review demonstrated that these studies did not present an integrated approach, yet

focused only on assessing one component of the network such as the stations. Therefore the proposed approaches could not be applied to the tunnels or auxiliary structures. Some have not evaluated the subway's structural deterioration over time, while others have considered solely visible flaws and failed in evaluating the hidden defects. Other drawbacks were found in researches that could not be validated due to the insufficiency of real-life data. Also, some of the models were budget allocation models rather than deterioration models.

Moreover, most of the previous studies used criteria weights that were determined on the basis of experts' opinion and judgment. Therefore, these studies were subjective and did not deliver condition assessment models that tackle the structural performance of subway networks. The rest of research was inconsistent due to its reliance on the visual inspection reports. Therefore, these researches could not provide an accurate estimation of the size of defect. Other models required a vast amount of data, which in turn make their applications very expensive and impractical to be implemented in future plans. As a result, there is a certain need for an integrated condition assessment tool that is expected to provide more objective, accurate and quantitative results.

In the literature review, some automated methods were found to be effective in measuring the severity of defects in metro systems. For example, image analysis and processing techniques were found to be very robust in detecting and measuring surface defects. These techniques can deliver better results when they are combined with other pattern recognition approaches, such as the ANNs and regression analysis. On the other hand, the NDE technologies can be used to collect the data for subsurface distresses. Subsequently, the data are analyzed to quantify the defects and generate deterioration maps for the structure. And finally, it was found that fuzzy logic and neuro-fuzzy inference systems are conducive to modeling the uncertainty and imperfections associated with

the ANNs and NDE outputs. Accordingly, these systems could be incorporated to enable the overall condition assessment of subway networks.

CHAPTER 3: RESEARCH METHODOLOGY

3.1 Overall Research Methodology

This research proposes a detailed framework for an integrated condition assessment of subway networks. The overall flow diagram of the research is displayed in Figure 3.1, which consists of three stages namely; knowledge acquisition, model development, and model assessment. As illustrated, in the first stage, a comprehensive literature review is conducted, which includes current practices developed by transit subway authorities worldwide, an elaboration of the factors and distresses related to RC deterioration, available studies on subway condition assessment, and previous studies related to the automated evaluation of defects. This section also touches on the modelling techniques that are selected to develop the proposed model. Such techniques include; image processing, machine learning, and nondestructive evaluation technologies of concrete infrastructure. In the second stage, the subway network is broken down into its components to facilitate the collection of data. Then several sub-models are developed to address the objectives of this research. First, digital images for different types of surface defects are acquired, and the data is processed. Separate models with multiple algorithms are developed. Consequently, a uniform platform for the assessment of surface defects is built. On the other hand, subsurface defects are detected by the use of NDE techniques. Later, interpretation methods are utilized for analyzing and mapping the data. The results of these methods are compared, and a subsurface defect-based assessment model is derived. Finally, the surface assessment and subsurface assessment models are embedded in a unified platform entitled integrated defect-based condition assessment model. In the third stage, the model is validated, and the conclusions and subsequent recommendations are drawn.

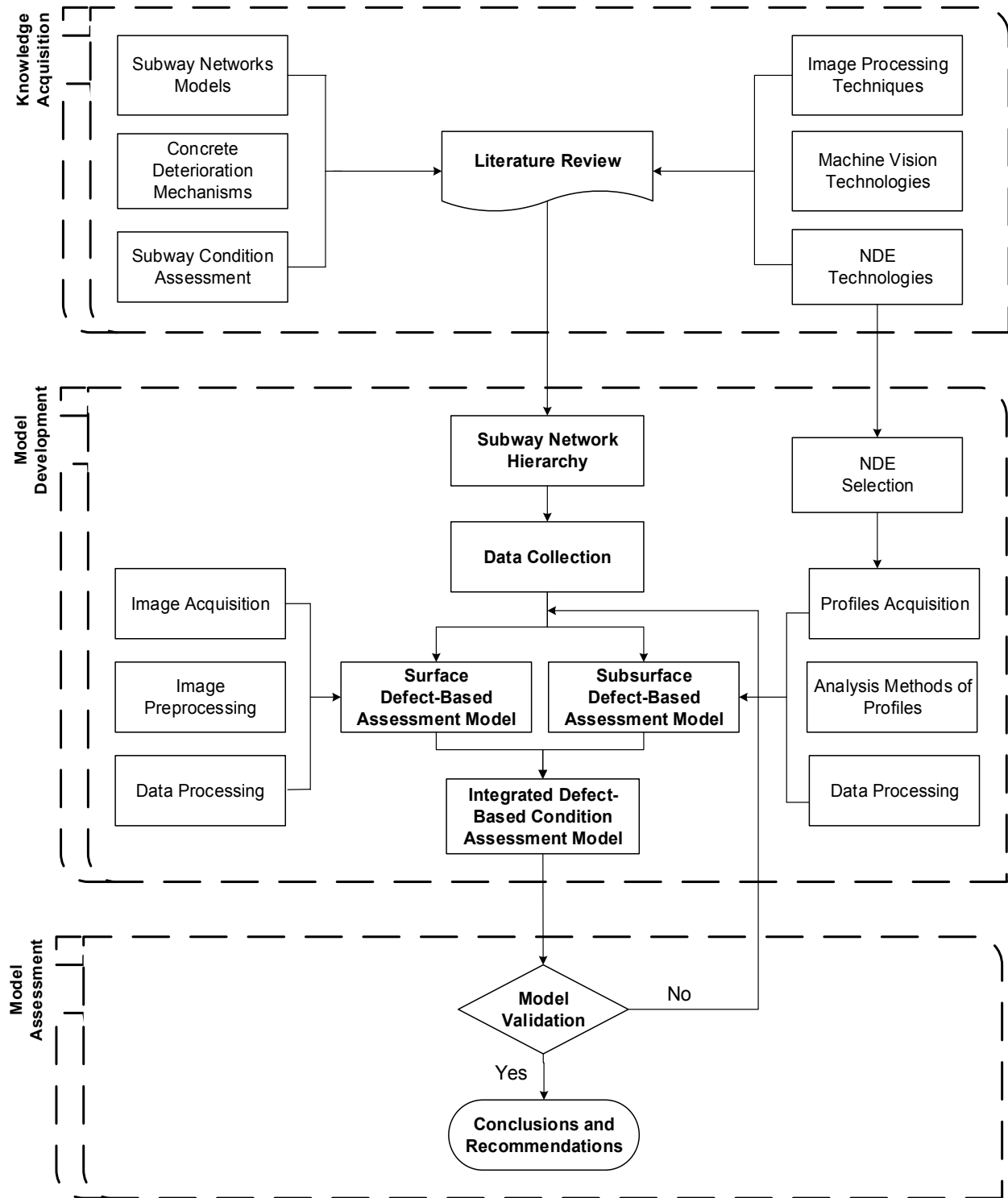


Figure 3.1 Overall Model Flowchart

3.2 Surface Defect-Based Assessment Model

A framework for the evaluation of surface defects in subway networks is proposed. This framework integrates image processing and artificial intelligence techniques to automatically estimate and measure the surface distresses. Figure 3.2 presents the flowchart of the model architecture. It includes four major phases namely; image acquisition, image preprocessing, machine learning-based processing, and condition assessment of surface defects.

3.2.1 Image Acquisition

In this phase, a myriad of images of the subway facility is acquired using a digital camera. Image data demonstrate all the visible flaws on the structure's surface. After the acquisition, the images are transferred to the computer via a Universal Serial Bus (USB). The stages encompassed in this phase are depicted in Figure 3.3.

Subsequent to conducting a comprehensive state of the art literature review, this research considered only surface defects previously prioritized by transit agencies in the USA and Canada. These defects include moisture marks, spalling, scaling, and cracks. Figure 3.4 illustrates the flowchart of the prioritization process and their related attributes.

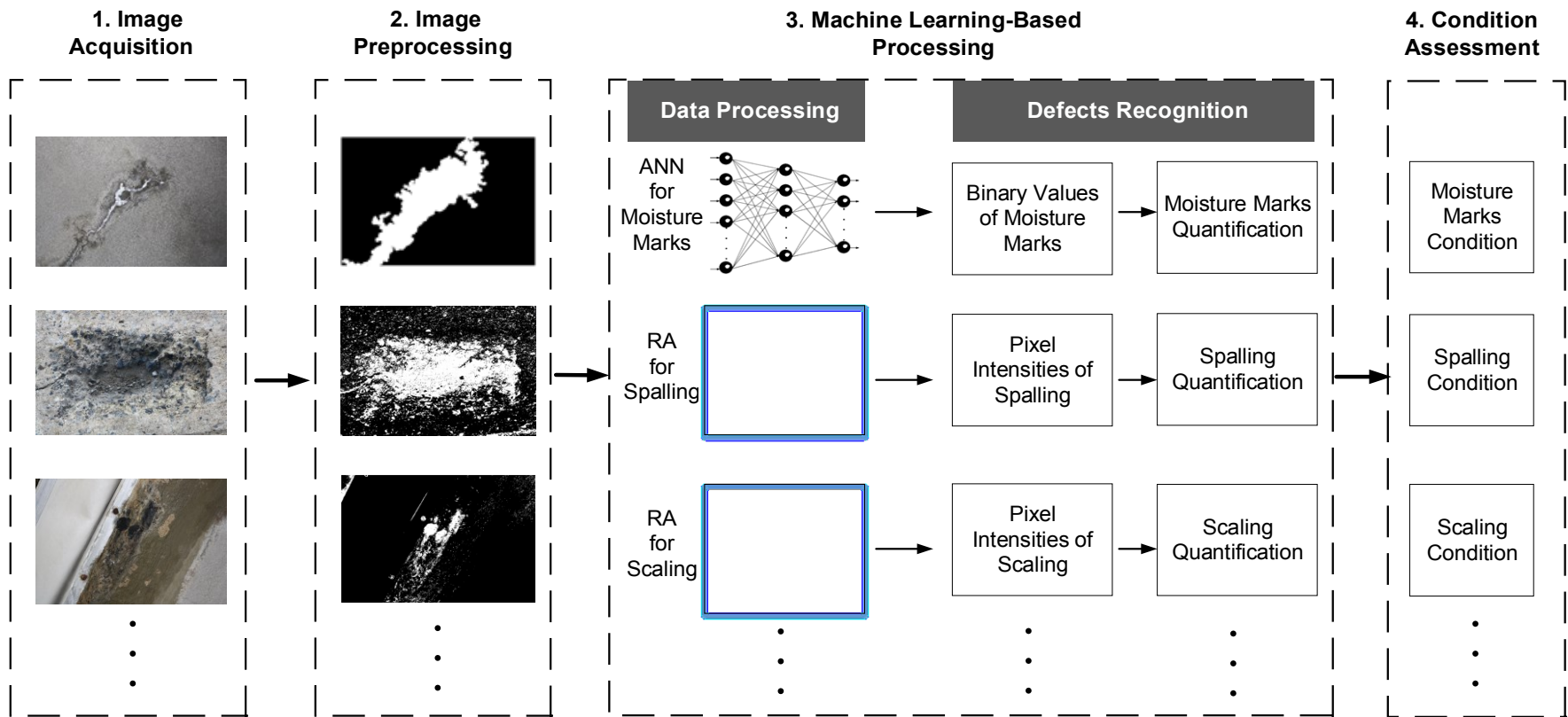


Figure 3.2 Overall Flowchart for Surface Defects Condition Assessment

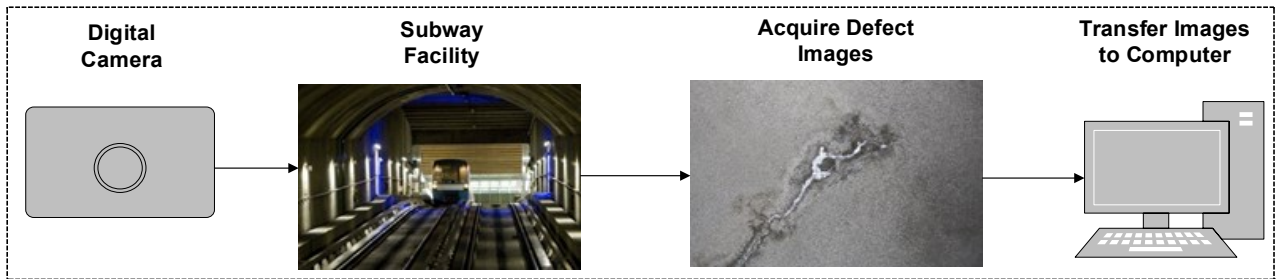


Figure 3.3 Image Acquisition Phase

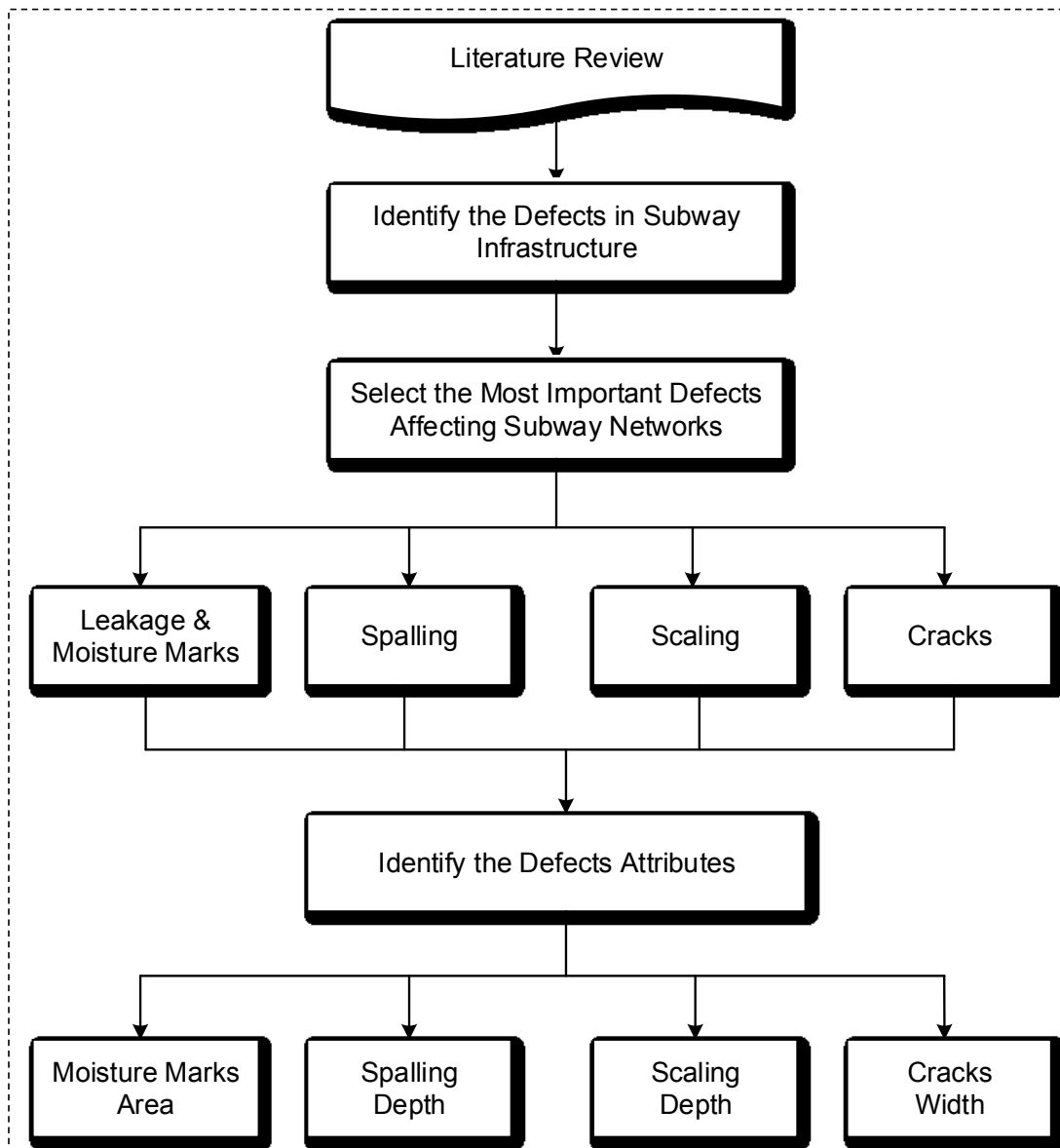


Figure 3.4 Defects Prioritization and Related Attributes

Some essential considerations should be taken into account while capturing digital images in order to optimize data analysis. Hence the identification and quantification of the defect can be accurately accomplished. First, the images should be acquired orthogonal to the surface with sufficient overlapping to reduce the error of projection and provide better area coverage (McRobbie 2008). Westoby et al. (2012) claimed that it is necessary to maintain an overlap of 80% or more between the images to facilitate image processing and feature extraction. Second, close-range images are capable of delivering detailed information about the physical attributes of the objects (Fryer 2000). And third, blurry images should be avoided since they can cause low image resolution that may affect pixel matching throughout the blurry images. Hence, the camera should be adjusted to be in focus while acquiring the images. However, there exist other influential factors that may affect pixels' intensity values of an image and cause a nuisance variability, such factors include but are not limited to, lighting, shadowing, and discoloration of a concrete surface. Lighting should be used when needed to guarantee the images are consistent. The impact of this factor is intensified in the enclosed nature of subway systems where the tunnels are poorly lit. To mitigate the lighting (illumination) variability, several techniques could be investigated, such as single image color-normalization, color-constancy, and specifically Multi-Scale Retinex (MSR) technique (Jobson et al. 1997) is widely utilized to circumvent both low-and high-frequency lighting problems (Stent et al. 2016). The second factor (shadowing) is associated with a lack of clarity as intensity levels drop in the shadowed areas. Generally, this drop is ranging 10–20% of the sunlit value, and it pertains to the depth of shadow. This factor could be controlled by applying a compression technique. Stronger compression is needed for large shadow regions as opposed to smaller ones. The scenes that comprise substantial shadowing variations require dynamic range algorithmic compression (Jobson et al. 1997). In this research, the lighting and shadowing aspects

are countered by maintaining proper illumination through utilizing flash photography during image acquisition. The flash photography helps to illuminate the dark scene in subway environment and can guarantee the coherence of image analysis. Regarding the third factor, discoloration defect is known to have no specific boundaries or textures. Also, its gray-level histogram shows no clear threshold value, which in turn renders it difficult to distinguish discoloration distress from the regular concrete surface. Accordingly, in the images acquired to a concrete element, the detection of this distress could be regulated as follows: (1) Perform global measurement of the degree of discoloration of concrete via computing the standard deviation of color values in the image. The smaller the standard deviation is, the lesser the concrete discoloration and so forth. Once the standard deviation exceeds a certain threshold value, it shows that discoloration is initiated and could be found on a concrete element; (2) apply multiple segmentation and classification methods to separate discoloration zones from the background of the image (Zhu and Brilakis 2010).

3.2.2 Image Preprocessing

Proper preprocessing is a significant step to make the images appropriate for different purposes, such as preprocessing an image to make it discernable for the user or more suitable for machine learning. The preprocessing will not generate new data from the original image. It enhances and improves the quality of the image since the acquired images usually contain noise (Bow 1992).

Different image processing algorithms are performed on the original images, such as extracting the grayscale images from the RGB images, histogram plotting, thresholding, image enhancement, etc. Moreover, the numerical format and the binary format of the gray-level values are obtained at this stage, as well as, some feature vectors such as the length, width ...etc. By applying image processing algorithms, each defect is isolated from the background of the image or in other words, the object of interest (OOI) is determined. Multiple algorithms are utilized to detect, interpret and

measure surface defects. Such algorithms vary in detecting one defect from another, as will be explained subsequently. Figure 3.5 illustrates the overall flow of the preprocessing phase.

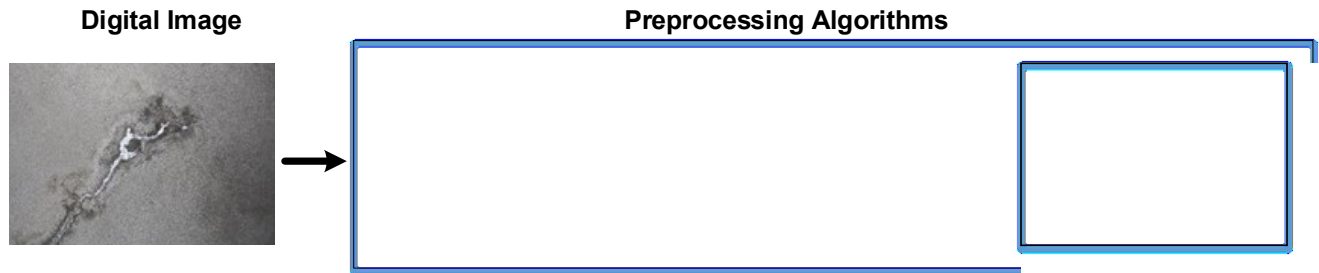


Figure 3.5 Image Preprocessing Phase

3.2.2.1 Preprocessing of Moisture Marks

An algorithm that relies on various spatial domain filters is proposed in this study to enable wet areas extraction, which will eventually result in the detection of the distress. Figure 3.6 illustrates the workflow of the proposed model. It starts by reading, adjusting, and displaying the images. Since the acquired images are RGB images, it is essential to convert the RGB image into an 8-bit gray-level image. This image will be more convenient for further enhancement and detection processes.

Subsequently, an image smoothing technique is applied to the grayscale image. This technique is one of the most important and broadly studied topics in computer vision field and is also known as image blurring (Wang and Wang 2016). Image smoothing can decrease the variance among pixels' intensities without considerably affecting the information pertaining to the region of interest (ROI), which improves distress isolation from the background of the image (Li et al. 2016_b). By using this technique, significant patterns in the image are retained notwithstanding leaving out background noise, which will in return assist in the data analysis by obtaining more feature vectors from the image. In this research, the anisotropic diffusion method (Perona and Malik 1990) is utilized to smooth image data. It applies partial differential equations, local gradient

function, and implements sequential iterations to allow smoothing operations to solely occur in the internal part of ROI without crossing the boundaries between sharp pixel intensities.

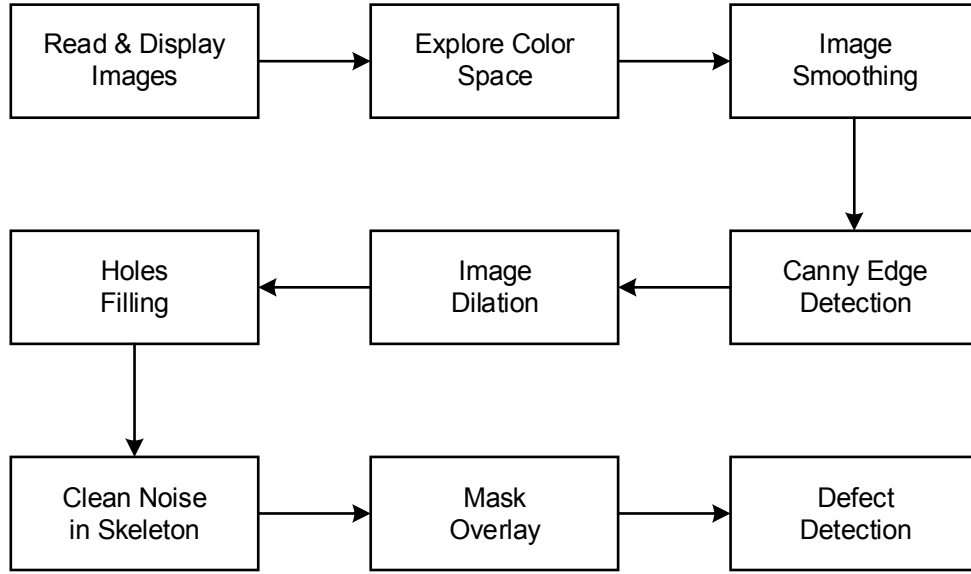


Figure 3.6 Moisture Marks Detection Algorithm (Dawood et al. 2017_b)

Consequently, an edge detection algorithm is employed to eliminate the noise and reduce fluctuations of pixel values. There are six different types of edge detection algorithms, though Canny edge detector performance is superior to the rest of detectors (Canny 1986). It accomplishes the smoothing operation by convolving with a Gaussian mask to form a smoothed image (Gonzalez and Woods 2008), as expressed by Equation (3.1).

$$f_s(x, y) = G(x, y) \times f(x, y) \quad (3.1)$$

Where, $f_s(x, y)$ is a smoothed image, $f(x, y)$ is the input image, and $G(x, y)$ is the Gaussian function. Then, the algorithm attempts to find edges at the maxima of the gradient by computing the gradient magnitude and direction (angle) as defined in Equations (3.2) and (3.3) respectively.

$$M(x, y) = \sqrt{g_x^2 + g_y^2} \quad (3.2)$$

$$\alpha(x, y) = \tan^{-1} \left[\frac{g_y}{g_x} \right] \quad (3.3)$$

Where, $M(x, y)$ is the magnitude of the gradient, g_x and g_y are derivatives in both directions x and y respectively, $\alpha(x, y)$ is the direction of the edge, and $\left[\frac{g_y}{g_x} \right]$ is the derivative ratio.

Then, a couple of morphological operations are applied (i.e., dilation, hole filling). The first operator is utilized to dilate the image through successive iterations. Dilation is the process of thickening the boundaries of an object in a binary image, hence the object will be clearly visualized (Gonzalez and Woods 2008). This process is achieved by probing an image with a structuring element, which is a matrix comprising of any complement of 0's and 1's, and may take any shape and size. It is crucial to select the size and shape of a structuring element since a morphological operation that is sensitive to a specific shape can be constructed accordingly. While Pixel values of 1 define the neighborhood, the value of each pixel in the dilated image is determined on the basis of comparing its corresponding value in the input image with neighbors.

The second morphological processing is conducted via a hole filling mask. A hole in an image is a background region bounded by a closed border of forefront pixels (Gonzalez and Woods 2008). Therefore, after performing filling operations on a dilated image, small black spots within the moisture marks region can be filled. The process continues with cleaning the noise in the skeleton image. This step is conducive to segmenting and isolating the defect from the background of the image. Moreover, a mask is created to be later displayed as an overlay on the grayscale image for the final detection of moisture marks in the image frame.

3.2.2.2 Preprocessing of Spalling

A hybrid algorithm of various spatial and frequency domain filters is proposed by Dawood et al. (2017_a) to enable spalling region extraction, which will subsequently result in the detection and recognition of the defect. Figure 3.7 illustrates the workflow of the proposed algorithm.

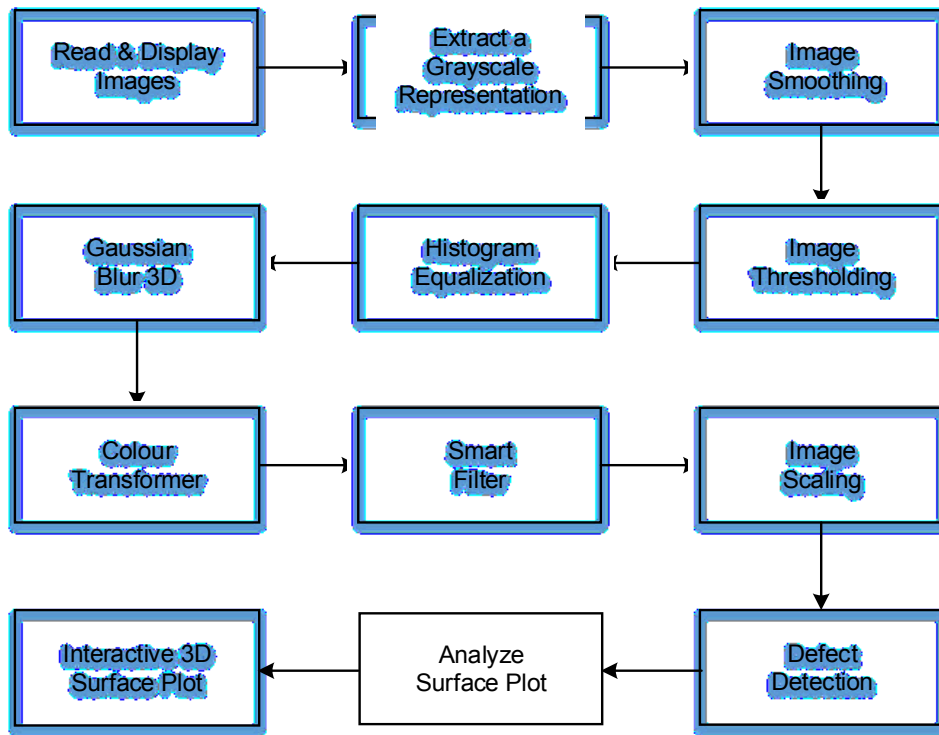


Figure 3.7 Spalling Detection Algorithm (Dawood et al. 2017_a)

It starts by reading, adjusting, and displaying the images. Since the acquired images are RGB images, it is necessary to explore the color space and split the RGB image into three different planes (i.e., red, green, and blue). This step permits the selection of an appropriate color plane for spalling identification and to extract a grayscale representation, which will prepare the image for the next steps including image enhancement and detection processes. The conversion of RGB images to grayscale images is defined mathematically by Equations (3.4) and (3.5) (ImageJ).

$$Gray = (Red + Green + Blue) / 3 \quad (3.4)$$

$$Gray = 0.299 \times Red + 0.587 \times Green + 0.114 \times Blue \quad (3.5)$$

Subsequently, the anisotropic diffusion algorithm mentioned previously will be utilized to smooth image data. This algorithm is considered one of the most widespread smoothing techniques because it has accomplished a decent trade-off between image denoising problems and edge conservation. Moreover, it has overcome the adverse outcomes of linear smoothing filtering and has the immediate localization feature that preserves the ROI boundaries at each image resolution. In addition to, enabling piecewise smoothing at different scales where the intra-region smoothing operation should take place rather than the inter-region process. Other studies, such as Chan et al. (2005) applied the algorithm for image restoration, which involved a series of operations such as de-blurring, blind deconvolution, and inpainting (Wang and Wang 2016).

Consequently, the image is thresholded by segmenting the spalling defect from the surrounding background. The main idea behind thresholding is to select a threshold value T that splits an image into two discrete gray-level sets (Weeks 1996), as expressed by Equation (3.6).

$$b(x, y) = \begin{cases} Gr_i \rightarrow f(x, y) \leq T \\ Gr_j \rightarrow f(x, y) > T \end{cases} \quad (3.6)$$

Where, Gr_i and Gr_j are two selected gray-levels in the thresholded image, $f(x, y)$ is an image function, and $b(x, y)$ is the binarized image function after applying the threshold process. Through thresholding, multiple gray-levels in an image are reduced to only two gray-levels (i.e., Gr_i, Gr_j). At this stage, it is crucial to plot an image histogram and select a threshold value T that separates an image into two distinct regions, namely; object (spall) region and background region. The

selection of the best threshold value is employed by using a trial-and-error technique to determine if the selected value has extracted the required OOI.

Then, a Gaussian Blur 3D filter is used to decrease the noise and enhance image resolution. It performs a three dimensional (3D) convolution based on the two dimensions (2D) form of filtering (Gonzalez and Woods 2008), as defined in Equation (3.7).

$$H(u, v) = e^{-D^2(u,v)/2\sigma^2} \quad (3.7)$$

Where, $H(u, v)$ is a filter transfer function, $D(u, v)$ is the distance from point (u, v) to the center of the frequency rectangle, and σ is a measure of spread about the center.

The Gaussian Blur 3D filtering is also established on using stacks and hyperstacks. The stack is composed of multiple slices (spatially linked images) for the same image, which could be displayed in a single window. The slices that make up a stack must have similar size and depth features. Image pixels in a 2D image are called voxels in a stack. Each voxel is a volumetric pixel that possesses an intensity value in a 3D space. Whereas, the hyperstack is a multi-dimensional image that encompasses a 4D or a 5D dimension, i.e., w (width), h (height), s (slices), l (wavelengths), and t (time) (image J).

Then, a couple of colored filters are applied (i.e., color transformer, smart filter), which filter the image pixels so that the pixels close to a distinct color are solely highlighted. Therefore, when a colored filter is applied to a grayscale image, it produces an indexed color image that is a single plane grayscale image with color. The color differences in the processed image reveal different intensity levels of the OOI rather than color differences of the viewed image. The process continues with scaling and calibrating the images. Prior to image calibration, any measurement for a randomly selected object inside the image such as a spall width is taken in situ, then this measurement will be set as an entry data in the software. Consequently, image overlay is created

and the OOI is selected using a colored edge detection algorithm. Afterwards, the surface graph is analyzed and an interactive 3D scene presentation is plotted. These illustrations display pixel intensities in a three-dimensional plot, thus, allowing a de facto visualization of spalling defect. Different software packages were used in the preprocessing and recognition of spalling defects, such packages include MATLAB® R2013b, Image Processing Toolbox and ImageJ software.

3.2.2.3 Preprocessing of Scaling

A processor comprising of sequential filtering operations is designed for the analysis of scaling defect in subway networks. As described previously, first the images are read and adjusted, then the RGB space is explored and the best-visualized plane is chosen for further processing. This is followed by thresholding the image, which involved histogram manipulation and Gamma correction. The histogram of a gray-level image is plotted in order to specify the position of the best threshold value. Image histogram describes the gray-level distribution of all the pixels in the image (Russ and Woods 1995). Therefore, for an image function $f(x, y)$ with a distinct gray-level from 0 to 255, the gray-level histogram $H(g)$ is the distinct chart plotted with the amount of pixels at gray-level g versus g as defined by Equation (3.8) (Bow 1992).

$$H(g) = \iint [f(x, y) = g] dx dy \quad (3.8)$$

At this stage, it was necessary to adjust the image by using the maximum entropy method. Three filters are employed on the adjusted image, this practice starts by convolving the image by utilizing a normalized kernel, then a Gaussian blur filter with sigma of a radius of 2 pixels is applied, and finally, a Variance filter with a radius of 2 pixels is used to preprocess the image. Mask processing is the next step to be implemented. This step includes the creation of a morphological mask that is

utilized later as an overlay on the grayscale image to accurately detect the scaling defect. Figure 3.8 depicts the scheme utilized to preprocess and identify the scaling defect in the acquired images.

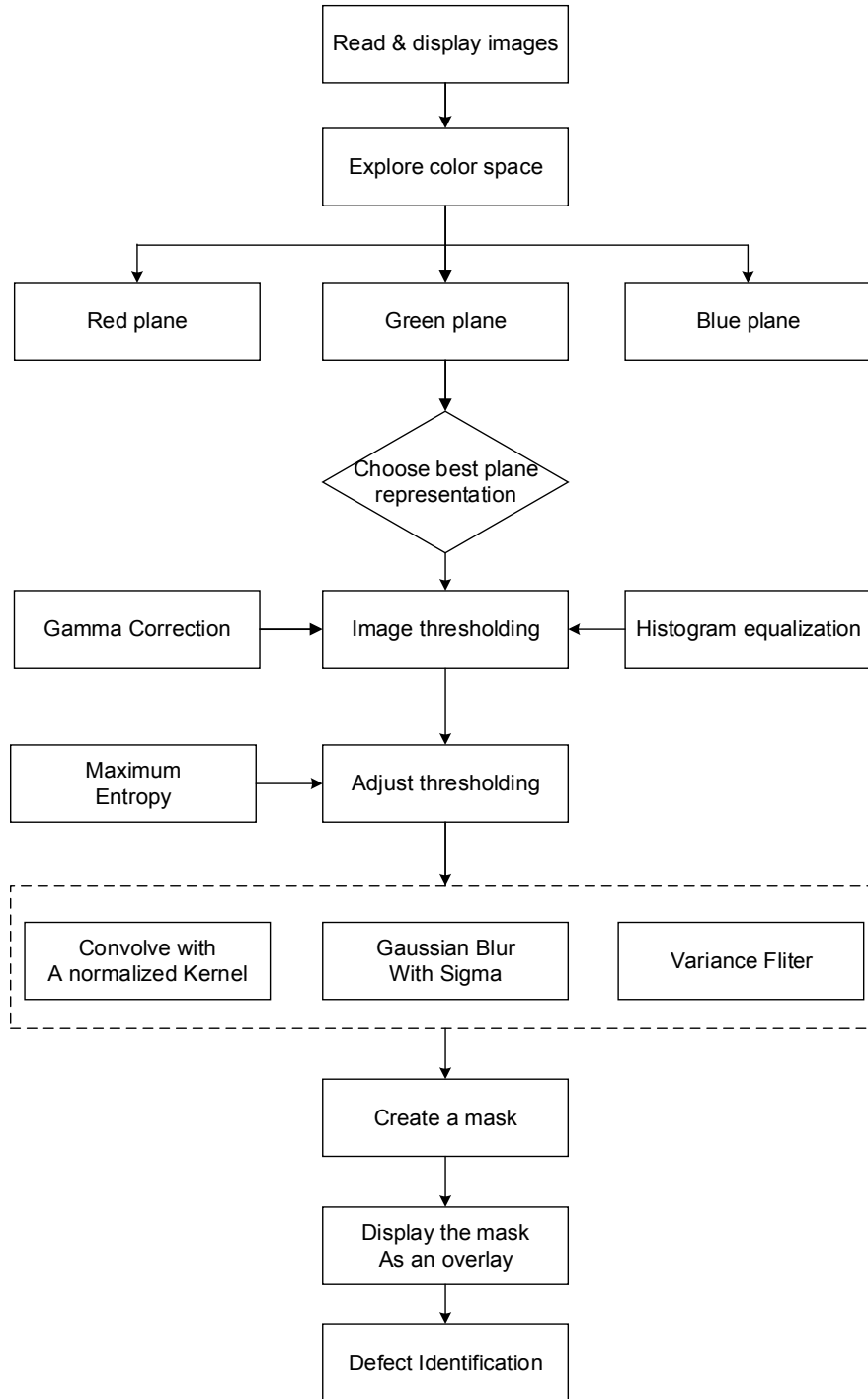


Figure 3.8 Scaling Detection Algorithm Flowchart

3.2.2.4 Preprocessing of Cracks

The detection of cracks involves multiple algorithms as shown in Figure 3.9. This model starts by reading, adjusting, and displaying each image. Followed by exploring the color space and selecting the most enhanced plane as a grayscale representation. Afterwards, the image is thresholded through segmentation that involves separating the object of interest (defect) from its background using Canny edge detection. A set of morphological algorithms including thinning, dilation, and hole filling is applied to the thresholded image to detect its boundaries. After several trials on the thresholded image, it was found that the algorithm developed on the fusion of set dilation, complementation, and intersection (Gonzalez and Woods 2008) delivers the best results. For this purpose, a structuring element B of a size 3×3 is used for filling the holes and connecting the discontinuous objects according to Equation (3.9).

$$X_k = (X_{k-1} \oplus B) \cap A^c \quad k = 1, 2, 3, \dots \quad (3.9)$$

Where, X_k is the set that encompasses all the filled holes, k is the iteration step where the algorithm terminates if $X_k = X_{k-1}$, A is the set whose components are multiple connected boundaries, and A^c is the complement of A . The dilation in the above shown equation may fill the whole area if left unrestricted. Therefore, the intersection at each iteration step with A^c is essential to limit the outcome of holes filling to solely the region of interest (ROI). The process continues by obtaining the skeleton and cleaning the noise in the image. And finally, a mask is displayed as an overlay on the grayscale image to detect the defect.

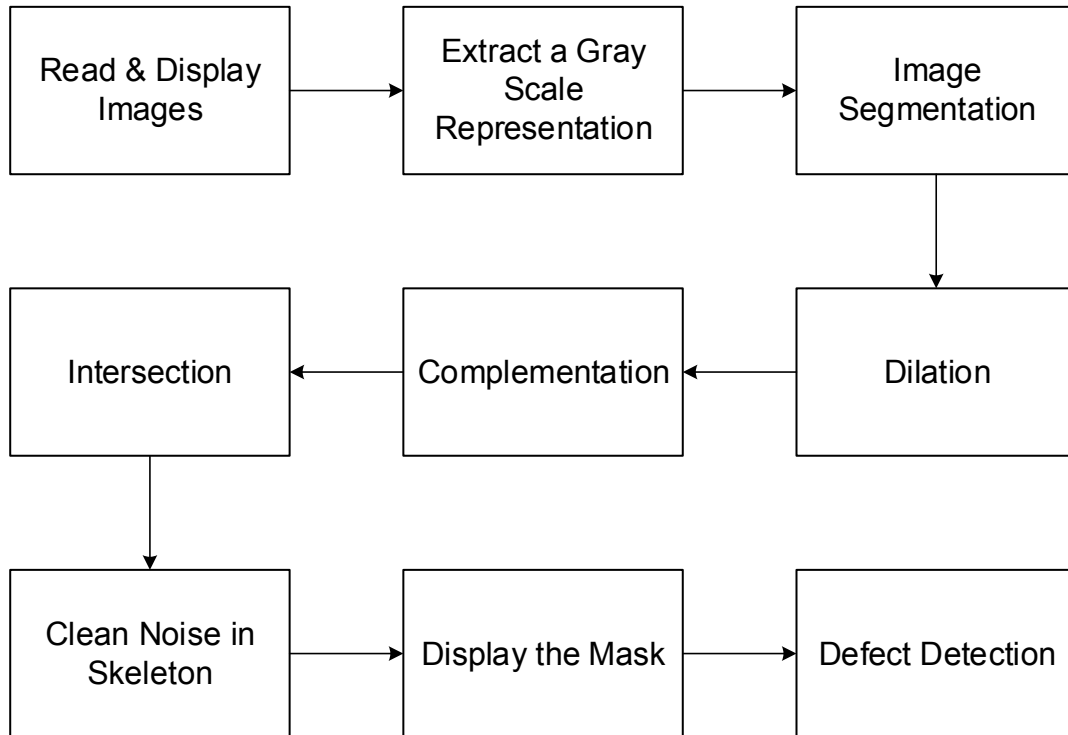


Figure 3.9 Cracks Detection Algorithm

3.2.3 Machine Learning-Based Processing

The proposed framework for machine learning-based processing encompasses systematic approaches that embark upon the preprocessed data of metro networks to accomplish the ultimate research goal of defect evaluation and quantification. As presented in Figure 3.2, this phase includes two steps, namely; data processing and defects recognition. Subsequent to the preprocessing phase, image attributes are passed to various supervised machine learning techniques so that predictions can be made. In this phase, several models are developed each of which analyzes and evaluates a specific type of defect. Accordingly, different machine intelligence techniques are leveraged to estimate the severity of different surface distresses. For instance, ANN is created for the processing of moisture marks attributes, regression analysis (RA) is applied for the prediction of spalling and scaling, and so on. It is essential at this stage to design the

architecture of each model and define the input and output feature vectors for their datasets. The following section explains the details of each model along with its schematic representation.

3.2.3.1 ANN-Based Model for Moisture Marks

The overall framework of the ANN model for moisture marks recognition is shown in Figure 3.10. Subsequent to capturing and preprocessing the moisture marks images, the attributes of the filtered image are channeled to be processed via ANN due to the non-linear relationship between the inputs and outputs. The ANN model building comprises several steps that involve mapping the inputs to outputs in order to detect and quantify wet regions in the images. First, the data preprocessed previously are categorized as input and output datasets. Also, this process includes defining the samples and elements in terms of matrix columns and rows. The ANN is fed by the input dataset (numerical format of the image) represented by the normalized values of pixels' gray-levels ranging from 0 to 255. Followed by supplying the output dataset (binary format of the image) characterized by the mapped values of 0 or 1 for each corresponding pixel's intensity, depending on whether it represents a non-defective or a defective area respectively. Second, each dataset is divided randomly into three sets; namely training (60%), validation (20%), and testing (20%). The training dataset is used to train the network in order to recognize the pattern between data entries and output variables. Thus ANN is tuned according to the generalized error. The validation dataset is used to validate the results generated in the training phase. One of the challenges that occurs during training a large network as in this image processing case is what is known as overfitting. ANN memorizes the introduced patterns in the training phase; however, it cannot generalize to new samples. In order to avoid overfitting the network and also fine-tuning the model, the validation dataset is used since it offers an unbiased evaluation of the generalization error, tests if the error is within the tolerable range, and determines a stopping point while training the network.

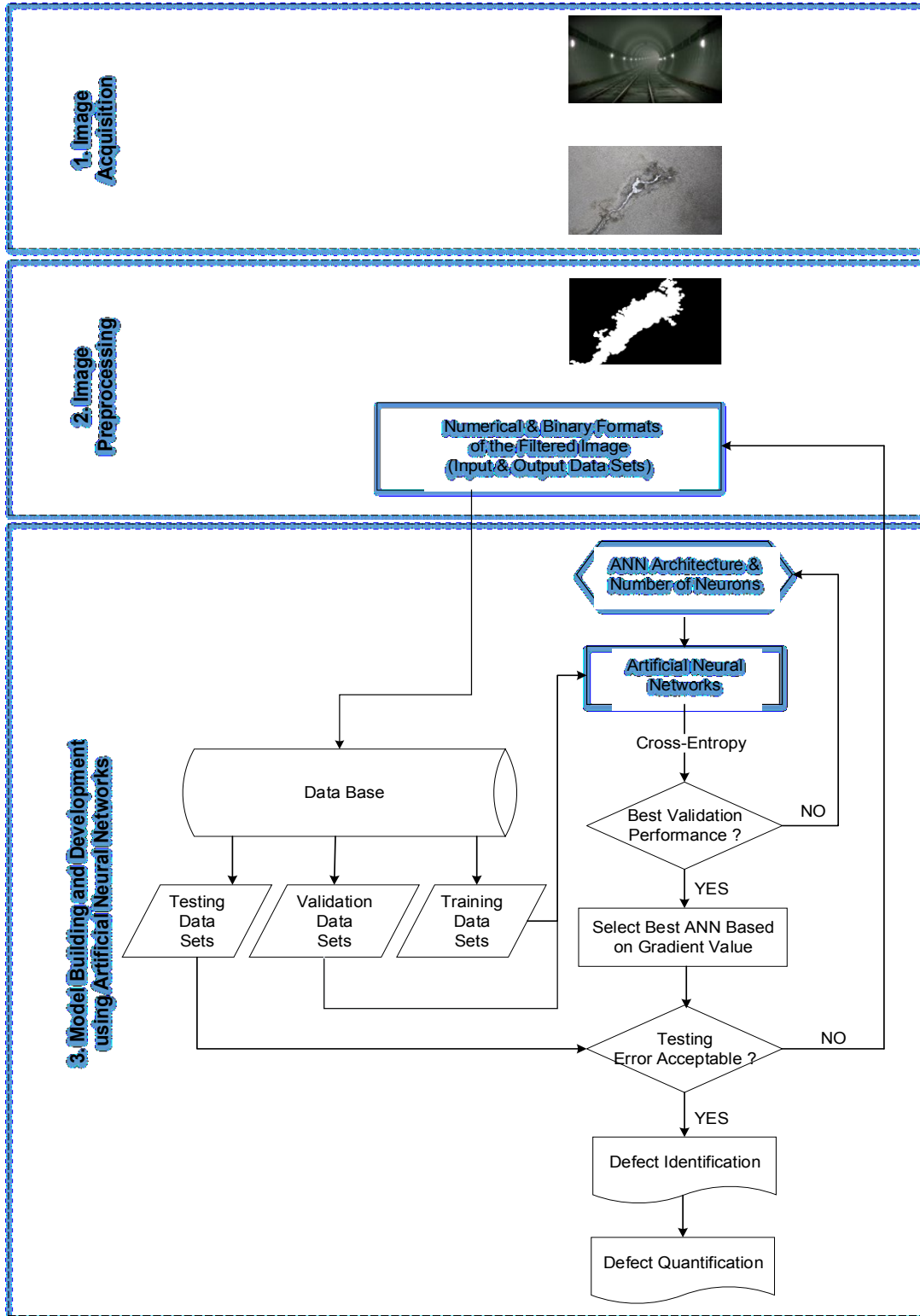


Figure 3.10 Moisture Marks Model Development via ANN

The testing dataset is utilized to measure ANN performance throughout and after the training phase. The third step involves designing the ANN architecture, which is composed of three layers; specifically input, hidden, and output. It also comprises setting the number of neurons in the hidden layer. This number could be changed in the case of the network malfunctioning until the appropriate number is reached. The fourth step is to set the network for training in order to fit the inputs to targets. Subsequent to several iterations using cross-entropy optimization function and confusion matrices, the error is computed and the optimized performance is generated when the ANN included 1000 neurons in the hidden layer. The best validation dataset is passed to the trained model in order to predict and recognize the defect. The ultimate goal of training the network is to automate the process in the future. After the training phase, ANN can recall its memory functions, thus simulating new output sets from new input data. The network will identify the distress in images by assigning a 0 value for the non-moisture-mark pixel (background of the image) and a 1 value for the moisture-mark pixel (object). Figure 3.11 illustrates training the network with input and output variables. Input data are the normalized values of gray-level pixel intensities, while output data are the binary values of pixel intensities.

Consequent to obtaining the pixels' binary values of 0 or 1, the moisture marks area can be measured and assessed by summing up the 1 values and dividing the result by the total number of pixels in the image as illustrated in Figure 3.12. Hence, the defect's severity can be quantified by evaluating its percentage in each image. This procedure is repeated for all the images that cover the structural element; then, the results are aggregated to compute the global defects' percentage in that element.

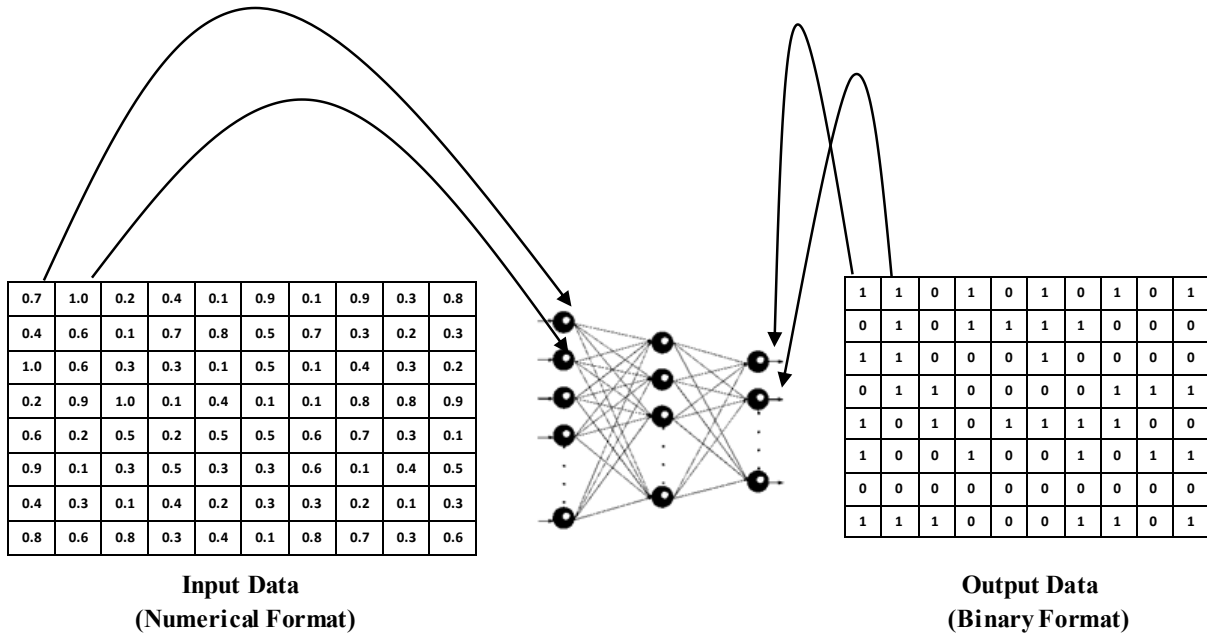


Figure 3.11 ANN Training and Fitting Stage (Dawood et al. 2017_b)

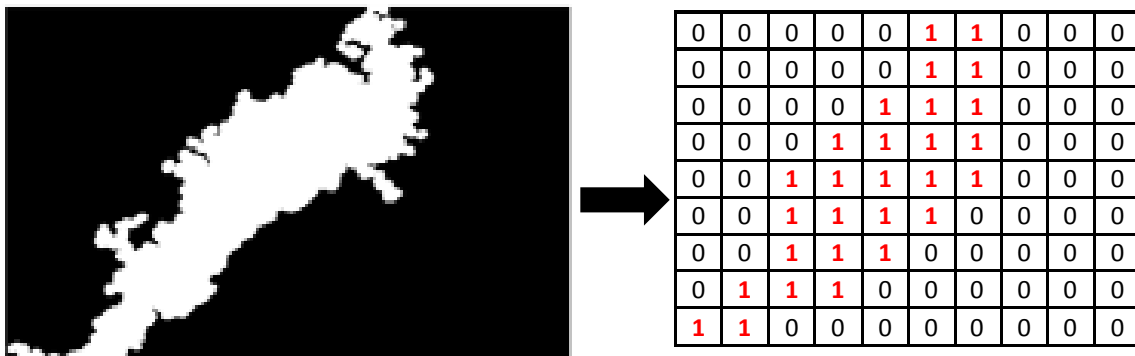


Figure 3.12 Quantifying Moisture Marks Distress (Dawood et al. 2017_b)

3.2.3.2 Regression-Based Model for Spalling and Scaling

The overall architecture of regression-based model for spalling and scaling evaluation is depicted in Figure 3.13. After acquiring the 2D images for spalling/scaling distresses and preprocessing the images via the previously described algorithm for each distress (spalling, scaling), a supervised machine learning using regression analysis (RA) technique is leveraged to process image features.

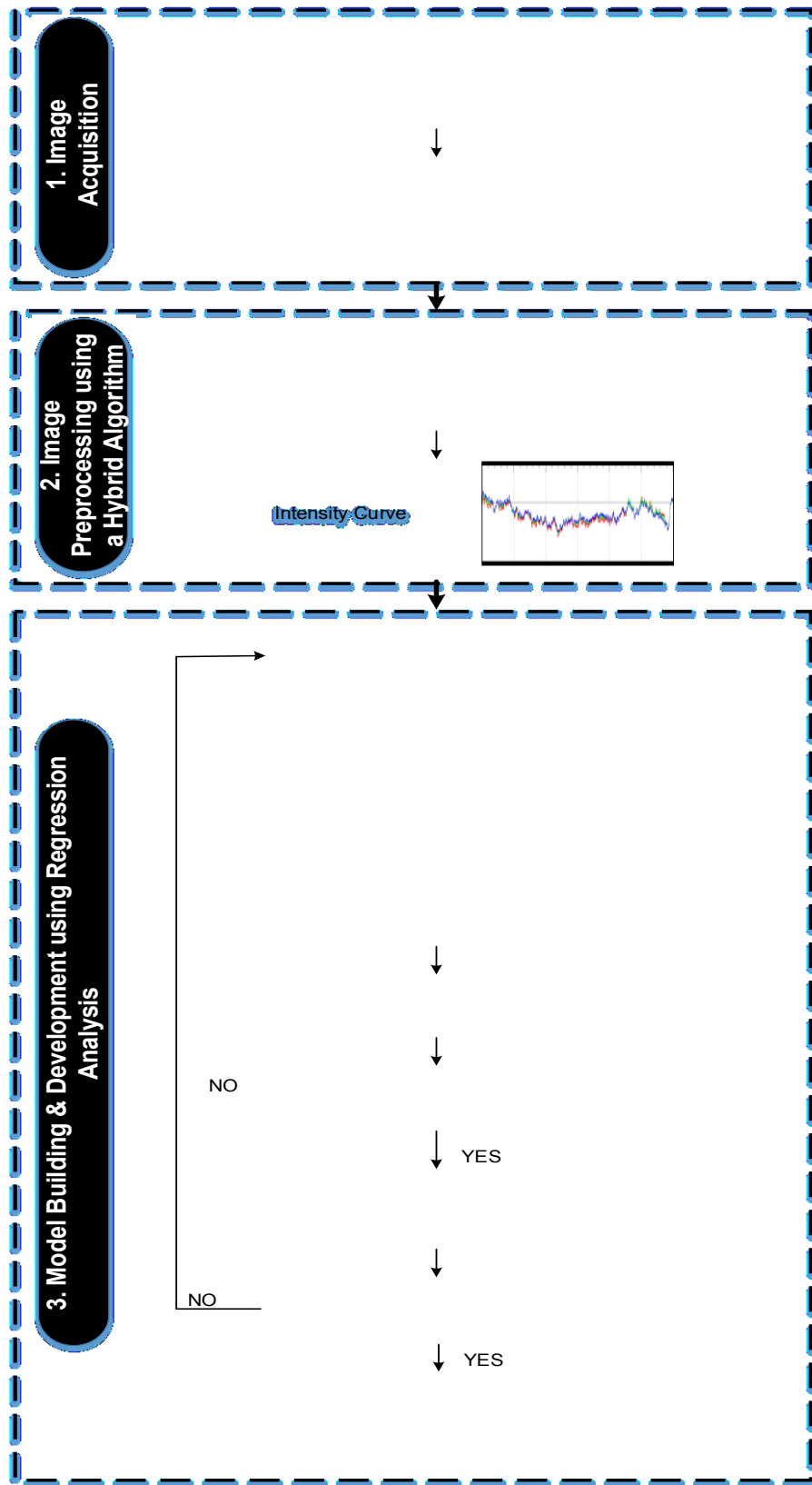


Figure 3.13 Quantifying Spalling/Scaling Distress (Dawood et al. 2017_b)

This technique allows modelling the linear trend between the predictor variable and response variable. Therefore, it is applied to the preprocessed data to predict the defect depth. The regression model building starts by the selection of the predictor and response variables that are prepared from the collected data. The data are divided into two sets; first dataset is for building the model and setting its parameters, and the second dataset is for model validation and testing its efficacy to predict the output attributes. Several diagnostic tests are performed to check the interactions between different functions and variables of a regression model; then the model is developed by synchronizing the input and output attributes according to the following steps:

1) Defining input and output attributes of the proposed model; input variables comprise pixels intensities represented as RGB profile generated from the preprocessing stage, whereas output variables include the defect depths taken from in situ measurements (actual depths). These measurements are executed by placing a steel plate on top of the defect region represented in Figure 3.14, then taking depth values from the bottom surface of the plate to each point included in the regression model using a measuring tape.

2) RGB profile of pixels intensities is projected upon the defect region in the image, thereby intensities from the projected curve will correlate with actual depth measurements as shown in Figure 3.14. The process continues by defining the sequential functional forms of regression analysis (e.g., linear, quadratic, and cubic) that could best fit the data.

3) Analyzing the data using a scatter plot to determine the best fit model that delivers a prediction of distress depth.

4) Testing the model against several statistical criteria to check its efficacy. Four criteria are selected to underscore the goodness of fit and choose the best fit model. These criteria include R-square (R^2), adjusted R-square ($Adj R^2$), the sum of squares due to error (SSE), and root mean

squared error (RMSE). The best fit model is selected according to the highest R^2 and Adj R^2 , the least SSE and RMSE. Therefore, the model that fulfills the aforementioned criteria is chosen to be the best model, which will be used later for the prediction of defect depth. Further statistical checks are accomplished to ensure the robustness of the selected model.

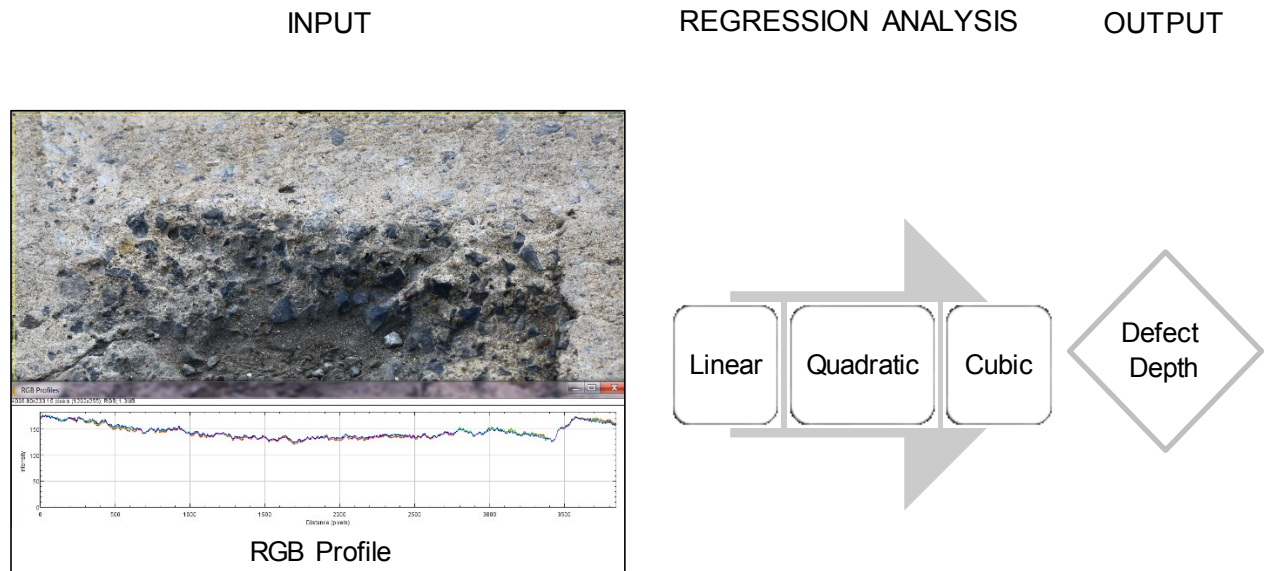


Figure 3.14 Regression Model Overview

3.2.3.3 Cracks Recognition Model

An automatic processor is utilized in this stage to measure the severity of cracks in metro networks. Figure 3.15 demonstrates the different steps included in this model, which starts by calibrating the preprocessed images. Prior to image calibration, any measurement for a randomly selected object inside the image such as a crack length should be taken in situ. This measurement will be set as an entry data in the software, thereby pixel values will correlate with this distance. Consequently, it is feasible to automatically determine the average crack width, by dividing the crack into several segments and measuring the width of each segment by the processor, then computing the average width of all the segments.

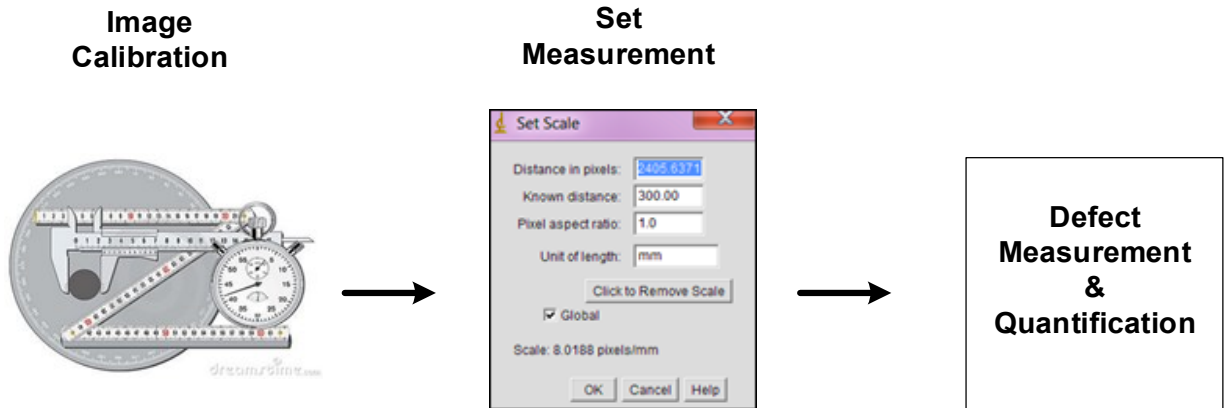


Figure 3.15 Cracks Processing and Recognition Scheme

3.2.4 Condition Assessment of Surface Defects

The final phase involves assigning condition rating to each distress using a condition rating scale. This scale is utilized to exemplify the numeric values pertaining to the linguistic representation. The proposed condition index (CI) scale ranges from “0” to “100”, with “0” representing the worst condition and “100” representing the excellent condition. The condition assessment guidelines of the Ontario Structure Inspection Manual (OSIM 2008) and TOMIE (2015) have been leveraged to develop the condition index scales for the four surface defects. Thus, each defect is evaluated against specific condition rating scale and considering specific feature vector. For instance, moisture marks evaluation is based on the area, spalling and scaling measurements are based on the depth, while cracks evaluation is based on the width attribute. Since the ranges differ from one scale to another, it is essential to normalize the categories of each scale. Table 3.1, Table 3.2, Table 3.3, and Table 3.4 illustrate the condition ratings of moisture marks, spalling, scaling, and cracks respectively, after performing the normalization process.

Table 3.1 Moisture Marks (MM) Condition Ratings

Severity	MM Area Percentage	Condition Index
Light	0 - 20	80 - 100
Moderate	20 - 40	60 - 80
Severe	40 - 60	40 - 60
Very severe	60 - 100	0 - 40

Table 3.2 Spalling (SP) Condition Ratings

Severity	SP Depth (cm)	Normalized SP Depth (cm)	Condition Index
Light	0 - 2.5	0 - 12.5	87.5 - 100
Moderate	2.5 - 5	12.5 - 25	75 - 87.5
Severe	5 - 10	25 - 50	50 - 75
Very severe	> 10	50 - 100	0 - 50

Table 3.3 Scaling (SC) Condition Ratings

Severity	SC Depth (mm)	Normalized SC Depth (mm)	Condition Index
Light	0 - 5	0 - 12.5	87.5 - 100
Moderate	5 - 10	12.5 - 25	75 - 87.5
Severe	10 - 20	25 - 50	50 - 75
Very severe	> 20	50 - 100	0 - 50

Table 3.4 Cracks (CR) Condition Ratings

Severity	CR Width (mm)	Normalized CR Width (mm)	Condition Index
Light	0 - 0.1	0 - 5	95 - 100
Moderate	0.1 - 0.3	5 - 15	85 - 95
Severe	0.3 - 1	15 - 50	50 - 85
Very severe	> 1	50 - 100	0 - 50

3.3 Selection of the Most Appropriate NDE Technology

The methodology of selecting the most appropriate NDE method for subway inspection is depicted in Figure 3.16. As presented, an extensive literature review is conducted to study and classify various NDE technologies. The information is collected from NDE equipment companies and previous research studies. Then, the advantages and limitations of each NDE method are analyzed, by considering its application to concrete subway facilities. This step is followed by establishing a set of selection criteria, which is utilized in turn to compare each NDE technology in terms of providing the best inspection results. And finally, the best NDE technology for subway inspection is selected.

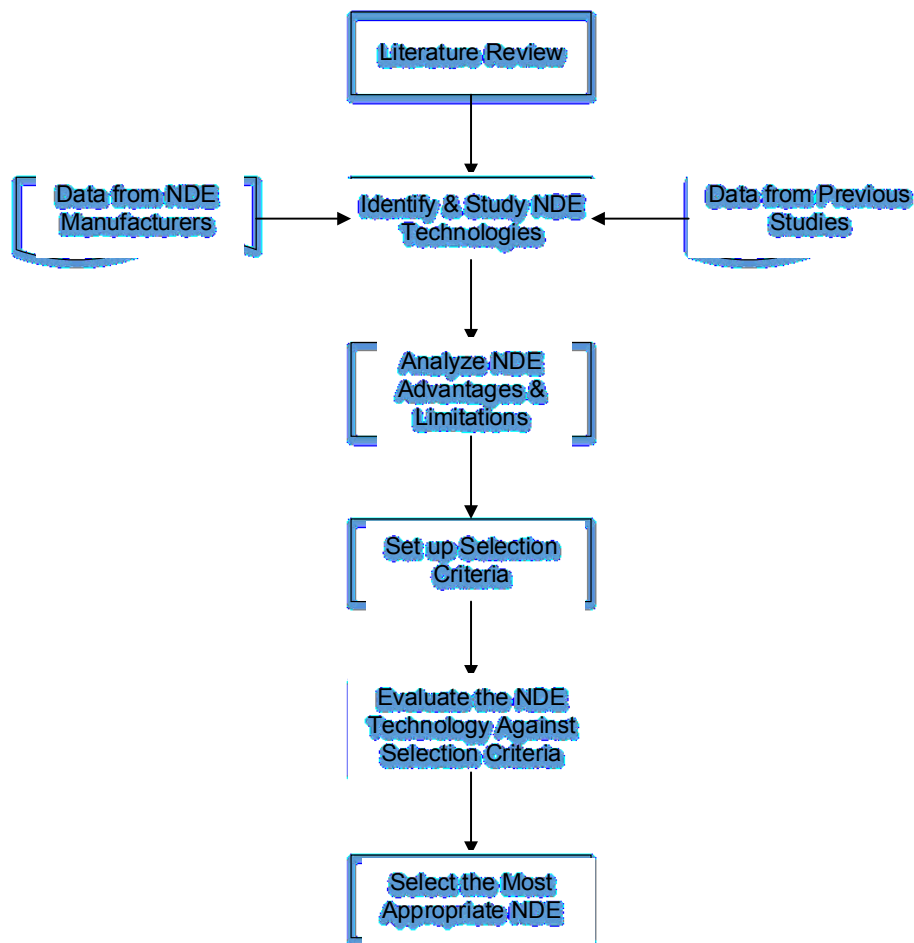


Figure 3.16 NDE Technology Selection Flowchart

3.3.1 Advantages and Disadvantages of Different NDE Technologies

Upon gathering the information of NDE techniques from former researches and the manufacturers, their advantages and limitations for subway inspection are analyzed and tabulated in Table 3.5.

3.3.2 Comparison of NDE Technologies versus Selection Criteria

This stage comprises establishing technical criteria, where each technique will be compared individually versus these criteria. The following characterize the selection criteria: (1) capable of detecting water infiltration; (2) capable of detecting chloride ingress; (3) capable of detecting corrosion; (4) capable of detecting delamination; (5) capable of detecting concrete liners; (6) capable of detecting cracking; (7) capable of detecting voids; (8) rapidity of data collection and analysis; (9) requires minimal human analysis; (10) could be used as a stand-alone method; (11) inspection outputs could be reproducible. Table 3.6 presents the comparison of each NDE technique against the selection criteria. As can be noticed from the comparison results of the table that Ground Penetrating Radar (GPR) is the most appropriate technique for the inspection of subway networks, therefore it will be used in the following subsurface model development.

Table 3.5 Advantages and Disadvantages of Various NDE Technologies for Subway Evaluation

NDE Technology	Generally Applied for	Advantages	Disadvantages
Diagnostic Train	Concrete tunnels, e.g., subway tunnels	High speed of data collection. Ease of reproducing results Detects cracks, flakes, voids, tracks.	Cannot detect rebar corrosion. Cannot detect infiltration. Requires experienced inspector.
Infrared (IR) Thermography	Bridge decks; Building facades	Near-surface delamination could be detected. Cost and time effective.	Cannot detect rebar corrosion. Costly detection. Requires trained inspector. Can only detect shallow defects.
Ground Penetrating Radar (GPR)	Bridge decks; Concrete tunnels	High-speed scanning. Can detect metal & moisture. Results are reproducible. Availability of software.	Cannot detect cracks < 2mm. Cannot detect delamination. Requires experienced inspector & interpreter.
Half-Cell Potential	Detection of rebar corrosion in RC structures	Lightweight equipment. Offers an immediate probability of corrosion.	Low speed. Little penetration depth. Requires experienced inspector. Requires connection to rebars. Requires moist concrete Epoxy-coated bars cannot be detected.
Manual Acoustic Methods	Detection of delamination in RC structures	Lightweight equipment. Easy to use. Can effectively detect delamination.	Cannot detect rebar corrosion. Subjective to operator's interpretation. Cannot detect defects >127 mm depth.
Impulse Response	Concrete & wood structures	Capable of detecting several defects, e.g., cracks, voids, and soil intrusion.	Cannot function without the sonic echo method.
Spectral Analysis of Surface Waves (SASW)	Buildings; tunnels; pavements; monuments; Soil and rock	Capable of detecting concrete liners in tunnels. Can determine elastic properties of materials.	Cannot detect rebar corrosion. Requires experienced inspector. Cannot effectively detect delamination.
Impact Echo	Concrete & Masonry structures	Capable of detecting several defects, e.g., cracks, voids, and delamination. Requires only one side access to concrete.	Cannot detect rebar corrosion. Requires experienced inspector. Low operating speed.
Cover Meter	Location & size of rebar in the top layer	High operating speed. Easy to use. Immediate field results.	Cannot detect rebars >127 mm depth. Can detect only top rebar layer.
Ultrasonic Pulse Velocity (UPV)	Concrete, wood, metal, stone, ceramics and masonry structures	Capable of detecting several defects, e.g., cracks, voids, and delamination.	Requires two-sided access to concrete.

Table 3.6 Evaluation and Selection of NDE Method

NDE Technology	Selection Criteria*										
	1	2	3	4	5	6	7	8	9	10	11
Diagnostic Train						x	x	x			x
IR Thermography				x		x	x	x	x	x	
GPR	x	x	x		x	x	x	x	x	x	x
Half-Cell Potential			x						x	x	x
Acoustic Methods				x				x		x	
Impulse Response						x	x				
SASW					x	x			x	x	x
Impact Echo				x		x	x		x	x	x
Cover Meter								x	x		x
UPV				x		x	x		x	x	x

Selection Criteria*

- (1): Capable of detecting water infiltration.
- (2): Capable of detecting chloride ingress.
- (3): Capable of detecting corrosion.
- (4): Capable of detecting delamination.
- (5): Capable of detecting concrete liners.
- (6): Capable of detecting cracking.
- (7): Capable of detecting voids.
- (8): Rapidity of data collection and analysis.
- (9): Requires minimal human analysis.
- (10): Could be used as a stand-alone method.
- (11): Inspection outputs could be reproducible.

3.4 Subsurface Defect-Based Assessment Model

The development of a subsurface defect-based assessment model is described in this section. This system integrates two analysis methods for the interpretation of GPR profiles, namely; numerical analysis method and image-based analysis (IBA) method. Figure 3.17 presents the flowchart of the proposed system. It includes four major phases as the following: profiles acquisition, data interpretation and analysis, data processing, and condition assessment of subsurface defects. It is worth mentioning that only IBA method involves another stage that is the data preprocessing stage.

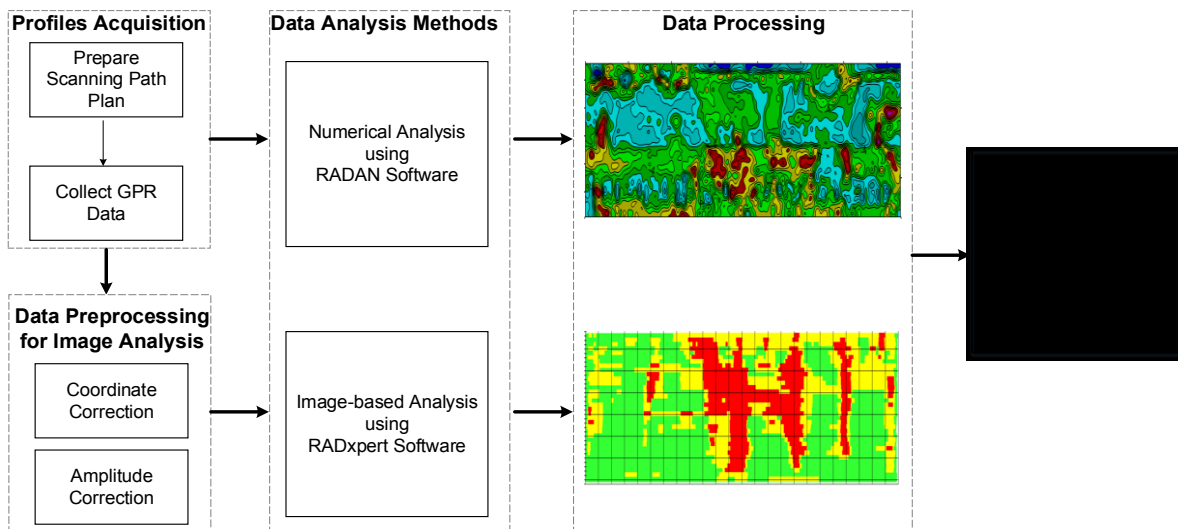


Figure 3.17 Overall Flowchart for Subsurface Defects Condition Assessment

3.4.1 Profiles Acquisition

Since Ground Penetrating Radar is selected as the most applicable technique for the inspection of subway networks, it will be utilized for the acquisition of subsurface data. Such data include a list of internal defects such as steel corrosion, delamination, air voids, water voids, etc. However, this research considers three subsurface defects namely; rebar corrosion, air voids, and water voids. Rebar corrosion is investigated in this research since it is recognized the third priority among

transit infrastructure problems (refer to Table 2.2). While air and water voids defects are studied because of the huge water accumulation between the rock and concrete liners in Montréal subway systems (Chaussée 2012).

In the profiles acquisition phase, the inspector prepares a plan of the facility's component, on which the scanning paths are marked. This is followed by collecting the GPR data based on the previously prepared plan. The output of the survey is a myriad of GPR profiles of a form of B-scan, these profiles are transferred to the computer to be interpreted. Figure 3.18 illustrates the steps included in this phase.

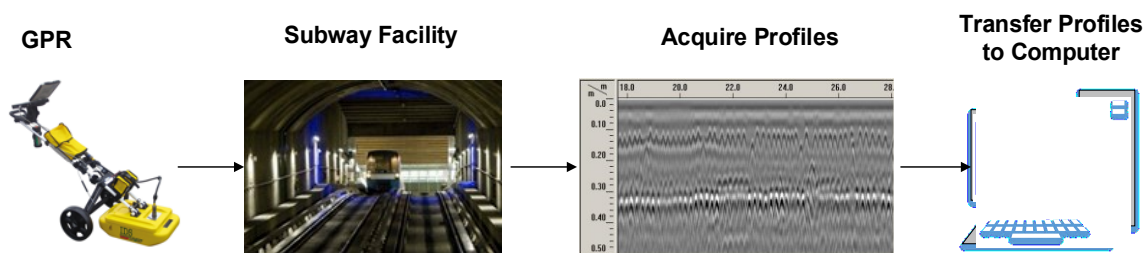


Figure 3.18 Profiles Acquisition Phase

3.4.2 Data Analysis

After transferring GPR profiles to the computer, they are analyzed to detect and measure subsurface distresses. Two techniques are performed so that each technique will eliminate the limitations of the other.

3.4.2.1 Numerical Analysis of Reflection Amplitude

A numerical analysis of reflection amplitude at different medium interfaces is executed using RADAN[®] software. Generally, the reflection amplitude at the top rebar layer is used to infer the condition of concrete element. As the rebars are contaminated with chloride ingress, the

reflected GPR signal will attenuate. Therefore, the process of extracting rebar reflections is represented in Figure 3.19.



Figure 3.19 Amplitude Analysis of Rebar Reflections

3.4.2.2 Image-Based Data Analysis

This analysis method is used to infer the quality of the structure based on the operator's experience in interpreting GPR signals visually. A specialized software tool (RADxpert[®]) is utilized for data analysis. Figure 3.20 demonstrates the overflow of the image-based analysis (IBA). Prior to the analysis process, a preprocessing phase is required to organize each profile into a two-dimensional grid. Thus, the coordinates and the amplitudes are corrected and optimized to be visually interpreted as the proper differential gain is applied to the profiles. Then an experienced analyst may scroll through each GPR profile and determine the deteriorated regions by marking the moderate corrosion regions in yellow and the severe corrosion regions in red as illustrated in Figure 3.21. Finally, the analyst identifies the flaws that are initiated by corrosion and excludes the anomalies that are unrelated to rebar corrosion such as structural elements or previous repairs.

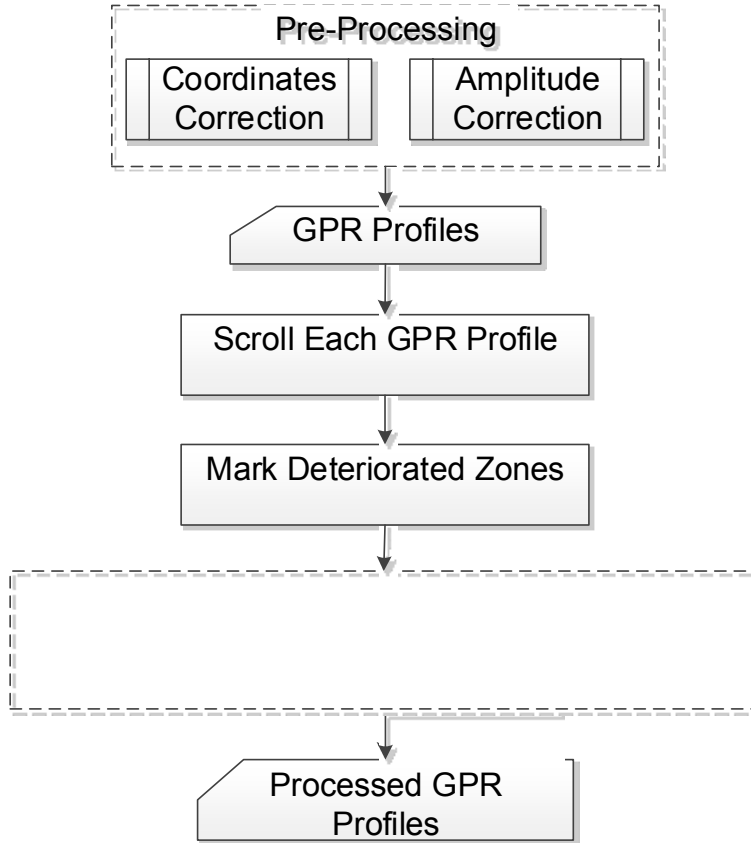


Figure 3.20 Image-Based Analysis Flowchart

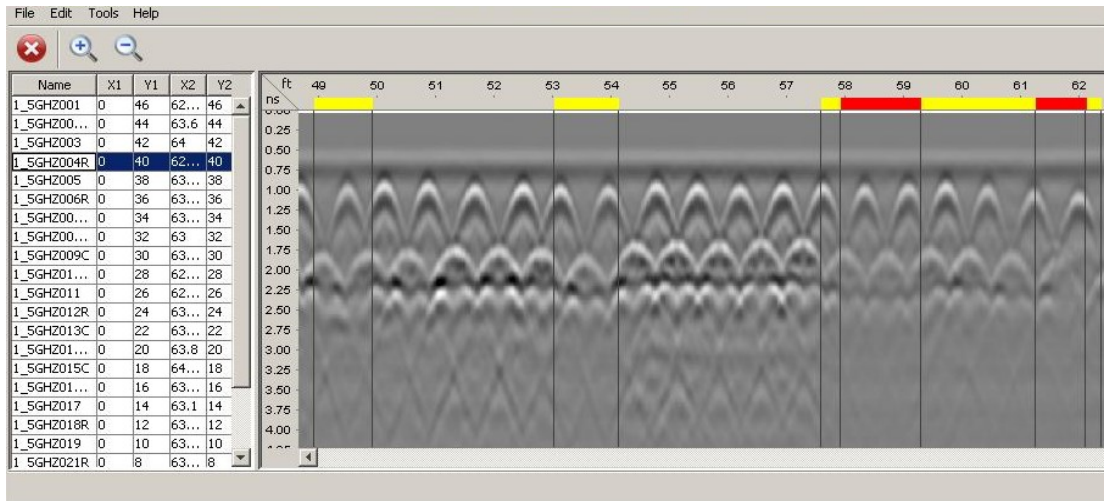


Figure 3.21 Example of the IBA Software

3.4.3 Data Processing

In this phase, deterioration maps of the structural element are produced by the two aforementioned software. First, an attenuation map is automatically generated after performing the amplitude analysis on the GPR profiles by RADAN[®] software tool. Such map is formed of numerous contour lines and different colors. An associated scale is also produced, which defines the severity of each colored zone. Second, the deteriorated regions identified by the image-based analysis (IBA) are automatically mapped by the use of RADxpert[®] software. A complete condition map of the component is plotted by connecting similar region colors from different scanned lines. Examples of the maps generated by the two analysis methods could be found in a research conducted by Dawood et al. (2015_c). In this research, the entire deck of Highway 40 Bridge in Montréal was scanned using the GPR. Followed by generating two deterioration maps for the deck. Figure 3.22 shows the attenuation map produced for this bridge by the amplitude analysis, while Figure 3.23 displays the corrosiveness map generated for the same bridge by the IBA.

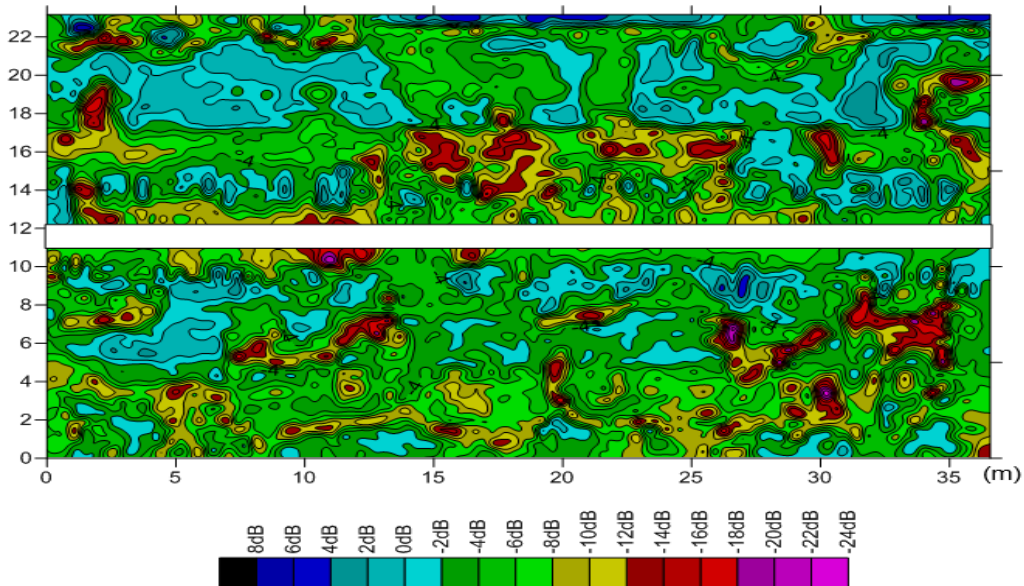


Figure 3.22 Amplitude Attenuation Map

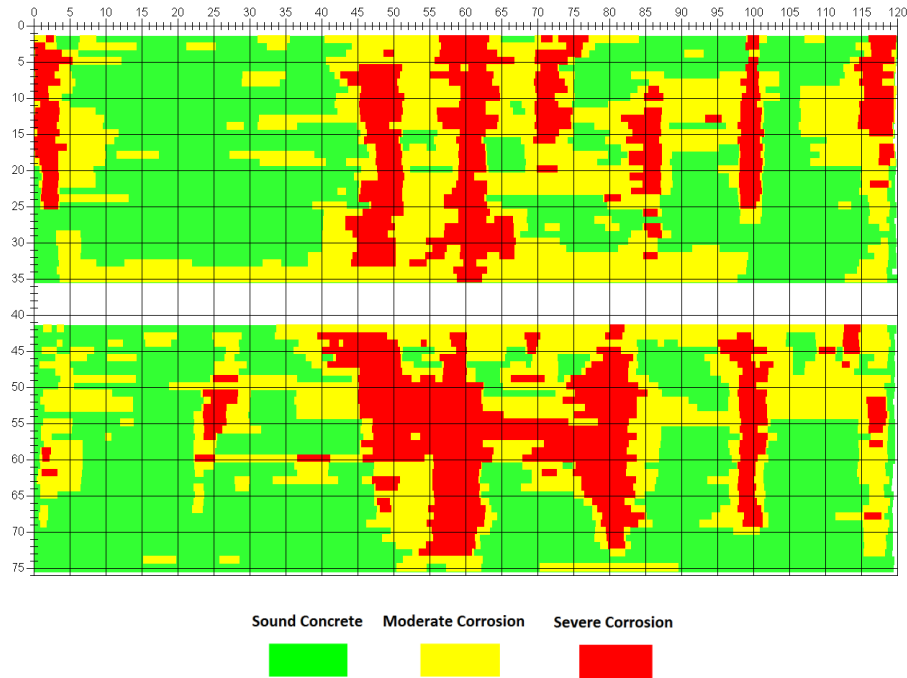


Figure 3.23 Image-Based Corrosiveness Map

3.4.4 Condition Assessment of Subsurface Defects

In the final phase, the condition assessment of subsurface defects is drawn by comparing the deterioration maps previously generated by the two analysis techniques. The measured amplitudes, in addition to the amount of signal attenuation in GPR profiles, are taken into consideration to determine the state of concrete. Later, a condition rating is assigned to each distress using a condition rating scale. The proposed condition index (CI) scale for subsurface defects ranges from “0” to “100”, with “0” representing the worst condition and “100” representing the excellent condition. In this context, several condition assessment guidelines and scales are incorporated to develop CI scales for the three subsurface defects. Such guidelines include OSIM (2008), TOMIE (2015), and Dinh (2014). Subsequent to a lot of discussions with subway managers and experts, the CI scales for corrosion, air voids, and water voids are developed and finalized. Table 3.7 presents the corrosion condition ratings, while Table 3.8 shows the condition ratings for the air voids and water voids.

Table 3.7 Corrosion (CO) Condition Ratings

Severity	CO Percentage	Condition Index
Light	≤ 11.6	88.4 - 100
Moderate	32 - 38	62 - 68
Severe	≥ 78.5	0 - 21.5

Table 3.8 Air Voids (AV) and Water Voids (WV) Condition Ratings

Severity	AV/WV Percentage	Condition Index
Light	0 - 20	80 - 100
Moderate	20 - 40	60 - 80
Severe	40 - 60	40 - 60
Very severe	60 - 100	0 - 40

3.5 Integrated Defect-Based Condition Assessment Model

In the final stage, the surface defect-based assessment model and the subsurface defect-based assessment model are fused to form an integrated defect-based condition assessment model. In this perspective, a scale is required to characterize the numeric values related to the linguistic representation of condition index. A condition index (CI) scale ranging from “0” to “100” and

based on the Canadian Infrastructure Report Card (CIRC 2016) is proposed. Table 3.9 presents the description of each condition rating.

Table 3.9 Integrated Condition Index

Condition Rating	Weighted Average Percentage	Condition Index
Very Good	≥ 80	80 - 100
Good	70 – 79.9	70 – 79.9
Fair	60 – 69.9	60 – 69.9
Poor	50 – 59.9	50 – 59.9
Very Poor	< 50	0 – 49.9

The schematic representation of the integrated defect-based condition assessment model is depicted in Figure 3.24. This figure includes the development of four sub-models. First, the defects' condition indices of each element are calculated via simulation. Second, the existing inspection guidelines are translated to defects' indices, then consolidated into one element condition index using the fuzzy expert system. Third, the neuro-fuzzy technique is utilized to predict the element's condition index. And finally, the subway condition index is computed based on fuzzy reasoning. The following subsections explain the framework pertaining to each sub-model.

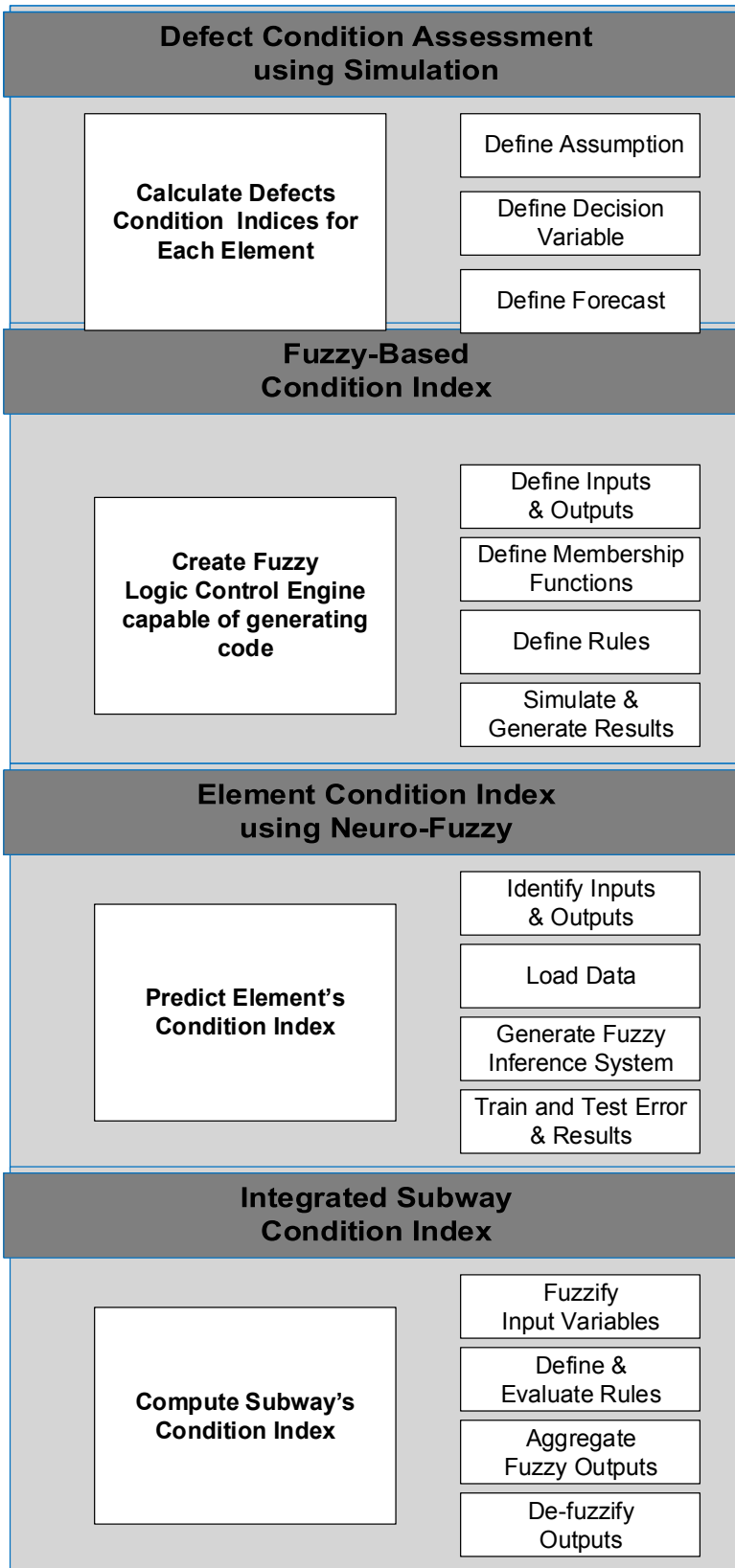


Figure 3.24 Integrated Condition Assessment Scheme

3.5.1 Defect Condition Assessment using Simulation

Crystal Ball software produced by ORACLE® is applied to develop this predictive model. The proposed model builds on Monte Carlo simulation in order to deliver advanced optimization and accurate estimation for the condition index of each defect in the subway element.

The framework of this model includes several steps as demonstrated in Figure 3.25. First, MS Excel spreadsheets comprising the defects' indices are prepared to be analyzed. Statistical analysis of the data is conducted, and several parameters are computed. Second, a probabilistic input to a Crystal Ball model is defined to characterize the behavior of these indices. This includes defining the range of distress indices, followed by performing a probability distribution analysis to identify which distribution best fits the data. Crystal Ball reports the results through three goodness-of-fit statistical tests, the Anderson-Darling (AD), Kolmogorov-Smirnov (KS), and Chi-Square. Also, the P-values of these distributions are generated. The lesser value of these statistics is associated with the best fit. Hence, the software judges the performance of each fit and ranks the distributions in order of their best fit using a comparison chart. In this research, the best fit distribution is selected based on Chi-Square test by accounting for the first rank of the sorted distributions. The Chi-Square gauges the precision of the fit by breaking down the distribution into equal probability zones and comparing the data points within each zone to the number of forecasted data points.

The third step involves defining forecast with the associated goodness of fit by designating the output, which is the defect's condition index (CI) of each element. Finally, the number of simulation trials are determined, to be followed by running the simulation until the so-indicated number of trials is reached. This procedure proceeds by the analysis of the simulation results against different statistical metrics such as mean standard error, variance, skewness, kurtosis, and

coefficient of variation. This analysis is conducted in an ad hoc way. Accordingly, the least error will determine the CI of each distress in the element.

Sensitivity analysis is beneficial in terms of specifying which of the uncertain inputs is generating variance of the model. This is accomplished by interpreting the produced sensitivity chart.

Sensitivity analysis is executed in order to: 1) validate the model, and check the impact of these variable inputs on the results; 2) decrease and allocate the variations through an optimization strategy that is conducive to choosing the most expedient variables.

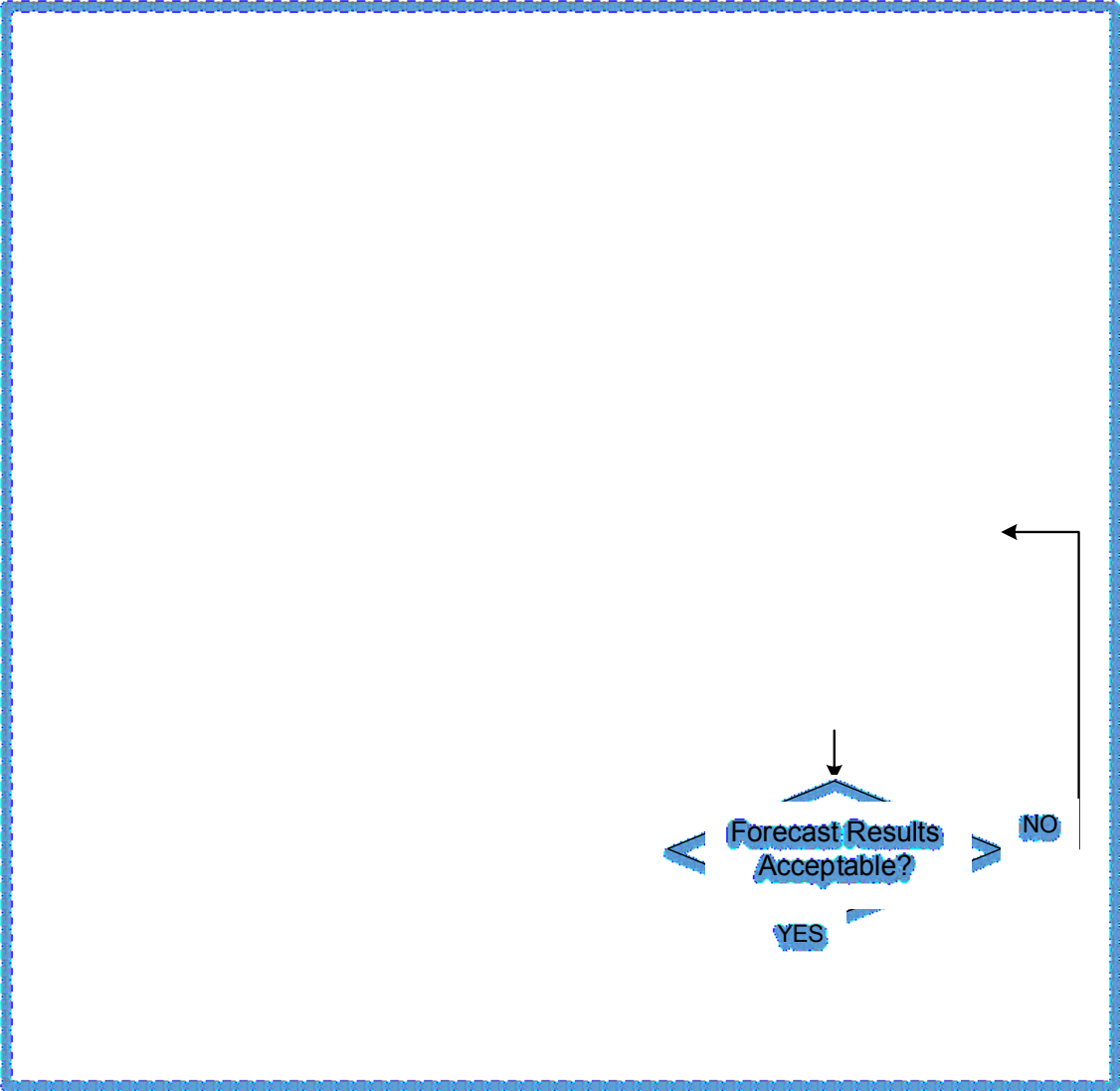


Figure 3.25 Crystal Ball Model Framework

3.5.2 Fuzzy-Based Condition Index

The obtained data from the previously developed models have inherently certain degrees of vagueness and uncertainty. The fuzziness may appear due to the imprecision of surveying conditions, Discrepancies between the real values of the defects and inconsistent input/output sets in the artificial neural networks. At the same time, according to the condition rating definition, the precise condition of a structural element cannot be defined because a condition rating index is an indication of the state of concrete at a certain time (Wang and Hu 2006). Deterioration symptoms in the RC component cannot be easily considered and encoded into a condition index. This is true regarding the amplitude analysis method that provides consistent decibel scale, yet it holds a major shortcoming in the subjectivity of selecting the threshold value. On the other hand, the IBA offers reasonable condition map with exact condition categories. However the boundaries between these categories remain subjective. In addition, the GPR technique that has been utilized to collect the subsurface data may provide more accurate results compared to the traditional inspection methods. Nevertheless the interpretation of these results requires an experienced operator who has a good knowledge of the structural components and design. Therefore, the GPR analysis results hold some degree of vagueness. To overcome these problems and eliminate the imperfections, uncertainty, and vagueness of information, the fuzzy-based condition index model is proposed in this research. This system translates subway inspection results to one condition index as it consolidates the results from surface defect-based model and subsurface defect-based model. In addition, this expert system can provide a wealth of coherent and crisp data that assist in the development process. Figure 3.26 shows the inspection results decoded into the fuzzy expert system.

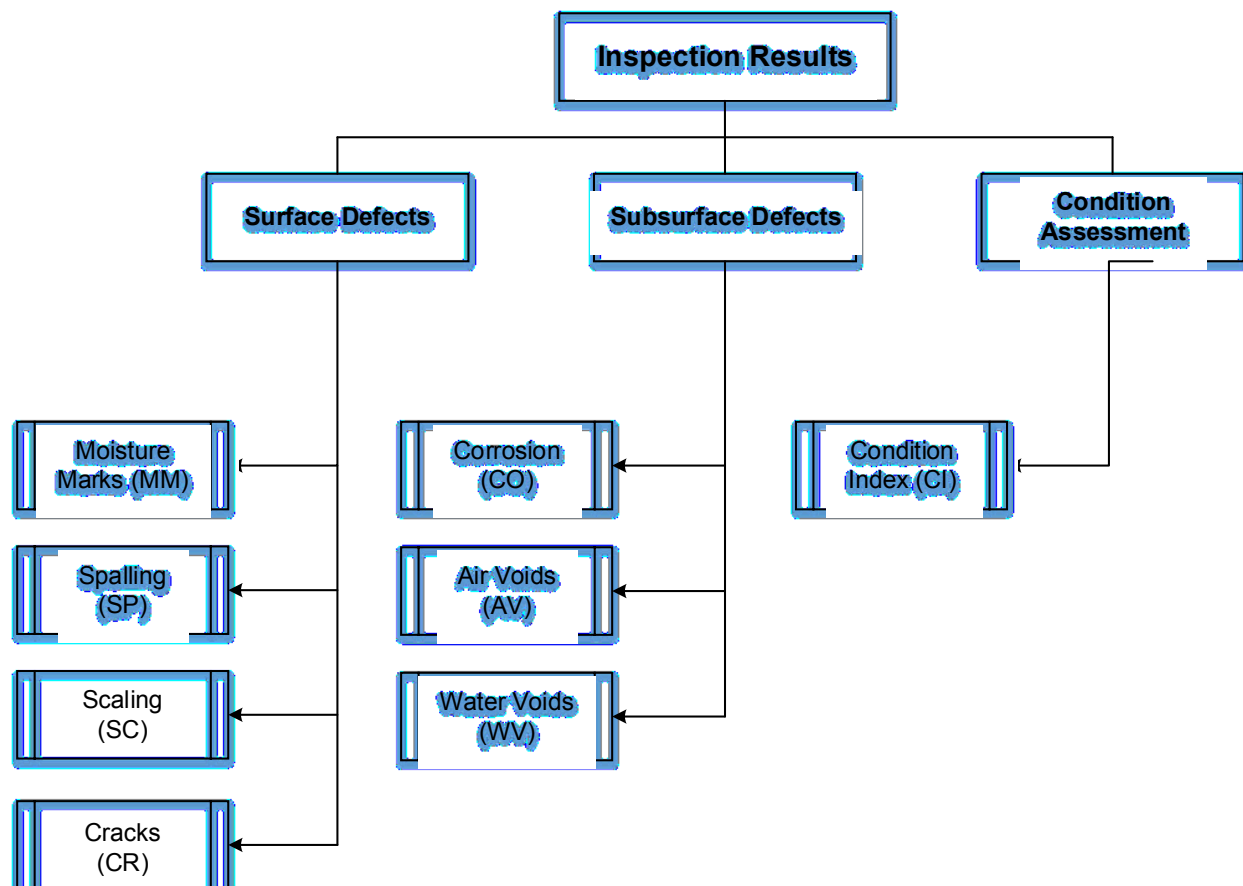


Figure 3.26 Types of Inspection Results

The proposed fuzzy-based condition index model is synthesized based on the Mamdani's method to assess the severity of distress. The following steps describe the configuration of the model:

1) Defining input and output datasets of the proposed model; input set (I) to the fuzzy estimator are the seven defects and the output set (O) are identified as follows:

$$I = \{Moisture\ Marks, Spalling, Scaling, Cracks, Corrosion, Air\ Voids, Water\ Voids\}$$

$$O = \{Condition\ Index\}$$

2) Defining membership functions; this step embarks upon assigning the number of MFs for each distress. This number and associated thresholds are derived from the proposed tables, i.e., Table 3.1, Table 3.2, Table 3.3, Table 3.4, Table 3.7, Table 3.8, and Table 3.9. Therefore, four MFs are

designated for all the inputs except the corrosion distress that is assigned three, whereas the MFs initiated for the output is five.

3) Fuzzy reasoning and rule evaluation; A chain of 136 Fuzzy If-Then rules is generated in the fuzzy operator to map the inputs of seven defects to the output identified as the condition index. The reasoning of rules is obtained and derived from the condition assessment guidelines and expert's judgment.

4) Simulating to generate outputs; this step involves the aggregation of inputs and outputs along with the defined rules to produce a list of crisp defects indices and their corresponding condition indices. This is basically a de-fuzzification process that is accomplished by a technique so-called center of mass or the centroid. Equation (3.10) demonstrates the mathematical computation of the centroid. Where, c is the centroid, m_c is the membership in class c at value X_i .

$$c = \frac{\sum_{i=1}^n X_i m_c(X_i)}{\sum_{i=1}^n m_c(X_i)} \quad (3.10)$$

3.5.3 Element Condition Index using Neuro-Fuzzy

The outputs of the fuzzy-based condition index model are channeled to the neuro-fuzzy engine to develop a model capable of predicting the element condition index. Thus, defects indices and condition indices generated from the previous model are utilized as inputs to build the element condition index using neuro-fuzzy as demonstrated in Figure 3.27. Multi neuro-fuzzy networks are created to test the interactions of different scenarios; then the model is selected based on an optimization procedure. The following steps characterize the model development:

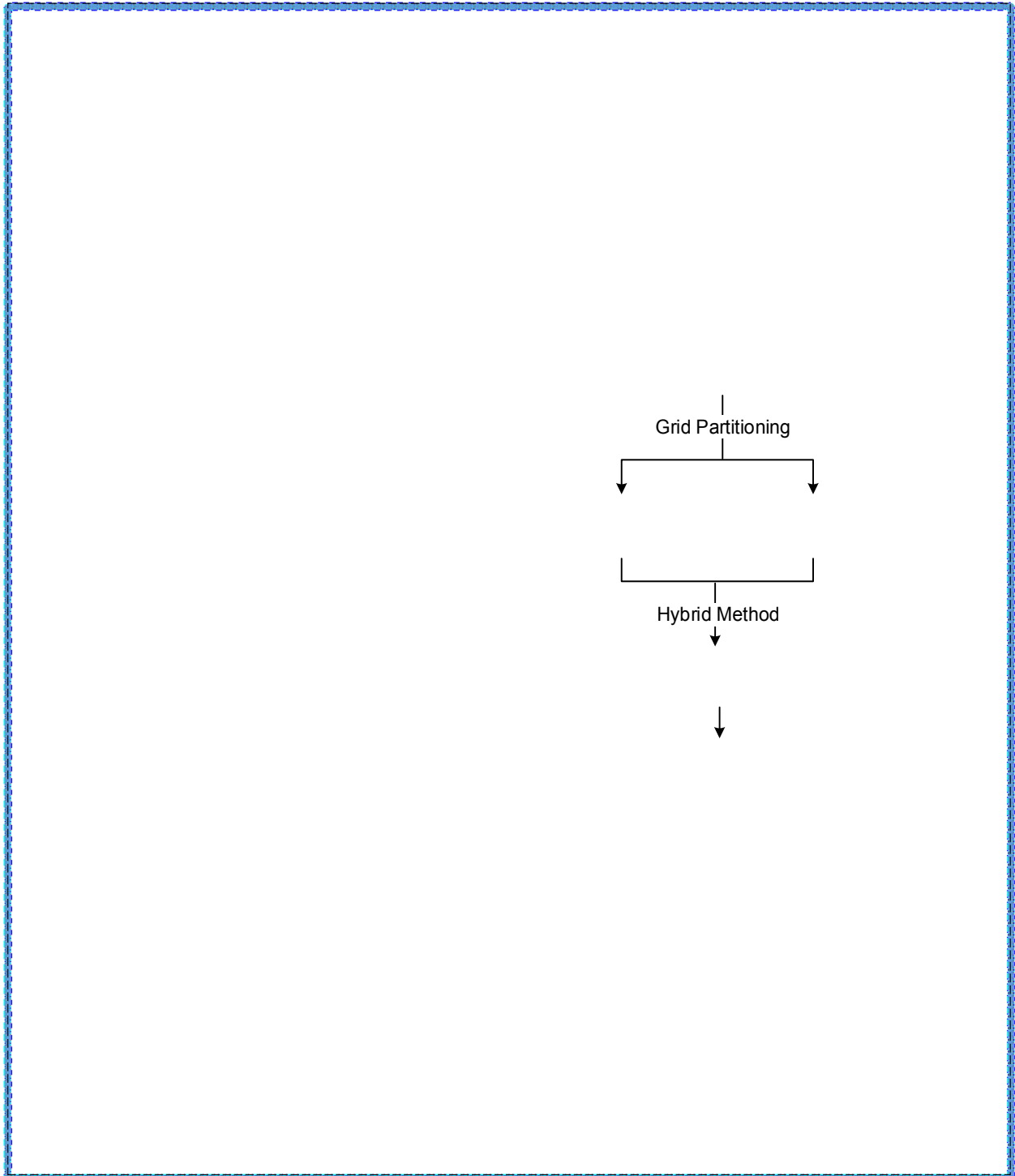


Figure 3.27 Neuro-Fuzzy Prediction Model

1) Dividing the data randomly into three sets; namely training (60%), checking (20%), and testing (20%). The training set is used to train and tune the model until the results are acquired with least error. It is a learning process through which errors are generated and checked thoroughly against the checking dataset in what's known as epochs, whose function is to stop the training as soon as the error increases. The testing dataset is utilized to measure the network performance during and after the training phase by evaluating the produced error. The three datasets are loaded in the Sugeno Adaptive Neuro-Fuzzy Inference System (ANFIS). Sugeno system is more compact and offers more powerful and effective computational approaches than a Mamdani system (Vaidhehi 2014), thus enhancing the structure's capabilities.

2) Generating the Fuzzy Inference System (FIS); it is an optimization process that is achieved by selecting one of the inherent clustering methods, i.e., grid partitioning or subtractive clustering. Grid partitioning algorithm produces clusters with an equal number of cells while it reduces the number of partition interfaces and partition neighbors. This algorithm runs precisely with a small number of MFs, which involve less simulation time and attain low error. Whereas, subtractive clustering requires a large number of MFs, which in turn require more simulation time (Vaidhehi 2014). Therefore, it is feasible to apply the grid partitioning method in this research, since few MFs are utilized to generate FIS. Later, the number and type of MFs are determined. Such types include but are not limited to, triangular, trapezoidal, and Gaussian.

3) Training ANFIS; yet before training the system, some parameters should be chosen such as the optimum training method, i.e., hybrid or backpropagation. The hybrid method incorporates the gradient descent and the least squares estimation to recognize the ANFIS parameters. The basic function of the gradient descent algorithm is to tune the nonlinear parameters. However the mean least squares algorithm is applied to optimize the linear consequent parameters. On the other hand,

back propagation method is limited to finding the optimal values of the nonlinear parameters, e.g., Gaussian MF parameters (Jang 1993). In this research, the hybrid method is used as it presents a more comprehensive paradigm. In addition, the number of epochs is assigned in this step. At each epoch, the error that is the sum of the squared difference between actual and predicted output is minimized. Subsequent to determining the parameters, The ANFIS engine is set for training. It starts by mapping input data to input MFs and related parameters, and mapping the MFs to a set of If-Then fuzzy rules. Then, rules are mapped to output MFs, until crisp outputs are finally generated (Mathworks 2013). Training stops once the pre-assigned epoch number is reached or when the produced error starts increasing due to over-fitting. This is followed by testing and checking the network and recording the associated produced errors.

4) Developing multi neuro-fuzzy networks through different interactions, which include changing the number and type of MFs, and recording the errors of training, testing, and checking the network. Moreover, 2D or 3D surface views can be produced to interpret the relationship of one or two of the inputs against the output. These schematic presentations are basically a sensitivity analysis of the output variable against the input variables. Thus, the network will be deleted if its associated surface view is negative. After forming various scenarios that encompass different types and MFs, the best model is selected according to the least mean squared error (MSE) and the positive 3D presentation. The MSE that measures the average of the squares of errors between the estimated and actual value of the output is calculated by Equation (3.11).

$$\text{MSE} = \frac{1}{n} \sum_{i=1}^n (C_i - E_i)^2 \quad (3.11)$$

Where, C_i is the actual output, E_i is the estimated output, and n is the number of data points in each dataset. Thus, the final selected model will be used to predict the elements condition indices of subway infrastructure.

3.5.4 Integrated Subway Condition Index

There exist two primary approaches for modeling the deterioration in subway infrastructure, especially when it requires the consolidation of a set of results. One of the well-known approaches that gained a lot of acceptance in academia is the reliability-based models. These models utilize the probabilistic theory and comprise sophisticated convolution integrals to assess the structural behavior. The merit of applying the reliability-based models is their resilience to analyze the condition of one element, as well as a system of elements, such as the series and parallel system analysis. However, the major shortcoming pertaining to such methods is the huge volume of input data required to accomplish decent analysis outcome, besides they entail a significant computational burden. Therefore, these methods might not arrive at an optimal solution and address the issues of this research. The second approach that can deliver coherent results is the fuzzy implication system. This system dictates the expert rules to model the interrelationships between subway elements and the final condition index. It features the fusion of the elements' condition indices into one platform to provide coherent condition assessment through exploiting logical linguistic values. Figure 3.28 presents the integrated fuzzy-based framework for the condition assessment of subway networks.

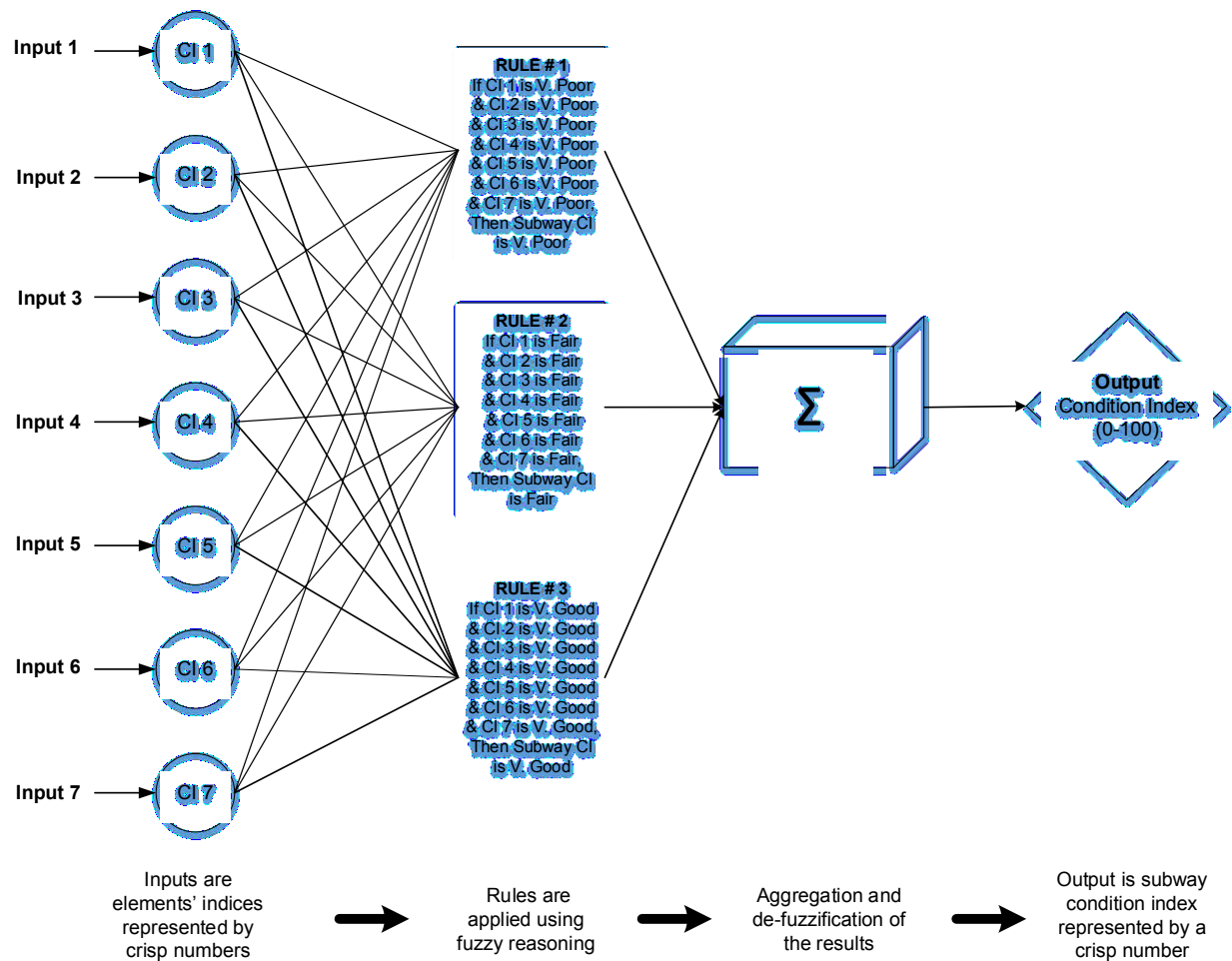


Figure 3.28 Fuzzy Consolidation Model Structure

The Mamdani style technique is performed to create the fuzzy consolidation model. First, the fuzzy inference system is developed by identifying and naming the inputs and output variable. Inputs are the elements condition indices while the output represents the subway condition index. Second, membership functions (MFs) are created for each input, as well as for the output variable. The MFs describe different levels of damage, which are assigned thresholds in accordance with Table 3.9. Hence, five MFs are assigned for each of the input/output variables. Third, constructing the fuzzy rule base, the design of which is drawn from the experts' guidelines. The process mechanism of the model shown in Figure 3.28 is elaborated in the following steps:

- 1) Fuzzification of input variables; this step involves taking the crisp elements' indices, e.g., CI 1, CI 2, CI 3, etc. and defining the degree of MFs, each of the inputs belongs to in the fuzzy sets.
- 2) Applying fuzzy rule operator; the fuzzified inputs are treated by the fuzzy operator (AND/OR), which regulates the stipulations of rules and executes fuzzy reasoning. The outcome of this step is mapped to the resultant MFs.
- 3) Aggregation and de-fuzzification of the output; this process implicates the fusion of rule consequents, which is basically the aggregation of inputs and outputs along with the defined rules to produce a single crisp output that is the subway condition index.

CHAPTER 4: DATA COLLECTION

4.1 Preliminary Data Collection

Given the scope of this research, and in order to exemplify the implementation of the proposed methodology and validate its results, it was imperative to perform data collection in Montréal subway network. Prior to data collection, the subway network hierarchy has been identified to facilitate the data collection and analysis procedure. Figure 4.1 depicts the generic hierarchy of the subway network.

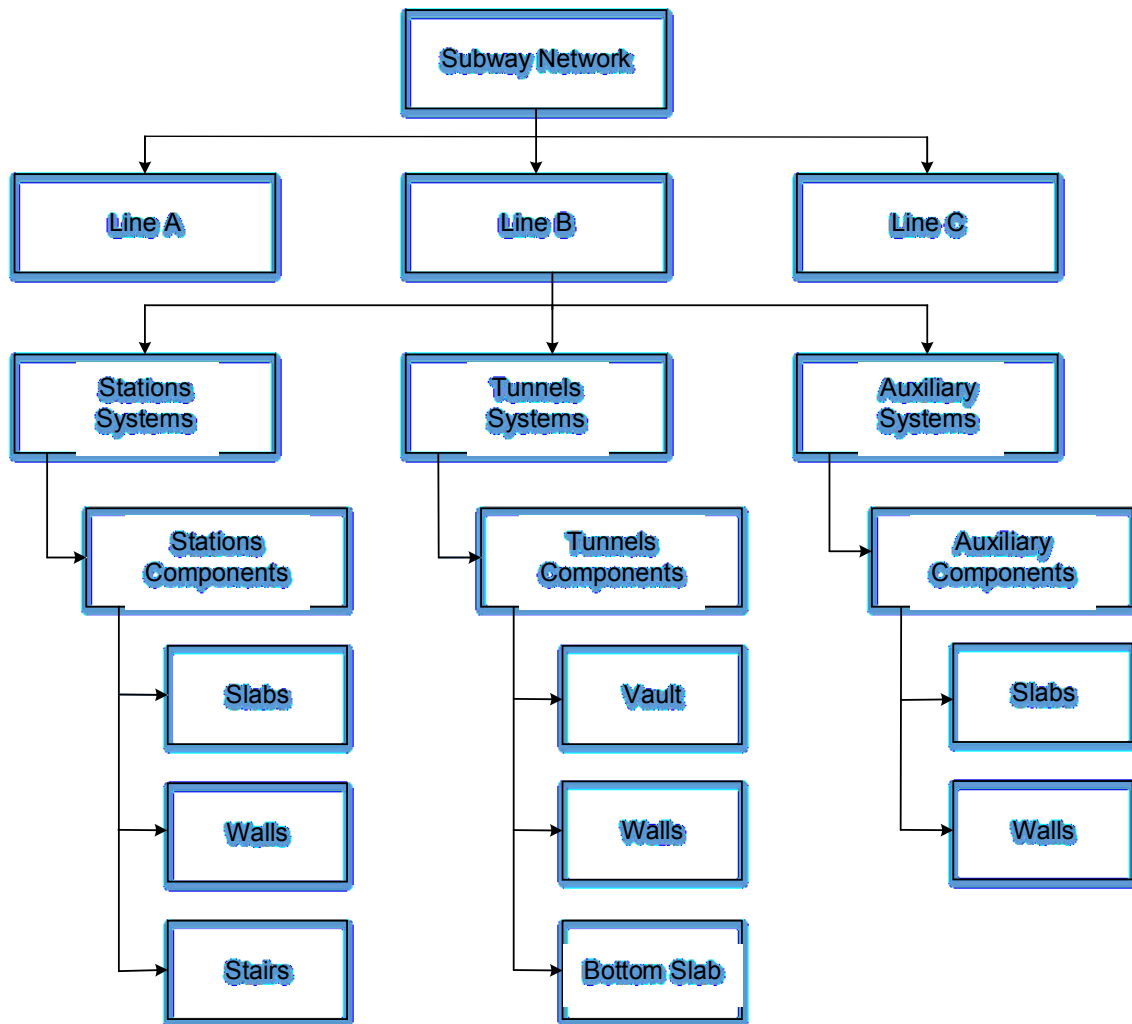


Figure 4.1 Subway Network Hierarchy

After breaking down each system in the network into its elements, several visual inspection visits were organized in collaboration with the Société de Transport de Montréal (STM) to select and determine the most deteriorated systems in the network. These systems included several locations on different metro lines, such as the Orange, Green, and Blue Line. This process took almost seven months, from July 9, 2015, till February 12, 2016. Some of the visits took place during normal daytime hours, and the rest after 1:00 am when metro services were shut down, especially when the inspection targeted those elements next to the railways. Since visual data, i.e. images play a vital role in the recording and archiving of surface damages of RC structures; hundreds of images were taken for different subway components to enable the visualization and comparison processes. Thus, assisting in the optimal selection of the stations, tunnels, and auxiliary structures to be included in the final data collection plan. Subsequent to several discussions with the STM managers, it was decided to exclude the auxiliary structures from the research data collection, and solely focus on the stations and tunnels of Montréal subway network. Table 4.1 summarizes the information related to these preliminary visits.

Post inspection analysis of the acquired images provided invaluable information and assisted in the selection of the candidate stations and tunnels to be studied. After careful visual assessment and extensive research, four systems were selected for data collection. These include Outremont station on the Blue Line, Vendôme station on the Orange Line, inter Frontenac and Papineau tunnel on the Green Line, and inter St. Laurent and Place-Des-Arts tunnel on the Green Line as presented in Figure 4.2. The four systems were chosen to demonstrate the proposed methodology for one or a combination of the following reasons: (1) the system is considered one of the most congested systems in Montréal's Metro network; (2) it is an intermodal transit station, where more than one mode of transportation in a journey is used; (3) symptoms of damage are quite visible on the

surfaces of its elements; (4) it started showing signs of deterioration. These deterioration rates are higher than their counterparts in other subway systems.

Table 4.1 Montréal Metro Preliminary Visits

System Type	Location	Metro Line	Date	Time
Station	Mont-Royal	Orange	July 9, 2015	12:15 am - 1:05 am
Station	Lucien-L'Allier	Orange	July 9, 2015	1:15 am - 1:30 am
Tunnel	Inter Lucien-L'Allier & Georges-Vanier	Orange	July 9, 2015	1:30 am - 3:15 am
Station	Angrignon	Green	July 9, 2015	3:30 am - 5:00 am
Tunnel	Inter Frontenac & Papineau	Green	January 29, 2016	2:50 am - 5:00 am
Station	Jean-Talon	Orange, Blue	February 12, 2016	10:15 am - 11:00 am
Station	Place-des-Arts	Green	February 12, 2016	11:07 am - 12:00 pm
Station	Vendôme	Orange	February 12, 2016	1:00 pm - 1:30 pm
Station	Snowdon	Orange, Blue	February 12, 2016	1:35 pm - 2:00 pm
Station	Outremont	Blue	February 12, 2016	2:05 pm - 2:55 pm
Station	Acadie	Blue	February 12, 2016	3:00 pm - 4:00 pm

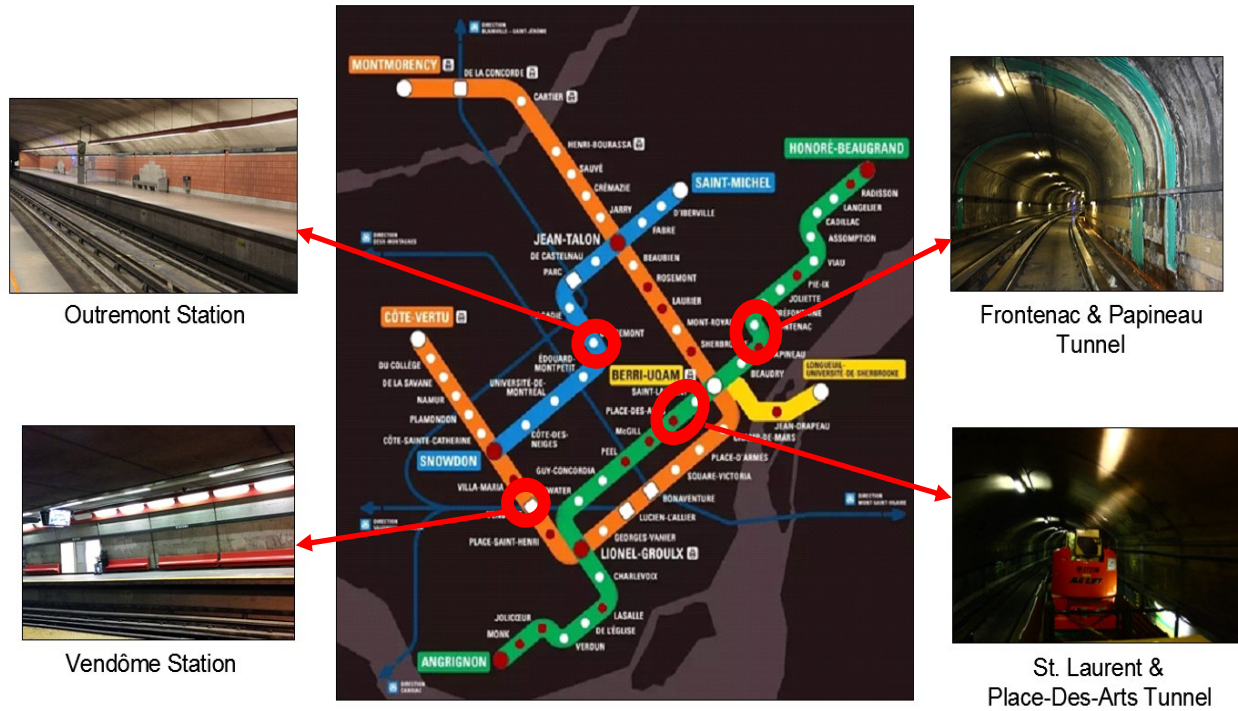


Figure 4.2 Selected Stations and Tunnels in Montréal Subway

Then, a plan was set to perform data collection in Montréal subway network; this plan comprised determining various parameters. First, the number of surveyors executing the inspection was decided to be four including the cameraman. Second, the time and date of each inspection. Third, the tunnel segments and/or subway elements to be inspected. And fourth, the utilized equipment and technologies. During this research, numerous optical sensors and imaging technologies were applied to accomplish its objectives. The two main objectives were modeling the surface and subsurface defects in subway networks. Therefore it was crucial to identify the exact equipment and technology for a specific task after studying different criteria in order to optimize the final results.

4.2 Key Indicators in Data Collection

4.2.1 Key Indicators in Surface Data Collection

The spectacular advancements in imaging technologies resulted in a more enhanced image, adding to that the moderate cost of cameras, which made them the optimal sensors for multi automation approaches. Optical data were collected through utilizing a digital imaging system. A digital camera with a built-in flash (Canon EOS Rebel XS, 10.1-megapixel) and a telephoto 55-250 mm were employed to acquire images that target the surface defects on concrete as shown in Figure 4.3. The camera has a high resolution of 2592×3888 pixels, CMOS sensor that captures sharp photos, large 2.5-inch LCD display, and DIGIC III image processor that provides quick, precise image processing and clear details.



Figure 4.3 Canon EOS Rebel XS and its Telephoto (Canon 2015)

Regarding, the accessible elements in the subway such as the lower slabs, close-range images were captured orthogonal to the surface with sufficient overlapping. Whereas, an inspection train equipped with a man lift was used to specifically approach the inaccessible surfaces such as the tunnel vaults. This process was applied to ensure that proximity is attained while capturing the

images, also to allow for smooth transition and high accuracy of data collection as shown in Figure 4.4.



Figure 4.4 Image Acquisition Process in a Montréal Subway Tunnel (Dawood et al. 2017_a)

Also, Figure 4.5 represents the acquired images for different surface defects in Montréal Metro systems. Figure 4.5(a) shows an open crack on the upper slab in Montréal subway. It can be noted that the crack is surrounded by moisture marks and filled with salty oxidations. This phenomenon can be widely noticed on the elements of the subway. Figure 4.5(b) represents a spalling distress on a lower slab, while Figure 4.5(c) depicts a scaling flaw on the upper slab of a station. It could be noted the amount of water infiltration represented in a form of wet areas surrounding the scaling defect. The defects presented in the aforementioned figures will be utilized in the image processing and model implementation of this research.



(a)



(b)



(c)

Figure 4.5 Various Defects in Montréal Subway Network (a) Cracks and Moisture Marks; (b) Spalling; (c) Scaling

4.2.2 Key Indicators in Subsurface Data Collection

Since the Ground Penetrating Radar (GPR) was identified earlier in this research as the most suitable technique for subway inspection, it was exploited for subsurface data collection. Prior to opting for any GPR system or executing data collection, several aspects were studied, considered and organized, such as GPR's operating frequency that is literally the frequency bandwidth of GPR antenna. It controls the waves' penetration depth and spatial resolution. According to Annan and Cosway (1994), there is a trade-off between penetration depth, resolution, clutter reduction, and GPR mobility. It is recommended to trade-off spatial resolution for signal penetration depth since there is no benefit of attaining high resolution while the object cannot be detected. In general, the

high frequency of the antenna will bring about high-resolution intensity, but low penetration depth. The second aspect is the scanning paths or survey lines that should be established perpendicular to the targets with sufficient spacing. In this research, line spacing was planned between 0.3m - 0.5m, depending on the size and dispersion of targets. The smaller and more dispersed the objects, the lesser spacing required. Figure 4.6 represents the scanning paths plan inter Frontenac and Papineau tunnel in Montréal Metro. Third, data processing software that was determined based on the structure under investigation. It is noteworthy that there exist two types of tunnels in Montréal subway network; reinforced and non-reinforced concrete tunnel structures. Therefore, it was of utmost significance to choose the proper software to accomplish data interpretation and analysis. For example, amplitude analysis was found to be dysfunctional in the profile analysis of non-reinforced elements of the structures, since this analysis necessitates rebar picking in order to record the reflection amplitude of the rebars, thus generating the attenuation map of the structure. In this context, IBA was selected as a stand-alone technique to infer the non-reinforced concrete condition.

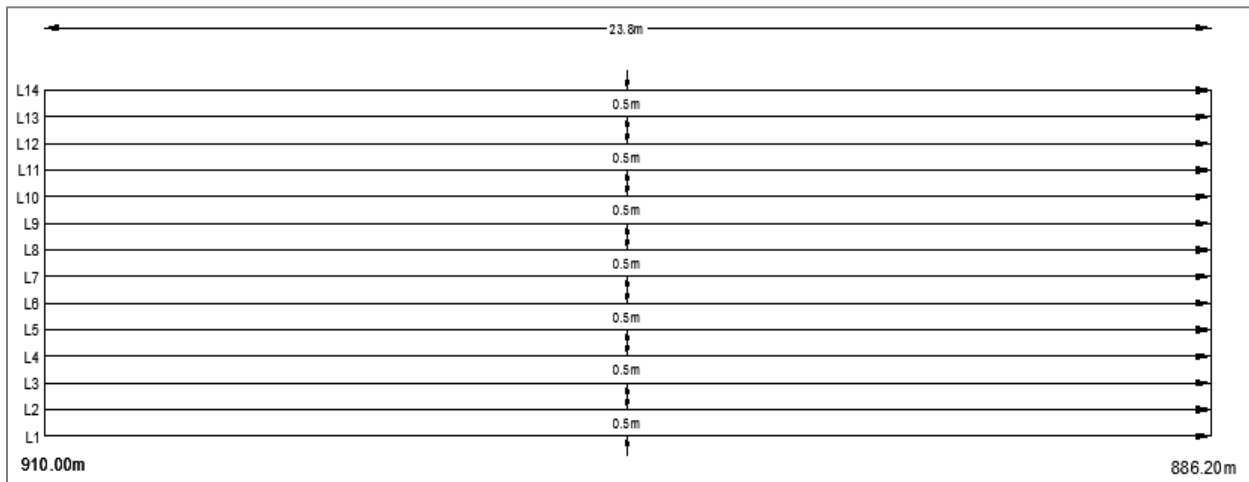


Figure 4.6 Tunnel Plan and Scanning Paths

The structure of each of the selected systems was scanned via a dual polarization technique. Using this technique, the structure is scanned once in the longitudinal direction, and in the second time in the transversal direction. The dual polarization technique is quite beneficial for probing the huge structures such as subway systems inside which rebars are closely spaced, which render it hard to detect subsurface defects such as rebar corrosion by large antennas. Therefore, this technique offers a reasonable horizontal resolution to distinguish the anomalies in concrete.

Before using the GPR to scan each path, the area to be inspected was marked into survey lines with chalk. These lines control the transversal and longitudinal scans and provide precise coordinates in data mapping. A Ground-coupled GPR system was utilized to probe the structures. This system radiates the electromagnetic (EM) signals into the ground. It is characterized by higher resolution, signal/noise ratio, and penetration depth than the air coupled GPR system. After calibrating the GPR, surveys were conducted for the selected elements in subway systems. Similar to surface data collection, a man lift attached to an inspection train was used to reach the inaccessible places.

It's worth noting that both the coordinate systems of surface data and subsurface data were synchronized according to the chainage system in Montréal subway. This step was crucial to ensure the exact mapping and precise assessment of the structure. Figure 4.7 illustrates the subsurface data collection using GPR. Figure 4.8(a) demonstrates a GPR profile of a wall inter St. Laurent and Place-Des-Arts tunnel, scanned using the 900 MHz antenna, while Figure 4.8(b) presents a GPR profile of a lower slab in Vendôme Station, scanned using the SS-MINI antenna.



Figure 4.7 Profiles Acquisition Process in a Montréal Subway Tunnel

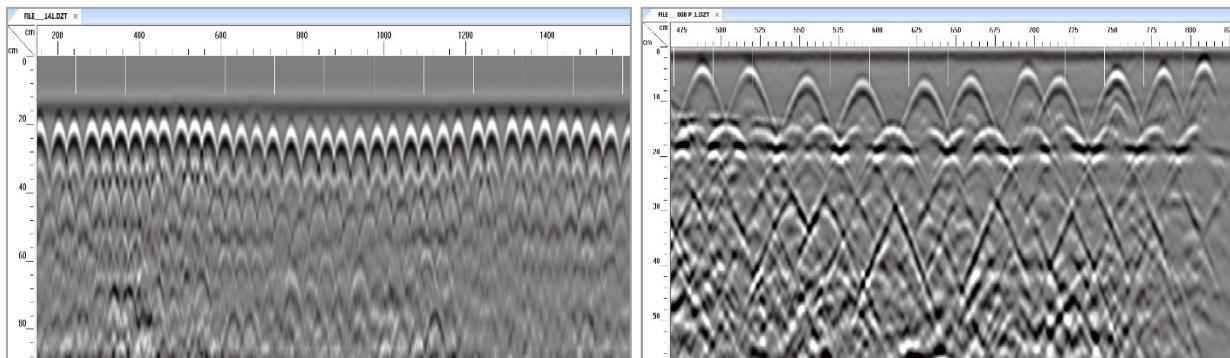


Figure 4.8 GPR Profiles Samples (a) inter St. Laurent and Place-Des-Arts Tunnel using 900 MHz Antenna; (b) in Vendôme Station using SS-MINI Antenna

Table 4.2 summarizes the various aspects pertaining to scanning the selected systems in Montréal Metro network using the GPR. As represented in the table, certain components were investigated in each of the four selected systems. For example in Vendôme Station, only the slab was inspected, while in Outremont Station, three components were examined (i.e., wall #1, wall #2, and a slab). Afterwards, a segment of each component was selected to undergo the inspection. Each of these

segments was labeled according to a coding scheme. The table also shows the antenna configuration used to evaluate the condition of each element. Prior to selecting the appropriate antenna frequency for each element, elements' plans were studied and analyzed to determine the required penetration depth, thereby optimizing the selection of the best GPR antenna frequency.

Table 4.2 Subsurface System Scanning Related Data

Information	Frontenac & Papineau Tunnel	Vendôme Station	Outremont Station			St. Laurent & Place-Des-Arts Tunnel	
	Vault	Slab	Wall #1	Wall #2	Slab	Wall	Slab
Segment Code	FPTV	VSS	OSW1	OSW2	OSS	SPTW	SPTS
Scanned Length (m)	23.80	8.25	5.20	2.20	10.00	23.00	22.25
Scanned Width (m)	6.50	4.56	2.10	2.08	4.00	0.80	1.20
Number of Scanning Lines	14	17	10	5	9	3	4
Spacing (m)	0.50	0.50	0.50	0.40	0.40	0.30	0.30
Scanning Date (Year 2016)	April 23 & 30	April 26	May 3	May 3	May 3	June 4	June 4
Scanning Time	2:15 am - 5:00 am	9:00 am - 5:00 pm	9:00 am - 5:00 pm			2:15 am - 5:00 am	
Temperature °(C)	12, 14	14	19	19	19	28	28
Antenna	900 MHz	SS-MINI	SS-MINI	SS-MINI	SS-MINI	900 MHz	900 MHz
Scans/Second	160	260	260	260	260	64	64

CHAPTER 5: MODEL DEVELOPMENT AND IMPLEMENTATION

This chapter describes the development of the methodology proposed in chapter 3. The image preprocessing, profile preprocessing, and data processing for surface and subsurface defects were performed on a desktop PC (Intel Core i3-3220 CPU @3.30 GHz, 64-bit operating system), by utilizing the MATLAB® R2013b Toolboxes. First, different image preprocessing algorithms were applied to the images to enhance their quality. These algorithms involve computational approaches to image data through utilizing multiple operators and filters that can detect the surface distresses. Second, various machine intelligence tool boxes and statistical packages were used to evaluate the severity of distresses. Third, GPR profiles were analyzed via sequential interactive processes to accomplish multi-objective outcomes, such as mapping the deteriorated regions. Fourth, indices are produced and aggregated in the computer vision-based control system design to develop an integrated model for the condition assessment of subway networks. The following sections entail the development process and model implementation for each of the seven defects.

5.1 Moisture Marks Model

5.1.1 Preprocessing of Moisture Marks

One of the main purposes of preprocessing the original image is to segment the image into sub-elements e.g., moisture marks, spalling, and cracks, that can be handled easily in the processing phase by the artificial intelligence machines, such as ANNs. In fact, ANNs can handle RGB images to identify the distresses without the preprocessing phase. However, the size of the applied RGB image is very large. Because the RGB image has three layers of matrices, each pixel in the RGB image has three intensity values. Feeding the network with a very large number of values in the input and output layer is unfeasible and may imply longer computational time. Hence, the

second purpose of image preprocessing is to reduce the computational time and prepare the images to be easily treated by ANNs. Multiple image processing algorithms and filters were applied to the images to enhance their quality. Moreover, RGB space in the original image shown in Figure 4.5(a) was split into three planes; red, green, and blue to extract a grayscale representation as depicted in Figure 5.1. Each of the three planes shares the same size and bit depth, and it represents a gray-level image. Then, the blue plane was chosen to be further processed, as it offers the best-enhanced image.

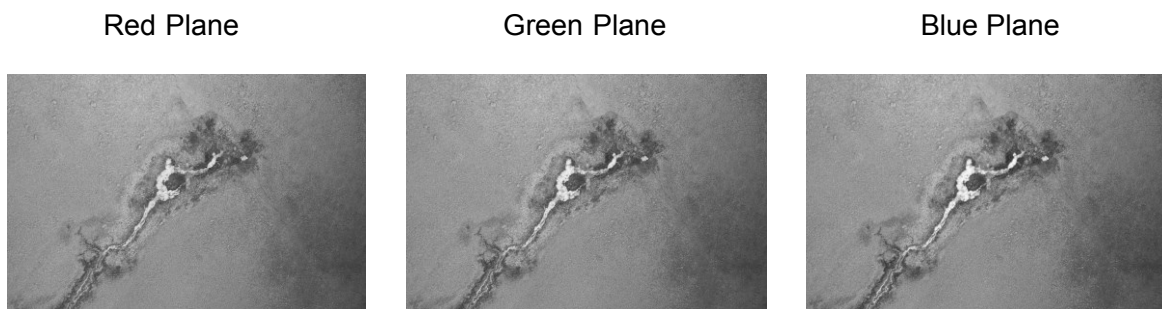


Figure 5.1 Three Planes of Moisture Marks Image (Dawood et al. 2015_b)

Dawood et al. (2017_b) developed an algorithm that relies on various spatial domain filters to enable wet areas extraction. In their study, a series of techniques were performed such as image smoothing and segmentation. The intuition behind the smoothing technique is to decrease the variance among pixels' intensities, which may in turn assist in the separation of distress from the background of the image. Then, an edge enhancement algorithm was employed to modify the grayscale image into a new image whose edges are amplified. Figure 5.2 presents the detection of moisture marks boundaries using the Canny edge detection technique.

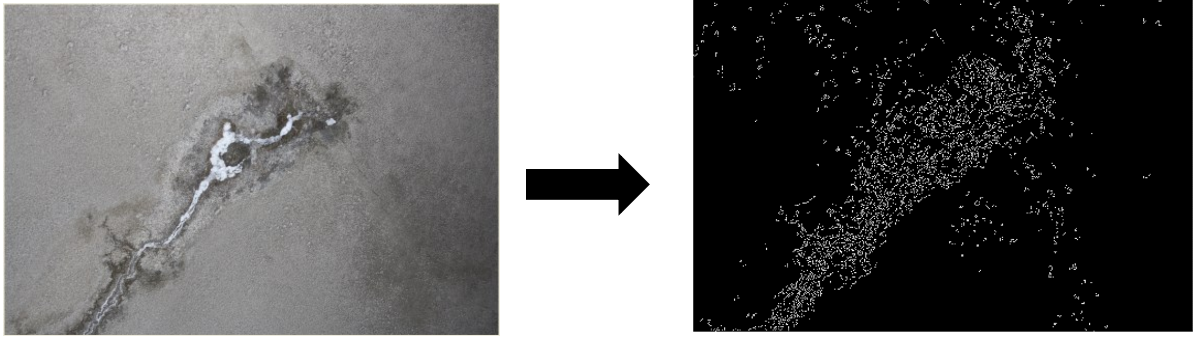


Figure 5.2 Moisture Marks Edge Detection (Dawood et al. 2017_b)

In order to thicken and enhance image boundaries, some morphological operations were incorporated, such as dilation. This algorithm has a thickening effect on the boundaries of the distress. Thus, it allows the viewer to clearly distinguish the defect in the image frame. This is followed by employing other morphological algorithms that can be used concurrently with dilation. For instance, a hole filling filter can eliminate small black spots within the moisture marks region by filling it with foreground pixels. Figure 5.3 shows conducting the morphological operations on the segmented image.

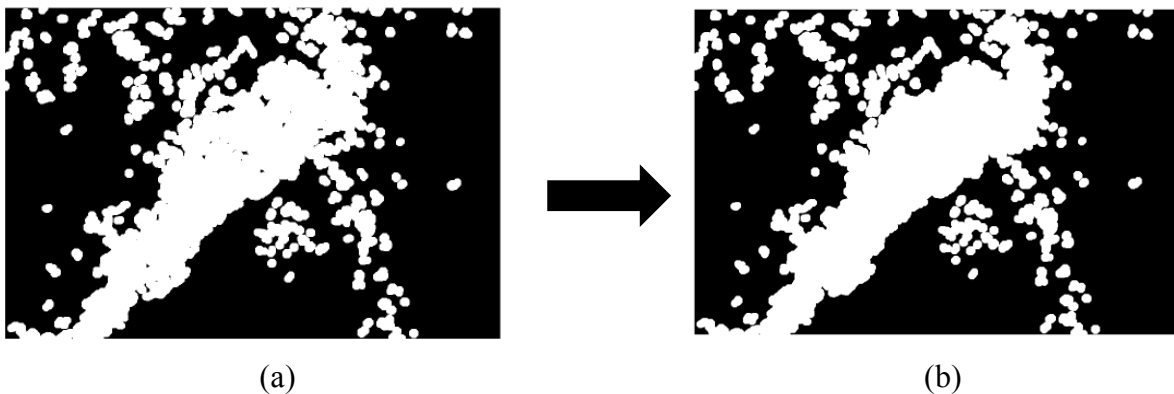


Figure 5.3 Morphological Operations (a) Image Dilation; (B) Image Holes Filling (Dawood et al. 2017_b)

Furthermore, a filter was used to clean the noise in the skeleton image, followed by generating a mask that was displayed as an overlay on the grayscale image in order to finally detect wet areas

in the image as illustrated in Figure 5.4. Because Figure 5.4 was the final result of the detection process, it will be utilized as an input to the ANN, as will be elaborated in the following subsection.

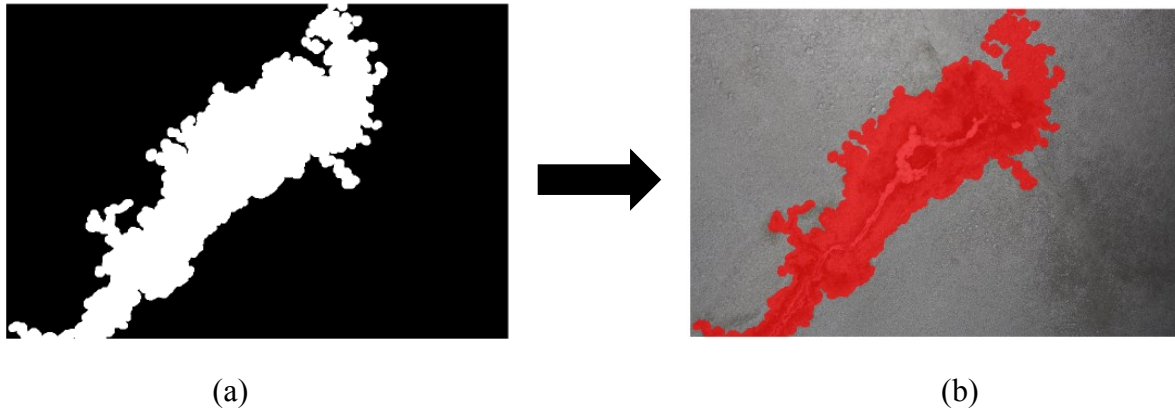


Figure 5.4 Defect Detection (a) Image Noise Cleaning; (b) Mask Overlay (Dawood et al. 2017_b)

5.1.2 ANN Model for Moisture Marks Recognition

The previously explained steps in the ANN model building and shown in Figure 3.10 were implemented in MATLAB® R2013b and utilizing the embedded statistical package. A total of 165 images showing moisture marks distress were introduced to the ANN engine; these images were divided up into 99 for training, 33 for testing, and 33 for validation. A back-propagation neural network that consisted of three layers was used to identify the defect. The ANN was supplied with inputs and targets of 165 images after performing a uniform normalization. Normalization or scaling is a vital step because it transfers the input data into the range of the sigmoid activation function, in addition to eliminating the necessity of having an intermediate layer for scaling the inputs. Therefore, the architecture of ANN involved three layers (one input, one hidden, one output) as shown in Figure 5.5. The inputs to the ANN formed a 1600x165 matrix that accounted for 1600 neurons, as well as the outputs, which formed a 1600x165 matrix and accounted for 1600 neurons.

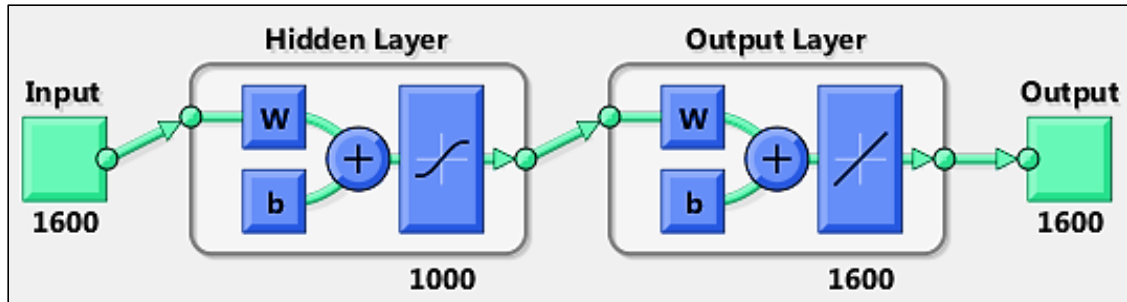


Figure 5.5 ANN Architecture (Mathworks 2013) (Dawood et al. 2017_b)

Figure 5.6 represents the input and output datasets to ANN. The gray-level values ranging from 0 to 255 were normalized and fed to the input layer, while the values of 0 and 1 were fed to the output layer of the network. The output value of 0 defines the sound concrete area, whereas the 1 value represents the defected (wet) area. After synchronizing the numerical and binary formats in the ANN engine, the network was set for training the input and output attributes. The training stopped with best validation performance registered as 0.047314 at epoch 1000 as shown in Figure 5.7(a). Moreover, the trained network was verified against the magnitude of gradient and the number of validation checks to assess various interactions pertaining to constructing the ANN model. Figure 5.7(b) shows a training gradient of 0.015345 at epoch 1000, which reveals a satisfactory degree of accuracy, whereas Figure 5.7(c) depicts the resulted error histogram. After training the network and obtaining the binary values of 0 and 1, the calculation of moisture marks areas in each image was performed by counting the total number of wet pixels with the value of 1, followed by dividing this number by the total number of pixels in the image frame.

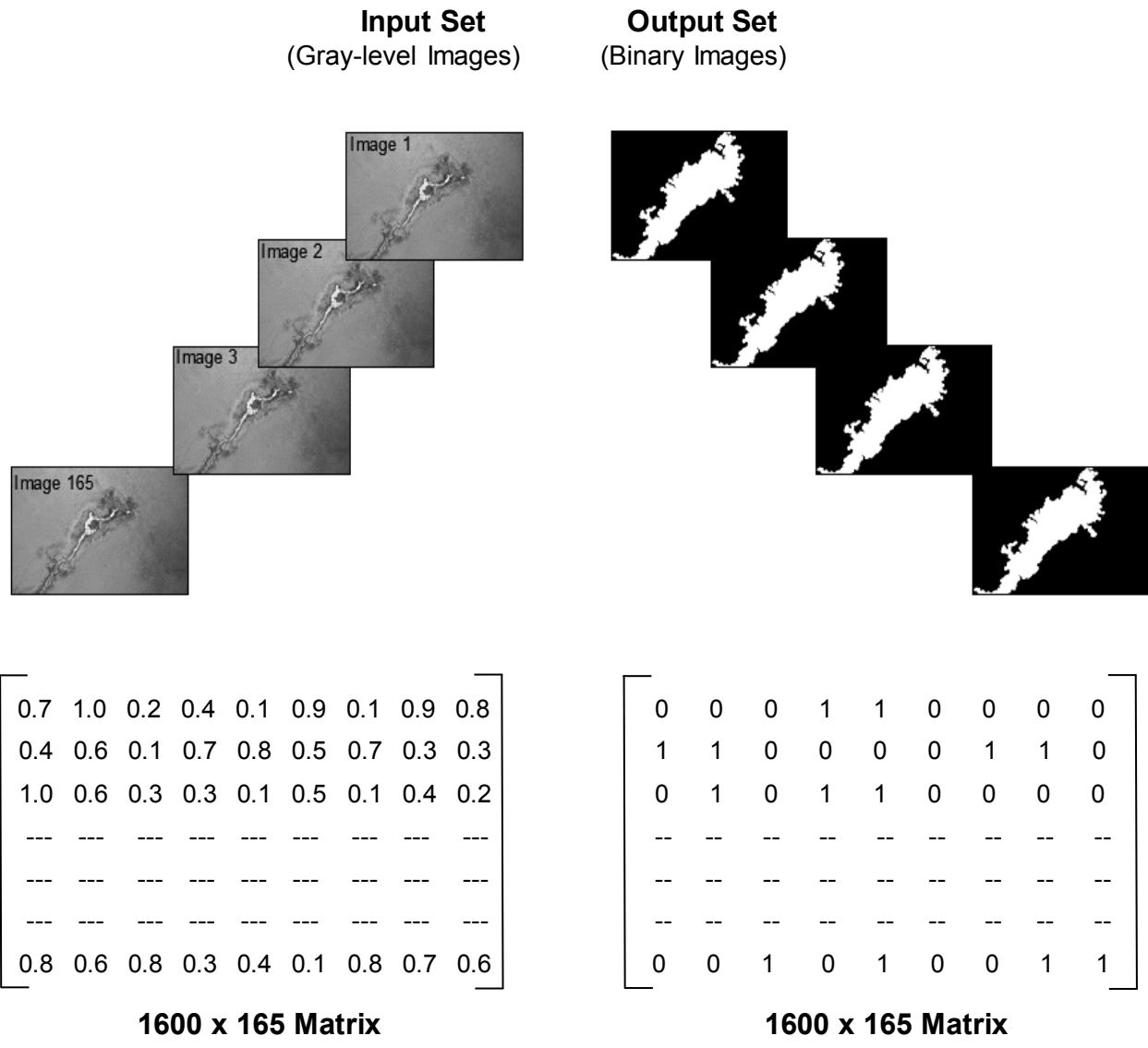
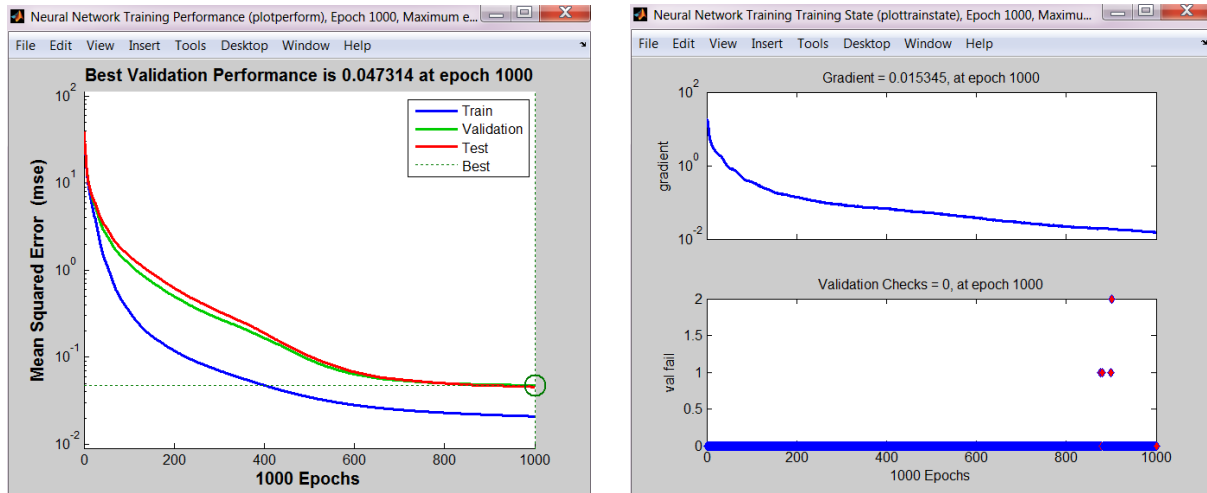
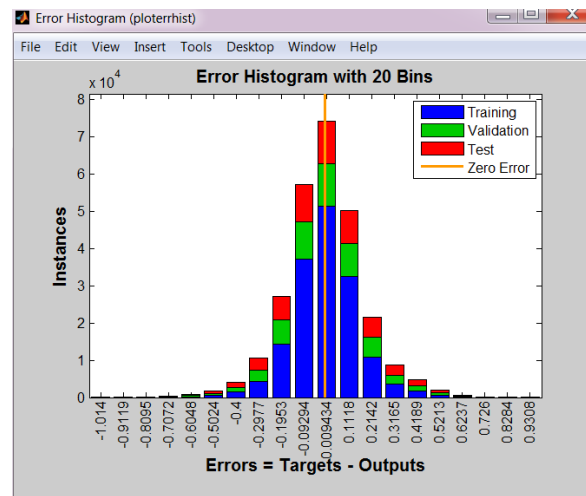


Figure 5.6 ANN Datasets and Their Matrices



(a)

(b)



(c)

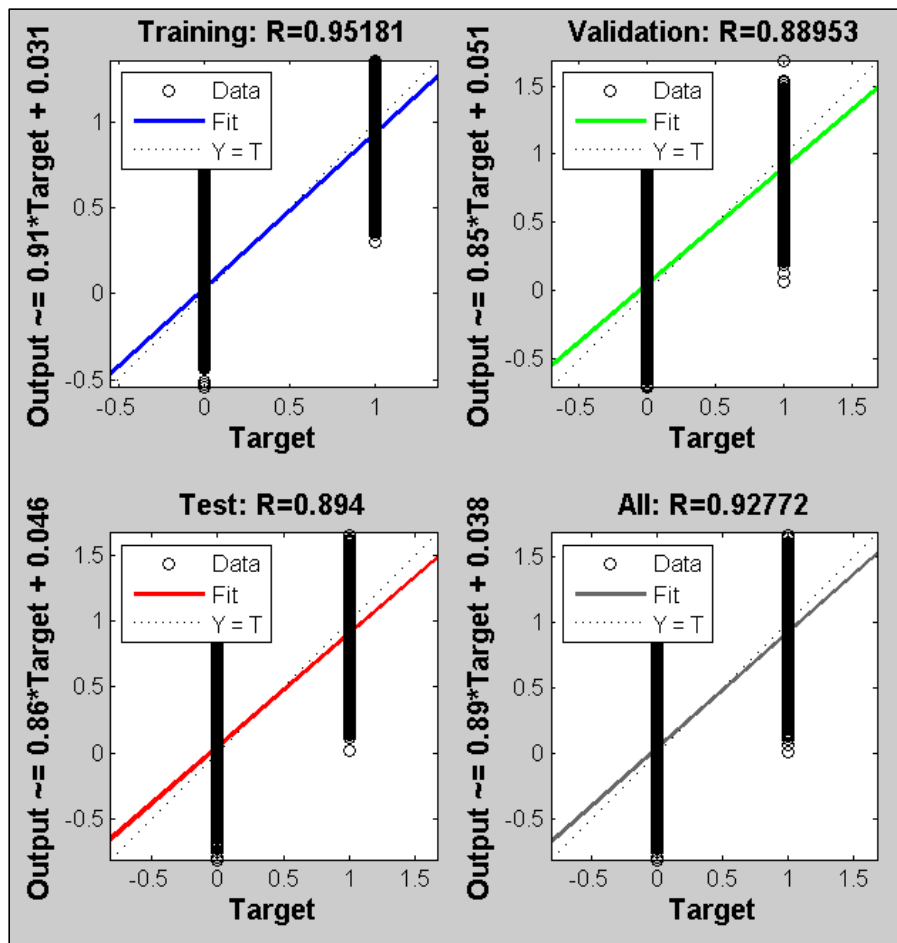
Figure 5.7 ANN Validation Scheme (a) Validation Performance; (b) Training State; (c) Error Histogram

Statistical tests are conducive to evaluating the network's goodness in recognizing the pattern among input and output datasets. Hence the performance of the ANN model was assessed based on two criteria, namely mean squared error (MSE), and R^2 . Examining these criteria shows reasonable results as presented in Figure 5.8(a). The MSE values for the training, validation, and testing samples were found to be 0.021, 0.047, and 0.046 respectively. While the R^2 values for the same samples were recorded as 0.952, 0.890, and 0.894 respectively. Figure 5.8(b) illustrates the

regression analysis plot for the training, validation, and testing samples along with the averaged R^2 of 0.928.

Results			
	Samples	MSE	R
Training:	99	2.09073e-2	9.51808e-1
Validation:	33	4.73135e-2	8.89528e-1
Testing:	33	4.56627e-2	8.94004e-1

(a)



(b)

Figure 5.8 ANN Samples Results (a) MSE and R2 Results; (b) Regression Analysis Scheme

5.1.3 Moisture Marks (MM) Model Validation

5.1.3.1 Validation of Image Preprocessing Algorithm for MM Detection

The performance of the proposed algorithm for moisture marks detection was evaluated for all the captured images. For that purpose, moisture pixels detected automatically were compared with the manual detection of the same wet regions according to the procedure proposed by Iyer and Sinha (2006). Three key performance metrics were applied; recall, precision, and accuracy. Recall also identified as sensitivity, measures the detection completeness. Precision refers to the detection exactness or reliability, while accuracy describes the average detection correctness. The performance metrics are defined mathematically by Equations (5.1), (5.2), and (5.3).

$$\text{Recall} = \text{Sensitivity} = \frac{TP}{TP+FN} \quad (5.1)$$

$$\text{Precision} = \frac{TP}{TP+FP} \quad (5.2)$$

$$\text{Accuracy} = \frac{TP+TN}{TP+FP+TN+FN} \quad (5.3)$$

Where, TP is a true positive, e.g., the number of correctly detected spalls, FP is a false positive, e.g., the number of wrongly detected spalls, TN is a true negative, e.g., the number of correctly detected as false spalls, and FN is a false negative, e.g., the number of wrongly detected as false spalls.

Table 5.1 presents the results calculated with this procedure. The table demonstrates that the proposed method attained 93.2% recall, 96.1% precision, and an overall accuracy of 91.5%. Based

on the previous results, the proposed image preprocessing model for moisture marks is considered sound.

Table 5.1 Detection Performance Evaluation (Dawood et al. 2017_b)

Performance measure	Value
Recall (%)	93.2
Precision (%)	96.1
Accuracy (%)	91.5

In addition, the actual moisture marks area (in situ) was determined subsequent to taking on-site measurements for the wet region. This actual area was compared with the detected moisture marks area (in the image), and the accuracy of detection was investigated by computing the error percentage of shape extraction according to Equation (5.4).

$$e = \frac{|A_d - A_a|}{A_a} \times 100\% \quad (5.4)$$

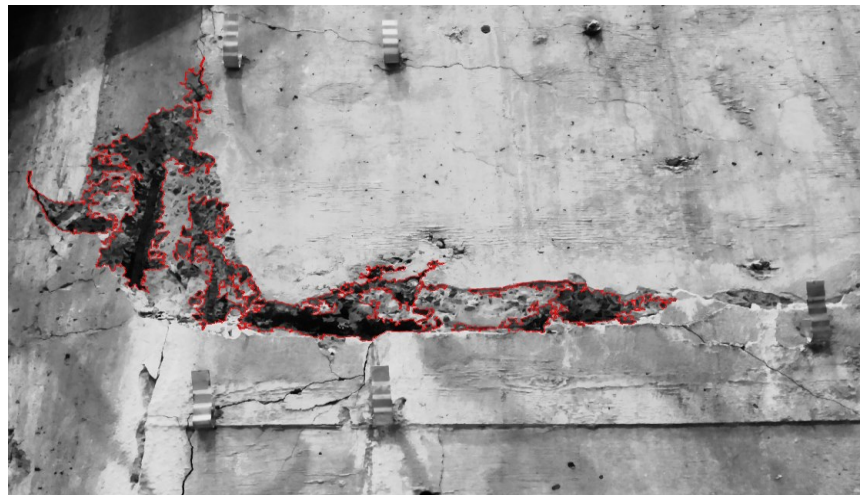
Where, e is the error percentage, A_d is the detected moisture marks (defect) area, and A_a is the actual moisture marks (defect) area. Thus, true positive results of wet region extraction show that the mean error percentage is 12.2%, and the standard deviation of error percentage is 7.9%. Figure 5.9 shows three false positive results, which represent upper slab scaling [Figure 5.9 (a)] and wall spalling [Figure 5.9 (b)].

The aforementioned cases were re-examined on site. Because water infiltration is a dominant scene in Montréal Metro network; it was found that these defects were surrounded by a thin layer of moisture. In some cases, the moisture marks were penetrating inside the defect area. Regarding the

wall spalling case (bottom image), some water infiltration was found inside the spalling area. These moisture marks traces triggered the developed detection algorithm to falsely detect these defects as moisture marks.



(a)



(b)

Figure 5.9 Three False Positive Results (a) Upper Slab Scaling; (b) Wall Spalling (Dawood et al. 2017_b)

Figure 5.10 presents examples of the true positive results accomplished by the proposed algorithm. Whereas the grayscale image in Figure 5.11 was probed by other sets of parameters, such as threshold 0.1 and sigma 3, which could not detect the moisture marks region. Later, the ROI was detected after using threshold 0.2, sigma 5, disk diameter 30, and opacity 0.7 as represented in Figure 5.11.

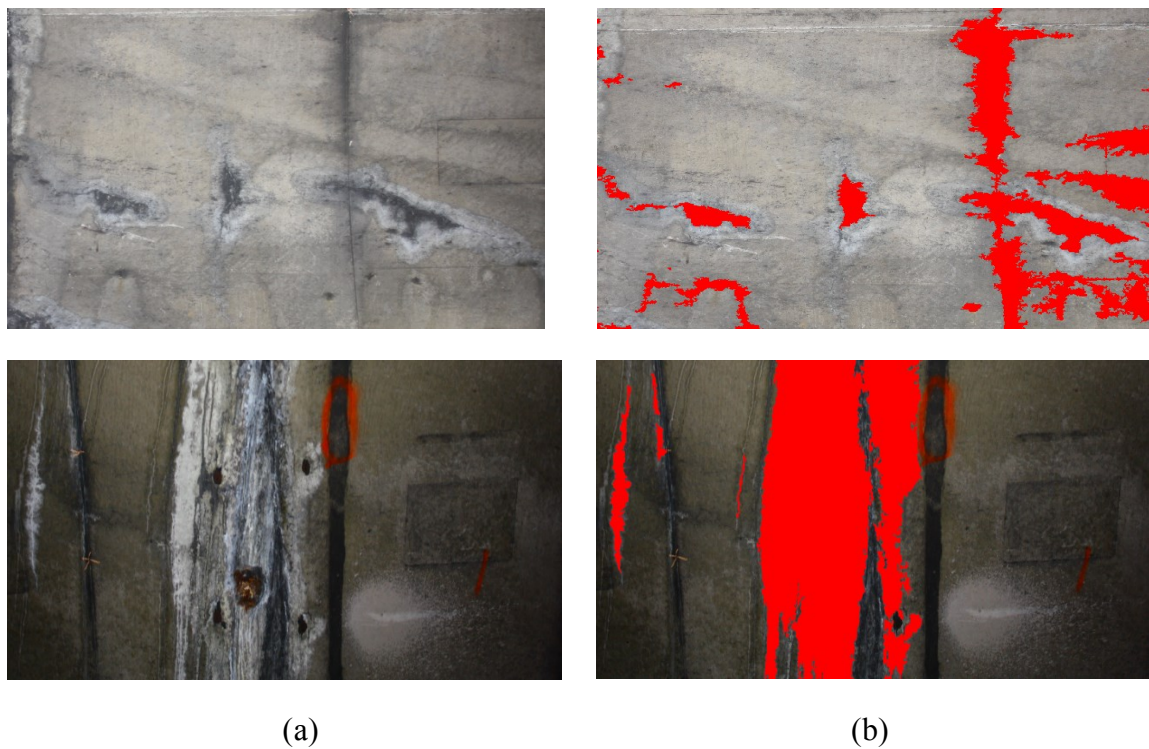


Figure 5.10 Samples of True Positive Results (a) Before Preprocessing; (b) After Preprocessing with Parameters; Threshold 0.2, Sigma 5, Disk Diameter 30, Opacity 0.7

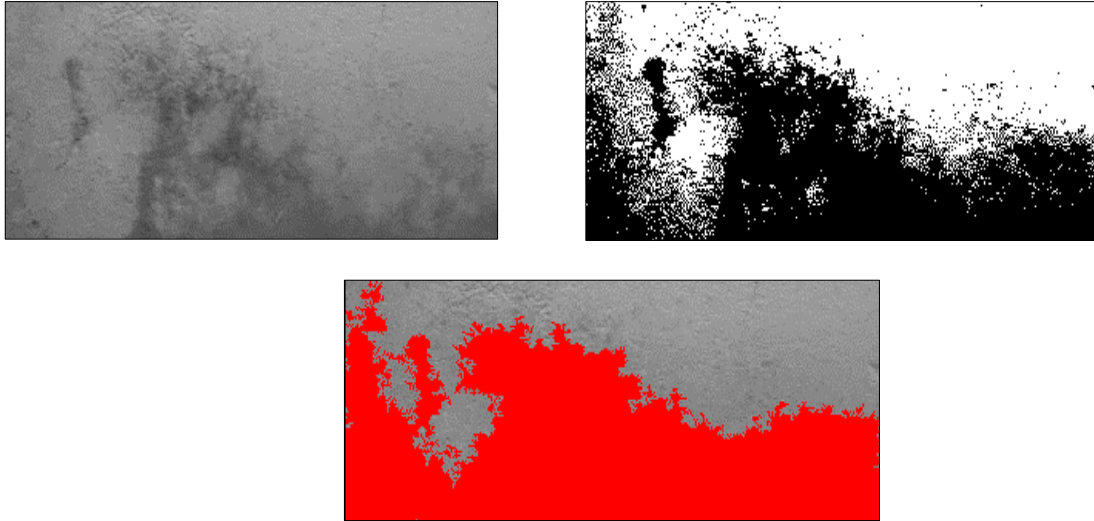


Figure 5.11 Intermediate Results of Preprocessing with Parameters; Threshold 0.2, Sigma 5, Disk Diameter 30, Opacity 0.7

5.1.3.2 Validation of ANN Model for MM Recognition

The efficacy of the neural network model could be investigated with different error terms. In this context, the developed model for defect recognition was tested using four different error terms. Namely, mean absolute error (MAE), root mean squared error (RMSE), average invalidity percent (AIP), and average validity percent (AVP). The MAE and RMSE values should be close to zero in order for the model to be reliable and vice versa (Dikmen et al. 2005). Because the moisture marks regions in the acquired images varied in size, as some images included very small wet areas and other images contained very large wet areas, the MAE and RMSE values were normalized and calculated using Equations (5.5) and (5.6) respectively. Similarly, the AIP and AVP approaches were applied to estimate the average validity and invalidity of the model as defined in Equations (5.7) and (5.8) respectively. The condition of using these two approaches is that the model is considered sound when the AIP value is close to zero and is rejected when this value approaches 100 (Zayed and Halpin 2005).

$$\text{NMAE} = \frac{\sum_{i=1}^n |C_i - E_i|}{n} / A_{max} - A_{min} \quad (5.5)$$

$$\text{NRMSE} = \frac{\sqrt{\sum_{i=1}^n (C_i - E_i)^2}}{n} / A_{max} - A_{min} \quad (5.6)$$

$$\text{AIP} = \left(\sum_{i=1}^n \left| 1 - \left(\frac{E_i}{C_i} \right) \right| \right) \times \frac{100}{n} \quad (5.7)$$

$$\text{AVP} = 100 - \text{AIP} \quad (5.8)$$

Where, NMAE is the normalized mean absolute error, NRMSE is the normalized root mean squared error, C_i is the actual moisture marks area (in situ), E_i is the estimated moisture marks area (predicted by the model), n is the number of events, A_{max} is the largest possible wet area, and A_{min} is the smallest possible wet area. Table 5.2 presents the results of ANN model validation, which stated that the NMAE is 0.07, the NRMSE is 0.12, the AIP is 4, and the AVP is 96. All the investigated evaluation criteria in terms of errors delivered acceptable results. Consequently, the proposed model for moisture marks quantification is consistent and robust.

Table 5.2 Model Validation Results (Dawood et al. 2017_b)

Evaluation criteria	Value
NMAE	0.07
NRMSE	0.12
AIP	4
AVP	96

5.2 Spalling Model

5.2.1 Preprocessing of Spalling using Hybrid Algorithm

The hybrid algorithm proposed in chapter 3 and shown in Figure 3.7 was implemented to preprocess the spalling distress. Multiple spatial and frequency domain operators were applied sequentially on the image. The process commenced with converting the RGB (color) image to a gray-level image through splitting the original image shown in Figure 4.5(b) into three planes; red, green, and blue as depicted in Figure 5.12. As a result, the red plane was chosen to be further processed, as it offers the best-enhanced image.

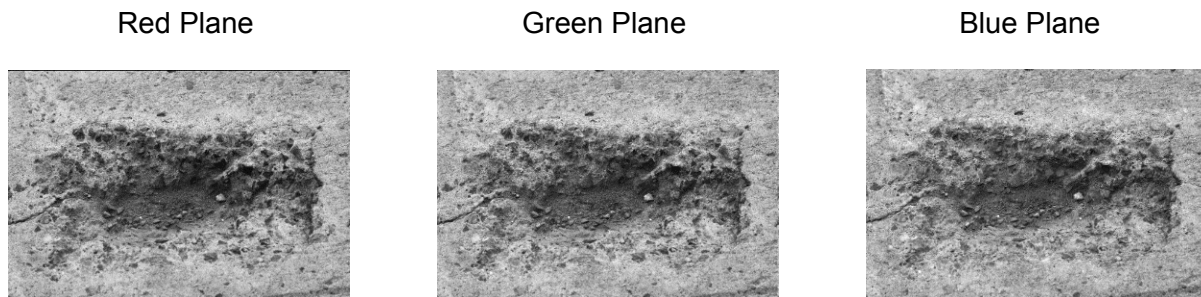


Figure 5.12 Three Planes of Spalling Image

Subsequently, several imaging techniques were performed such as smoothing and thresholding the image through segmentation. Thresholding is the method of separating the object of interest from the background of the image. The selection of the best threshold value of a gray-level image is correlated to plotting its histogram. Therefore, the histogram of the image was generated since it can assist in manipulating the binary transformation through a trial-and-error procedure. Figure 5.13 shows image thresholding and its histogram. It is clearly shown from Figure 5.13(b) that the spall (in white) has been separated from the background of the image (in black).

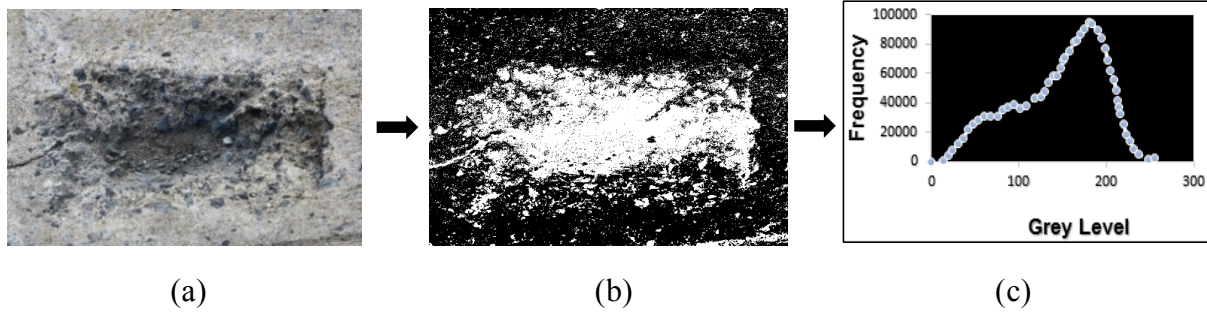


Figure 5.13 Filtering in the Spatial Domain (a) Gray-Level Image; (b) Image Thresholding; (c) Image Histogram

In order to reduce the noise and enhance image resolution, a 3D convolution filter with Gaussian function was applied. This technique has a blurring effect, it computes a 3D Gaussian low pass filter as depicted in Figure 5.14(a). This is followed by employing two color transformer filters, such algorithms allow the viewer to distinguish the depth in the image frame. Figure 5.14(b) and (c) represent the depth perception after using these filters.

Next, the image was calibrated by setting the appropriate scale. For the purpose of calibration, a major axis of a spalling region was measured in the station and entered into the software as illustrated in Figure 5.15(a), thereby pixel values may correlate with this entry data. Then, the region was selected, which enabled defect extraction using a colored edge detection algorithm as shown in Figure 5.15(b).

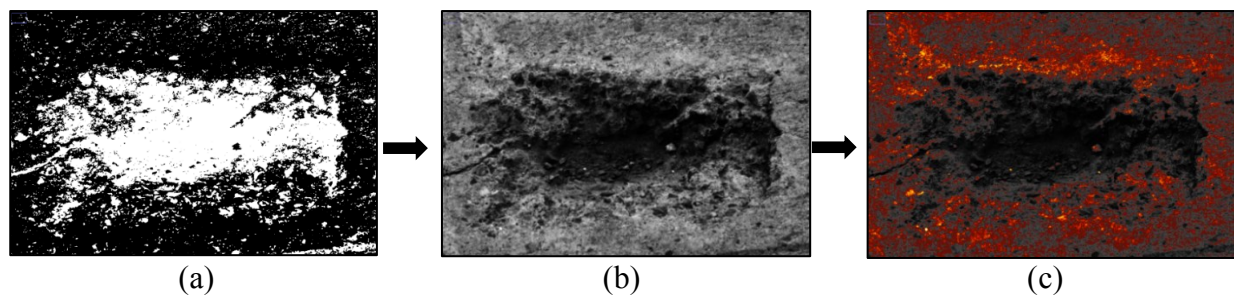


Figure 5.14 Filtering in the Frequency Domain (a) Gaussian Blur 3D Filter; (b) Color Transformer Filter; (c) Smart Filter (Dawood et al. 2017_a)

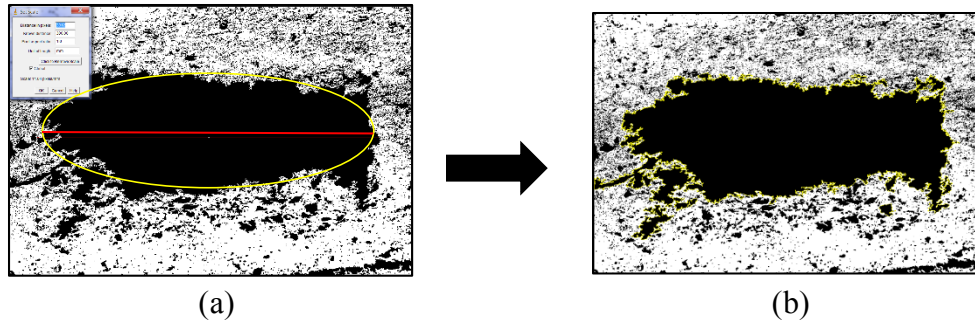
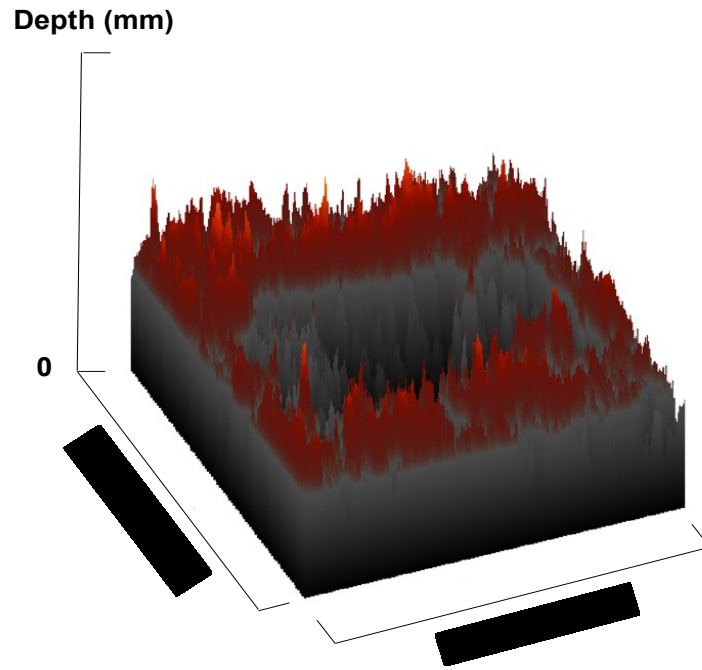


Figure 5.15 Defect Detection (a) Image Calibration; (b) Shape Extraction (Dawood et al. 2017_a)

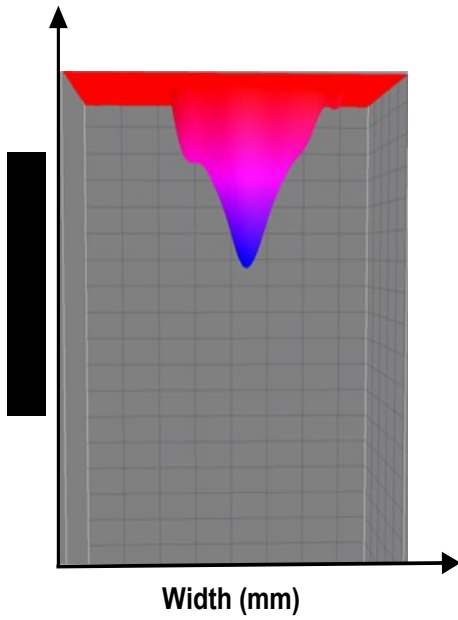
The 3D visualization model of a spalling region was developed after analyzing the surface plot. As a result, a 3D graph of pixels intensities was displayed in a pseudo color image (non-RGB image) as shown in Figure 5.16(a). Then, texture data were projected from the digital images directly on a three-dimensional grid scheme to mimic the on-site scene through the incorporation of depth perception as depicted in Figure 5.16(b) and (c). The previously described algorithm not only analyzes and streamlines the whole image processing technique but also presents a consistent and accurate detection and visualization method.

5.2.2 Regression Model for Spalling Quantification

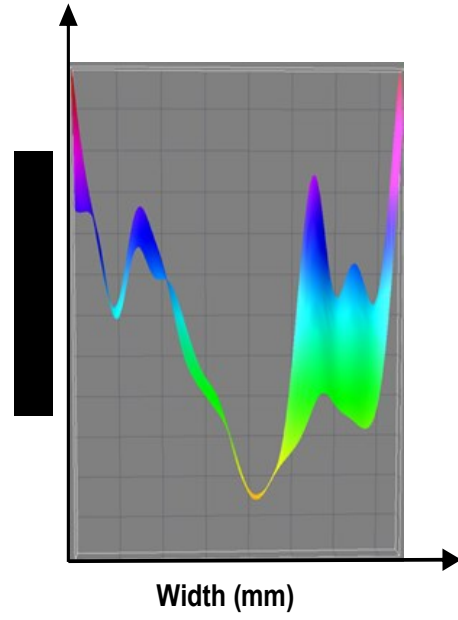
The regression model is developed to evaluate the extent of spalling damage in RC structures. It's worth noting that this same model can be applied to assess the severity of scaling defect as well, since both of the defects are assessed based on the depth attribute in accordance with Table 3.2 and Table 3.3. Therefore, the previously described steps in regression model building and shown in Figure 3.13 were implemented in MATLAB® R2013b, in addition to exploiting the statistical embedded platform.



(a)



(b)



(c)

Figure 5.16 Spalling 3D Model (a) Schematic Representation of Spalling Depth; (b) Interactive 3D Surface Plot; (c) Defect Profile (Dawood et al. 2017_a)

Subsequent to correlating pixel intensities from an RGB profile with their actual depths, the first step in analyzing the data was by creating a scatter plot and testing the form of relationship, which revealed a negative linear relationship. Several models were fitted with the data using three polynomial functions, e.g., first order (linear), second order (quadratic), and third order (cubic) as displayed in Figure 5.17, and expressed in Equations (5.9), (5.10), and (5.11) respectively. Where, x is a pixel intensity taken from the RGB profile, and y is the corresponding spalling depth.

$$y = -0.093x + 17 \quad (5.9)$$

$$y = 0.00043x^2 - 0.22x + 26 \quad (5.10)$$

$$y = 0.000033x^3 - 0.014x^2 + 2x - 83 \quad (5.11)$$

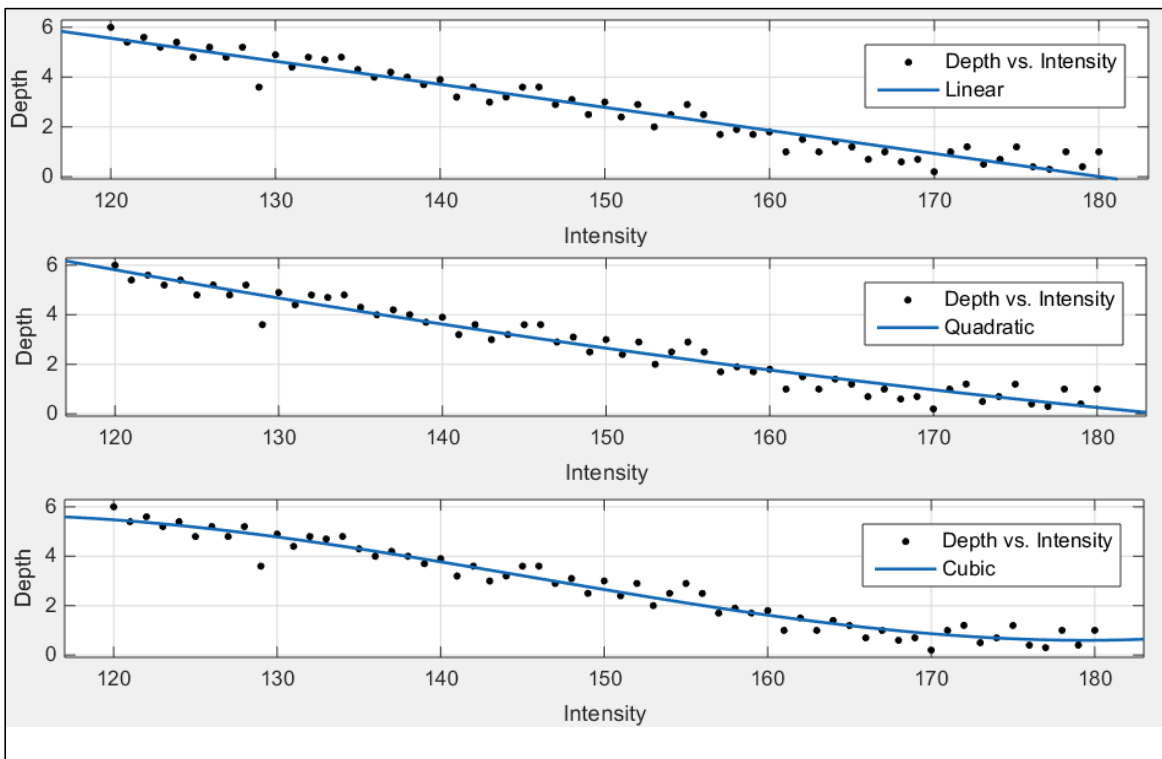


Figure 5.17 Fitted Regression Models (Dawood et al. 2017_a)

Statistical tests are conducive to evaluating the goodness of fit and selecting the best model. Hence they were employed on each of the three models. Basic diagnostic criteria were extracted and compared, as well as relationships and interactions. The best possible scenario among data fitting variations determines the best model with respect to the largest R^2 and Adj R^2 , and the lowest deviation SSE and RMSE. Table 5.3 summarizes the analysis results of statistical tests.

Table 5.3 Statistical Diagnostic Tests (Dawood et al. 2017_a)

Model	R^2	Adj R^2	SSE	RMSE
Linear	0.9445	0.9436	9.5158	0.0916
Quadratic	0.9495	0.9478	8.6616	0.0864
Cubic	0.9567	0.9544	7.4364	0.0631

Examining the four criteria shows that the highest R^2 and Adj R^2 are 0.9567 and 0.9544 respectively, whereas the least SSE and RMSE are 7.4364 and 0.0631 respectively. This comparative procedure confirms that the cubic model achieves the best trend.

Furthermore, a residual analysis of the proposed model was conducted to verify various assumptions pertaining to constructing the regression model; such assumptions comprise normality of the error distribution, homoscedasticity, and lack of correlation. The normal probability technique that determines the departures from normality was generated. The visual interpretation shows no serious outliers or major errors in the probability normal distribution trend. Hence, the outcomes of this assumption are considered reasonable with high correlation among data points.

The second assumption specifies that the deviation from the regression line is the same for all values of X, which could be verified by producing the plot of residuals versus pixel intensity as

demonstrated in Figure 5.18. The developed model seems to be sound under this assumption since the residuals had tendencies to be constant except for little violations.

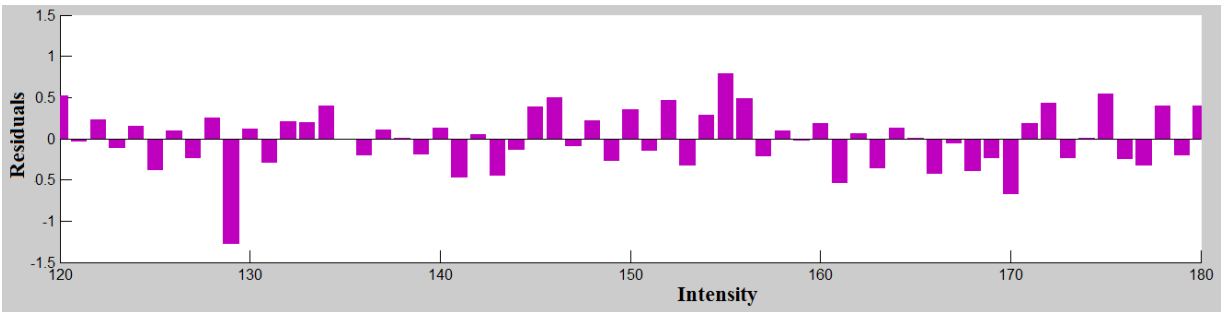


Figure 5.18 Residual Analysis Scheme (Dawood et al. 2017_a)

And finally, lack of correlation gages the independency of error around the regression line. Examining the order of data plot reveals satisfactory results as the positive residuals and the negative residuals were symmetrically distributed around zero as shown in Figure 5.18. According to the aforementioned statistical analysis, the proposed model is considered statistically sound.

5.2.3 Spalling (SP) Model Validation

5.2.3.1 Validation of Hybrid Algorithm for SP Detection

The performance of the proposed algorithm for spalling detection was evaluated for all the captured images. For that purpose, spalled pixels detected automatically were compared with the manual detection of the same spalling regions by employing the performance metrics mentioned previously according to Equations (5.1), (5.2), and (5.3). Table 5.4 presents the results calculated with this procedure. The table demonstrates that the proposed method attained 91.7% recall, 94.8% precision, and an overall accuracy of 89.3%. The previous results were promising as compared to a study developed by German et al. (2012), which achieved 80.2% recall with 81.1% precision.

Table 5.4 Detection Performance Evaluation (Dawood et al. 2017_a)

Performance Measure	Value
True positive (TP)	55
False positive (FP)	3
True negative (TN)	12
False negative (FN)	5
Recall (%)	91.7
Precision (%)	94.8
Accuracy (%)	89.3

In addition, the actual spalling area (in situ) was determined subsequent to taking on-site measurements for the spalling region. For example, the actual area for spalling region shown in Figure 5.15(a) was calculated after taking actual dimensions of the major and minor axes of this region that takes the form of an ellipse. Then, this actual area was compared to the detected spalling area (in the image), and the accuracy of detection was investigated by computing the error of spalling region extraction according to Equation (5.4). Thus, true positive results of spalling region extraction show that the mean error percentage is 11%, the standard deviation of error percentage is 7.1%, and the variance is 25.

Figure 5.19 shows the three false positive results of this study. The extracted distresses represent either crocodile (fatigue) cracks or wide cracks. Based on the Ontario Structure Inspection Manual (OSIM 2008), these distresses must not be identified as spalls. Nevertheless, the increased diffusion of chloride and moisture inflow may cause these cracks to worsen and develop serious spalling regions. The five false negative cases found in this research, were due to insufficient

lighting or the non-orthogonal position when acquiring the images. Also, the far-distance images might mislead and cause erroneous results.

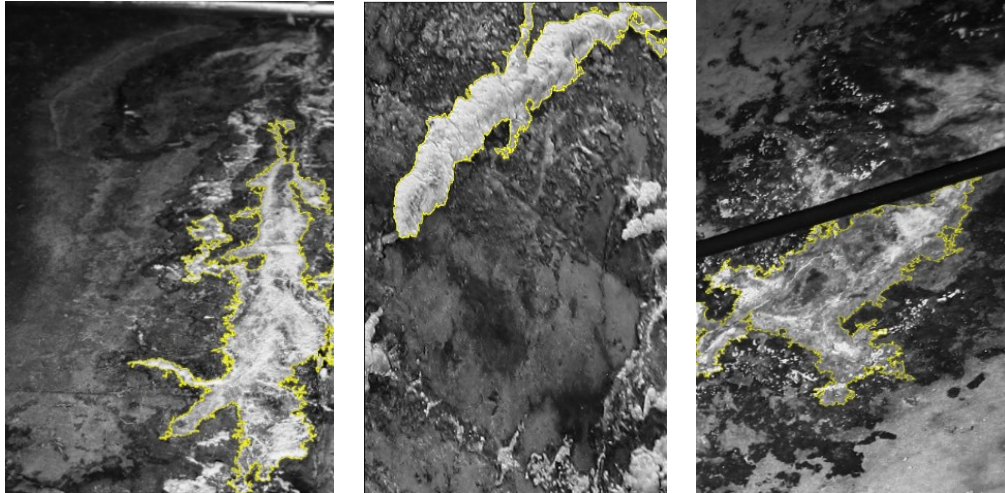


Figure 5.19 Three False Positive Results (Dawood et al. 2017_a)

5.2.3.2 Validation of Regression Model for SP Quantification

The robustness of a regression analysis model could be examined with various error tests. In this regard, the developed model for depth quantification was tested using three different error terms, namely, mean absolute error (MAE), average invalidity percent (AIP), and average validity percent (AVP). The MAE was calculated using Equation (5.12). The value of MAE should be close to zero in order for the model to be reliable and vice versa. Similarly, the AIP and AVP approaches were applied to estimate the average validity/invalidity of the model as defined in Equations (5.7) and (5.8) respectively. The model is considered sound when the AIP value is close to zero and is rejected when this value approaches 100.

$$\text{MAE} = \frac{\sum_{i=1}^n |C_i - E_i|}{n} \quad (5.12)$$

Where, C_i is the actual depth value (in situ), E_i is the estimated depth value (predicted by the model), and n is the number of events. Table 5.5 presents the results of regression model validation, which stated that the MAE is 0.20, the AIP is 7, and the AVP is 93. All the investigated evaluation criteria in terms of errors delivered acceptable results. Consequently, the proposed model for depth quantification is coherent and robust.

Table 5.5 Model Validation Results (Dawood et al. 2017_a)

Evaluation Criteria	Value
MAE	0.20
AIP	7
AVP	93

5.3 Scaling Model

5.3.1 Preprocessing of Scaling

The preprocessing of scaling starts in the same manner, described beforehand for moisture marks and spalling. Hence color space was explored to extract the grayscale representation from the RGB image. The original image for scaling defect shown in Figure 4.5(c) was split into three channels as depicted in Figure 5.20. Then, the red plane was selected to be further processed as it offers the best contrast.

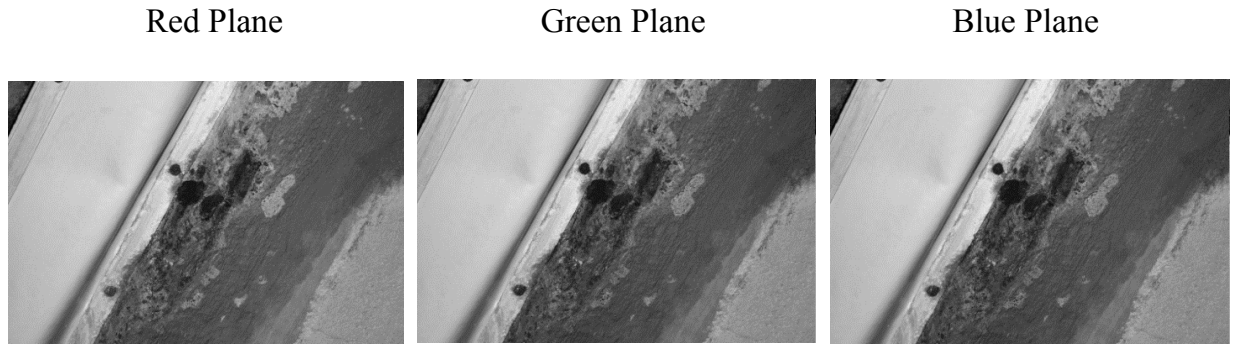


Figure 5.20 Exploring the Color Space

The red plane was thresholded to separate the defects from the background of the image as shown in Figure 5.21. The thresholding procedure was accomplished by manipulating the image histogram, which indicates the position of the best threshold value as presented in Figure 5.21(c). The horizontal axis represents the intensity of the gray-level, and the vertical axis is the frequency of occurrence of a pixel value in the image.

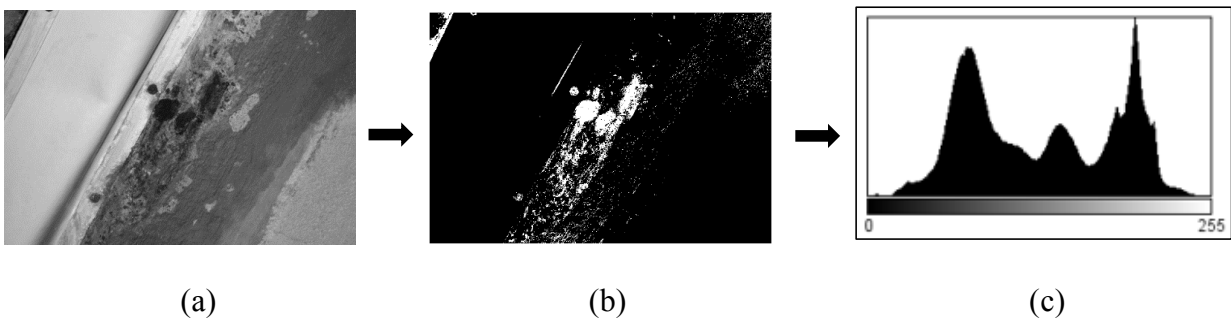


Figure 5.21 Scaling Binary Transformation (a) Gray-Level Image; (b) Image Thresholding; (c) Image Histogram

Several adaptive thresholding techniques aspire to adjust the threshold value in an attempt to reduce the error, one of these techniques is the maximum entropy. Hence, this method was conducted to produce the image illustrated in Figure 5.22(a). Followed by a set of computer vision operations that involved convolving the image with a normalized kernel, using Gaussian Blur filter with sigma of a radius of 2 pixels, and a Variance filter of a radius of 2 pixels. These algorithms

aimed to prepare the image for the final step of creating a mask that will be exposed as an overlay on the gray-level image, thereby the scaling defect was highlighted as represented in Figure 5.22.

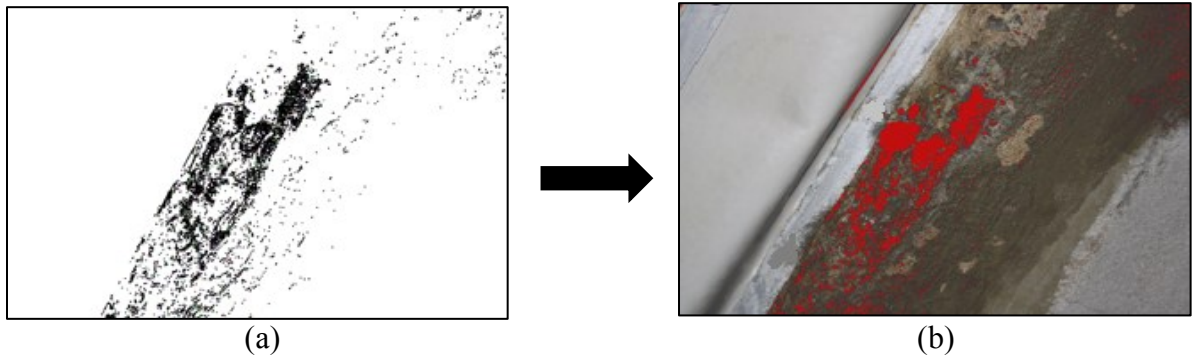


Figure 5.22 Filtering Scaling Defect (a) Processing with Maximum Entropy; (b) Scaling Detection

5.4 Cracks Model

5.4.1 Preprocessing of Cracks

The same RGB image utilized formerly in the preprocessing of moisture marks was used once more in the preprocessing of cracks, as it comprises both of the defects. Thus, it was necessary to apply a different paradigm with another fusion of parameters to accomplish the final outcome of detecting cracks distress. In this respect, the original image that was captured for a wide crack in one of Montréal's Metro stations was transformed into an 8-bit grayscale image as illustrated in Figure 5.23.

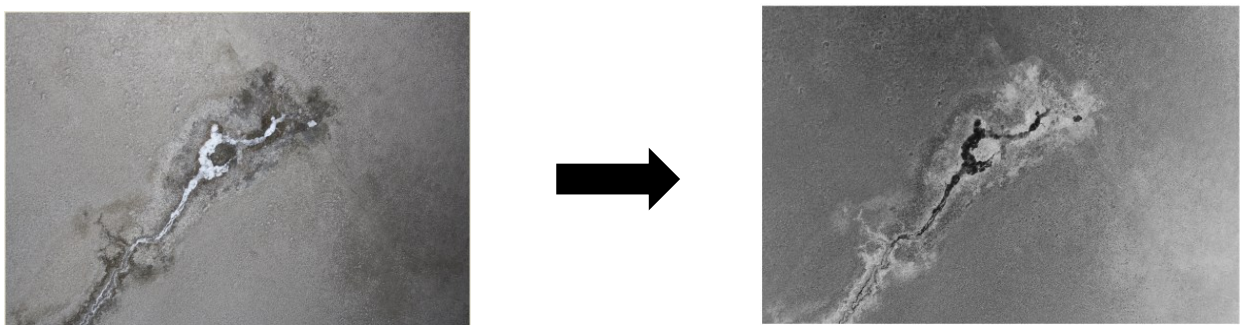


Figure 5.23 Converting the RGB Image to Grayscale Image

Next, an edge detection technique was applied to make the edges look sharper for the viewer. There are six different types of edge detection algorithms, though Canny edge detection algorithm is considered the most powerful one (Canny 1986). Therefore, it was applied to the selected grayscale image to detect its boundaries as shown in Figure 5.24. In this figure, it is clear that the crack was segmented from the background of the image simultaneously with thresholding.

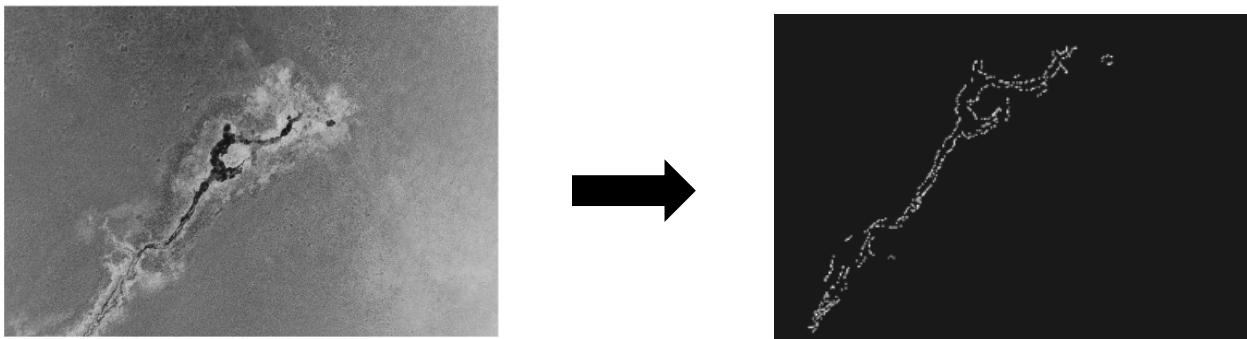


Figure 5.24 Crack Edge Detection

It is quite useful to utilize some morphological algorithms such as dilation on the binary image. There are other techniques and operators that can be used concurrently with dilation, for instance, thinning, thickening, etc. However, it was found that the fusion of dilation, complementation, and intersection attained the best results as it performed filling the holes. Figure 5.25 represents the processed image after using different morphological operations on the binary image. Next, an algorithm was applied to find the skeleton of the image, followed by cleaning the noise in the processed image. In the final step, a mask was created to be displayed as an overlay on the grayscale image. This step resulted in the detection of crack defect in the image as shown in Figure 5.26.

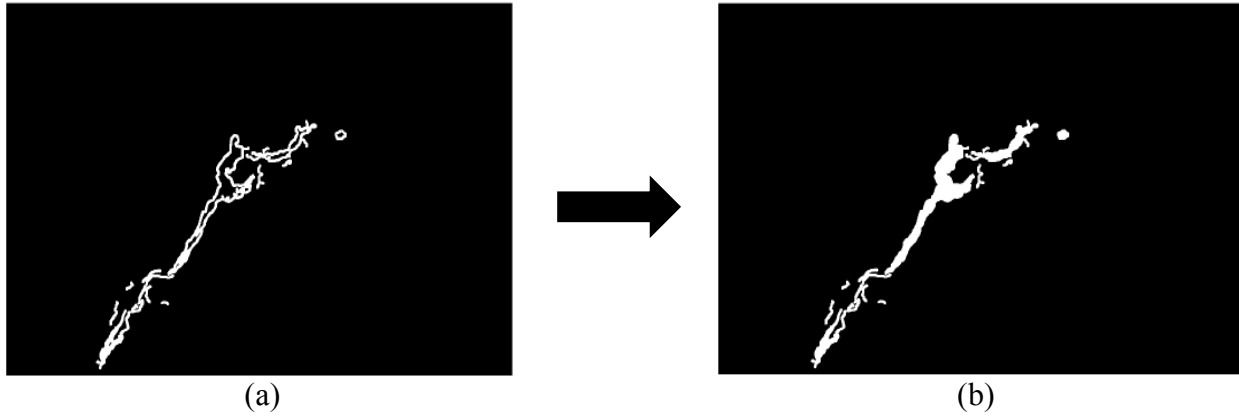


Figure 5.25 Morphological Operations (a) Image Dilation; (b) Image Hole Filling

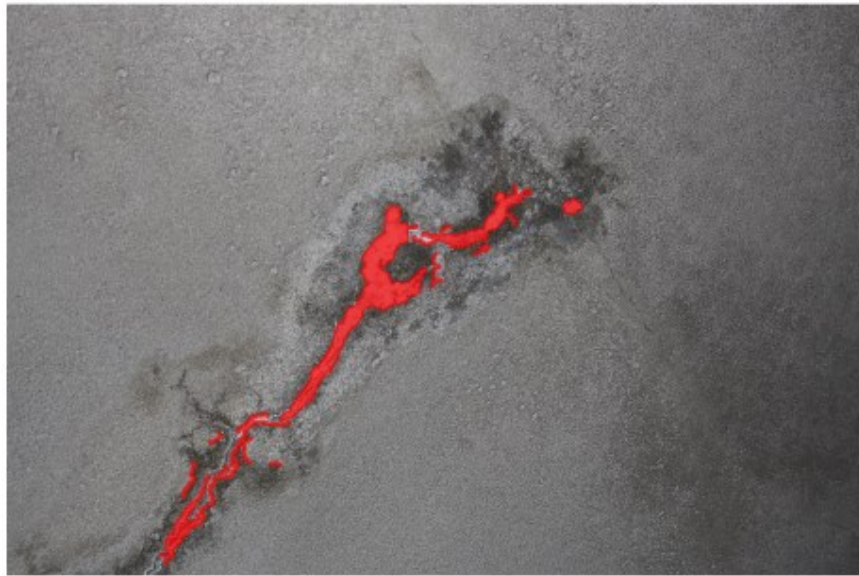
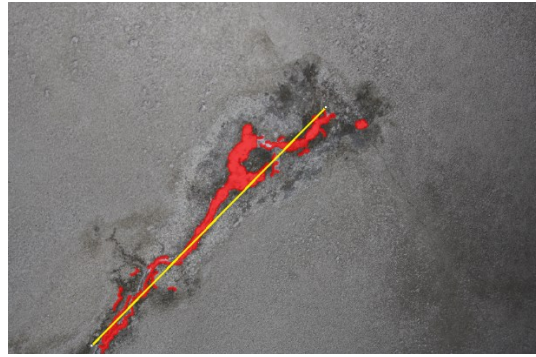


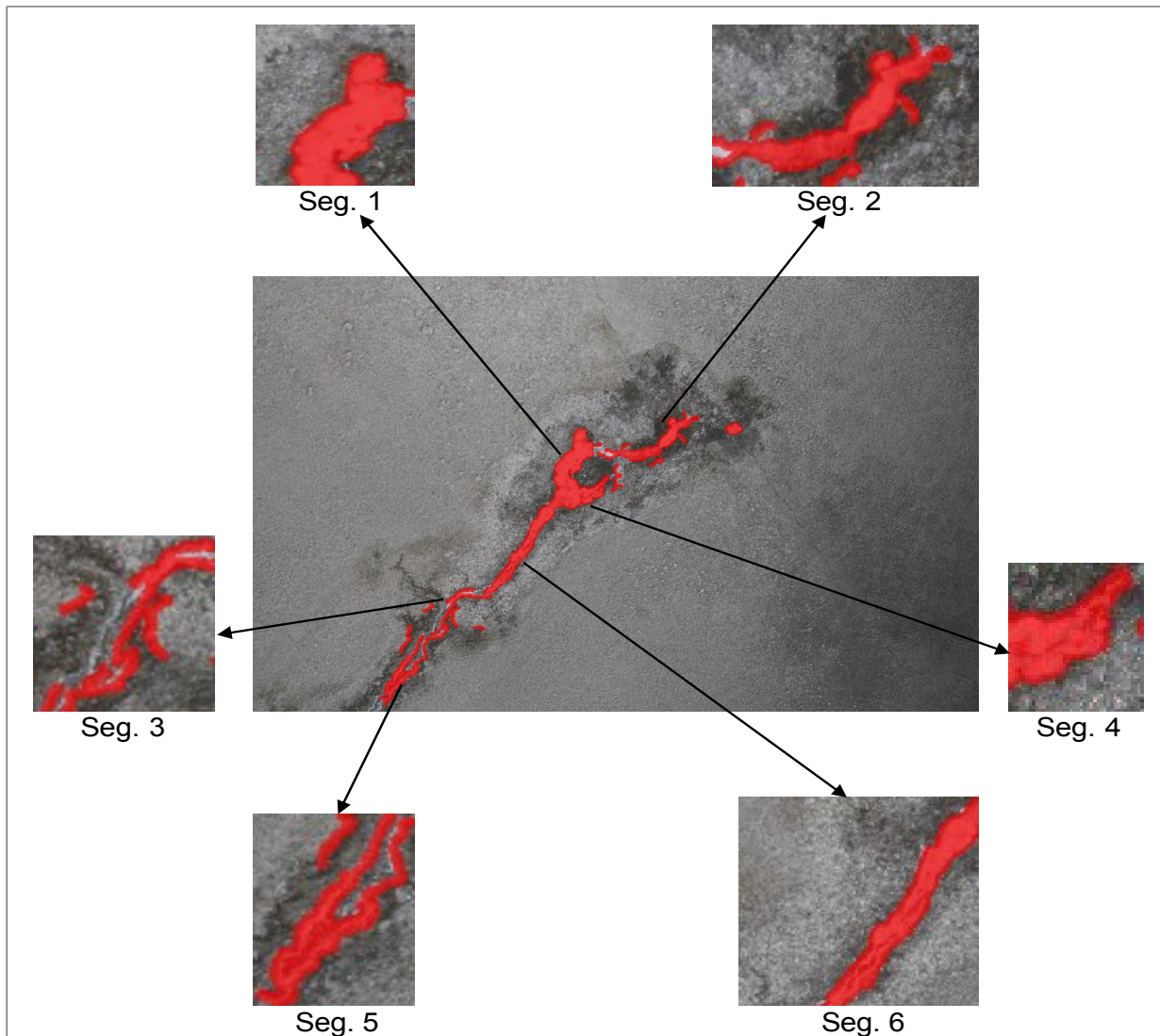
Figure 5.26 Crack Detection

5.4.2 Cracks Recognition

This phase includes measuring the severity of cracks in subway structures by automatically computing the crack width. First, the preprocessed image was calibrated by setting the appropriate scale. For the purpose of calibration, the distance illustrated in Figure 5.27(a), which characterizes the length of a crack on the upper slab of a station, was measured in situ and entered into the software.



(a)



(b)

Figure 5.27 Image Calibration (a) Setting Image Scale; (b) Crack Segments

In this manner, pixels values were correlated with the measured distance. Second, the crack was divided into six segments, each of which was labeled according to a coding number, then zoomed to enlarge its scale in accordance with reasonable resolution. The intuition behind the enlargement strategy is to enable and facilitate the measurement of even the very tiny cracks in the image frame as shown in Figure 5.27(b). Third, multiple aligned linear measurements were taken along the crack via the automatic processor. These edge-to-edge measurements were executed as many times as possible to achieve the best accuracy. And finally, the average crack width was computed. Figure 5.28 illustrates a sample of the crack width measurements. After conducting multiple width measurements, the crack showed an average width of 1.6 mm. Therefore, this crack is considered very severe according to the condition ratings of Table 3.4.

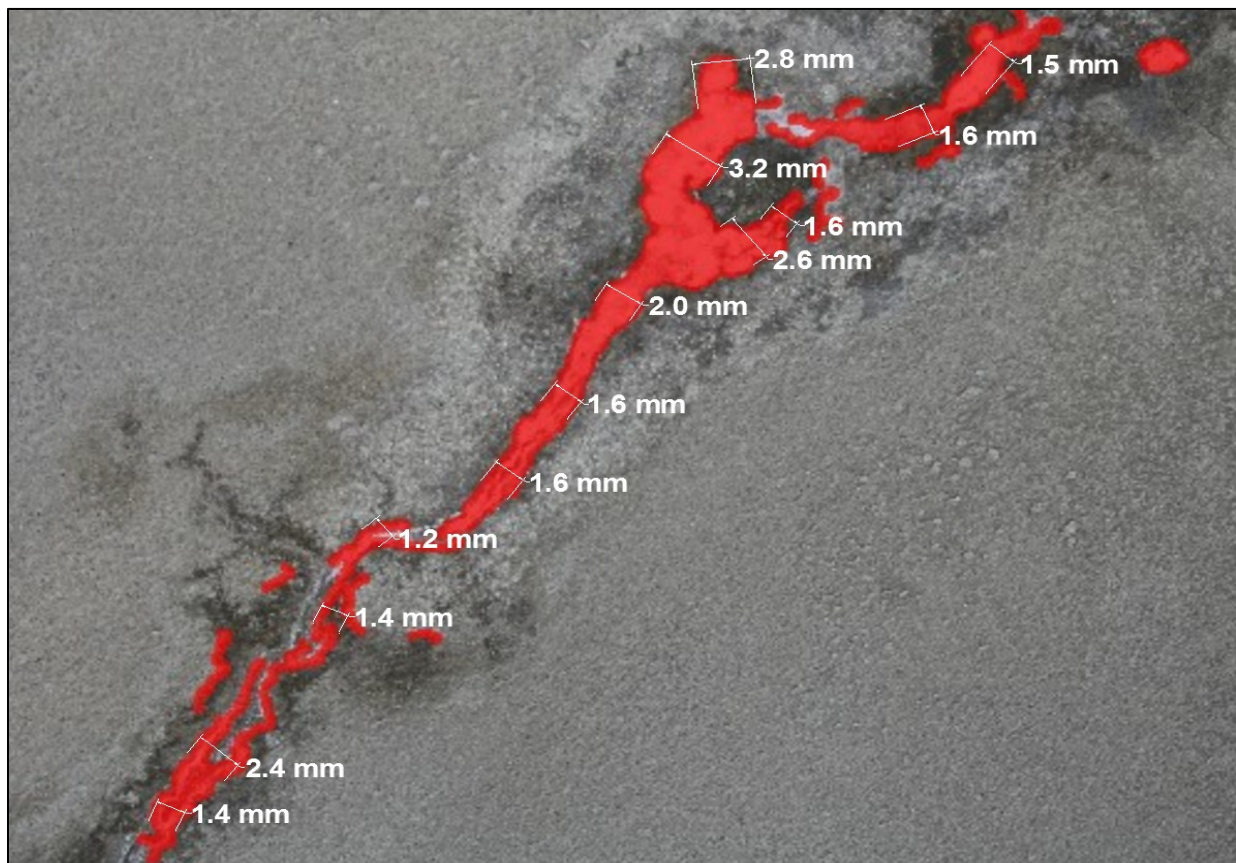


Figure 5.28 Sample of Crack Width Measurements

5.5 Subsurface Data Analysis

The electromagnetic (EM) waves received by GPR antenna are recorded as profiles (radargrams) that represent various medium properties. Each profile represents a B-scan that includes all the traces registered from one scanning path. GPR data are processed as a scalar magnitude whereas EM fields are treated by vector analysis. EM waves are recognized by a convolution of sequential time functions as a result of noise sources (Daniels 2008). Additional noise will cause the attenuation of these waves due to signal propagation, absorption, and subsurface spherical deviation. Therefore, data analysis methods should emphasize on the variations of EM impedance associated with the presence of defects in concrete, and eliminate GPR signal attenuation as a result of various anomalies such as a structural element.

A huge amount of GPR data were collected using dual polarization technique to assure the best possible accuracy. However, the collected data needed to be interpreted, analyzed, and finally presented in the form of deterioration maps. Two analysis techniques were applied to the collected B-scans. First, amplitude analysis using GSSI RADAN[®] software, and second, IBA using RADxpert[®] software. The main objective of utilizing these analysis techniques is to process GPR profiles and create a map that can assist decision makers to optimize their course of action, or locate a subsurface target, or test a simulation model.

5.5.1 Mapping using Amplitude Analysis

The numerical analysis of reflection amplitude is the most commonly used technique to analyze GPR data based on the reflection amplitudes measured at different layer interfaces, e.g., top rebar, bottom rebar, and slab bottom. The amplitude analysis procedure was implemented on all the collected B-scans as illustrated in Figure 5.29, and in accordance with the following steps:

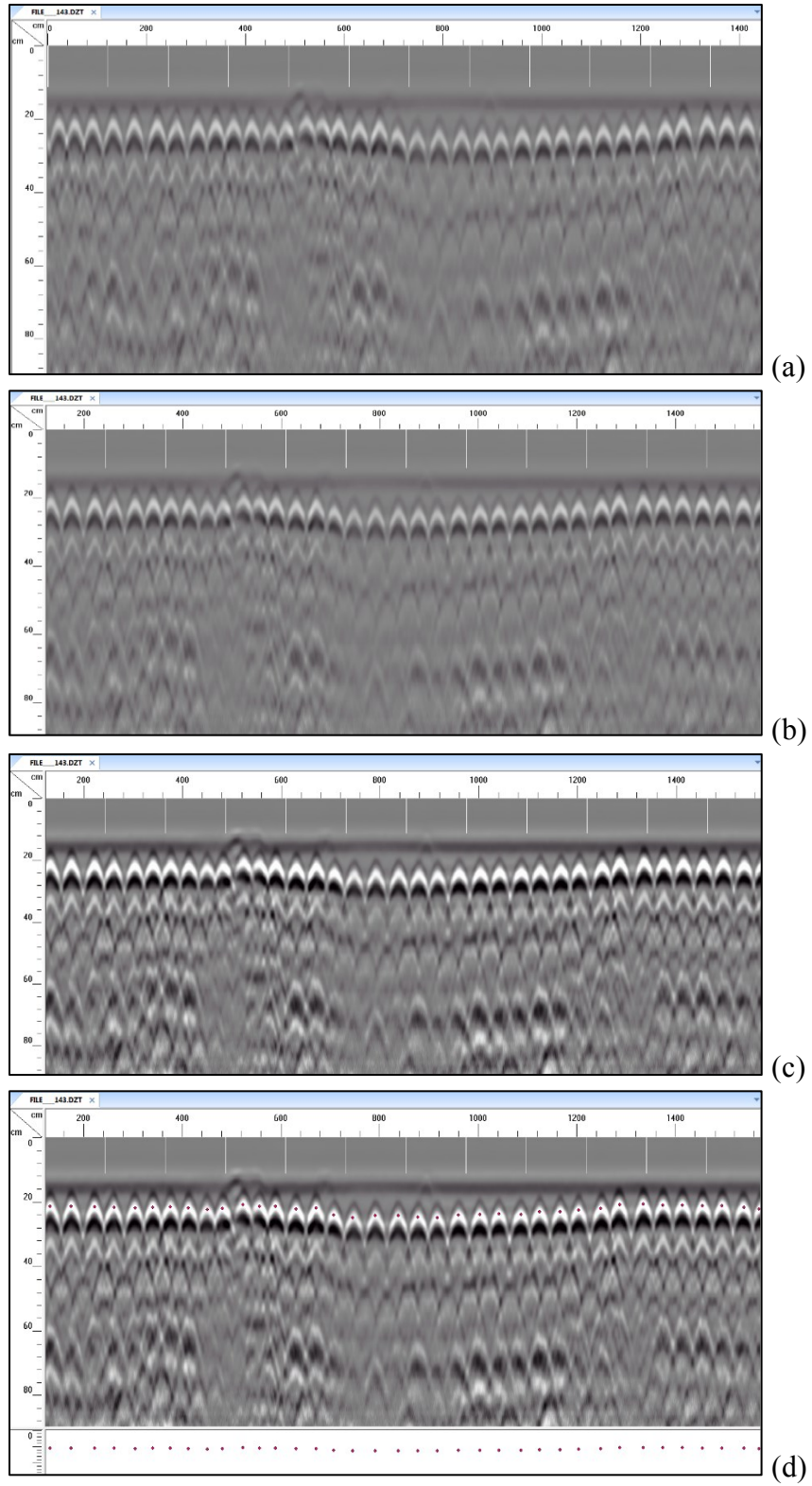


Figure 5.29 Data Processing using Amplitude Analysis (a) Raw Profile; (b) Edited Profile; (c) Gain Application; (d) Migration and Rebar Picking

1) Data Editing

Since GPR profiles contain big data, they were systematically maintained to accomplish further processing while avoiding the repetitive process of adjusting the acquisition parameters due to GPR configuration. In addition, data were re-organized, files were merged, and profiles were cut. While collecting GPR profiles, it's very common that the operator starts before the area under investigation and finishes after the ending line. Therefore, it's essential to cut the excessive parts of the profile to guarantee that the profile correlates exactly to the starting and ending lines of scanning.

2) Gain Application

The second step of post-processing encompassed selecting an appropriate time gain to be applied to the dataset. As radar signals travel through concrete, they attenuate with depth. Thus, recorded radar signals from deeper layers are very weak compared to those registered from shallower depths. Displaying the information simultaneously from various depths is difficult. Therefore, time gains were applied to enhance the diminished signals with depth, and boost low amplitude reflections.

3) Hyperbola Migration

Migration is an iterative mathematical process that involves a synthetic aperture image reconstruction to focus dispersed signals, collapse hyperbolic shapes to their apices, and reposition dropping reflections. The definitive goal of data migration is to locate peaks of hyperbolas, which is the exact rebars locations, to enable rebars picking and to increase image resolution. Therefore, GPR profiles were subjected to hyperbola migration where background velocity was adjusted to optimize the processing results. One of the required parameters to be determined is the window width that was constantly set to 1 meter.

4) Rebar Reflection Picking

Although the embedded algorithms in RADAN[®] software can detect the rebars reflections automatically after performing the migration process, this research applied an extra step in what's known rebar picking to enhance the accuracy of the results. This interactive process included the successive picking of each rebar in the migrated profile while simultaneously checking the corresponding raw profile. Next, consequential rebar picking information was exported to an ASCII comma-separated value (.csv) file. This information comprised of, the scan number, amplitude, and 2-way travel time of each rebar.

5) Attenuation Mapping Normalized by Depth-Correction

The resulted files from the previous step were read by a MATLAB software to create an Excel (.xls) file that contains the coordinate and reflection amplitude of each rebar. Afterwards, a mapping software (Surfer[®]) was utilized to read the Excel's file for each dataset and to create an attenuation map that could be used later to infer the condition of the structure. Three condition states could be determined for RC structures, based on the Corrosiveness Index Technique developed by Dinh (2014). Such states are delineated in Figure 5.30 and defined as: (a) probable sound concrete, which is analogous to light severity; (b) concrete with probable moderate corrosion; and (c) concrete with probable severe corrosion.



Figure 5.30 Condition States using Amplitude Analysis

Also, the area corresponding to each condition state was computed to show the extent of damage. It's worth noting that the amplitudes were depth-corrected in the abovementioned MATLAB[®]

software according to the procedure proposed by Barnes et al. (2008). This procedure was implemented to account for the varying depths of rebars since the placement of reinforcing steel during construction is not executed at the same level throughout the structure. Accordingly, recorded amplitudes from deeper rebars are lower than those recorded at higher levels, because of the dissipation of energy as EM waves propagate into the ground, which will in turn, cause erroneous results. Figure 5.31 and Figure 5.32 display the attenuation maps for different elements in 2 stations and a tunnel in Montréal Metro network using the amplitude analysis. Based on the map in Figure 5.31(a), the right side of Vendôme station slab (VSS), as well as, the center appears to be severely deteriorated, in contrast to the left side that seems to be in a very good condition in most of its parts. The central part is surrounded by a moderately-deteriorated region along with small regions that range from good to severely-deteriorated. Figure 5.31(b) illustrates that the general condition of the wall inter St. Laurent and Place-Des-Arts tunnel (SPTW) is good. Whereas the amplitude analysis map for the slab (SPTS) of the same tunnel is shown in Figure 5.31(c). Different levels of deterioration can be identified as indicated by the different colors on the map. The right bottom edges of the slab have severe deterioration. However the majority of the slab is moderately-deteriorated. Figure 5.32(a) and (c) demonstrate the attenuation maps generated for wall #1 (OSW1) and the slab (OSS) of Outremont station respectively. Various problems confronted the analyst when processing GPR data for these cases. For instance, due to the chaotic reflections caused by actual distresses or by structural/material configuration, rebar picking could not be performed in many locations although for some areas the rebar reflection was discernable. Consequently, in these locations, the analyst had to decide whether the rebar should be picked or left. Specifically, if the rebar is neglected, it is obvious that the amplitude and 2-way travel time information will be missed in this location. Nonetheless, if the rebar is picked, information related

to amplitude is still not very precise. Neither of these options reveals the exact condition in that location. According to Figure 5.32(a), the good condition area extends from the upper part of OSW1 towards mid-span, followed by three different deterioration regions that range from moderate to severe to good condition.

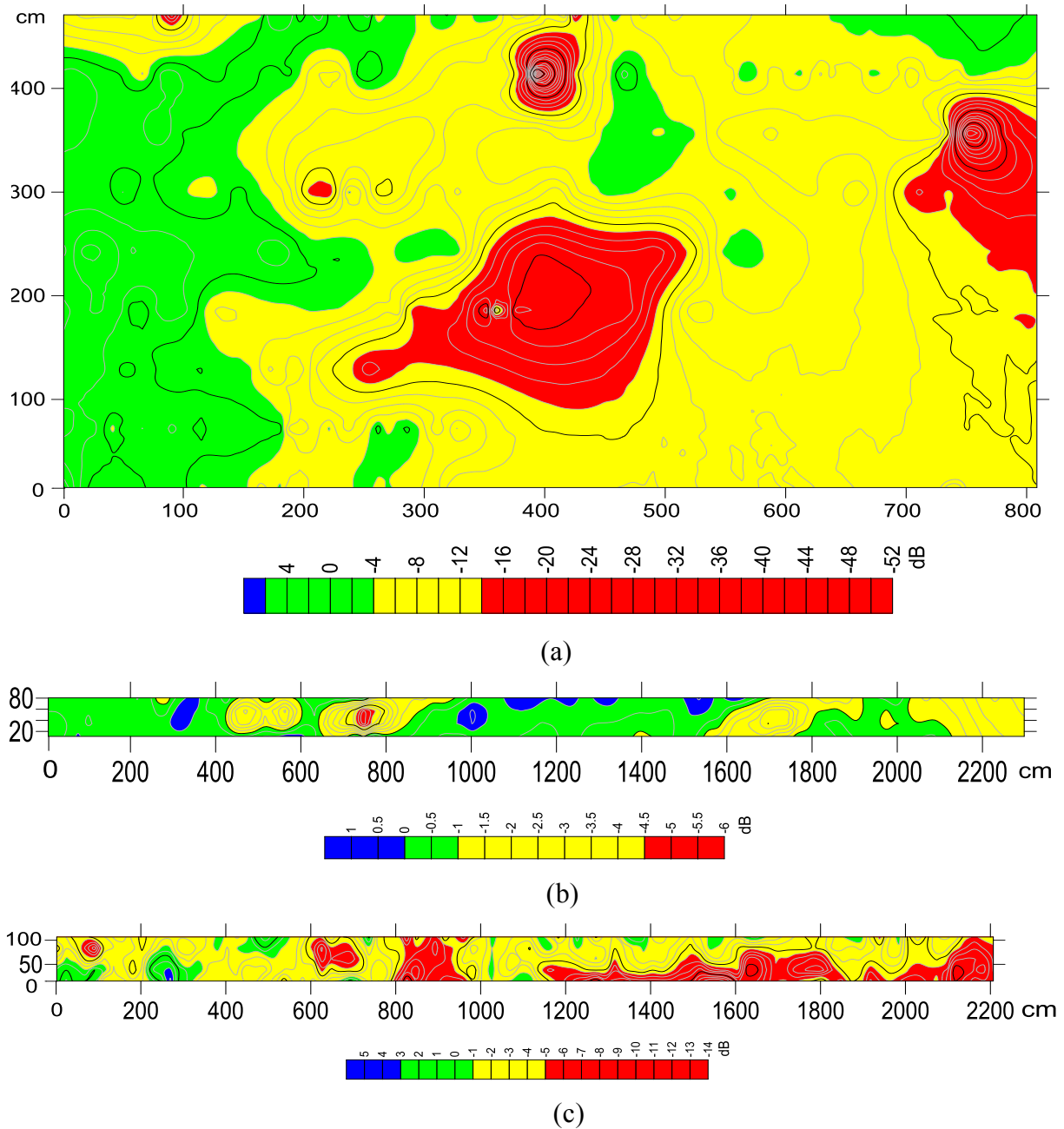


Figure 5.31 Attenuation Maps of (a) VSS; (b) SPTW; (c) SPTS

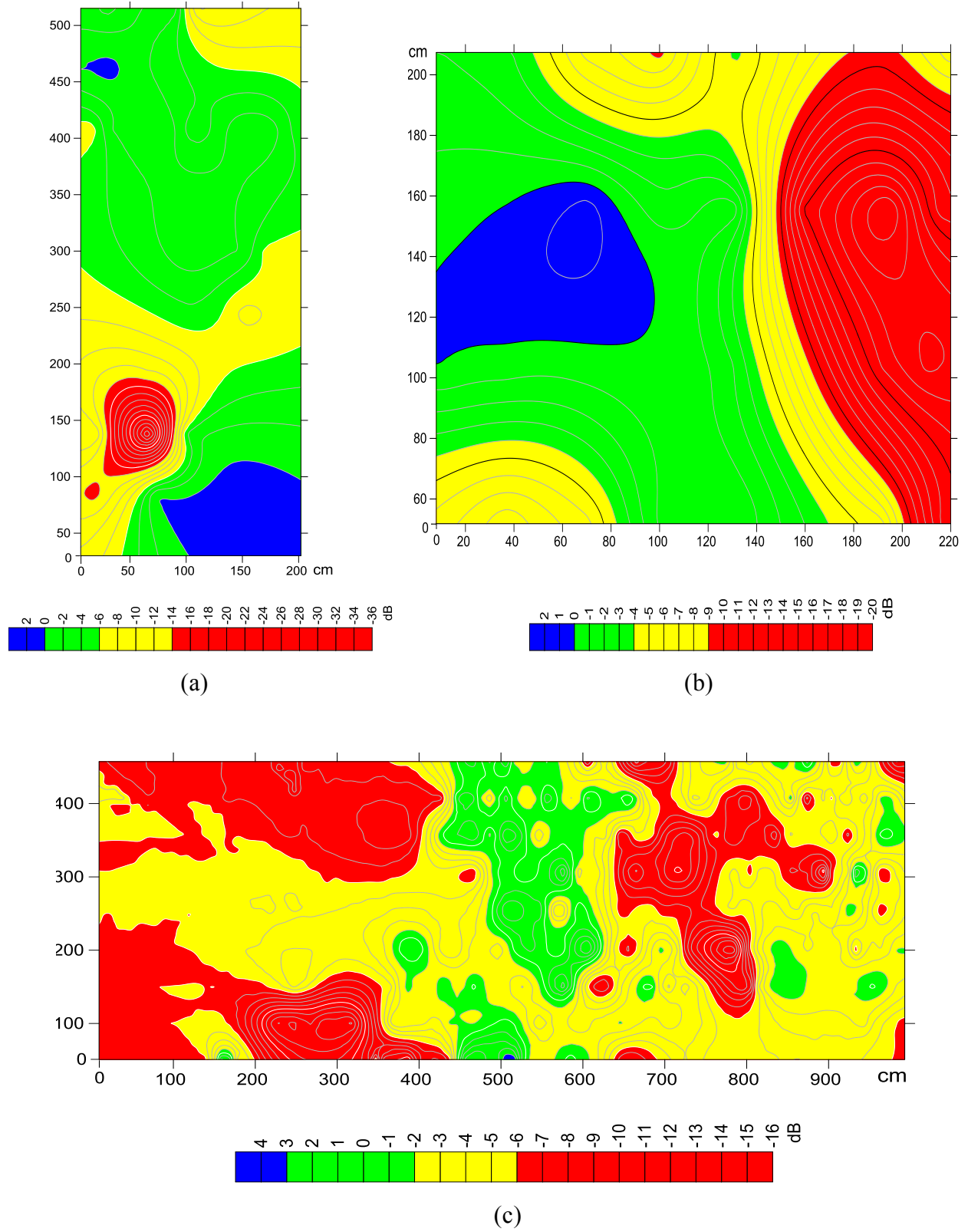


Figure 5.32 Attenuation Maps of Outremont Station (a) OSW1; (b) OSW2; (c) OSS

The numerical analysis map for wall #2 (OSW2) presented in Figure 5.32(b) indicates severe damage on the right side of the wall, followed by moderate deterioration. Whereas, the region that extends from the middle to the left side of the wall seems to be in a good concrete condition. Figure 5.32(c) depicts that the middle section of the slab (OSS) appears to be sound. On the contrary, most of the left region and some of the right region are severely-damaged. The in-between area looks moderately-deteriorated with some sporadic regions that range from being sound to severely-deteriorated. It should be noted, that the vault inter Frontenac and Papineau Tunnel (FPTV) that is a non-reinforced type, could not be analyzed by the amplitude method. Because in this method, the anomalies are identified based on the reflection amplitudes at top mat of reinforcing rebars. Therefore, the structure should contain steel bars in order to be analyzed by this technique.

5.5.1.1 Corrosion Assessment using Amplitude Analysis

The K-means clustering technique that is embedded in RADAN[®] software was implemented on the subway datasets to compute the percentages of each condition state. Using this technique, signal reflection amplitudes of top rebars are automatically grouped into a predefined number of condition categories, e.g., three categories. As a result, a graph that illustrates the relation between rebar picking and normalized amplitudes in disables is produced. Moreover, the thresholds of each condition category can be automatically determined. Figure 5.33 represents the clustering results of six datasets along with their thresholds and area percentages.

In parallel, a membership function of the weighted Fuzzy tool incorporated in the software facilitated the calculation of corrosiveness indices for the six datasets, together with suggesting the course of action or type of intervention needed as shown in Figure 5.34.

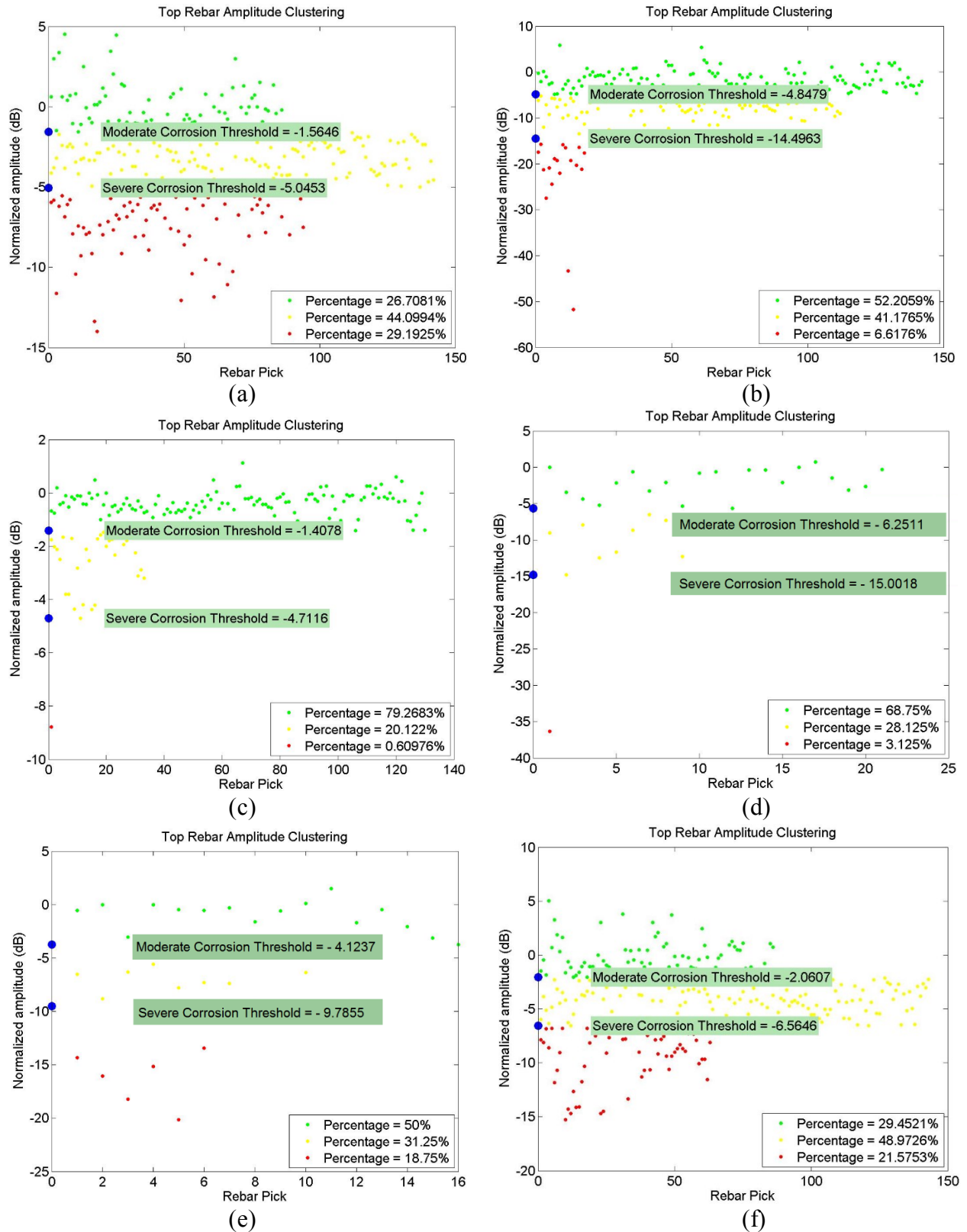


Figure 5.33 Amplitude Clustering for Six Datasets (a) VSS; (b) SPTW; (c) SPTS; (d) OSW1; (e) OSW2; (f) OSS

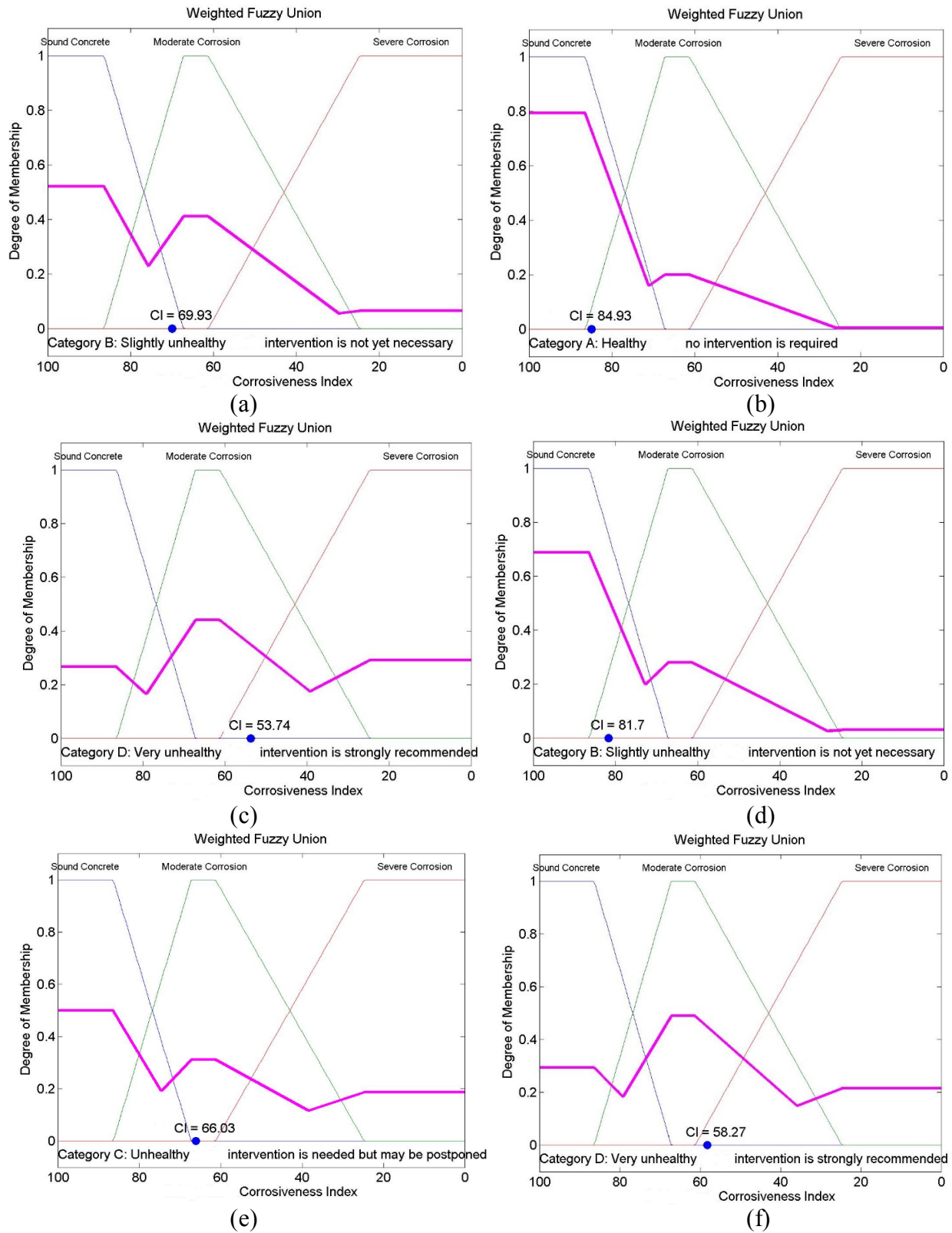


Figure 5.34 Corrosiveness Indices for Six Datasets (a) VSS; (b) SPTW; (c) SPTS; (d) OSW1; (e) OSW2; (f) OSS

Figure 5.34 demonstrates various levels of corrosiveness indices, ranging from healthy in SPTW, hence no intervention is needed, to very unhealthy in SPTS and OSS, thus intervention is strongly recommended. The in-between levels indicate that VSS and OSW1 are slightly unhealthy, thus the intervention is not yet necessary. While OSW2 is analyzed as unhealthy, therefore intervention is required but may be postponed. All these cases have been validated through real images featuring many parts of the structures, as will be elaborated in the validation section.

5.5.2 Mapping using Image-Based Analysis (IBA)

This technique is based on the operator's experience and understanding of the structure to visually interpret GPR signals. This could apply to all types of structures, whether they are reinforced or non-reinforced structures. IBA was applied on all the collected datasets to create deterioration maps. The systematic procedure for this analysis is based upon three main steps:

1) Pre-Processing of GPR Profiles

Prior to processing the data, each GPR profile was classified and systematized into a two-dimensional grid. Next, the coordinates and rebar amplitudes were adjusted along with the application of differential gain to enhance the visualization perception. This procedure is imperative because image analysis method is based on the visual interpretation, unlike the amplitude analysis method.

2) Defects Identification and Anomalies Elimination

In this step, each profile was scrolled to identify the deteriorated regions. Basically, this step involves several interrelated tasks. First, anomalies that are unrelated to rebar corrosion were eliminated, including; a) supporting structures such as main girders, beams, or columns, b) variations of rebar spacing, c) alignment and depth of rebar spacing, d) any previous repairs and surface anomalies. These factors are the main causes of error in the numerical analysis; yet, they

can be easily recognized and eliminated in the IBA. Second, corrosion-induced defects were identified while considering; a) top and bottom rebar amplitudes, b) slab bottom amplitude, c) deformation of the hyperbolas, d) radar velocity changes and visible cracks/delamination. These parameters are considered the most indicative of structural corrosiveness condition. Third, the deteriorated zones were marked in yellow to signify the regions of probable moderate corrosion, and red to indicate the regions of probable severe corrosion. Unmarked zones are probable healthy concrete and thus acquire the green color on the resultant deterioration map. The conditions under which this technique could be accomplished successfully is that the analyst has a good perception and explication capabilities of structural aspects.

3) Deterioration Mapping

Finally, the marked zones in each GPR profile were mapped to the grid prepared in step 1. Then, a comprehensive condition map of the subway element was produced by synchronizing the same concrete regions (states) from separate scan lines. One of the advantages of using the image-based method is that it can be applied to the reinforced concrete (RC) structures, as well as the non-reinforced structures as will be elaborated in the following sub-sections.

5.5.2.1 Corrosion Assessment using IBA

In the RC infrastructure, IBA can identify the deterioration of concrete based on the degree of signal attenuation in GPR profiles. According to the signal attenuation, the concrete can be classified into three states: (a) probable sound concrete; (b) concrete with probable moderate corrosion; and (c) concrete with probable severe corrosion. Table 5.6 identifies the different states of concrete and their corresponding description. The deterioration maps associated with the RC elements of 2 stations and a tunnel in Montréal subway network were created via the IBA for comparison and validation purposes as depicted in Figure 5.35, and Figure 5.36.

Table 5.6 Definition of Various RC States using IBA

Probable Sound Concrete	Probable Moderate Corrosion	Probable Severe Corrosion
Rebar reflection is strong, uniform and clear with hyperbola shape.	Rebar reflection is relatively weak, but hyperbola shape is still clearly visible.	Strong attenuation at top rebar level, hyperbola shape from rebar reflection is distorted / almost disappear.

A comparison was conducted between the maps generated by the two analysis methods, i.e., amplitude analysis, and IBA. Starting with the two maps of VSS shown in Figure 5.31(a) and Figure 5.35(a), which indicate that there is a similarity in some of the sections, specifically the sound concrete in the left, the severely-deteriorated part in the center, and the lower section that is moderately-deteriorated. Figure 5.31(b) and Figure 5.35(b) associated with the SPTW demonstrate great similarities in identifying the good condition regions, however the moderate regions according to the amplitude analysis were found to be severe in the IBA. On the other hand, the SPTS maps illustrated in Figure 5.31(c) and Figure 5.35(c) show huge differences between the schemes, except for some scattered areas of healthy concrete, which reveal resemblances. Upon examining the GPR profiles related to SPTS, it was found that there exist huge variations of rebar spacing, and this could be the reason that triggered false mapping information in the amplitude method. On the contrary, rebar spacing is one of the factors that are considered by the analyst while marking the visible anomalies via the image-based method. GPR-IBA differentiates between the different causes of signal attenuation and further identifies the attenuation as a corrosion-induced defect or non-corrosion-induced defect.

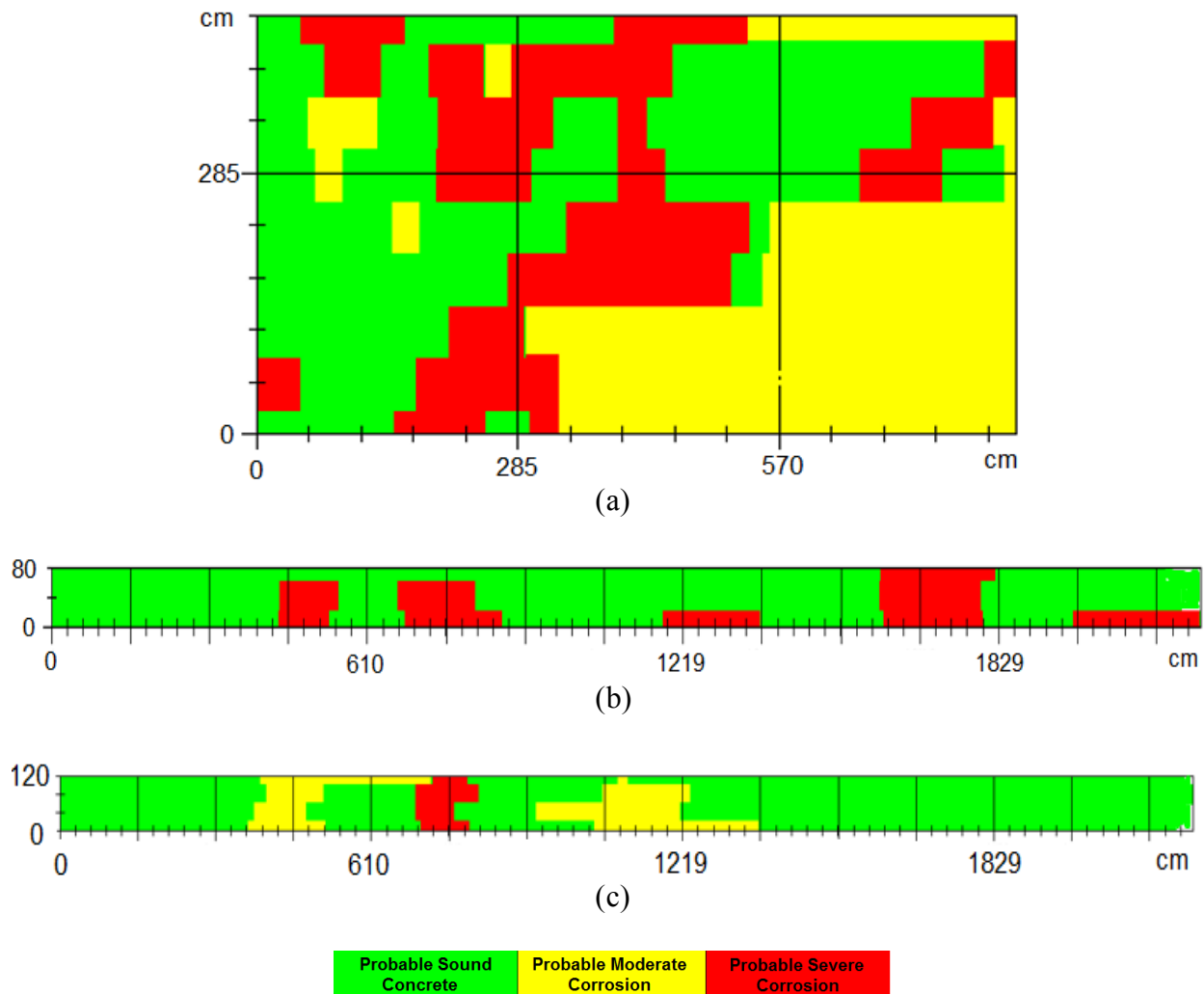


Figure 5.35 Deterioration Maps of (a) VSS; (b) SPTW; (c) SPTS

Comparing the maps in Figure 5.32(a) and Figure 5.36(a) obtained for OSW1 indicates that there is a similitude solely in the upper section of the wall, in contrast with the lower section that demonstrates huge dissimilarities. This is due to the chaotic reflections caused by real defects or structural aspects that prevented rebar picking in many locations, which might in return caused erroneous results. On the other hand, the interpretation of Figure 5.32(b) and Figure 5.36(b) confirms that the two maps are almost identical in identifying the condition of concrete in OSW2.

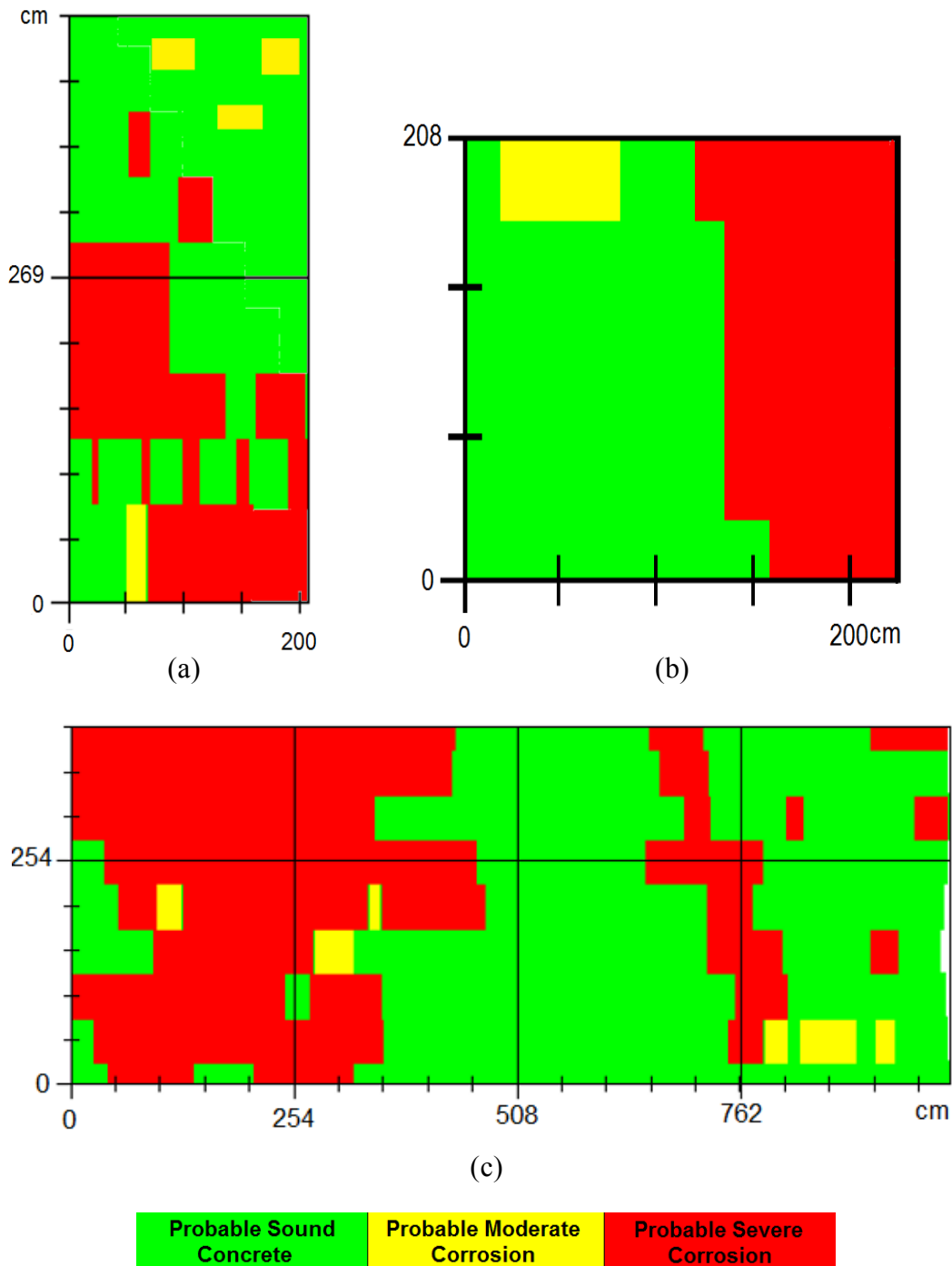


Figure 5.36 Deterioration Maps of Outremont Station (a) OSW1; (b) OSW2; (c) OSS

Figure 5.32(c) and Figure 5.36(c) characterize the resemblance in the severely-damaged zones, especially the upper and lower left zones, as well as the sound concrete in the middle span. The rest of the slab in the station demonstrates contrasts in interpreting various zones as a result of the

chaotic reflections that caused difficulties in the rebars picking in many locations, as mentioned earlier. The following sub-section portrays GPR profiles interpretation and the deterioration mapping in non-reinforced concrete infrastructure by the IBA.

5.5.2.2 Modelling of Air Voids and Water Voids

The other application of IBA, which cannot be achieved by the amplitude analysis, is the diagnosis and mapping of distresses in the non-reinforced concrete facilities. Since the vault inter Frontenac and Papineau tunnel (FPTV) contains no rebars, it was studied to model the presence of other distresses in concrete, i.e., air voids and water voids. Many parameters were identified to build a model for the detection of air voids and water voids in metro networks via IBA. Figure 5.37 illustrates the proposed model, which includes sequential steps as the following:

1) Selecting the Proper GPR Antenna for Scanning

Achieving the best outcomes in analyzing GPR profiles hinges on selecting the appropriate antenna frequency. Meanwhile, each antenna resolution is suitable for certain depth penetration. Therefore tunnel plans are probed and analyzed to determine the vault thickness, thereby allowing the selection of the best GPR antenna frequency.

2) Data Collection and Analysis

Data are collected for a segment of the tunnel vault using the selected GPR antenna. Before conducting these surveys, an accurate plan is predetermined, which involves the number of personnel, type of equipment, survey lines, distance, etc. Consequently, data analysis method is specified based upon the reinforcement existence in the structure. Since the tunnel's plans illustrate no reinforcement among all the components of the structure, a procedure grounded in IBA is proposed to analyze GPR data of the non-reinforced concrete elements. Prior to profiles processing, a preprocessing step is executed, which involves organizing each profile into a 2D

grid. The coordinates and signal amplitudes are adjusted, while the differential gain is applied to boost the visualization perception. Afterwards, the processing procedure is applied to generate a map for the structure. Figure 5.38 depicts the image-based analysis framework for the detection of air/water voids.

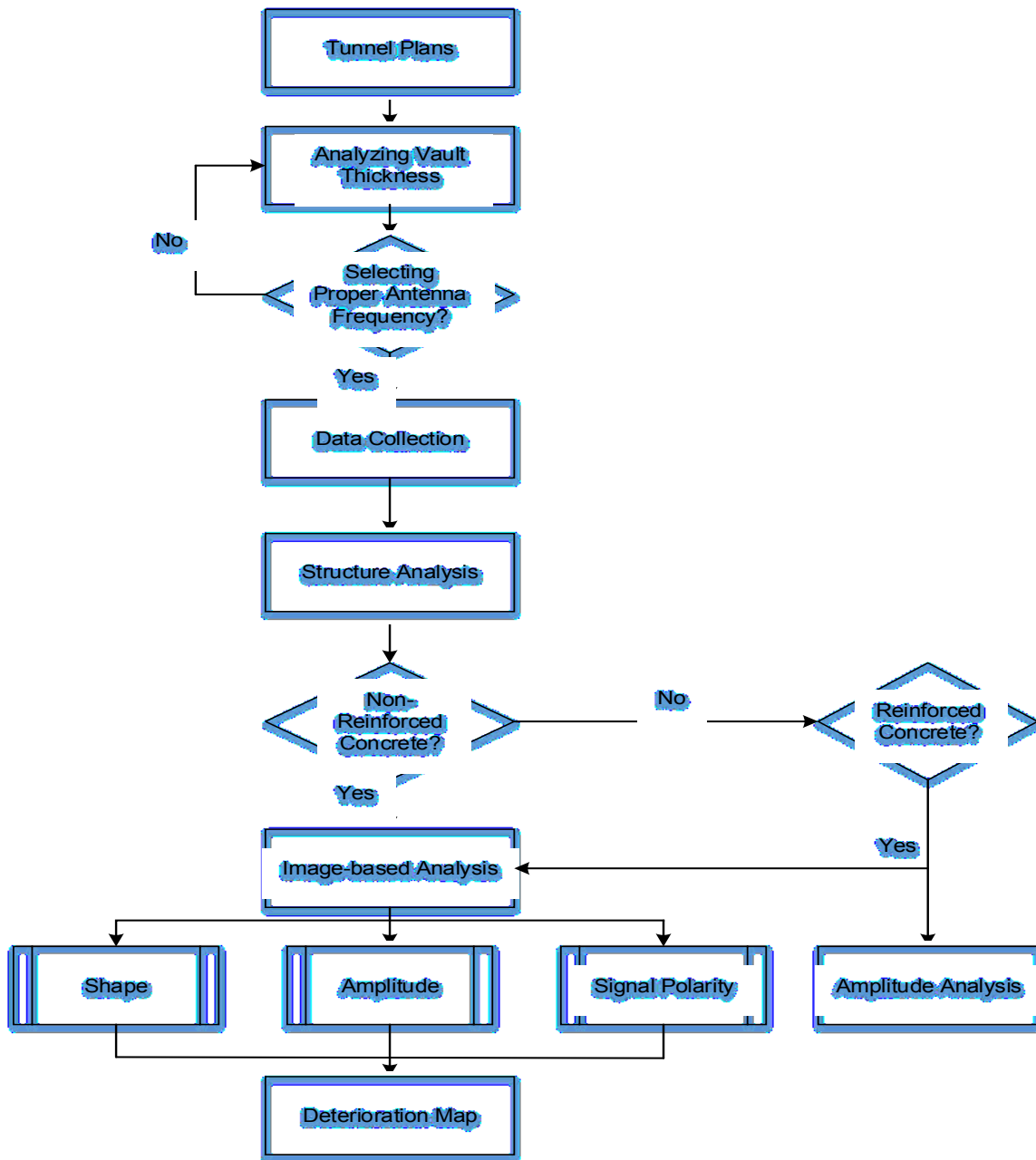


Figure 5.37 IBA Model in Non-Reinforced Concrete

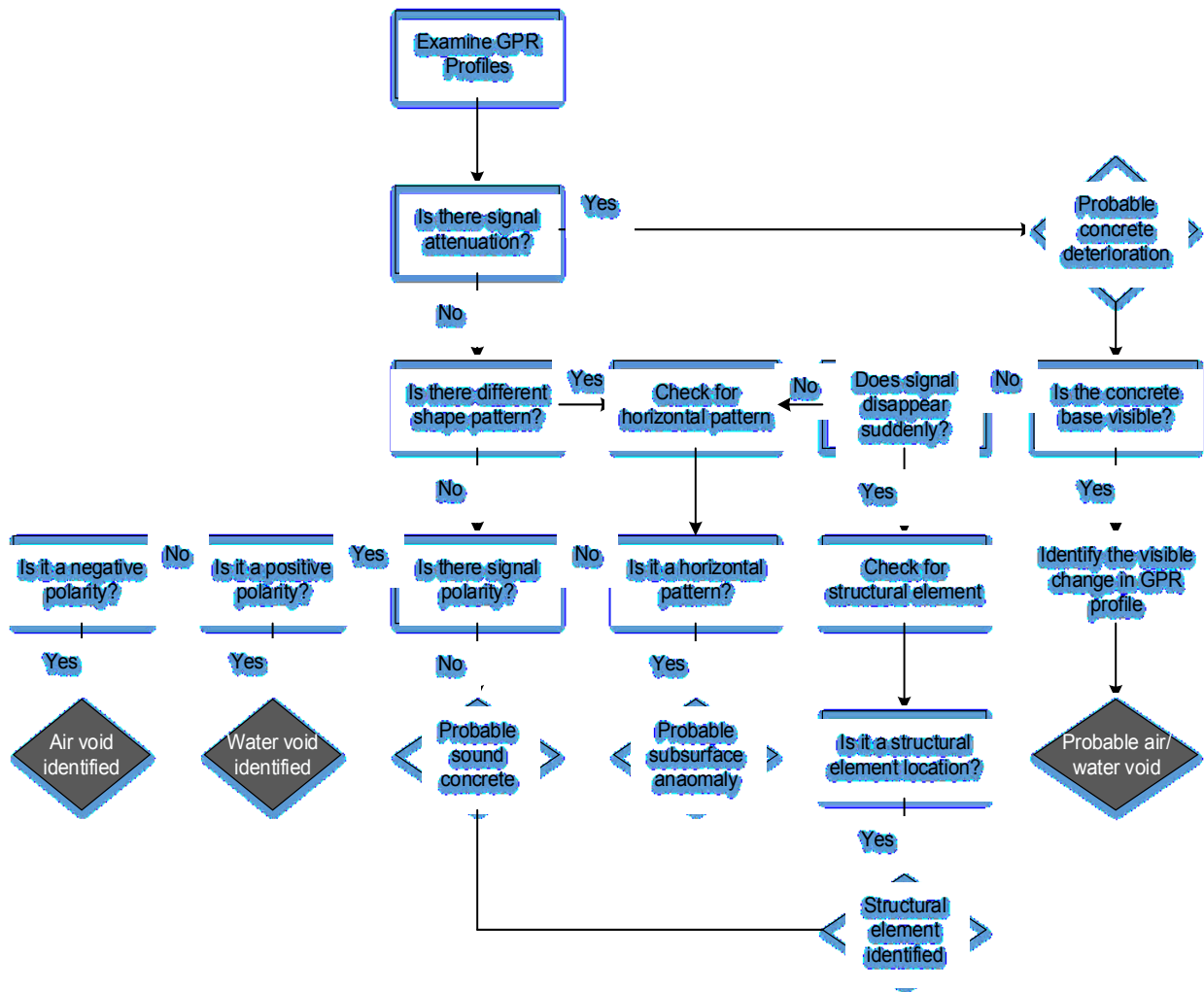


Figure 5.38 IBA Framework for Air/Water Voids Identification

The identification of voids defects in GPR profiles starts by checking the strength of signal, which in the case of attenuation indicates a probability of concrete deterioration. Next step involves eliminating structural elements and other anomalies. The GPR data processing is done using a series of If-Then rules based on the factors considered and/or eliminated for each GPR profile, and based on the understanding of the nature of the studied structure. The following factors have to be considered in this process:

- Shape: As the analyst scrolls the GPR profile and finds a distinct shape pattern, a visual analysis process of this pattern is performed. If it is a horizontal pattern, this signifies any

anomaly in the concrete other than air/water void distress, thus should be excluded from the analysis. If the pattern shows a non-horizontal shape, it could be an air/water void pocket.

- **Amplitude:** When a beam of electromagnetic wave encounters an interface between two media of different dielectric constants, its amplitude will alter accordingly. This is an indication of either a structural element or a deterioration in concrete, e.g., air/water void, or any concrete anomaly.
- **Signal Polarity:** Reflection polarity could gauge the subsurface condition because it is a function of dielectric constant between two media. The dielectric constants of air, water, and concrete are quite distant from each other, as it is equal to 1 for air, 81 for water, and ranges 6-12 for concrete (Gehrig et al. 2004). Positive polarity occurs when the dielectric constant of layer 1 is less than the dielectric constant of layer 2 and vice versa. Detecting air/water voids could be achieved easily since the air void will display a negative (reversed) polarity, while a positive polarity will appear when there is a water void in the vicinity.

3) Mapping of the Deteriorated Zones

The analysis method can be consistently performed using RADxpert[®] analysis software after marking the potentially deteriorated areas, i.e., air voids in yellow and water voids in red. Figure 5.39 depicts processing a sample of the tunnel's profiles via IBA. The system will automatically process the formerly marked areas and create a deterioration map. The state of concrete can be identified based on the degree of signal attenuation in GPR profiles. Thus, in the context of non-reinforced concrete, there exist 3 hypothesis for the interpretation of data as shown in Table 5.7.

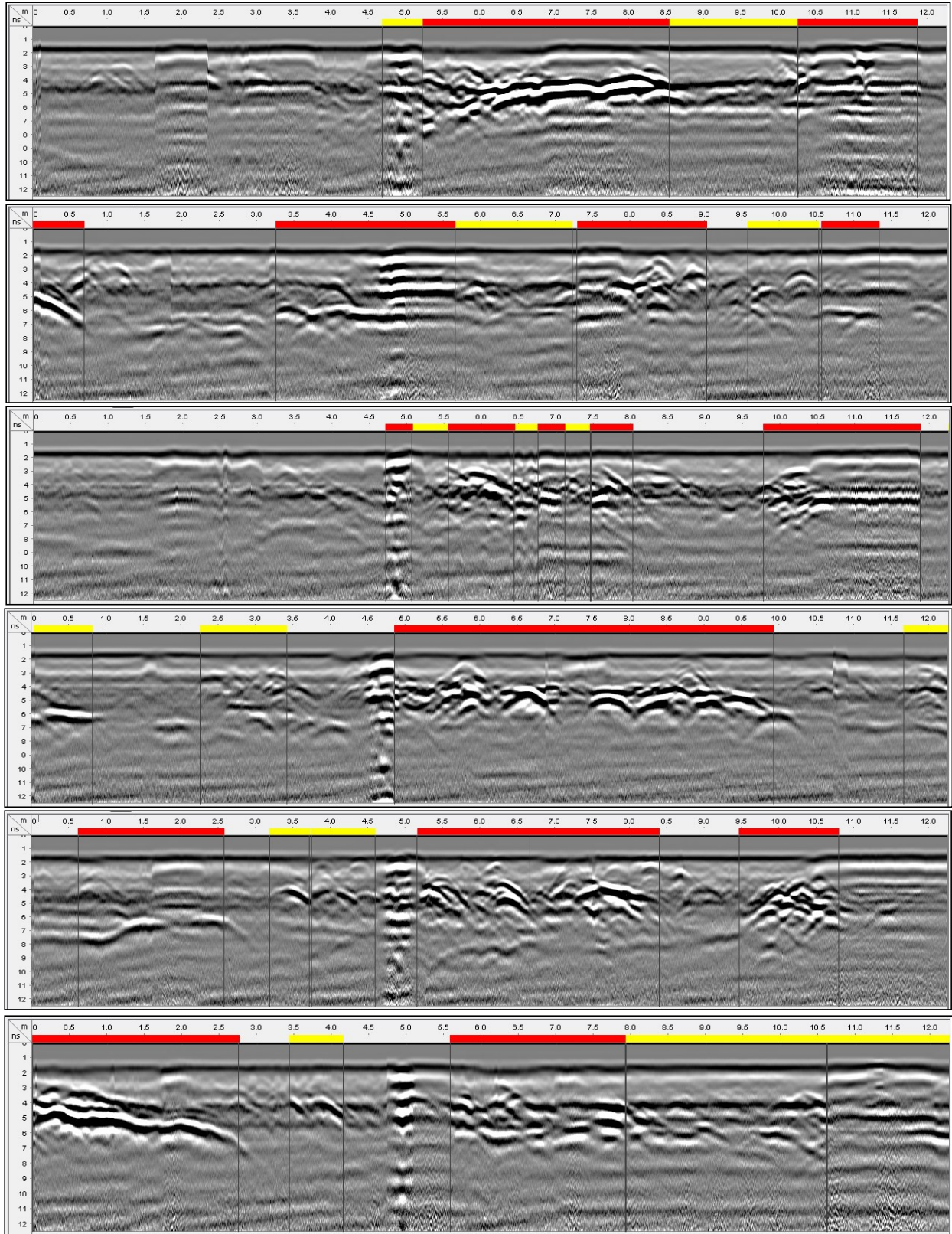


Figure 5.39 Sample of Scanned GPR Profiles in FPTV

Table 5.7 Definition of Various Non-RC States using IBA

Probable Sound Concrete	Probable Air Void	Probable Water Void
Wave amplitude is strong; there is no distinguished shape pattern or signal polarity.	Wave amplitude is relatively weak; there are distinguished shape patterns and negative signal polarity.	Wave amplitude is relatively weak; there are distinguished shape patterns and positive signal polarity.

Model Implementation and Results

The aforementioned IBA steps were implemented on a vault inter Frontenac and Papineau tunnel (FPTV) after shutting down the services. The tunnel is constructed in 1962 and is one of the systems on the Green Line of Montréal’s subway. First, The GSSI handheld GPR with antenna frequency of 900 MHz was selected to scan the concrete surface. The use of this frequency range is intuitively justified in the context of air/water void detection in this tunnel. The antenna offers a close-range penetrating depth of 0-1m and since the vault thickness in the tunnel is around 0.61m, the 900 MHz antenna resolution is quite satisfactory for data collection. The antenna was mounted on a man lift that was attached to an inspection train to allow a smooth transition and high accuracy of data collection. After calibrating the GPR and adjusting its setting, surveys were conducted for the vault between 910.00 m and 886.20 chainages. The surveys included 14 parallel lines of 23.8 m in length, 6.5m in width, and spaced 0.5 m as shown in Figure 4.6. The various features of this tunnel alongside the GPR antenna are displayed in Table 4.2. In the end, a deterioration map was produced for the tunnel’s vault as demonstrated in Figure 5.40.

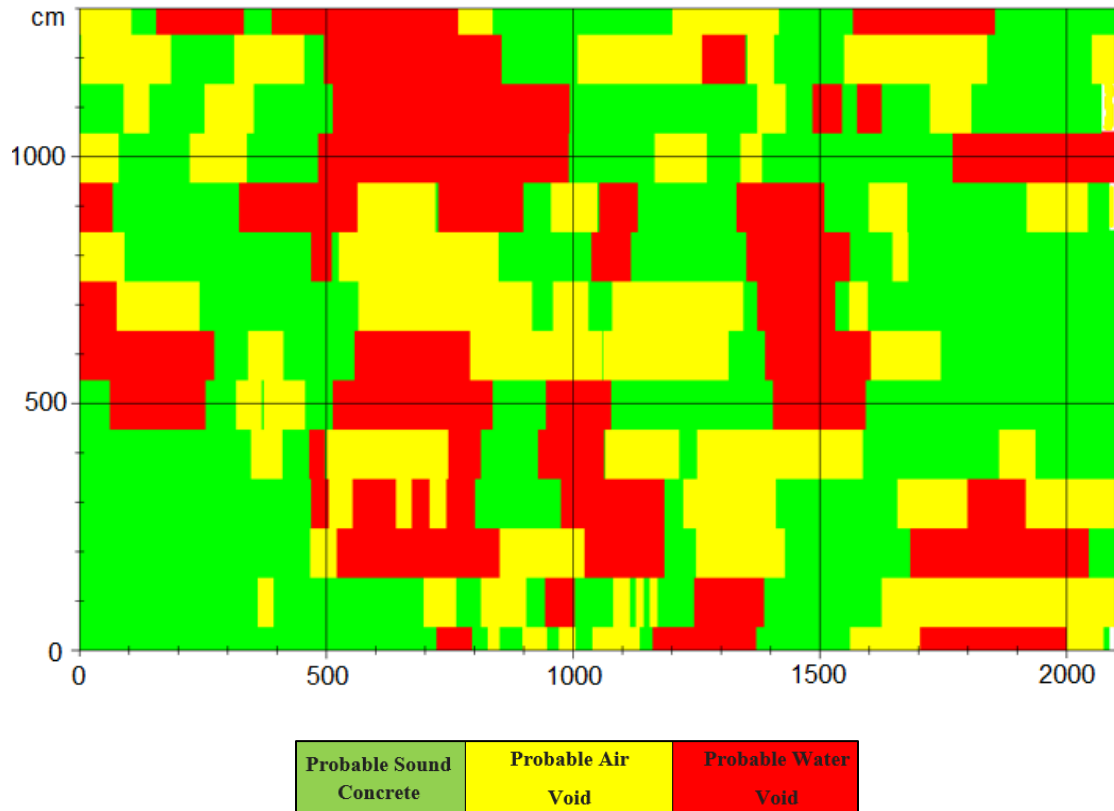


Figure 5.40 Deterioration Map of FPTV

Model Validation

The developed subsurface model of air/water voids using IBA was validated through various tests and techniques. The advantage of combining different verification methods is that they provide a comprehensive assessment of subsurface conditions all over the inspected area, not only at the selected locations. First, field inspection was undertaken to locate the healthy and damaged areas within the tunnel vault. In addition, camera images were captured at several locations of the vault to assure the robustness of the model. The correlation between the conditions provided by the GPR-IBA technique and the actual deterioration observed at different positions of the vault is apparent as shown in Figure 5.41.

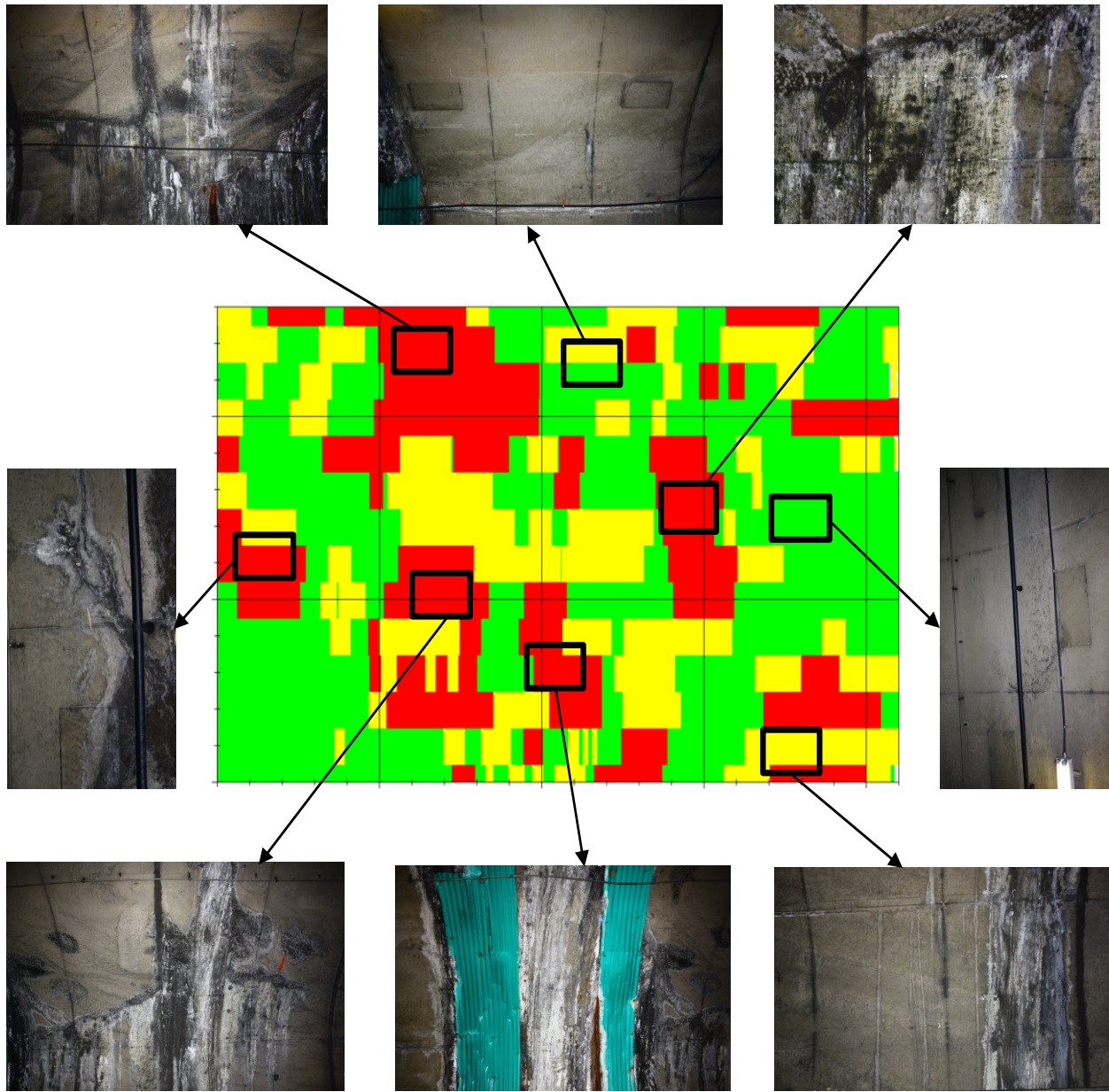


Figure 5.41 Correlation between GPR-IBA and Camera Images in FPTV

Second, destructive tests were performed including ground truth core tests. Five locations were selected throughout the vault to execute core drilling work. Each core was coded for easy identification. Figure 5.42 presents the coring positions along with their codes. Furthermore, a cross section was obtained from each specimen in order to undergo a moisture content test using a digital moisture meter.

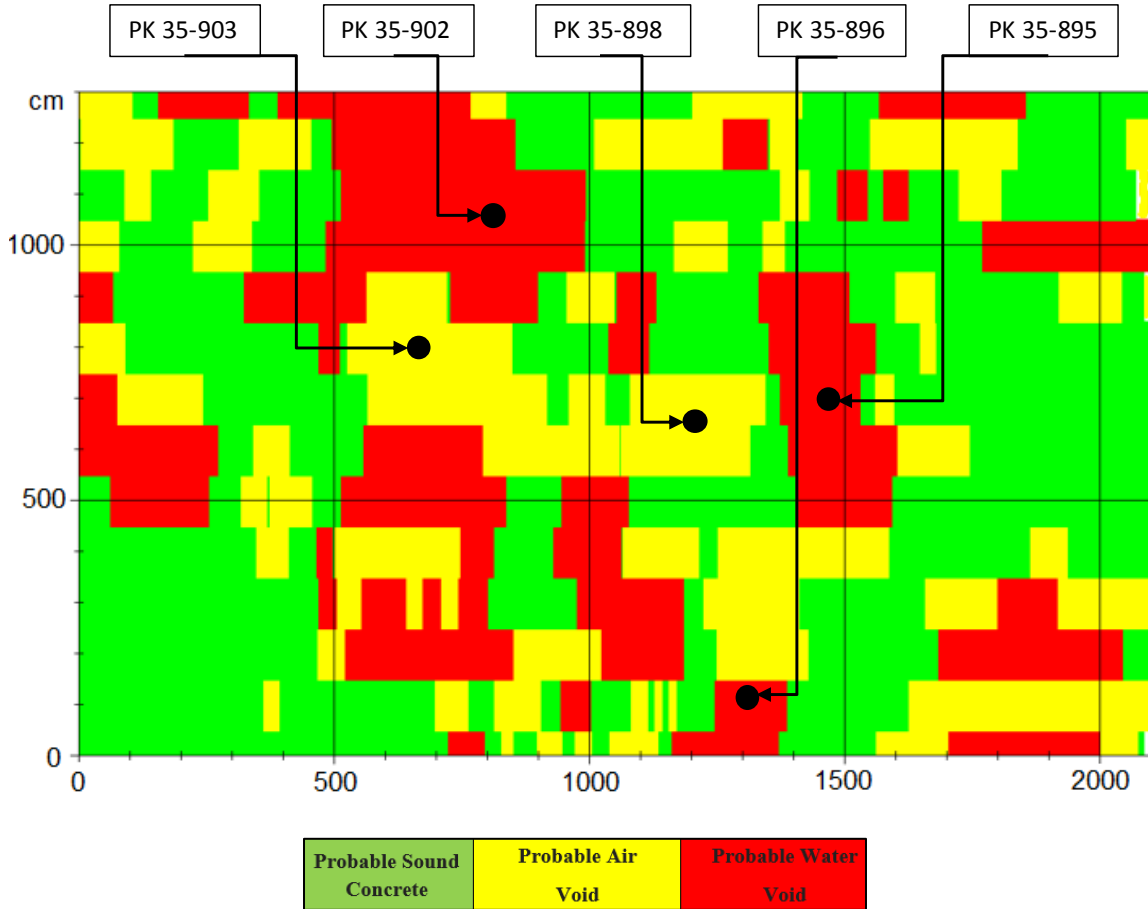












Figure 5.42 Coring Locations

Table 5.8 summarizes the five samples and their properties. As demonstrated, coring test results of samples PK 35-902, PK 35-896, and PK 35-895 indicated high percentages of moisture content, recorded as 86, 74, and 65 respectively. These wet samples can also be noticed from their images and cross sections in Table 5.8. These results perfectly correlated with GPR-IBA for these three samples as located in the water void (red) zone on the map. While the moisture content percentages for samples PK 35-903 and PK 35-898 were found to be 22 and 19 respectively. Hence they were categorized as dry samples, which correlated very well with GPR-IBA result and sited in the air void (yellow) zone on the map. Furthermore, examining the images and cross sections of these two samples in the table reflect dry areas.

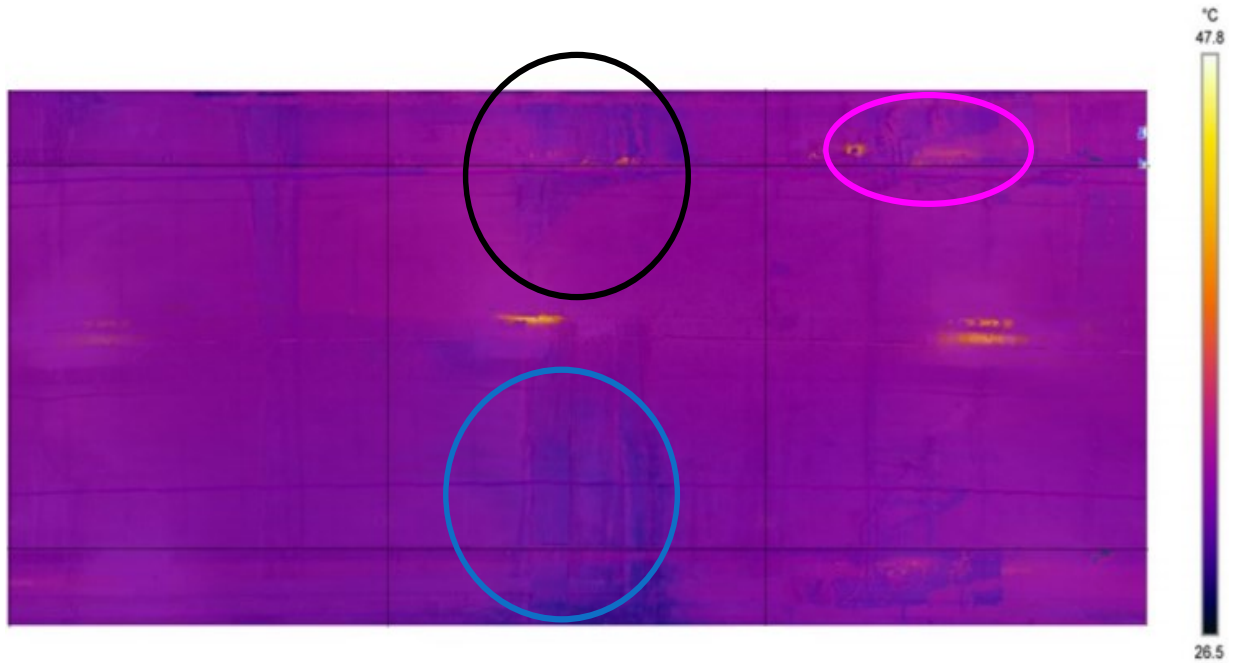
Table 5.8 Coring Samples and their Properties

Sample Code	Depth (cm)	Moisture Content (%)	Sample Image	Cross Section
PK 35-903	43.5	22		
PK 35-902	40	86		
PK 35-898	38.5	19		
PK 35-896	40	74		
PK 35-895	38	65		

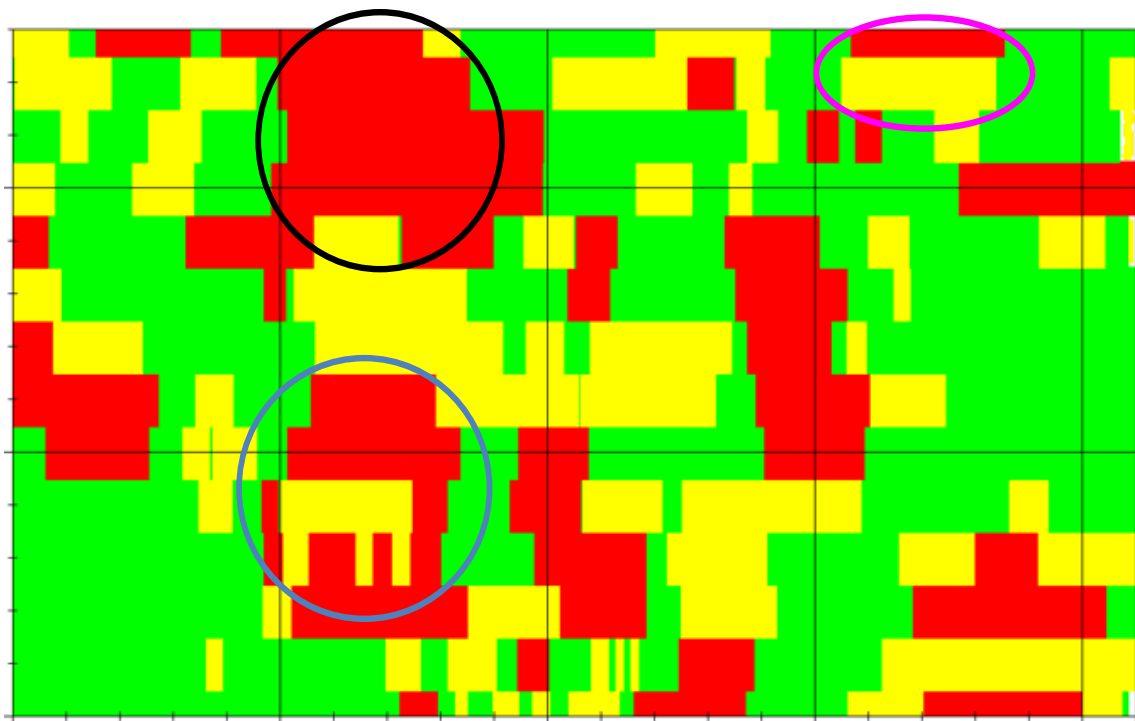
Third, additional NDE techniques such as infrared thermography (IR) and 3D laser scanner (LIDAR) were applied to further verify the results obtained using the proposed model and the designed tool. The IR approach utilized thermal and visible images to create a 3D point cloud model for the tunnel by performing the structure from motion method (Al Lafi et al. 2017). Moreover, overlapped thermal images were stitched in order to produce a panoramic image with precise temperature exemplification. Finally, thermal images were mapped to the 3D point cloud to enable measurements of subway tunnel components. Figure 5.43(a) depicts the as-is laser-based thermal photo for the subway tunnel environment. When comparing the laser-based thermal map to the map generated using the IBA and shown in Figure 5.43(b), a strong correlation between the two maps can be easily noted. The blue zones appearing on the laser-based thermal map indicate the cold areas according to the color visualization scale, which are the exact locations of water voids identified by the IBA. The validation outcomes reveal the feasibility of the developed model in terms of detecting air and water voids in metro systems.

5.6 Evaluation of Surface and Subsurface Defects

The selected segments in Montréal Metro systems were evaluated for both surface and subsurface defects according to condition indices. For the purpose of attaining high level of accuracy in the evaluation process, each segment was divided into equal sections. Then each section was assessed for the severity of each of the seven defects, i.e., moisture marks (MM), spalling (SP), scaling (SC), cracks (CR), corrosion (CO), air voids (AV), and water voids (WV). Table 5.9, Table 5.10, Table 5.11, Table 5.12, Table 5.13, Table 5.14, and Table 5.15 present the defects' condition indices of FPTV, VSS, OSW1, OSW2, OSS, SPTW, and SPTS respectively.



(a)



(b)

Figure 5.43 Comparison between Various NDE Techniques (a) Laser-Based Thermal Ortho-Photo (Al Lafi et al. 2017); (b) GPR-IBA Deterioration Map

Table 5.9 Condition Indices of FPTV

Defect Section	MM	SP	SC	CR	AV	WV
1	80	90	85	87	90	90
2	12	89	86	56	79	79
3	51	90	89	89	80	52
4	15	88	87	90	61	33
5	19	87	90	12	88	90
6	16	90	89	85	60	78
7	54	90	86	87	82	70
8	45	90	87	87	10	81
9	20	88	82	92	89	90
10	13	88	89	86	59	38
11	79	87	86	95	73	58
12	14	88	85	93	24	50
13	43	86	84	95	88	89
14	17	88	84	95	72	33
15	56	89	88	93	53	60
16	40	86	89	94	61	62
17	42	90	90	94	89	90
18	45	90	88	95	64	72
19	57	89	88	95	23	78
20	58	90	86	94	60	88
21	22	88	85	92	72	71
22	18	87	86	91	75	40
23	10	87	82	94	64	70
24	84	86	80	93	81	89
25	16	90	87	95	70	52
26	44	89	85	92	69	20
27	35	88	87	94	58	63
28	88	90	90	95	79	80
29	33	87	90	91	69	58
30	41	87	90	94	19	72
31	10	87	89	93	20	72
32	80	90	88	90	83	81
33	42	90	87	95	78	80
34	11	88	86	94	12	81
35	16	85	88	95	71	49
36	87	89	88	93	88	89

Table 5.9 Condition Indices of FPTV (Continued)

Defect Section	MM	SP	SC	CR	AV	WV
37	44	90	85	92	89	61
38	15	88	84	90	23	59
39	18	89	88	91	89	49
40	80	89	87	89	82	88
41	31	90	89	90	82	73
42	21	85	90	91	80	21
43	82	89	84	89	83	72
44	19	88	82	92	80	59
45	30	86	90	88	58	88
46	11	88	86	85	89	10
47	17	87	81	90	80	87
48	87	88	80	94	88	56
49	33	85	84	94	32	89
50	22	89	83	92	81	18
51	54	88	83	91	52	89
52	81	86	89	93	59	81
53	24	82	90	95	48	68
54	10	85	89	94	87	21
55	42	86	83	95	18	88
56	86	87	85	90	62	68

Table 5.9 demonstrates that the dominant phenomena in the vault inter Frontenac and Papineau tunnel (FPTV) is the huge amount of water presented in the low indices of both MM and WV. Therefore, the damage inflicted due to water accumulation in the tunnel is considered the first priority among other distresses. The indices of MM and WV show great fluctuations among their values; this is also the case for AV between the rock and concrete linings. Conversely, the rest of the defects, e.g., SP, SC, and CR were found to be in good condition, revealed by the high values of their indices. It's quite apparent that corrosion defect was not taken into consideration in the assessment process as the tunnel was constructed in the rock, therefore no reinforcement was requisite in the body of the tunnel.

Vis-à-vis the slab in Vendôme Station (VSS), Table 5.10 shows that solely SC indices denote sound surface concrete area with an average value of 87. The rest of the defects display tremendous fluctuations that could be noticed among the indices values of MM, SP, CR, CO, AV, and WV.

Table 5.10 Condition Indices of VSS

Defect Section	MM	SP	SC	CR	CO	AV	WV
1	80	82	88	40	90	85	80
2	25	90	88	89	72	90	30
3	17	83	85	87	68	20	80
4	23	85	84	87	68	20	82
5	82	84	82	86	68	20	90
6	85	89	87	46	82	90	60
7	30	87	90	90	68	90	86
8	32	88	89	91	60	20	87
9	22	84	87	95	68	25	85
10	82	85	86	86	68	20	90
11	85	90	87	85	85	87	60
12	81	85	84	84	42	70	50
13	30	81	90	82	25	23	89
14	80	10	86	80	68	20	90
15	81	20	86	86	68	21	87
16	90	87	85	92	85	90	90
17	89	80	88	92	50	85	50
18	85	20	83	91	35	82	40
19	82	33	90	95	58	20	86
20	82	10	90	93	60	20	90
21	87	88	90	53	87	82	85
22	90	84	90	60	77	90	50
23	85	25	89	96	22	89	21
24	84	34	87	26	50	30	80
25	83	10	84	95	53	20	83
26	90	87	90	80	89	58	80
27	90	80	90	80	60	87	34
28	89	15	88	33	72	90	72
29	85	17	90	33	60	88	80
30	87	25	87	85	32	90	50

Table 5.10 Condition Indices of VSS (Continued)

Defect Section	MM	SP	SC	CR	CO	AV	WV
31	90	88	84	53	88	50	90
32	89	45	85	60	68	82	25
33	88	13	88	23	77	84	80
34	88	10	90	93	72	85	81
35	81	45	85	91	42	82	53
36	90	86	86	86	90	88	53
37	88	25	86	66	77	60	24
38	82	23	90	36	65	89	32
39	81	20	85	90	72	90	88
40	81	45	87	22	68	85	80
41	88	84	90	86	35	88	33
42	89	27	90	25	87	60	87
43	88	10	86	56	42	85	20
44	82	18	82	56	70	20	87
45	81	82	84	16	79	23	90

Table 5.11, which pertains to wall #1 in Outremont station (OSW1), illustrates huge variations among the indices values of MM, CO, AV, and WV. While surface defects of SP and SC present very good scores in the first sections of the wall, which imply sound concrete; enormous deterioration could be noticed in the last sections, specifically sections 13, 14, 15, and 16. On the other hand, CR indices confirm a healthy concrete status as their calculated average value equals 91.4.

Regarding the indices of wall #2 in Outremont station (OSW2) depicted in Table 5.12, immense variations also could be found in the values of some of the distresses, such as MM, CR, AV, and WV. Dissimilar to wall #1 in the same station, SP scores show healthy concrete structure in all of its sections, and SC indices exemplify mediocre condition of the element. However, CO scores indicate a gradual descending of indices values, which signify that corrosion-prone zones are initiating in the wall. Thus inspection and maintenance actions should be considered.

Table 5.11 Condition Indices of OSW1

Defect Section	MM	SP	SC	CR	CO	AV	WV
1	87	90	89	93	23	80	85
2	90	90	87	95	40	12	44
3	90	88	90	95	77	82	31
4	88	87	89	91	83	81	30
5	80	86	90	93	10	90	10
6	21	90	90	80	16	80	18
7	10	85	84	82	40	85	60
8	12	85	87	92	44	80	58
9	81	89	83	95	85	87	70
10	24	84	86	89	90	78	58
11	13	86	83	90	89	77	56
12	16	88	90	94	72	88	85
13	87	21	66	95	82	33	82
14	78	12	10	93	90	19	75
15	82	14	16	91	57	12	85
16	88	10	12	95	38	10	86

In Table 5.13, indices values of the slab in Outremont station (OSS) demonstrate a general trend of great fluctuations and alarming conditions for the slab represented by the very low indices for MM, SP, SC, CR, CO, and WV. These results reveal very severe deterioration mechanisms where the extent of damage is huge, bearing in mind the amount of salt brought about by the passengers in the station as shown in Figure 5.44. Nevertheless, the AV indices score consistent values in the majority of the sections, which in turn ensure the structural integrity.

Table 5.12 Condition Indices of OSW2

Defect Section	MM	SP	SC	CR	CO	AV	WV
1	88	90	90	86	88	90	90
2	85	90	87	92	45	87	88
3	40	90	75	18	10	86	45
4	22	90	73	33	13	90	14
5	90	88	90	86	90	87	90
6	38	87	73	80	24	89	86
7	12	83	75	56	15	86	35
8	10	81	73	95	11	90	21
9	85	90	90	86	45	10	90
10	40	88	75	93	19	23	88
11	10	83	73	19	12	82	33
12	13	82	74	15	15	89	15
13	55	90	90	80	11	14	70
14	40	82	83	66	17	14	60
15	14	80	73	13	25	20	23
16	11	78	75	10	25	32	12

Table 5.13 Condition Indices of OSS

Defect Section	MM	SP	SC	CR	CO	AV	WV
1	90	89	90	33	37	90	52
2	39	86	23	92	10	88	55
3	80	85	90	10	70	90	88
4	38	62	56	95	50	87	89
5	20	11	33	94	59	85	89
6	50	88	89	16	32	87	10
7	33	85	16	88	30	86	33
8	81	84	50	12	77	85	88
9	31	12	83	93	68	80	80
10	12	15	50	90	58	50	90
11	45	90	90	18	35	86	11
12	10	89	17	93	40	84	40
13	70	87	50	22	77	84	89
14	10	15	86	90	37	80	60

Table 5.13 Condition Indices of OSS (Continued)

Defect Section	MM	SP	SC	CR	CO	AV	WV
15	12	11	66	91	51	52	90
16	40	90	90	17	32	85	51
17	17	87	12	88	70	70	59
18	50	87	33	34	77	85	88
19	13	12	90	91	37	90	60
20	20	50	56	35	71	90	82
21	32	88	86	89	68	78	50
22	11	82	17	95	68	88	17
23	54	80	31	56	75	89	52
24	17	45	72	88	30	90	81
25	14	10	86	26	68	89	90
26	13	90	83	87	68	80	25
27	15	88	10	89	66	89	14
28	77	88	75	77	77	90	62
29	14	14	80	87	35	90	34
30	15	13	86	19	40	89	90
31	17	90	82	88	24	90	18
32	40	87	31	11	10	90	35
33	82	86	73	15	87	89	88
34	12	10	89	87	32	88	32
35	14	11	83	16	70	90	74
36	41	89	90	85	30	90	20
37	53	86	83	13	14	88	18
38	79	84	81	18	73	90	80
39	10	17	88	86	45	89	73
40	10	19	80	17	51	87	89
41	82	90	90	22	11	88	19
42	90	87	80	41	23	86	17
43	69	88	83	10	87	89	81
44	16	18	89	93	47	90	76
45	25	12	86	15	48	87	55



Figure 5.44 Salt on Stairs in a Montréal Subway Station

Table 5.14 illustrates the evaluation results of a wall inter St. Laurent and Place-Des-Arts tunnel (SPTW). Although the calculated values of SP, SC, and AV display high indices that describe sound concrete condition, CR and WV infer such a wide variation among their indices and hence stating very severe conditions in some of the sections. On the other hand, moderate variations were found in the context of MM, and CO, which provide a good correlation between the two distresses in terms of assessing the wall's condition.

Concerning the condition of slab inter St. Laurent and Place-Des-Arts tunnel (SPTS) represented in Table 5.15, it is quite notable the extent of fluctuation among the indices of three distresses, i.e., CR, CO, and AV, which demonstrate very low indices in some of the sections and high indices in the others. On the contrary, measured values related to MM, SP, SC, and WV characterize consistent and healthy structural state of concrete.

Table 5.14 Condition Indices of SPTW

Defect Section	MM	SP	SC	CR	CO	AV	WV
1	90	88	82	17	88	85	89
2	45	90	85	95	77	87	70
3	85	89	88	95	70	90	40
4	45	88	85	23	90	88	85
5	47	85	90	10	89	84	50
6	88	90	90	95	70	85	35
7	90	87	84	95	90	90	45
8	85	90	87	95	68	82	12
9	48	89	90	14	85	82	88
10	87	88	82	86	77	85	65
11	82	85	89	90	30	81	50
12	87	90	89	20	90	90	80
13	65	90	84	88	88	84	87
14	67	84	90	56	72	90	33
15	70	87	85	10	87	89	81
16	90	88	88	89	65	80	88
17	70	86	90	22	87	84	90
18	43	84	88	16	72	88	82
19	47	90	90	16	40	84	84
20	75	84	86	20	85	90	81
21	48	87	82	95	90	90	88
22	65	82	90	56	77	87	88
23	63	90	85	20	74	89	90
24	81	85	87	33	63	82	87

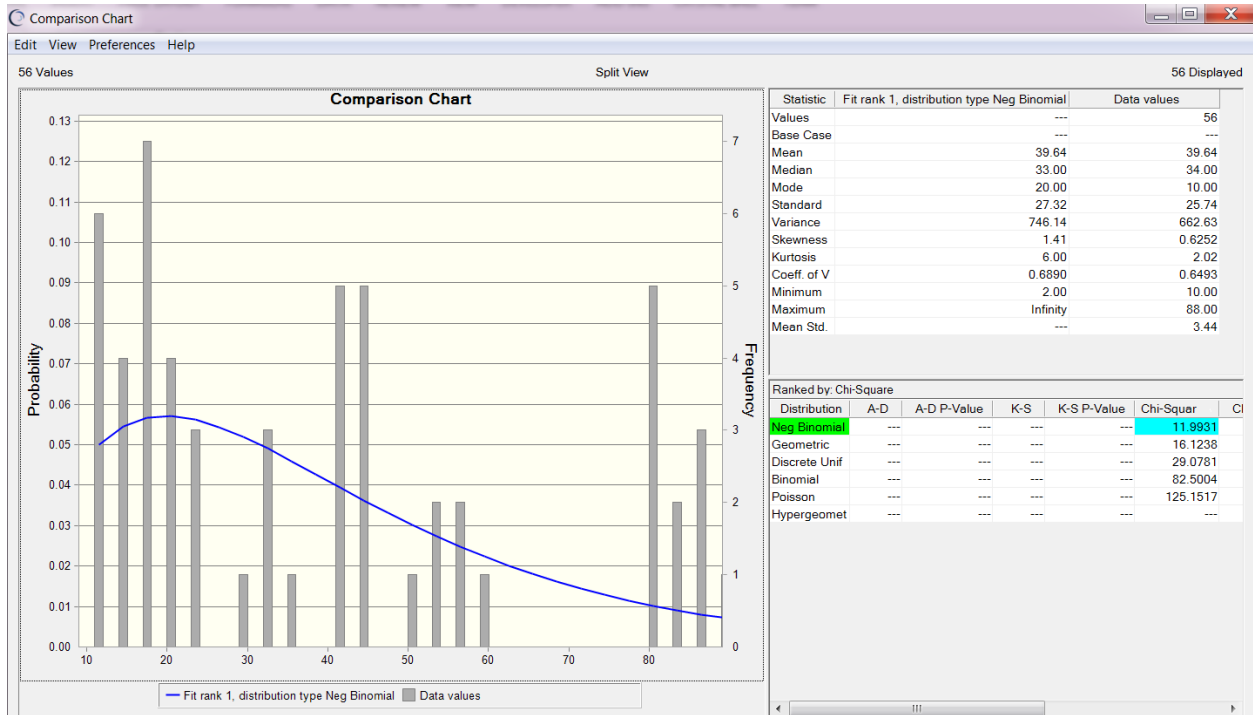
Table 5.15 Condition Indices of SPTS

Defect Section	MM	SP	SC	CR	CO	AV	WV
1	82	87	90	95	77	89	84
2	90	88	87	95	82	70	86
3	89	84	89	33	69	90	70
4	84	82	90	36	30	45	88
5	84	90	90	50	32	50	84
6	85	90	84	92	19	87	90
7	90	83	86	94	35	87	89
8	81	82	88	91	22	82	90
9	80	86	82	95	78	90	85
10	89	87	84	91	83	75	85
11	88	84	82	40	41	80	75
12	82	85	90	46	49	10	82
13	90	84	88	53	58	77	90
14	82	87	83	88	30	80	84
15	81	90	86	87	59	82	87
16	87	88	90	95	15	81	85
17	83	87	82	95	50	90	88
18	82	90	85	89	85	78	90
19	90	90	84	53	42	87	60
20	85	84	89	73	49	50	90
21	81	85	89	40	66	95	87
22	90	88	81	87	65	87	85
23	88	80	82	87	60	88	84
24	87	83	89	90	30	82	85
25	88	90	89	90	45	87	90
26	85	82	87	92	86	30	90
27	84	88	90	66	60	60	80
28	89	83	86	60	51	90	89
29	90	89	85	66	72	90	85
30	90	85	86	95	71	84	83
31	82	90	90	93	87	84	82
32	87	84	89	93	40	85	90

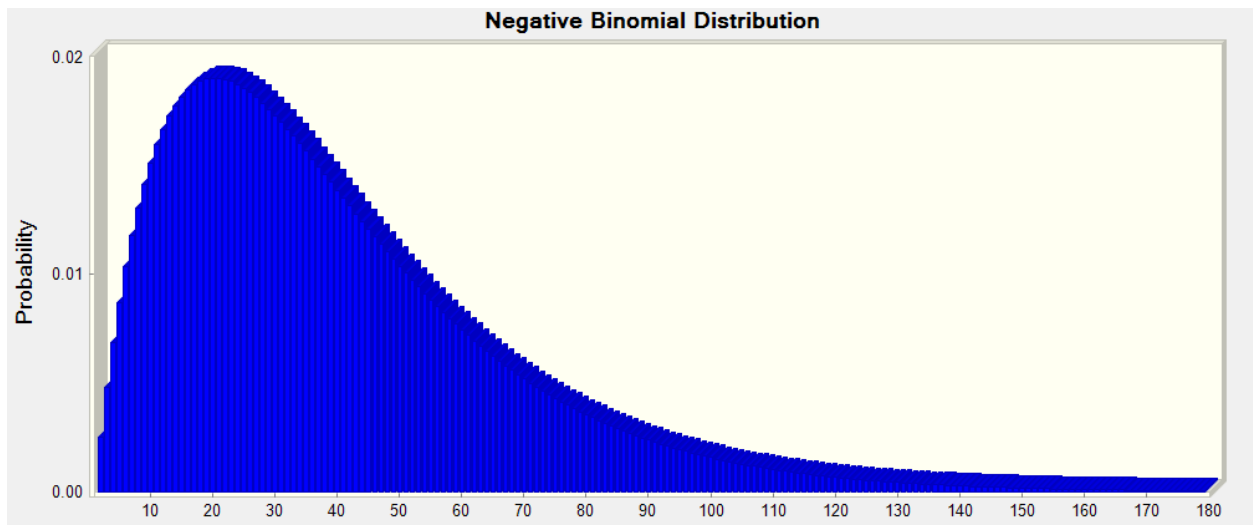
5.7 Integrated Defect-Based Condition Assessment Model

5.7.1 Defect Condition Assessment using Simulation

The defect condition assessment model was executed in ORACLE® Crystal Ball software by exploiting the embedded key metrics. A total of 48 Excel spreadsheets were prepared, each spreadsheet comprised the indices of one defect in each element. For example, one spreadsheet was generated for each defect (column) from Table 5.9 to Table 5.15. This is followed by defining the input variables, represented as defect's indices to the Crystal Ball engine and determining their range. After introducing these inputs to the Crystal Ball application, the assumption was defined by conducting a fit distribution test for the data. The software would report the probabilities of occurrence of various possible results. In parallel, the goodness of fit statistics would automatically emerge in a list form, ranking the outcomes from the best to the worst fit according to Chi-Square test, accompanied by a comparison chart. Hence, the best fit distribution could be recognized with the lesser Chi-Square value. The list also displayed statistic values of different attributes, such as the mean, standard deviation, skewness, kurtosis, coefficient of variation, etc. Figure 5.45 provides an illustrative sample of the results accomplished by the model. This sample is related to the probability distribution analysis of moisture marks (MM) in FPTV. It could be noted from Figure 5.45(a) that many statistical attributes were generated along with their values. Moreover, six distributions were produced and sorted from the best to the worst as Negative Binomial, Geometric, Discrete Uniform, Binomial, Poisson, and Hypergeometric Distribution respectively. Because the Negative Binomial distribution presented the least Chi-Square value of 11.9931, it was chosen as the best fit distribution for MM data points as shown in the comparison scheme incorporated in Figure 5.45(a). The Negative Binomial 3D distribution pattern is illustrated in Figure 5.45(b).



(a)



(b)

Figure 5.45 Probability Distribution Analysis of MM in FPTV (a) Statistics and Comparison Chart; (b) Best Fit Distribution

Then, an output variable for the simulation was identified as the defect condition index. Crystal Ball forecasts were defined for this variable by correlating input and output data. At the final stage, the number of simulation trials was determined to be 10000, and the predictor was set for running

the simulation. Each simulation round lasted for 18 seconds in average, during which around 570 random numbers/second were generated. Next, the forecast diagram was interpreted versus several quality metrics. Furthermore a sensitivity analysis was performed to determine which of the variable inputs is causing the preponderance of variance in the output. In the case of undesirable recorded outcomes, the simulation was reiterated. This procedure was repeated in order to select the defect condition index in accordance with the least coefficient of variation and mean standard error. The precision of forecast statistics was recorded as 95% percentile. Figure 5.46 depicts the prediction results for the aforementioned MM sample.

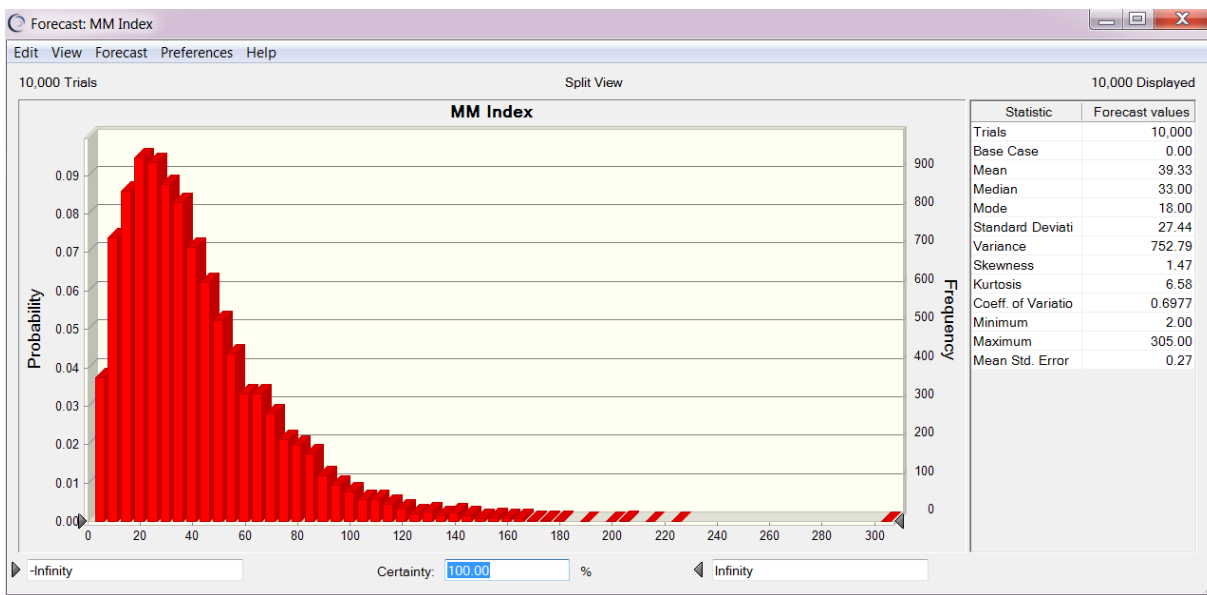


Figure 5.46 MM Condition Index Chart

Table 5.16 summarizes the results obtained from the simulation model. It is clear that the Negative Binomial distribution is dominating most of the events of the model, followed by Discrete Uniform, Geometric, Poisson, Binomial, and Hypergeometric, as they achieved 44%, 19%, 15%, 10%, 8%, and 4% respectively. The table recorded the least Chi-Square value of 0.0678 while fitting the Negative Binomial distribution to MM input variables in OSW2, whereas the largest Chi-Square was 71.3057 represented by the Geometric distribution of SP in OSS. The table also

indicated that the least coefficient of variation and mean standard error were found in forecasting the SP defect in FPTV as they accounted for 0.0198 and 0.02 respectively. However the largest coefficient of variation and mean standard error were found to be 1.01 and 0.73 respectively in forecasting the WV defect in SPTW. Lastly, the analysis results revealed that the crack in OSW1 scored the best defect index of 91.38, while the worst case scenario was recorded as 29.05 for CO distress in OSW2.

Table 5.16 Condition Indices of Defects

System Element	Defect	Distribution	Chi Square Test	Coeff. of Variation	Mean Std. Error	Defect Index
FPTV	MM	Neg. Binomial	11.9931	0.6977	0.27	39.33
	SP	Hypergeometric	1.4833	0.0198	0.02	88.00
	SC	Binomial	1.6120	0.0321	0.03	86.40
	CR	Binomial	50.5012	0.0818	0.07	89.82
	AV	Discrete Uniform	40.2719	0.4778	0.24	49.96
	WV	Neg. Binomial	33.6375	0.3322	0.22	66.09
VSS	MM	Poisson	53.9631	0.1158	0.09	76.18
	SP	Neg. Binomial	37.3917	0.5576	0.30	54.37
	SC	Neg. Binomial	1.4099	0.0296	0.03	87.07
	CR	Discrete Uniform	40.9444	0.4414	0.25	55.73
	CO	Neg. Binomial	12.5584	0.2737	0.18	65.16
	AV	Geometric	66.0121	0.9889	0.61	61.71
	WV	Discrete Uniform	35.9259	0.3946	0.22	55.03
OSW1	MM	Geometric	5.9881	0.9799	0.58	59.66
	SP	Discrete Uniform	11.9561	0.5252	0.26	49.86
	SC	Neg. Binomial	11.4998	0.4311	0.31	72.44
	CR	Hypergeometric	1.4939	0.0499	0.05	91.38
	CO	Poisson	0.4836	0.1305	0.08	58.49
	AV	Geometric	8.5638	1.00	0.62	61.71
	WV	Neg. Binomial	0.6522	0.4203	0.25	58.39

Table 5.16 Condition Indices of Defects (Continued)

OSW2	MM	Neg. Binomial	0.0678	0.9832	0.41	41.40
	SP	Neg. Binomial	0.0769	0.0491	0.04	85.90
	SC	Discrete Uniform	5.3187	0.0710	0.06	81.56
	CR	Geometric	3.5842	0.9981	0.59	58.97
	CO	Neg. Binomial	2.1347	0.6974	0.20	29.05
	AV	Binomial	0.0937	0.1234	0.08	61.82
	WV	Neg. Binomial	0.7283	0.6977	0.37	53.23
OSS	MM	Neg. Binomial	14.7163	0.6856	0.25	37.06
	SP	Geometric	71.3057	0.9725	0.59	60.55
	SC	Neg. Binomial	46.0383	0.4885	0.32	66.50
	CR	Discrete Uniform	39.7292	0.4959	0.26	52.54
	CO	Neg. Binomial	9.6190	0.4799	0.24	49.86
	AV	Neg. Binomial	50.7186	0.0997	0.09	85.32
	WV	Discrete Uniform	15.5704	0.4919	0.25	50.05
SPTW	MM	Neg. Binomial	2.5216	0.2496	0.17	69.35
	SP	Binomial	1.7312	0.0287	0.03	87.32
	SC	Neg. Binomial	0.8341	0.0364	0.03	86.89
	CR	Geometric	5.9712	0.9746	0.50	51.72
	CO	Poisson	2.1061	0.1150	0.09	75.98
	AV	Discrete Uniform	0.5056	0.0371	0.03	84.96
	WV	Geometric	10.7279	1.01	0.73	71.90
SPTS	MM	Discrete Uniform	4.0365	0.0371	0.03	84.96
	SP	Neg. Binomial	1.3417	0.0369	0.03	86.05
	SC	Neg. Binomial	1.8190	0.0378	0.03	86.61
	CR	Poisson	33.6248	0.1156	0.09	76.44
	CO	Neg. Binomial	1.7065	0.4273	0.23	54.77
	AV	Poisson	18.6695	0.1135	0.09	76.15
	WV	Neg. Binomial	6.3698	0.0734	0.06	84.80

5.7.2 Fuzzy-Based Condition Index

The condition index model was developed based on the Fuzzy Set Theory and fuzzy estimation technique, to enable encoding the defects symptoms into a condition index while dealing with the ambiguity and imprecision. Thus, the ultimate goal of creating this model is to establish a knowledge-based expert system capable of generating a database without the vagueness and subjective judgment. The indices of this database were computed via the fuzzy arithmetic rules inherent in the fuzzy inference system. The first step in building the fuzzy expert system was designing the model structure, which involved introducing seven input variables and one output variable to the Fuzzy Inference System (FIS) editor. Input variables encompass surface and subsurface defects, i.e., MM, SP, SC, CR, CO, AV, and WV. While the output variable is exemplified by the condition index (CI).

In the second step, fuzzy inference functions were adjusted such as the AND/OR method, besides the defuzzification method that was set as the centroid. The inputs were fuzzified by means of assigning the type and number of membership functions (MFs) for each distress. As displayed in Figure 5.47, all the inputs were assigned four MFs except the rebar corrosion input that was designated three, whereas MFs allocated to the output variable were five. All the aforementioned MFs were of trapezoidal type scattered on a range from 0 to 100. Later, 136 fuzzy If-Then rules were constructed in the rule editor. Input values were mapped to rules values that were in turn mapped to output values. A defuzzification and aggregation of output values resulted in crisp condition indices. The crisp input/output values produced in this model will be exploited to develop the upcoming model that is based on the Adaptive Neuro-Fuzzy Inference System (ANFIS).

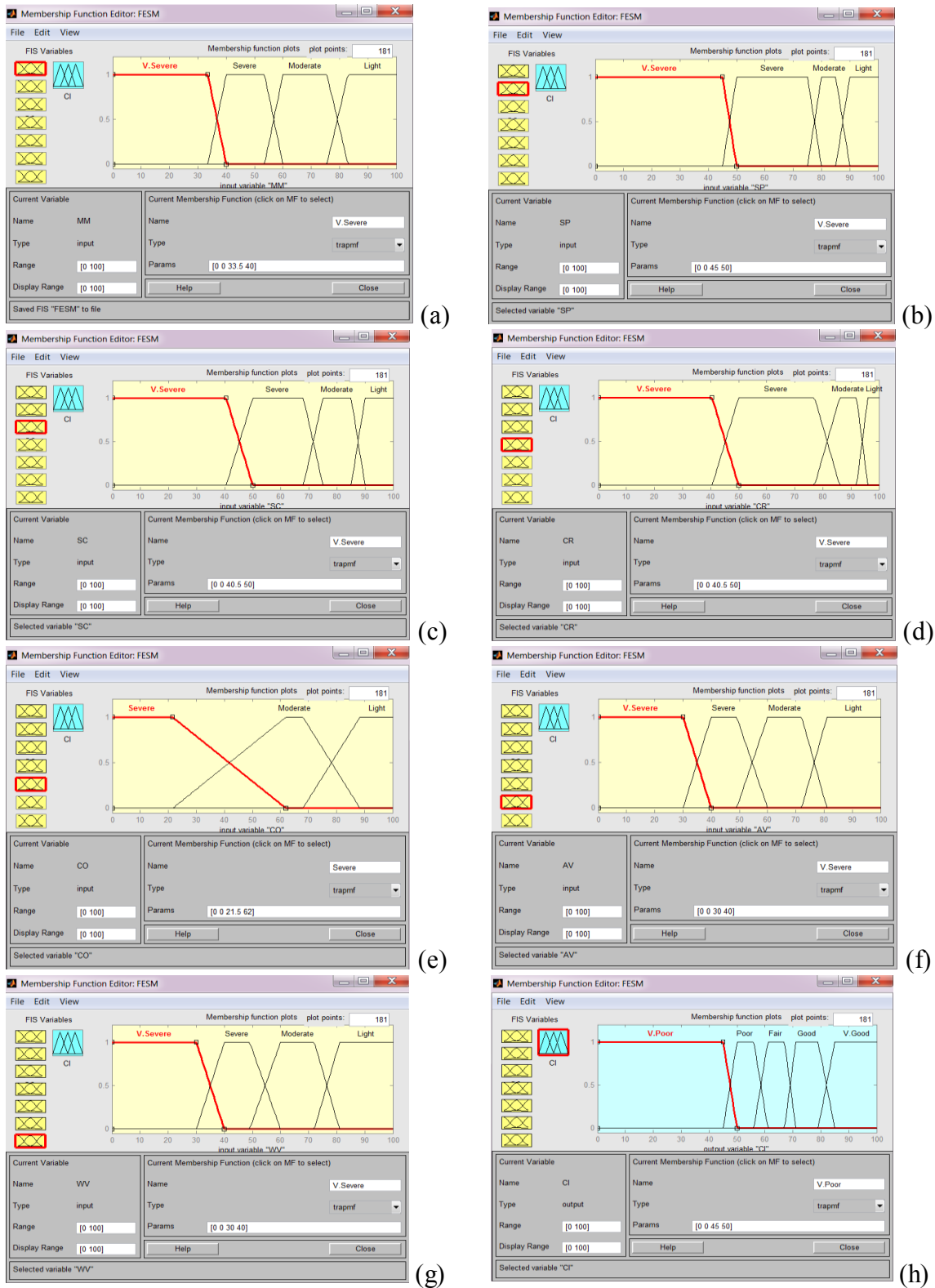


Figure 5.47 Inputs and Output Membership Functions (a) MM; (b) SP; (c) SC; (d) CR; (e) CO; (f) AV; (g) WV; (h) CI

5.7.3 Element Condition Index using Neuro-Fuzzy

In order to corroborate the performance of the previous model (fuzzy-based condition index model), another model was developed through the hybridization of ANNs and fuzzy logic. The efficacy of the synergic outcome could be utilized to predict the element condition index on the basis of an optimization technique. Therefore, the aforementioned steps delineated in Figure 3.27 were applied in MATLAB® R2013b by using the Neuro-Fuzzy design. After distributing the data into three sets and uploading them into the ANFIS editor, the grid partitioning technique was selected to cluster the data. An Excel spreadsheet was prepared to include 1872 data points. A sample of entry data to the ANFIS operator is shown in Table 5.17.

Table 5.17 Sample of Entry Data

MM	SP	SC	CR	CO	AV	WV	CI
22.8	88.4	85.3	72.1	90.3	72.7	71.1	46.9
88.5	90.6	90.0	45.4	78.7	79.0	80.2	57.7
44.3	89.9	85.6	72.4	60.2	93.8	42.0	73.8
56.0	42.1	60.7	44.4	75.6	55.5	69.3	37.6
80.7	69.4	34.4	88.0	40.9	23.6	55.1	41.3
62.2	73.7	77.0	54.2	55.4	88.1	90.0	67.5
77.4	20.5	45.5	61.3	63.1	30.4	29.6	33.7
35.6	55.3	26.8	39.7	77.5	21.2	90.9	45.4
91.0	32.2	55.9	27.8	38.0	66.3	75.7	46.1
15.9	78.8	17.1	90.7	87.8	90.4	35.0	47.0
90.3	70.1	80.4	88.8	90.7	78.2	90.2	82.6
85.4	90.0	90.7	93.2	80.3	90.6	90.5	84.9
27.7	82.2	59.6	64.9	32.0	89.1	45.0	43.8
74.0	70.4	35.8	90.7	66.6	49.7	77.8	39.4
62.1	34.5	87.2	68.6	79.4	50.0	81.4	47.1
27.2	61.6	37.0	14.1	88.5	79.8	57.9	46.7

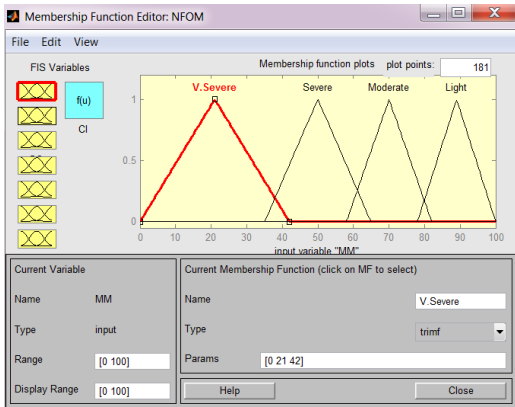
Next, it was essential to determine some aspects related to training the model. There exist two training modes; hybrid and backpropagation. In this research, the hybrid method was chosen in the training phase since it combines several estimation paradigms. Moreover, the number of epochs was identified as it plays a great role in preventing the overfitting while training the network. As the neuro-fuzzy engine is set for training, the produced error increases. However, the system utilizes the checking dataset to test the performance of the model at each epoch. Hence, the training will come to a halt as soon as the error starts escalating. Following the training phase, the model was tested consecutively versus the training, testing, and checking datasets, while recording the error related to each dataset. Multi neuro-fuzzy networks were formed through which numerous configurations for the type and number of MFs were tested. Eventually, the results of different neuro-fuzzy networks together with the computed errors were compared and listed, as illustrated in Table 5.18 that shows a sample of these models. As can be noted, the triangular and trapezoidal were the only types of membership functions that resulted in rational and rigorous outcomes. The error generated in each network is calculated by measuring the average of the squares of errors between the estimated and actual value of the output and using Equation (3.11). 3D surface views were produced at the end of each network assembly. The surface view shows how robust is the liaison between the inputs and the output. It is a sort of sensitivity analysis that displays the behavior of the output when one or more of the input variables are changed. Therefore, the positive patterns of surface views were taken into consideration, while the negative schemes were precluded and deemed rejected. Subsequent to the training and testing of as many as 120 networks, a procedure was conducted to compare the results of multi-configurations and select the best network on the basis of its performance to fulfill the two conditions of; 1) least mean square error (MSE), 2) generating the positive 3D surface view.

Table 5.18 Comparison of Multi Networks Results

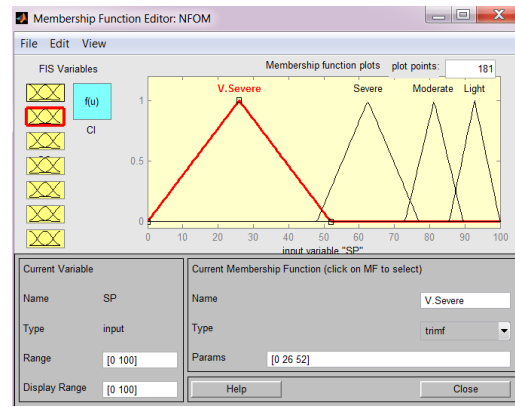
Network No.	Membership Function	No. of Membership functions							Error				3D Surface View Result
		MM	SP	SC	CR	CO	AV	WV	Training	Testing	Checking	MSE	
1	Triangular	4	4	4	4	4	4	3	1.72	1.70	1.92	1.80	X
2	Triangular	4	3	4	4	4	4	4	1.62	1.88	6.90	2.44	✓
3	Triangular	4	4	3	4	4	4	4	1.69	1.75	1.80	1.72	✓
4	Triangular	4	4	4	3	4	4	4	1.70	1.73	1.75	1.71	X
5	Triangular	4	4	4	4	3	4	4	1.69	1.88	1.85	1.74	✓
6	Triangular	4	4	4	4	4	3	4	1.65	1.79	5.88	2.49	X
7	Triangular	4	4	4	4	4	4	4	1.68	1.72	1.75	1.70	✓
8	Triangular	4	3	4	3	4	3	4	1.75	1.92	6.90	2.88	X
9	Triangular	3	4	3	4	3	4	3	1.56	2.00	2.20	1.72	X
10	Triangular	4	4	5	4	4	4	4	1.63	1.97	1.71	1.69	X
11	Trapezoidal	4	4	4	4	4	4	4	2.25	1.65	1.83	1.82	✓
12	Trapezoidal	3	4	3	4	3	4	3	1.64	1.97	1.71	1.70	X
13	Trapezoidal	4	4	4	4	4	3	4	1.62	1.75	5.40	2.50	X
14	Trapezoidal	4	4	4	4	3	4	4	1.55	6.08	1.71	2.25	X
15	Trapezoidal	4	3	4	4	4	4	4	1.56	2.00	2.20	1.72	✓
16	Trapezoidal	4	4	4	3	4	4	4	1.72	1.74	1.80	1.76	✓
17	Trapezoidal	4	4	4	4	4	4	3	1.70	1.80	1.72	1.75	X
18	Trapezoidal	3	3	3	3	3	3	3	1.69	1.73	1.75	1.71	X
19	Trapezoidal	4	4	3	4	4	4	4	1.72	1.70	1.80	1.85	✓
20	Trapezoidal	5	4	5	4	4	4	4	1.75	1.63	6.73	2.45	X

Finally, network number 7 was selected as it produced a schematic presentation and attained the lowest MSE of 1.70 as shown in Table 5.18. This optimal network is of a triangular type and incorporated four membership functions for each of the distresses. Each distress was clustered in a range of 0 to 100 into very severe, severe, moderate, and light as depicted in Figure 5.48.

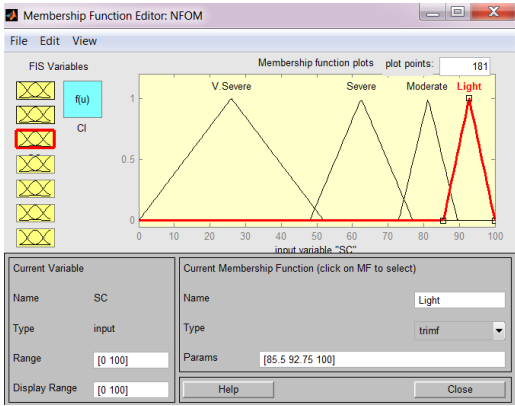
Several 3D surface views were extracted for the optimal model to reveal the sensitivity of the output variable when two input variables were changed. Figure 5.49 presents three of the generated surfaces. Figure 5.49(a) probes the changes effect of MM and SP parameters on the element CI. The figure demonstrates that the lowest values of MM and SP result in a low CI value, yet the surface shows a significant up rise when the MM percentages surpass 25, whereas the sharp increase in the CI occurs when SP depth exceeds 40cm. According to Figure 5.49(b), the CI rises dramatically as the CR width reaches 50mm. This is not the case regarding the CO distress since it shows a smooth transition of its values with respect to the CI values. The graph in Figure 5.49(c) looks symmetrical when the impact of AV values and WV values are compared versus the CI values. The 3D visualization scheme indicates that AV/WV values of 80% create a flat transit area in the center of the scheme. Exceeding this limit for both of the defects shows a substantial rise in the CI value subsequently. Generally, the surface representations illustrate proportional escalation of the output value in relation with the corresponding escalation of input values.



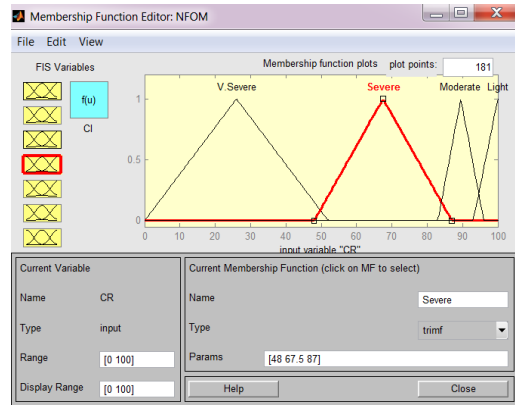
(a)



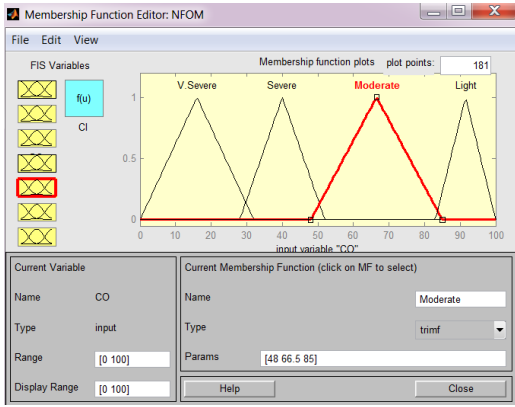
(b)



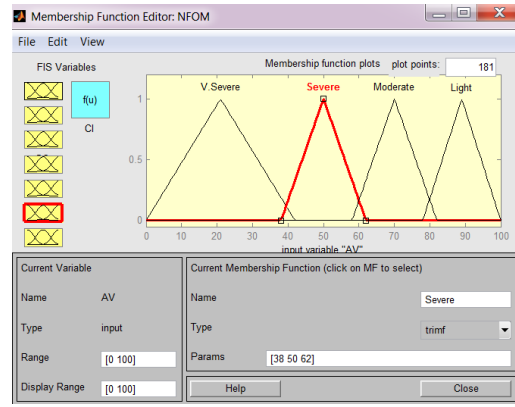
(c)



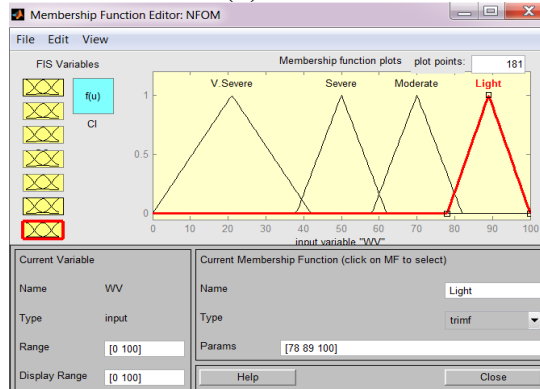
(d)



(e)



(f)



(g)

Figure 5.48 Inputs MFs of the Selected Network (a) MM; (b) SP; (c) SC; (d) CR; (e) CO; (f) AV; (g) WV

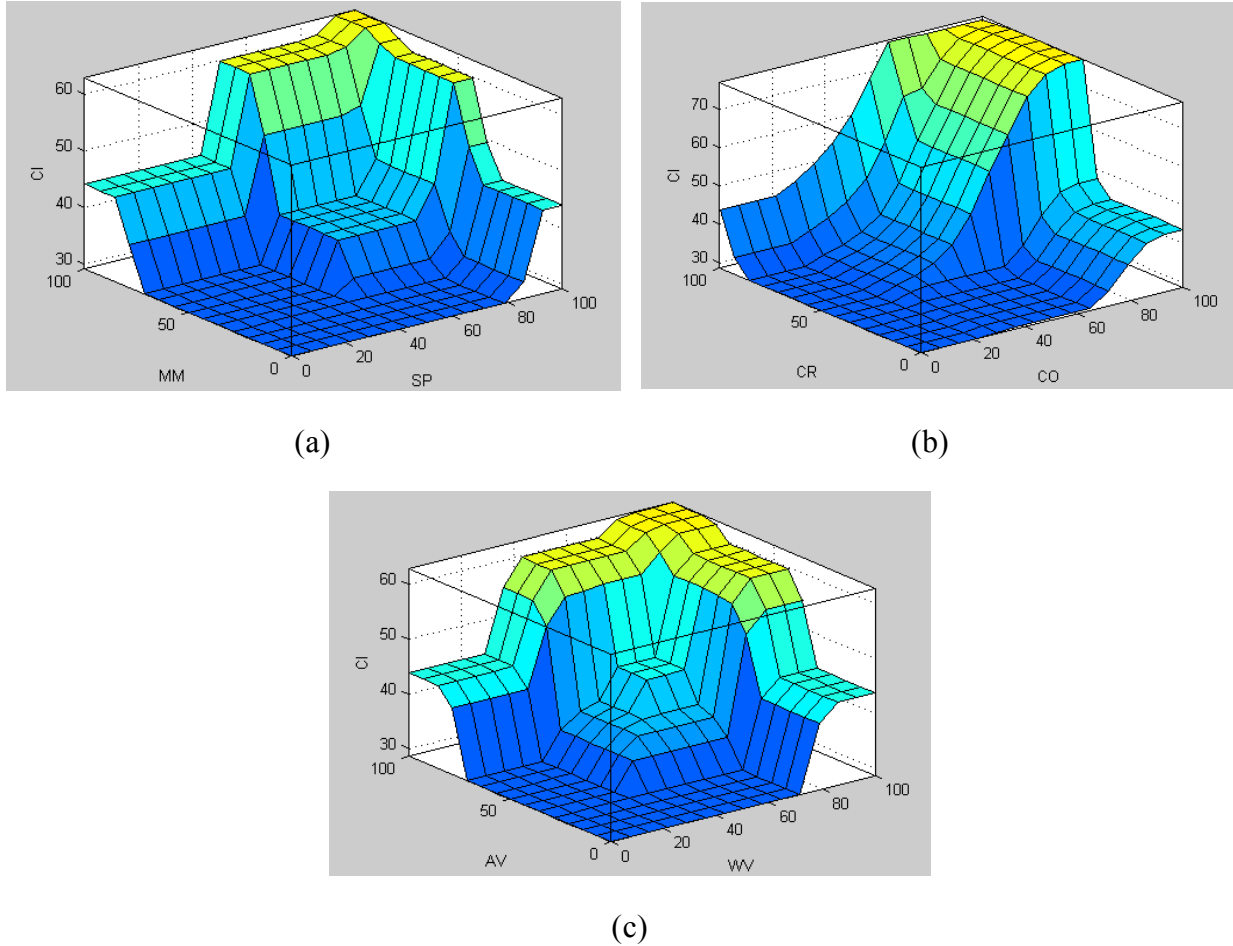


Figure 5.49 3D Surface Presentations (a) MM and SP Versus CI; (b) CR and CO Versus CI; (c) AV and WV Versus CI

The last stage involves the prediction of elements' condition indices using the Neuro-Fuzzy model. After introducing the defects indices of subway elements to the selected model, the forecasted values were produced as displayed in Table 5.19. The elements' condition indices in the table reflect different conditions in Montréal subway, ranging from sound concrete in the tunnel inter St. Laurent and Place-des-Arts to very poor in Outremont station. The good state of concrete is represented by the SPTW index of 74.8 and FPTV index of 69.7, which ensure the durability of concrete in these two components, whereas the OSW2 displays the worst index of 35.1. This very poor state of concrete is attributed to the concealed defects, also confirmed by the images that demonstrate various manifestations of distresses such as loopholes, MM, and severe chemical

attack. The other two indices of 51.9 and 54.4 in OSW1 and OSS respectively reveal serious structural mechanisms that may cause a premature degradation of the concrete structure in Outremont station. The rest of the cases are represented by 68.3 and 67.3 indices in VSS and SPTS respectively that show fair and moderate conditions of concrete in these two elements.

Table 5.19 Predicted Condition Indices for Subway Elements

Defect Element	MM	SP	SC	CR	CO	AV	WV	Element CI
FPTV	39.3	88.0	86.4	89.8	90.0	50.0	66.1	69.7
VSS	76.2	54.4	87.1	55.7	65.2	61.7	55.0	68.3
OSW1	59.7	49.9	72.4	91.4	58.5	61.7	58.4	51.9
OSW2	41.4	85.9	81.6	59.0	29.1	61.8	53.2	35.1
OSS	37.1	60.6	66.5	52.5	49.9	85.3	50.1	54.4
SPTW	69.4	87.3	86.9	51.7	76.0	85.0	71.9	74.8
SPTS	85.0	86.1	86.6	76.4	54.8	76.2	84.8	67.3

5.7.4 Integrated Subway Condition Index

To extrapolate one index number that describes the condition of the subway network, the proposed methodology illustrated in Figure 3.28 was applied. The results from the previous model were fused to compute the subway index. For this purpose, the fuzzy algorithm inherent in the fuzzy logic design of MATLAB® R2013b was utilized. The first step in constructing the fuzzy consolidation model was designing its configuration, which involved defining seven input variables and one output variable in the fuzzy operator as illustrated in Figure 5.50. Therefore, the

elements' condition indices were defined as CI 1, CI 2, CI 3, CI 4, CI 5, CI 6, and CI 7. While the subway condition index was named as SCI.

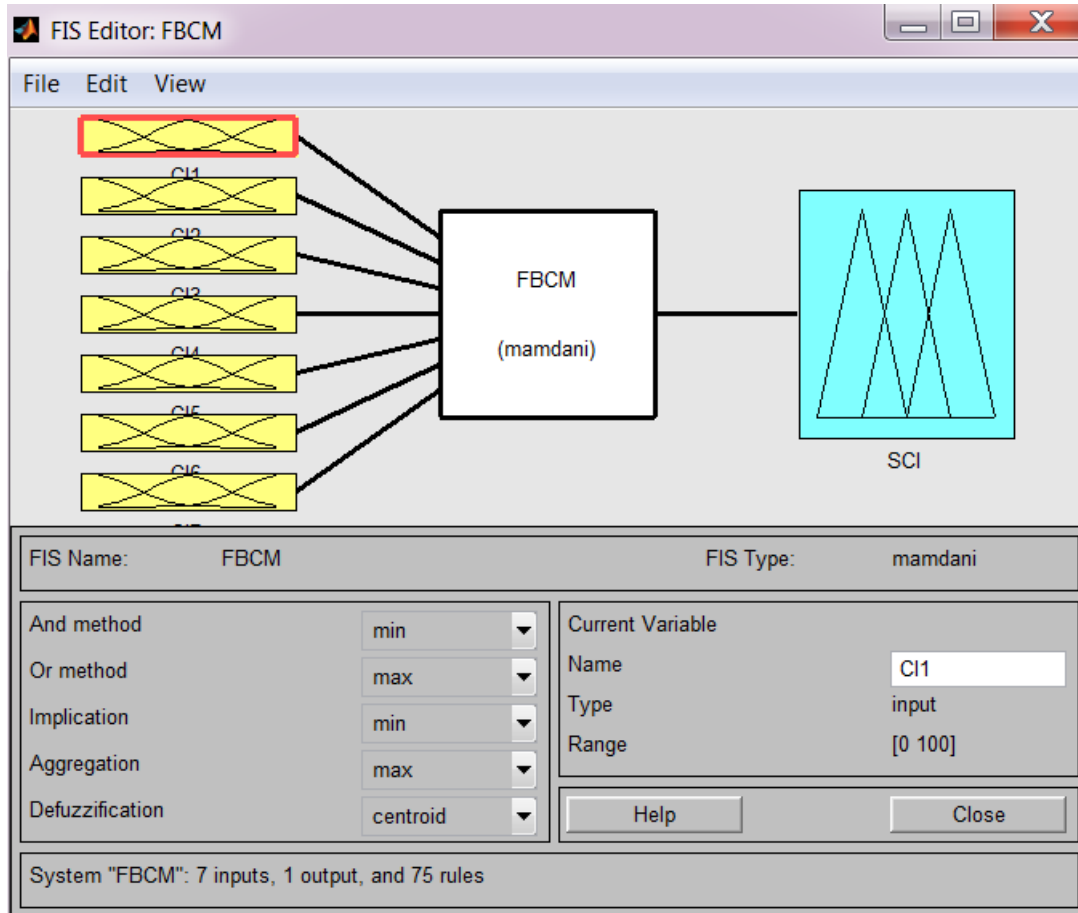


Figure 5.50 Fuzzy Consolidation Model Configuration

Next, membership functions (MFs) were designated using the 0-100 scoring range. Five MFs were allocated to each of the input/output variables. The MFs characterize five states of concrete; very poor, poor, fair, good, and very good. In this concern, the trapezoidal type of MFs was applied to all the variables incorporated in the model, including the output variable. MFs were extracted from the expert knowledge of regulations. The consolidation system functions by means of 75 rules as indicated in Figure 5.50. The elements' condition indices were combined with the rules that are based on the human expertise. Then, the rules were aggregated and de-fuzzified to generate a crisp

number, which is the subway condition index. Figure 5.51 depicts a sample of fuzzy rules implication. The figure shows that the elements' condition indices as inputs to the fuzzy consolidator have resulted in a subway condition index of 61.6. This index reveals a fair condition for Montréal Metro network.

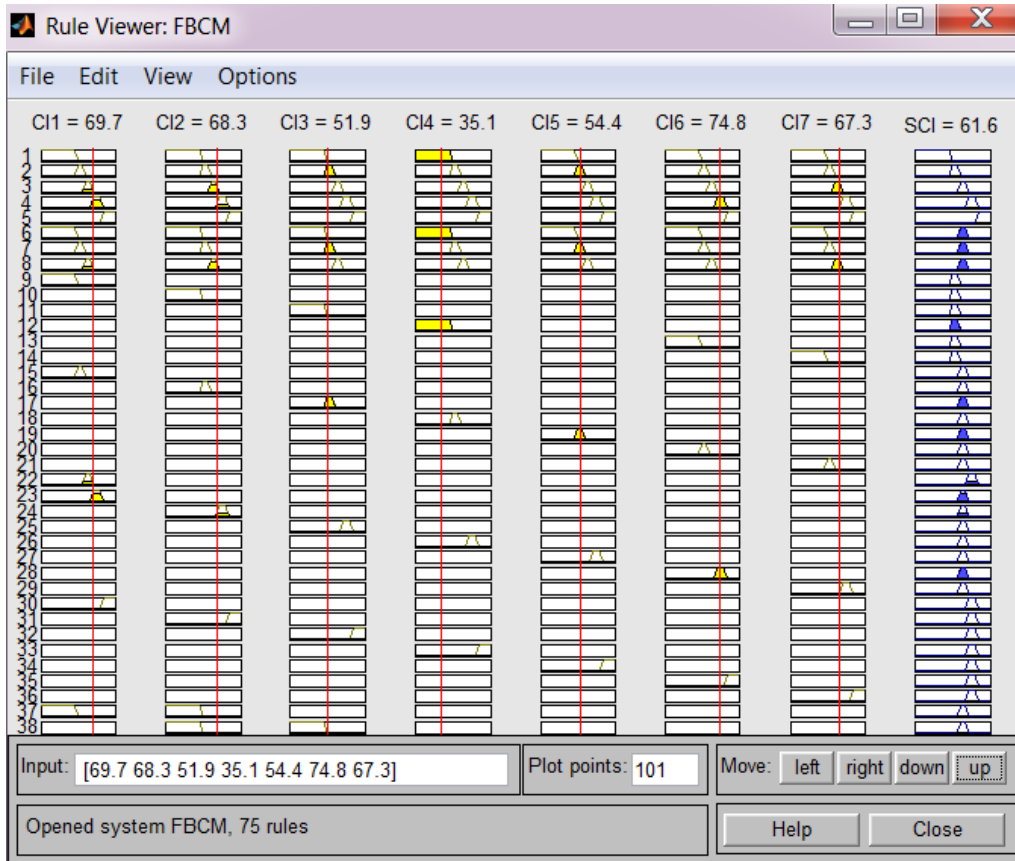


Figure 5.51 Fuzzy Estimator for Subway Condition Index

5.7.5 Sensitivity Analysis

A sensitivity analysis process was carried out to study and verify which of the seven studied elements has big influence or sensitive to the overall subway condition. To accomplish this, Table 5.19 with its predicted element condition indices was set up as a baseline scenario, to be followed by creating multiple different scenarios. In each scenario, all the element condition indices were

kept fixed, except for one element, which was changed in accordance with a specific percentage, and the overall subway condition was computed accordingly. Therefore, each scenario entailed changing the index of one element only. The mathematical form of the sensitivity analysis is defined in Equation (5.13).

$$CI_{dev_{e_n}} = \frac{\{CI_{New_{e_n}} - CI_{baseline_{e_n}}\}}{CI_{baseline_{e_n}}} \quad (5.13)$$

Where, $CI_{dev_{e_n}}$ is the condition index percentage deviation of element n in a certain scenario from the baseline, $CI_{New_{e_n}}$ is the new condition index of element n, $CI_{baseline_{e_n}}$ is the baseline condition index of element n.

The series of scenarios proceeded later in the same manner but involved changing one element's condition index according to a different percentage and calculating the overall subway condition for each case and so on. The calculated percentage for each scenario was plotted versus the change in subway condition percentage using a Spider Chart as shown in Figure 5.52.

Analyzing Figure 5.52 indicates that the subway condition is mostly influenced by OSW2 as it demonstrates a 76% change in metro condition. This percentage is noticed to be quite distant from the percentage of next element, represented by 55% in OSW1. Nevertheless, the graph reveals that OSS has almost the same sensitivity of 50% as the preceding element. The SPTS scores the fourth position as it displays a 31% variation in subway condition. The next sensitive element identified in the graph is the VSS that accounts for 23%, followed by FPTV that alters the subway condition by 19%. The least of these elements to influence the subway condition is shown to be the SPTW since it results in only a 3% variant. The sensitivity analysis of the subway condition with respect to all elements' conditions proves the soundness of the Integrated Subway Condition model.

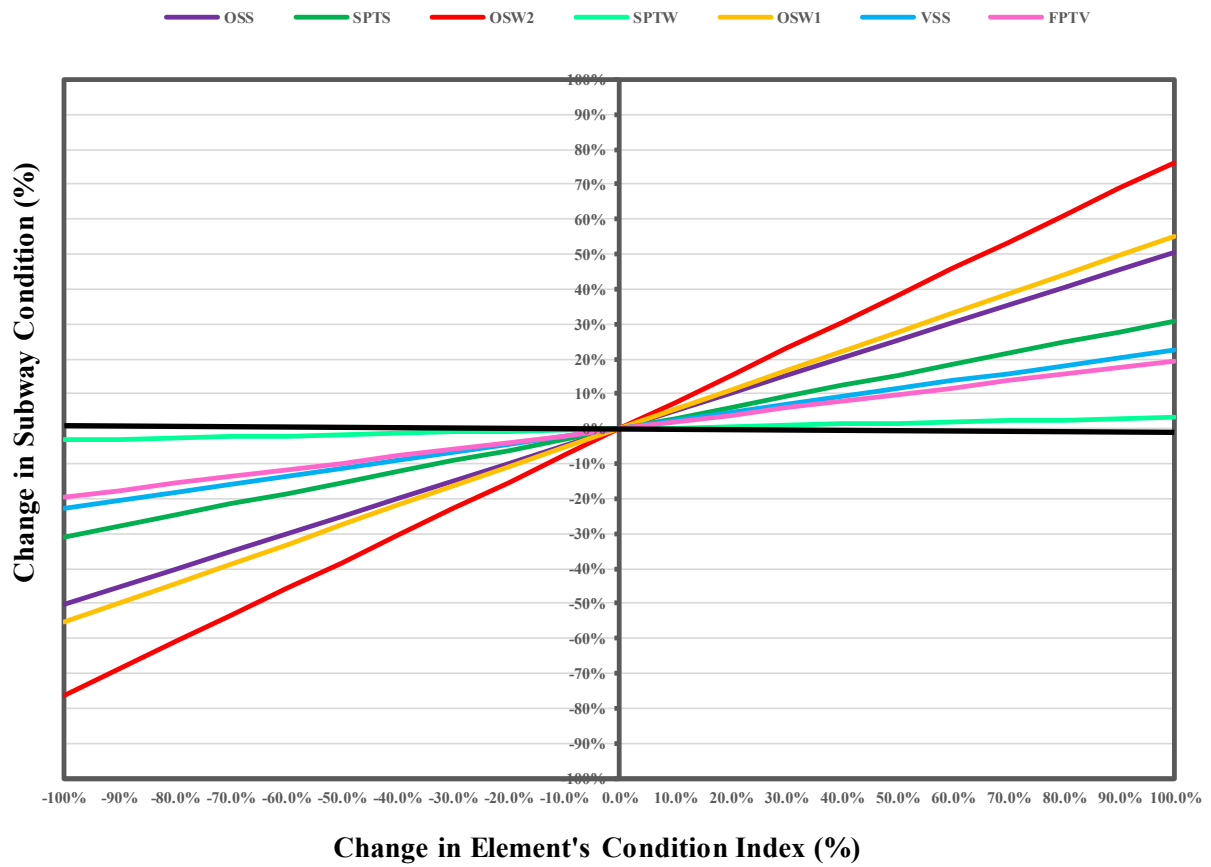


Figure 5.52 Sensitivity Analysis using Spider Chart

CHAPTER 6: AUTOMATED TOOL

This chapter entails the automation process for the proposed methodology presented in chapter 3. Figure 6.1 depicts the generic architecture of the process, which comprises three phases. In the first phase, the data are acquired through accessing images from the hardware (e.g., cameras, videos, computers), and the software packages. Followed by the automation phase that involves, exploring the data, discovering multi algorithms, analysis process, and algorithm tailoring and development. And finally, the final product will be shared with the professionals and experts in the form of documentation or automated vision application. Therefore, the spotlight will be shed on the second phase, which features the automated tool.

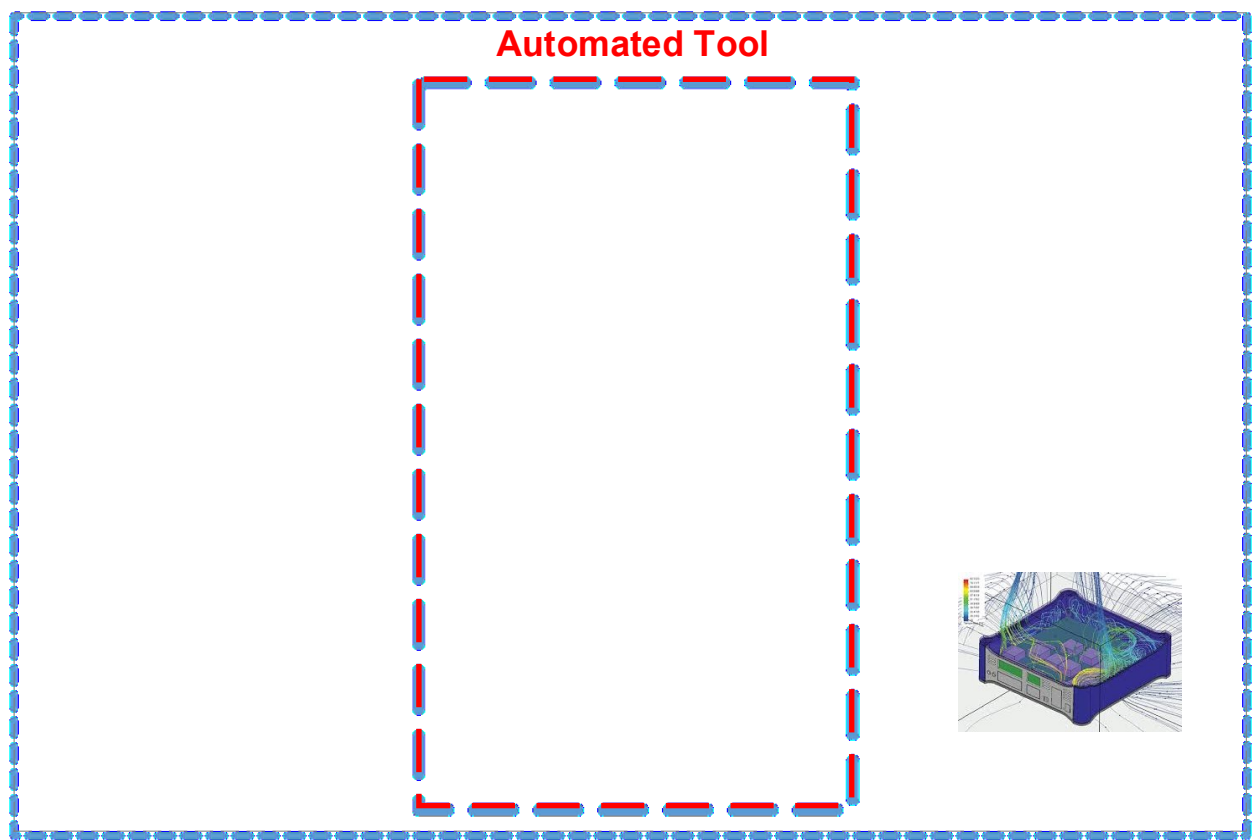


Figure 6.1 Workflow of the Automation Process

The automated tool is a three-tier procedure, which corresponds to the three main models developed in this research. The first tier pertains to the image processing application of the surface defect-based assessment model, in addition to the machine learning toolboxes. This application requires coding the proposed image processing algorithms in MATLAB® as a scripting language. The second tier is related to the subsurface defect-based assessment model; it demonstrates the main parameters and the structure organization of the two software involved in this application. The third tier tool shows the calculation sheets of the integrated defect-based condition assessment model along with defining the computation attributes.

6.1 MATLAB Coding for Surface Defects

6.1.1 Unique Properties of Moisture Marks and Algorithm Coding

Moisture marks are visible stains that appear in widely-spaced isolated patches or sizeable patches covering large areas. These distresses possess unique properties that differentiate them from other concrete surface defects. Such properties include color, texture, frequency and edge information. Color and texture have always been considered as decisive indicators for object recognition. Moisture marks can be distinguished as dark-colored regions with a unique texture that involves smooth and fine texture, unlike other surface defects such as scaling or spalling, which display a coarse texture in an image. Frequency and edge information are other crucial indicators. The rate of occurrence of wet areas in subway infrastructure is far more than the rest of distresses. In the Montréal subway network, it is quite obvious that these defects dominate the facilities' surfaces, and thus are regarded as the first priority among other defects. Also, they own explicit edges that are dissimilar from the aforementioned defects (scaling, spalling), which demonstrate clear depressions with indistinct boundaries. Therefore, the edge information properties were taken into consideration while assembling the detection algorithm. Also, the camera's high resolution of

2592x3888 pixels was considered while choosing the different related parameters. This algorithm includes image segmentation using Canny edge detection as a powerful algorithm because it delivers one outcome to a single edge (Ding and Goshtasby 2001), morphological filtering as a boundary thickening technique, and a cleaning mask that cleans the noise in the skeleton image. Since moisture marks own clear edges, and all the aforementioned techniques target the defect edges, a specific algorithm was inspired along with the camera configuration. Other physical properties of moisture marks, e.g., geometry could not be considered when selecting the parameter values of the algorithm, because there was no specific geometry that distinguishes moisture marks from scaling and spalling defects.

The Canny edge detection algorithm (Canny 1986) was applied to the grayscale image to detect the edges of wet areas and segment the defect from the background of the image. Several trials for empirical inputs were carried out to fine-tune the parameters of the algorithm and result in segmenting the image. Such trials involved threshold and sigma parameters. Threshold is a two-element vector that is comprised of low and high scalars. By specifying the high scaler, edge utilizes this value to threshold the image, whereas an automatic threshold value of 0.4 is assigned for the low scaler. Subsequent to numerous trials for the high threshold scaler, a value of 0.2 was selected. Likewise, the parameter sigma that represents the standard deviation of the Gaussian filter was tested, and a value of 5 was designated after conducting many tests. For image dilation, a disk template with a diameter of 30 was customized after successive tuning for its parameter. The final stage involved creating a detection filter to be exposed as an overlay of opacity and color overlay on the grayscale image. After several attempts to find the best setting for the opacity parameter, the value of 0.7 was selected. All the aforementioned parameters were determined based on trial-and-error.

The detailed paradigm of moisture marks detection is given in the following Algorithm.

```
togglefig('Original');
rgbImg = imread ('IMG_0974.JPG');
rgbImg = imadjust(rgbImg,[0.24 ; 1],[0.2;0.9]);
imshow(rgbImg)
whos img
exploreRGB(img);
togglefig('Grayscale')
grayImg = rgb2gray (img);
grayImg = 255-grayImg;
h(1) = imshow (grayImg);
Mask = edge (grayImg, 'canny', 0.2, 5);
imshow (Mask)
vs = imgca;
Mask = imdilate (Mask, strel ('disk', 30));
imshow (Mask)
eyeMask = imfill (Mask, 'holes');
imshow (eyeMask);
cc = bwconncomp (eyeMask);
stats = regionprops (cc, 'basic');
A = [stats.Area];
[~, biggest ] = max (A);
eyeMask (labelmatrix (cc) ~=biggest) = 0;
imshow (eyeMask)
togglefig ('Original')
Detection = showMaskAsOverlay (0.7, eyeMask, 'r');
imshow(Detection)
```

Published with MATLAB® R2013b

6.1.2 Scaling Algorithm Coding

The goal of synthesizing this algorithm is to detect scaling distress on the concrete surfaces of subway structures. Scaling defects are recognized as shallow depressions with coarse texture and indistinct boundaries.

The detailed paradigm of scaling detection is given in the following Algorithm.

```
togglefig('Original');
rgbImg = imread ('IMG_0978.JPG');
rgbImg = imadjust(rgbImg,[0.24 ; 1],[0.2;0.9]);
imshow(rgbImg)
whos img
exploreRGB(rgbImg,1)
gLayer = rgbImg ( : , : , 1);
figure
imshow(gLayer)
title ('red Plane');
tunnel = ~im2bw (gLayer,.2);
figure
imshow (tunnel)
togglefig ('Original')
Detection = showMaskAsOverlay (0.7, tunnel, 'r');
imshow(Detection)
```

Published with MATLAB® R2013b

6.1.3 Cracks Algorithm Coding

The algorithm is synthesized to detect cracks distress on the concrete surfaces of subway facilities. This algorithm is tailored specifically to isolate the cracks from the background of the image in accordance to the trial-and-error of the empirical parameters threshold, sigma, disk diameter, and

opacity. Several trials on the empirical inputs resulted in the detection of the open crack inside moisture mark region shown in Figure 4.5(a). The empirical values included threshold of 0.45, sigma of 6, disk template with 10 diameter, and opacity of 0.7.

The detailed paradigm of cracks detection is given in the following Algorithm.

```
togglefig('Original');
rgbImg = imread ('IMG_0974.JPG');
rgbImg = imadjust (rgbImg, [0.24 ; 1], [0.2;0.9]);
imshow (rgbImg)
whos img
exploreRGB (img);
togglefig('Grayscale')
grayImg = rgb2gray (img);
grayImg = 255-grayImg;
h(1) = imshow (grayImg);
Mask = edge (grayImg, 'canny', 0.45, 6);
imshow (Mask)
vs = imgca;
Mask = imdilate (Mask, strel ('disk', 10));
imshow (Mask)
eyeMask = imfill (Mask, 'holes');
imshow (eyeMask);
% togglefig('Out of Noise Segments'); cc = bwconncomp (eyeMask); stats =
regionprops (cc, 'basic'); A
= [stats.Area]; [~, biggest ] = max (A); eyeMask (labelmatrix (cc) ~=biggest)
= 0; imshow (eyeMask)
togglefig ('Original')
Detection = showMaskAsOverlay (0.7, eyeMask, 'r');
imshow (Detection)
```

6.1.4 Regression Analysis for Spalling Quantification

The depth and severity of spalling distress are measured using a novel regression analysis model in conjunction with image processing techniques in intensity curve projection. The model is implemented in MATLAB® by inserting pixel intensities and depth, thereby obtaining the scatter plot and testing the form of relationship that indicates a negative linear relationship. The basic fitting tool offers multiple polynomial function options, as well as plotting the residuals, equation formulation, and data statistics. The top graph in Figure 6.2 shows fitting the data to three polynomial functions, i.e., linear, quadratic, and cubic, along with their corresponding equations, while the bottom graph of the same figure shows the residuals of the three functions. Figure 6.3 illustrates the regression analysis calculation sheet in MATLAB®.

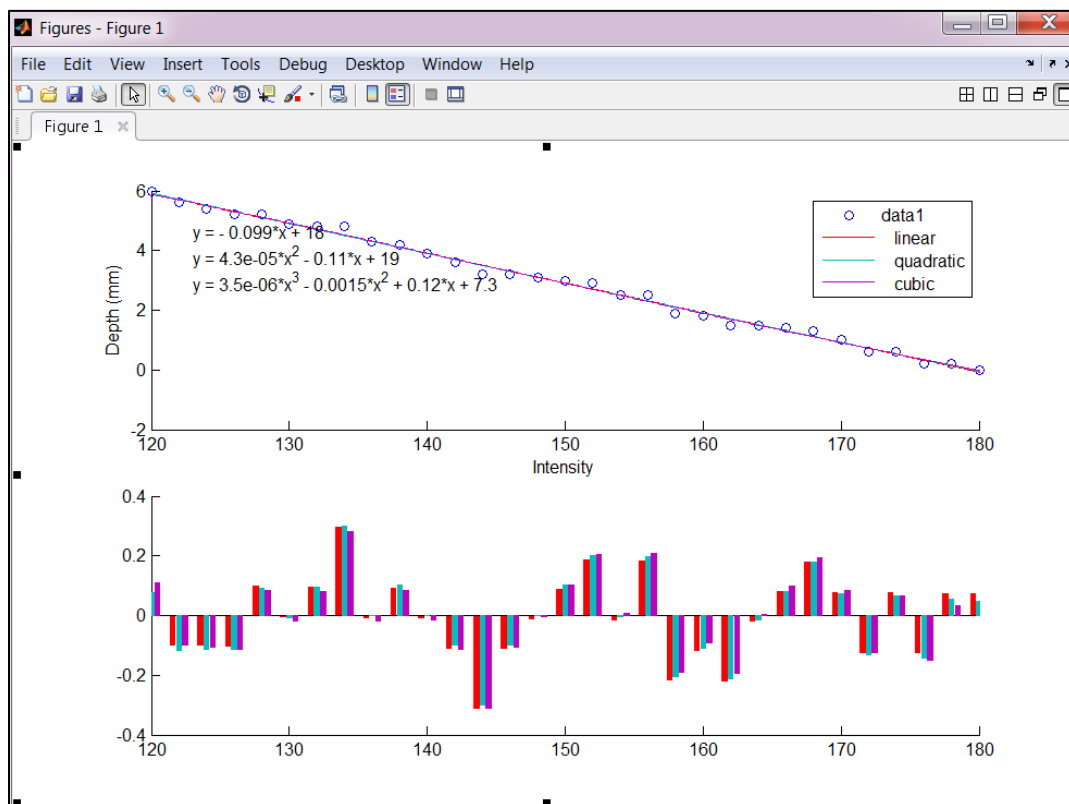


Figure 6.2 Curve Fitting Tool in MATLAB®

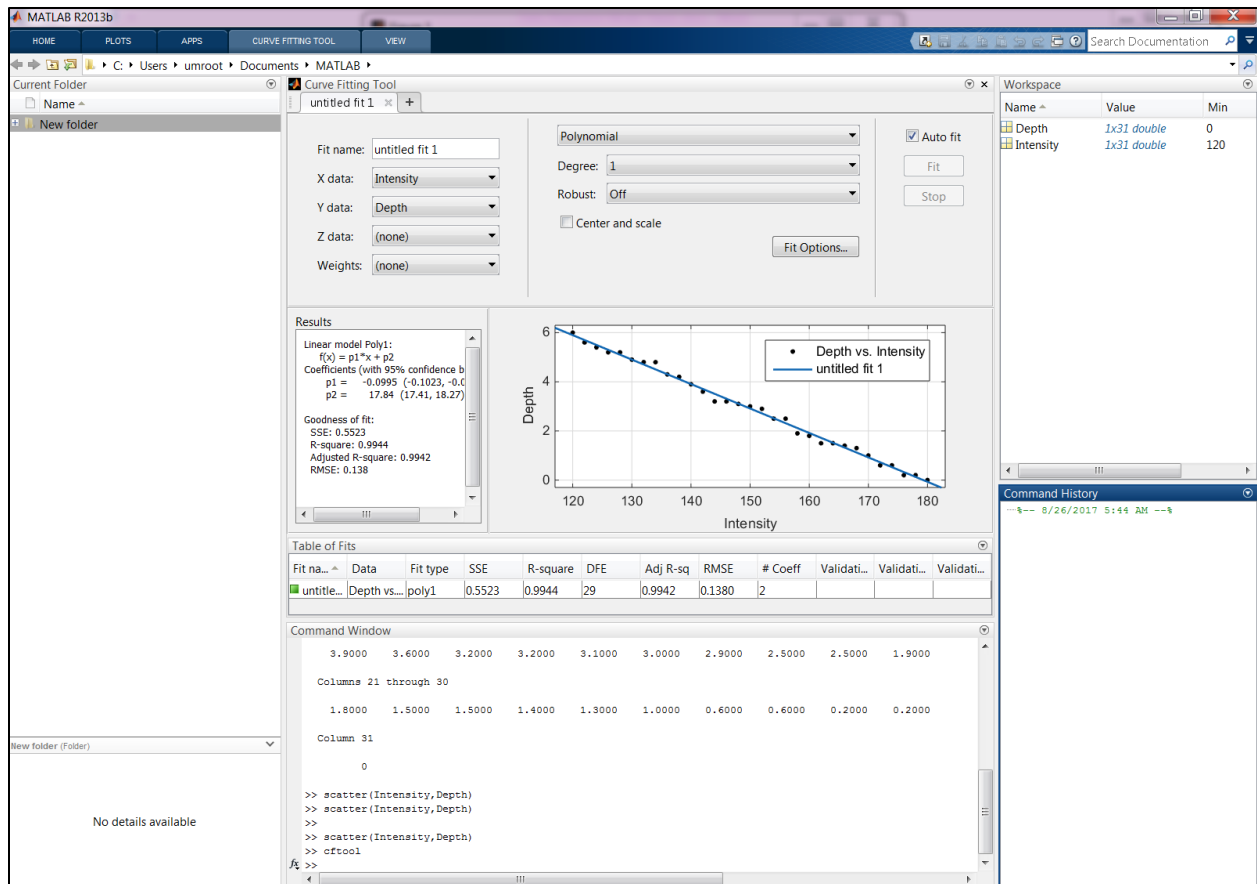


Figure 6.3 Spalling Depth Calculation Sheet

6.2 Subsurface Defects Software Application

Two analysis and mapping software are applied to automate the entire subsurface defect-based assessment model. The automation started by RADAN[®] software, which is the GSSI's state-of-the-art processing software. Its main application is the detection of rebar corrosion in concrete infrastructure. The modular design of this software functions in a user-friendly manner. The batch-processing feature offers a speeding enhancement to repetitive tasks such as the processing of big data. Once the GPR profiles are uploaded to the software, series of interactive operations are performed such as editing the block, picking the target, fixing the width to 1, and displaying the gain. At this stage, the user is able to pick the hyperbolas, which reflect the amplitude of the signal. Then, an ASCII comma-separated value (.csv) file is created. The file contains the scan number,

amplitude, and 2-way travel time for each rebar. This procedure is repeated in the exact way for all the GPR profiles. Figure 6.4 represents a screenshot of the processing procedure.

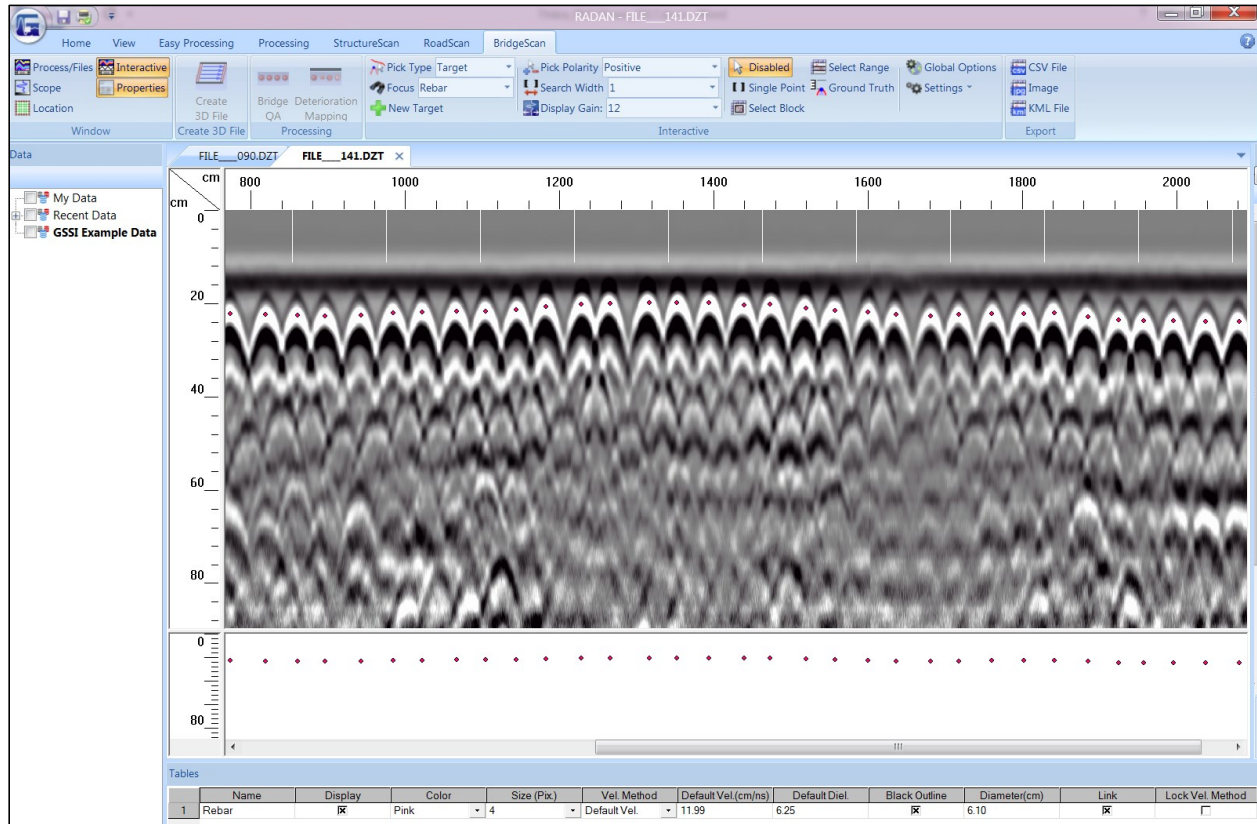


Figure 6.4 Sample of RADAN® Processing Sheet

Afterwards, the output data previously generated are channeled to another software application, namely, GPRApp.exe. The purpose of utilizing this application is to convert the electromagnetic wave unit (millivolt) to disables, as well as, conducting the amplitude depth correction. This procedure requires determining several attributes, such as the number of survey lines, number of scans per profile, length of the profile, starting scanning point, and spacing between each scanning path and another. A calculation process is launched by the software to cluster the data into a predetermined number of groups. Then, the results will be displayed in the form of diagrams together with their corresponding thresholds and the area percentage of each cluster. Moreover, a

membership function of the weighted fuzzy tool incorporated in the software will compute the corrosiveness index of the entry data. It will also provide a suggestion act that can assist the decision-makers in identifying the critical deficiencies in the RC structure. The final step in the post-processing process entails utilizing the Surfer[®] software to create a contour map of the inspected structure. The software adjusts the interpolation and performs gridding computations for various parameters to transform the spatial configuration into a map with different colors and associated scale.

The second automated tool in the subsurface analysis is RADxpert[®] software, which includes a two-tier procedure. The first is the preprocessing of GPR profiles, through which each GPR profile is organized into a 2D grid so that the coordinates and amplitudes are corrected. To be proceeded by applying a differential gain, which is a crucial step as it boosts the profile's resolution and augments the accuracy of interpretation. At this stage, the identification of defects-prone zones and the elimination of unrelated anomalies take place via marking the deteriorated zones with different colors. This is followed by the second procedure, which involves processing GPR profiles and mapping the marked zones to the 2D grid to produce a condition map of the structure. The automated RADxpert[®] tool is shown in Figure 6.5.

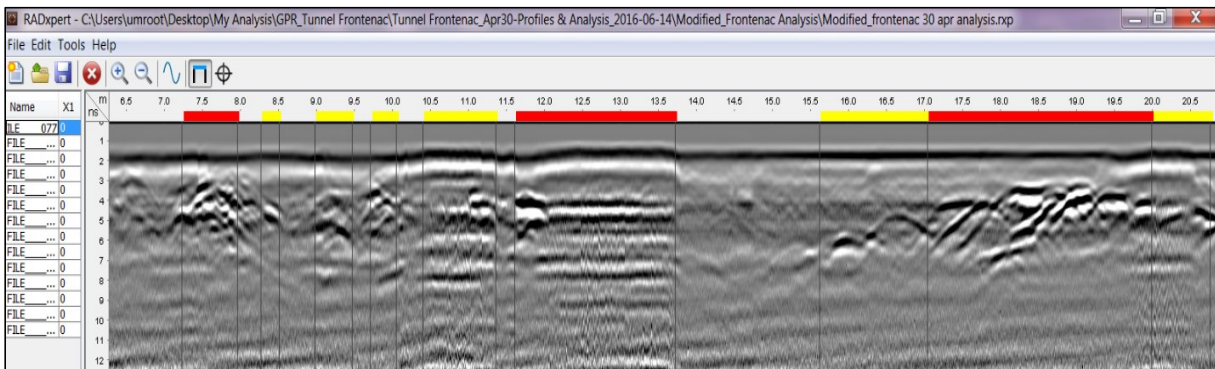


Figure 6.5 Sample of RADxpert[®] Processing Sheet

6.3 Integrated Assessment Software Application

The final stage of the research consolidated the results of four machine learning application tools. The first application tool is the ORACLE® Crystal Ball software whose core functionality is to predict the condition index of each defect in the subway element via simulation. Crystal Ball is an Excel application that is added as a ribbon to the Excel sheet. Once the assumption is defined by selecting a cell in Excel and introducing the defect's indices to the Crystal Ball machine, a sequence of systematic computations are proceeded to generate the best fit distribution. At this stage, the selected cell will turn green, which signifies Crystal Ball's coding for the assumption. Similarly, the forecast should be defined by selecting another cell in Excel. In this case, the cell will turn blue, which is color coding for the forecast. The procedure continues by running the simulation, which takes around 18 seconds/round, during which around 570 random numbers/second are generated. Figure 6.6 illustrates a sample of the Crystal Ball calculation sheet, while the simulation indicators are displayed in Figure 6.7.

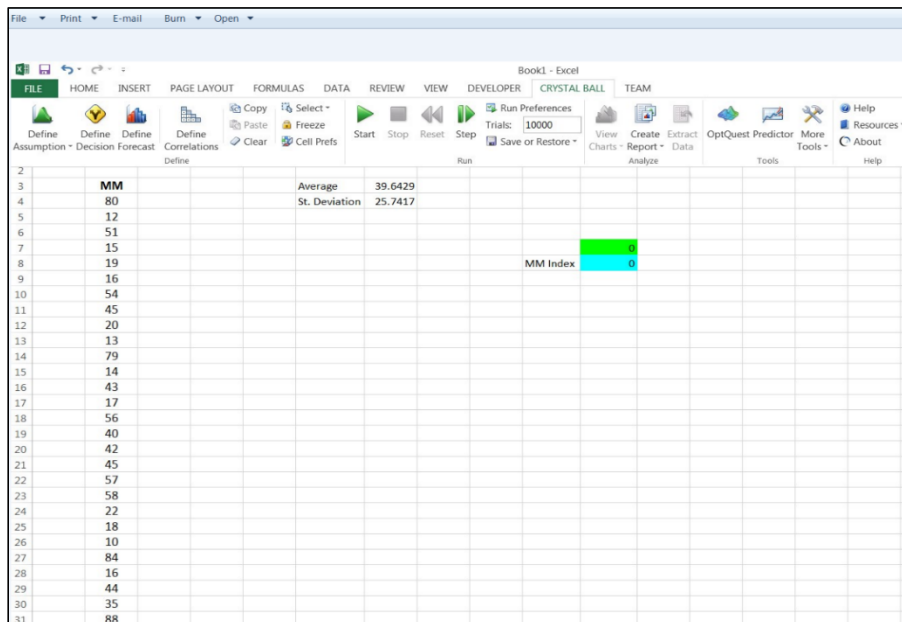


Figure 6.6 Sample of Crystal Ball Excel Spreadsheet

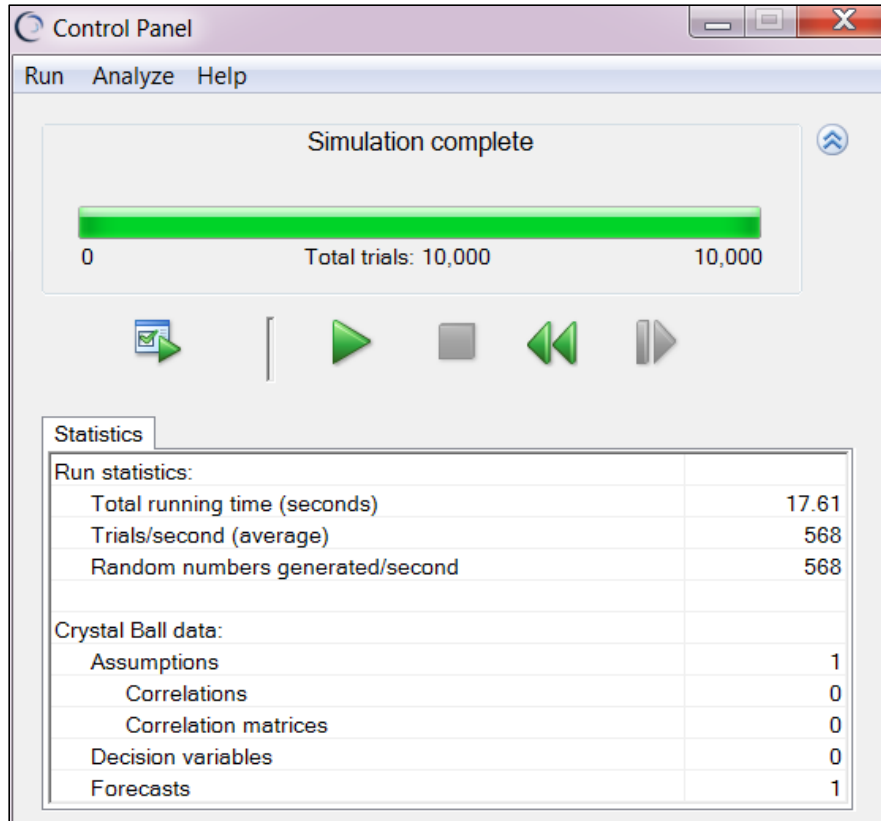


Figure 6.7 Sample of Simulation Statistics

The second machine learning tool provides a user-friendly interface grounded in the fuzzy inference system. This tool is leveraged to develop the fuzzy-based condition index model by defining the seven inputs as the defects and one output as the condition index. The fuzzy rule editor translates the experts' rules and inspection results into condition indices. A total of 136 rules are established to generate the code that facilitates the control and computations. Thus, the output may glide smoothly from the zones that are dominated by the different rules, rather than the acute switching between modes. The output is generated by using the Simulink blocks according to a de-fuzzification computational process, as shown in Figure 6.8.

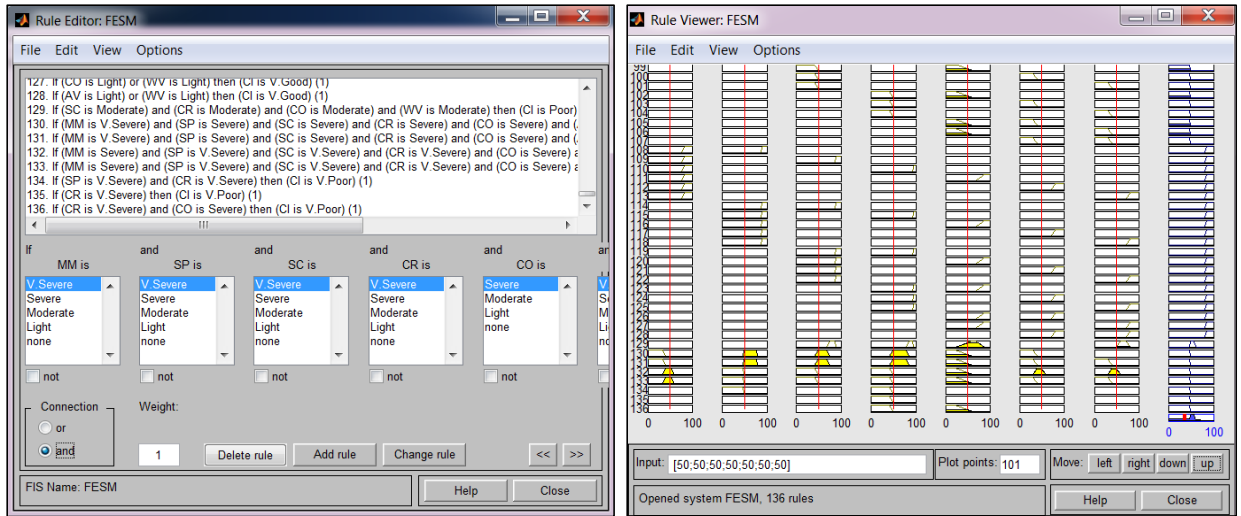
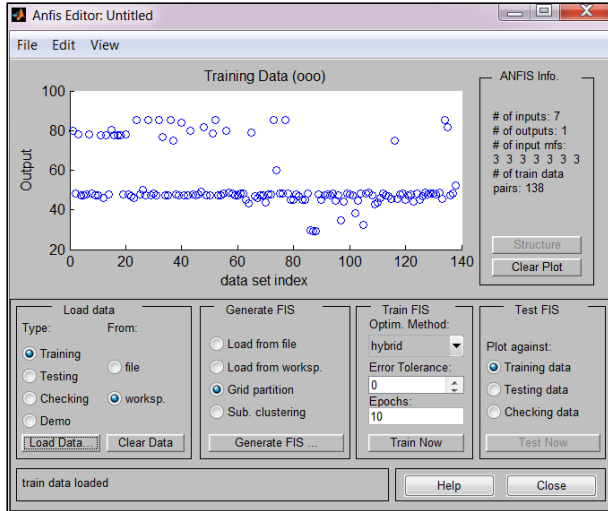


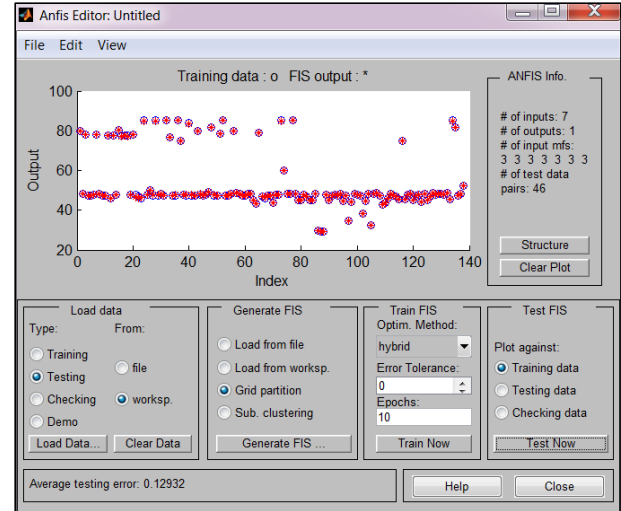
Figure 6.8 Sample Fuzzy Rules Configuration

Third, the element condition index using Neuro-Fuzzy Technique is developed by utilizing the machine learning aspect embedded in the automated tool. The core idea behind creating this model is to predict the element condition index. The system operates in three modes, namely training, testing, and checking. Eventually, the error produced during each of these modes is shown in a scheme. Multi neuro-fuzzy networks are designed and compared against the computed errors. Figure 6.9 depicts the training, testing, and checking modes of a trapezoidal model that incorporates three membership functions for each of the defects.

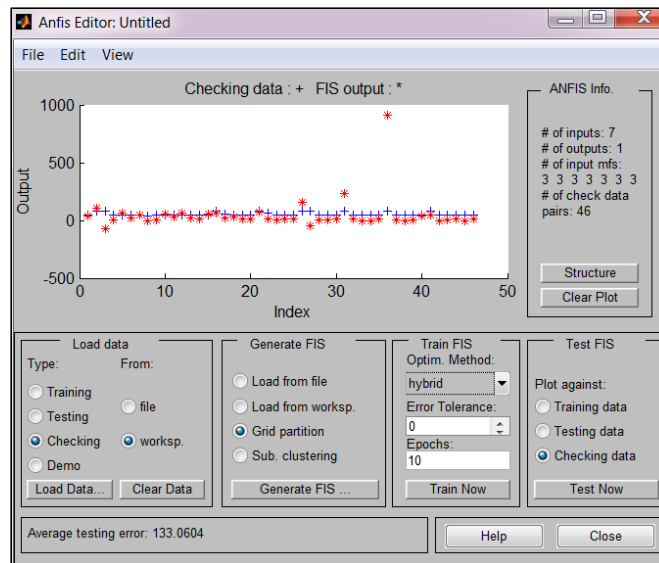
Finally, the fourth application is the consolidation tool, which is based on the Fuzzy Inference System (FIS). This tool is designed by defining seven inputs that characterize the elements' condition indices and one output that portrays the subway condition index. Once the membership functions are assigned to the input/output variables, as well as the 75 rules, the fuzzy estimator commences the aggregation and de-fuzzification procedures to compute the subway condition index. Figure 6.10 represents a sample calculation sheet in MATLAB®.



(a)



(b)



(c)

Figure 6.9 Sample of ANFIS Optimization Scheme (a) Data Training; (b) Data Testing; (c) Data Checking

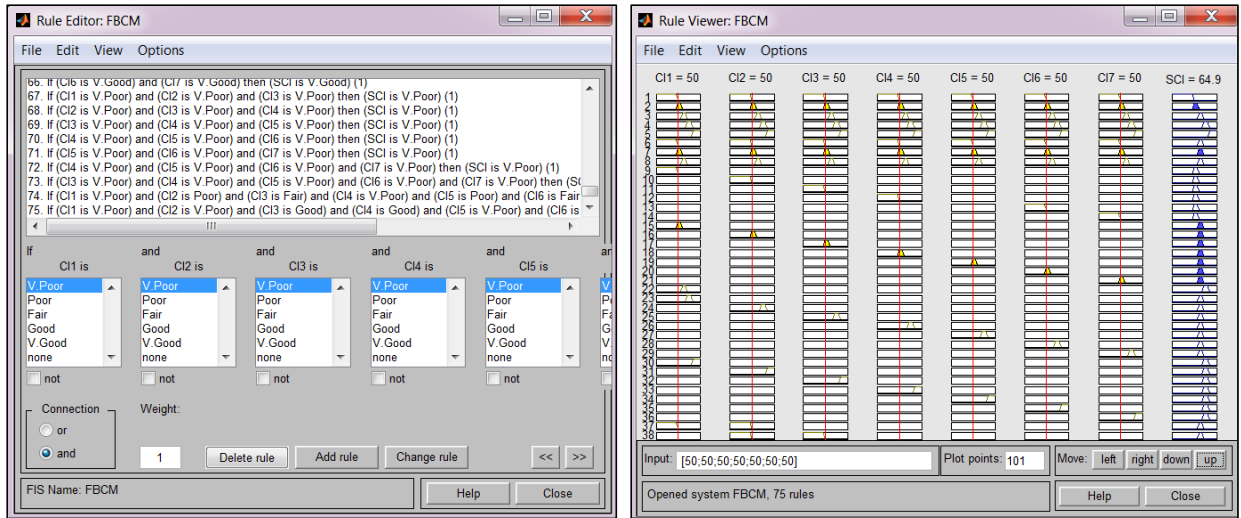


Figure 6.10 Consolidation Model Demonstration

CHAPTER 7: CONCLUSIONS AND RECOMMENDATIONS

7.1 Summary and Conclusions

In the sprawling cities, subway networks play a vital role in the smart mobility of millions of commuters every year. Transit ridership demonstrated an ascending trend in major metropolises in the last decade. In addition to this increase of ridership rate, the facilities in metro network are subjected to harsh environmental conditions, overloading capacity, and aging process. The synergic consequences may cause the degradation and deterioration of the subway facilities. With the high deterioration rates, the pressure has increased on public transit authorities to develop automated tools and new strategies that tackle this critical safety issue; especially during the economic recession that minimized the funding policies. Accordingly, a consistent condition assessment has become a crucial task to ensure the sustainability of the structure. In the literature review, there existed several endeavors to assess the condition of subway systems. Nevertheless, these efforts did not present an integrated framework since they were developed for the evaluation of solely one component instead of the entire network. Some of the models did not consider the structural deterioration over time, others required huge data to be implemented, while the rest could not be validated due to the scarcity of real-life data. The vast majority of these researches failed in evaluating the subsurface defects and/or based on the subjective criteria of the experts' knowledge and judgment. Therefore they could not deliver an accurate estimation of the level of damage in metro systems.

To bridge the gaps in the body of knowledge, an integrated model for the condition assessment of subway networks was developed in this research on the basis of image processing, artificial intelligence, and Non-Destructive Evaluation (NDE) techniques. The integrated model was tested on real-life data, collected from seven systems in Montréal subway network. It developed a

decision support tool, expected to improve the quality of decision making as it can assist transportation agencies in identifying critical deficiencies, and by focusing constrained funding on most deserving assets. As a result, subway facilities can be preserved and maintained more efficiently, leading to significantly reduced life-cycle costs of subway infrastructure.

In the course of this research, three main models were proposed to detect and quantify various surface, and subsurface distresses. The first model incorporated sequential processors for the detection of surface defects, and machine vision algorithms for defects recognition. In this perspective, various spatial domain filters and frequency domain filters were streamlined to detect different surface defects in the subway systems. The core idea behind this technique is to create a complementary scheme of image processing that is effective in de-noising, enhancing, and isolating the object of interest from the background of the image. Moreover, the depth perception of the defect was modeled via an interactive 3D presentation, which is conducive to envisioning the level of severity of the flaw. Then, the information resulted from the processing stage was channeled to various machine intelligence engines, such as the Artificial Neural Networks (ANNs) and Regression Analysis (RA) to develop models capable of quantifying the distresses. Both the ANN and RA models were able to satisfactorily quantify the distresses with an average validity of 96% and 93% respectively.

Prior to developing the second model, a comparative analysis was conducted to select the most appropriate NDE technology for subsurface inspection. As a result, the Ground Penetrating Radar (GPR) was superior to other methods according to the selection criteria. Hence it was exploited to probe the structures using the dual polarization technique. Later, the amplitude analysis was applied, complemented by image-based analysis (IBA) to process GPR profiles and create deterioration maps for the collected datasets. In parallel, the corrosiveness indices were

automatically generated, together with suggesting the course of action or type of intervention needed. Also in this context, a novel subsurface model for the detection and mapping of air/water voids was developed. The model was implemented on a non-reinforced concrete tunnel in Montréal Metro, and validated through numerous tests and techniques, including field inspection, camera images, ground truth coring, infrared thermography (IR), and 3D laser scanning (LIDAR). The validation results confirmed the robustness of the model.

Subsequently, the indices attained from the surface, and subsurface models were embedded into a unified platform, so-called the integrated defect-based condition assessment model, which encompassed four sub-models. The Crystal Ball software that builds on Monte Carlo simulation was leveraged to predict the condition index of each defect in the subway element through an optimization process. Forecast results were validated against several quality metrics and the sensitivity analysis. Afterwards, the fuzzy-based condition index model was configured by decoding the inspection results into condition indices while eliminating the ambiguity and imprecision. The indices of this database were computed via the fuzzy arithmetic rules inherent in the Fuzzy Inference System. The outputs of the previous model were then fed into the neuro-fuzzy engine to develop a model capable of predicting the element condition index. Multi neuro-fuzzy networks were created to test the interactions of different scenarios. Accordingly, the triangular network was selected as it produced a 3D surface view and achieved the lowest MSE of 1.70. This network was utilized to predict the elements' condition indices, which were ranging from sound concrete in the tunnel inter St. Laurent and Place-des-Arts to very poor in Outremont station. In order to compute one index number that describes the condition of subway network; the elements condition indices were fused into the fuzzy consolidator that resulted in a subway condition index of 61.6. Therefore, the integrated model revealed a fair condition for Montréal Metro network.

Finally, an automated tool was presented in a three-tier procedure. The first tier showed the MATLAB® coding for different surface defects. The paradigms for the detection of defects were elaborated in multiple algorithms, in addition to the machine learning toolboxes. The second tier tool involved the key parameters, attributes, and the structure organization of two analysis software that were applied in the processing of subsurface defects. In the third tier, the calculation sheets of the integrated defect-based condition assessment model were displayed along with defining the computation attributes.

7.2 Research Contributions

This research contributes to the body of knowledge by developing a comprehensive framework for the condition assessment of subway networks. The key contributions of the research can be highlighted as the following:

1. An artificial neural network-based model for the detection and recognition of moisture marks defects.
2. A regression analysis-based model for the detection and quantification of spalling and scaling distresses.
3. A complementary scheme for the assessment of concrete surface defects, considering the prioritized surface defects by transit agencies in the US and Canada.
4. An image-based analysis model for the identification and mapping of air voids and water voids in concrete infrastructure.
5. A systematic approach for the evaluation of subsurface defects and generating of deterioration maps using multi-analysis techniques.
6. An integrated framework based on sequential machine learning operations for the condition assessment of subway networks. The merit of the integrated model can be accomplished

by fusing and linking data streams from multiple simulations and optimization systems, such as Crystal Ball, Fuzzy Inference System, and Neuro-Fuzzy Technique.

7.3 Research Limitations

The proposed methodology includes some limitations that might undermine the accuracy of the model. The following features these limitations:

1. This work is based on acquiring close-range images, orthogonal to the surface with appropriate overlapping, which is not the real case scenario in the field. Also, the effect of lighting and shadowing is controlled through using flash photography during image capturing. Failing to consider one or multiple of these factors will yield false and erroneous results.
2. The camera configuration and its related parameters that are utilized in this study are not generic. The selection of these parameters might be changed according to the best case scenario that fits each situation in order to avoid going through the entire image processing.
3. The discoloration of concrete surface is not taken into consideration in the development of the surface defect-based assessment model.
4. The generic subway hierarchy identifies the stations, tunnels, and auxiliary systems. Nonetheless, the auxiliary systems are not involved in the data collection of this research.
5. The image-based analysis of GPR profiles is not a fully automated tool since it necessitates the analyst's interpretation and marking of the deteriorated regions.
6. The automated tool included the coding of surface defects. These algorithms are tailored based on some of the images that are used in the course of this study.

7.4 Recommendations for Future Work

Several interesting and promising topics could be researched in the future. Some of these directions may enhance and ameliorate the current research, while other fundamental challenges are needed to further extend the efficacy and capability of this model. Recommended future topics are listed in the following subsections:

7.4.1 Current Research Enhancement Areas

- In the image preprocessing phase, new detection processors may be probed, such as applying the image sharpening method for scene detection, as well as, investigating other selective filtering in the frequency domain, such as bandpass filters, and notch filters.
- Since delamination is one of the prioritized problems by subway transit agencies as shown in Table 2.2, subway facilities could be inspected by another NDE technology, such as the Impact Echo (IE) in conjunction with the GPR. The IE can identify and characterize the delamination in concrete structures, thereby elevating the coherence of the recent model.
- Apply the reverse time technique for the interpretation of GPR profiles and the detection of subsurface defects. Such technique is based on the Finite Difference Time Domain (FDTD) method that attains the reverse time process of electromagnetic waves. The convolution product of this technique may be utilized to identify the location of even the very small distresses in concrete.
- The model could be enhanced by collecting data from other components, such as the stairs in subway stations, and the components of auxiliary structures, e.g., slabs and walls. In addition, more data may be collected from multiple floors in the stations.

7.4.2 Future Research Extension Areas

- Perform data collection in metro networks using the new generation of inspection systems, such as the fully autonomous robotic system. The robot is a self-localization system that can autonomously maneuver on the slabs of the structure to acquire digital images and conduct NDE procedures. This system may include a surface camera, panoramic camera, GPS, GPR, IE, laser scanner, and electrical resistivity (ER).
- Innovative machine vision-based technologies could be used to probe the walls and vaults of subway facilities. This automated equipment may be mounted on the rail and dragged as it captures surface images. The recorded data are transmitted to the image processing system that is encompassed in the equipment in order to detect the defects and measure the severity of the damage.
- Develop an automated subway management system that is based on the imaging data of NDE techniques. A subway network should be first broken down into its basic elements. Each element is covered by overlapped images, which are then analyzed by multiple image processing algorithms. The resulted information model is transferred and stored in a digital database system. This automated system can be revisited where the data can be retrieved using metadata and compared with former inspection results. Also, the system can be updated on a regular basis, which will optimize the monitoring process. Eventually, this system will enhance the accuracy of the subway condition assessment.
- Create a big data-driven model for subway networks and apply cloud-based machine learning to produce predictive analytics to tackle various asset management problems. Such problems include but are not limited to, forecasting the life-cycle structural performance, predicting the deterioration patterns over time, and the consequent amount

of investments required for future maintenance and rehabilitation. Thus, the merits of subway management programs can be accomplished literally.

REFERENCES

- Abouhamad, M. (2014). "An integrated risk-based asset management framework for subway systems." Ph.D. Thesis, Concordia University, Montréal, QC., Canada.
- Abouhamad, M., Dawood, T., Jabri, A., Alsharqawi M., and Zayed, T. (2017). "Corrosiveness mapping of bridge decks using image-based analysis of GPR data." *Automation in Construction*, 80, 104-117. <http://dx.doi.org/10.1016/j.autcon.2017.03.004>.
- Abu Dabous, S., Alkass, S., and Zaki, A. (2008). "A probabilistic methodology for bridge deck condition assessment." *Journal of Bridge Structures*, 4(1), 49-56.
- Abudayyeh, O., Al Bataineh, M., and Abdel-Qader, I. (2004). "An imaging data model for concrete bridge inspection." *Advances in Engineering Software*, 35(8-9), 473-480. <http://dx.doi.org/10.1016/j.advengsoft.2004.06.010>.
- Abu-Mallouh, M. (1999). "Model for station rehabilitation and planning (MSRP)." Ph.D. Thesis, Polytechnic University, New York, USA.
- ACI (2008). *Guide for conducting a visual inspection of concrete in service*, ACI 201.1R-08, American Concrete Institute Committee 201, Farmington Hills, MI.
- Adhikari, R.S., Moselhi, O., and Bagchi, A. (2013_a). "Image-based retrieval of concrete crack properties for bridge inspection." *Automation in Construction*, 39, 180-194. <http://dx.doi.org/10.1016/j.autcon.2013.06.011>.
- Adhikari, R.S., Moselhi, O., and Bagchi, A. (2013_b). "A study of image-based element condition index for bridge inspection." *Proc., 30th International Symposium on Automation and Robotics in Construction (ISARC 2013)*, Montréal, QC., Canada. <https://pdfs.semanticscholar.org/de84/948f4ac9a819fc6e55728687e3b2d7adbf0b.pdf>.

- Al-Barqawi, H., and Zayed, T. (2006). "Condition rating model for underground infrastructure sustainable water mains." *J. Perform. Constr. Facil.*, 20(2), 126-135.
- Al Lafi, G., Zhu, Z., Dawood, T., and Zayed, T. (2017). "3D thermal and spatial modeling of a subway tunnel: a case study." *Congress on Computing in Civil Engineering, Proceedings (ASCE)*, Seattle, WA, USA. 386-394. <https://doi.org/10.1061/9780784480823.046>.
- Annan, A. P., and Cosway, S. W. (1994). "GPR frequency selection." *Proceeding of the Fifth International Conference on Ground-Penetrating Radar*, Kitchener, Ontario, Canada, 747-760.
- APTA (2016). *American public transportation association ridership report- fourth quarter 2016*. Washington, D.C., USA.
<<http://www.apta.com/resources/statistics/Documents/Ridership/2016-q4-ridership-APTA.pdf>> (June 15, 2017).
- Arndt, R., Jalinoos, F., Cui, J. and Huston, D. (2010). "Periodic NDE for bridge maintenance." *Proceedings of the 13th International Conference of Structural Faults and Repair*, Edinburgh, Scotland, UK.
- ASCE (2017). *2017 infrastructure report card*. American Society of Civil Engineering, <<https://www.infrastructurereportcard.org/cat-item/transit/>> (July 12, 2017).
- Atef, A., Zayed, T., Hawari, A., Khader, M., and Moselhi, O. (2015). "Multi-tier method using infrared photography and GPR to detect and locate water leaks." *Automation in Construction*, 61, 162-170. <http://dx.doi.org/10.1016/j.autcon.2015.10.006>.
- Barnes, C., Trottier, J. F., and Forgeron, D. (2008). "Improved concrete bridge deck evaluation using GPR by accounting for signal depth-amplitude effects." *NDT & E International*, 41(6), 427-433.

- Barraza, G. A., (2011). “Probabilistic estimation and allocation of project time contingency.” *Journal of Construction Engineering and Management*, 137(4).
[http://ascelibrary.org/doi/abs/10.1061/\(ASCE\)CO.1943-7862.0000280#sthash.XhRlIbKI.dpuf](http://ascelibrary.org/doi/abs/10.1061/(ASCE)CO.1943-7862.0000280#sthash.XhRlIbKI.dpuf).
- Barraza, G., and Bueno, R. (2007). “Cost contingency management.” *Journal of Management in Engineering*. 23(3). DOI: 10.1061/(ASCE)0742 597X(2007)23:3(140).
- Bow, S. (1992). *Pattern recognition and image preprocessing*, Marcel Dekker, New York, USA.
- Brandt, E., and Rasmussen, M. H. (2002). “Assessment of building conditions.” *Energy & Build.*, 34(2), 121–125.
- Canny, J.F. (1986). “A computational approach to edge detection.” *IEEE Transactions on Pattern Analysis and Machine Intelligence*, PAMI-8(6), 679-698.
 DOI: 10.1109/TPAMI.1986.4767851.
- Canon (2015). <http://www.canon.ca/inetCA/en/products/method/gp/pid/8256>. (June, 2015).
- Chan, T., Esedoglu, S., Park, F., and Yip, A. (2005). “Recent developments in total variation image restoration.” *Mathematical models of computer vision: the handbook*, Los Angeles, CA., USA. <<ftp://ftp.math.ucla.edu/pub/camreport/cam05-01.pdf>> (June 3, 2017).
- Chatterjee, S., and Hadi, A. S. (2012). *Regression Analysis by Example*, 5th Edition, Wiley, A John Wiley & Sons Inc. Publication, Hoboken, NJ., USA.
- Chaussée, D. (2012). “Montréal’s subway system: challenges with an aging system.” <<https://www.icri.org/EVENTS/Spring12Present/16%20STM%20Montréal%20Subway%20System.pdf>> (June 6, 2013).

- Chen, D., and Wimsatt, A. (2010). “Inspection and condition assessment using ground penetrating radar.” *Journal of Geotechnical and Geoenvironmental Engineering*, 136(1), 207–214.
- Cheng, E., Ryan, N., and Kelly, S. (2012). “Exploring the perceived influence of safety management practices on project performance in the construction industry.” *Safety Science*, 50, 363–369. DOI:10.1016/j.ssci.2011.09.016.
- Chughtai, F., and Zayed, T. (2007). “Sewer pipeline operational condition prediction using multiple regression.” *International Conference on Pipeline Engineering and Construction*, Boston, Massachusetts, USA. [https://doi.org/10.1061/40934\(252\)18](https://doi.org/10.1061/40934(252)18).
- CIRC (2016). Canadian Infrastructure Report Card,
<http://www.canadainfrastructure.ca/downloads/Canadian_Infrastructure_Report_2016.pdf>
(May 26, 2017).
- Daniels, D. J. (2008). “Ground Penetrating Radar” In: Skolnik, M. I. (Editor), *Radar Handbook*, McGraw Hill, New York, 21.1–21.41. http://airspot.ru/book/file/961/radar_handbook.pdf.
- Dawood, T., Zhu, Z., and Zayed, T. (2015_a). “An image-based data model for subway condition assessment.” *Proc., The International Construction Specialty Conference*, Vancouver, BC, Canada.
- Dawood, T., Zhu, Z., and Zayed, T. (2015_b). “Automated recognition of surface defects in subway systems.”, *Proc., The Fourth International Conference on Soft Computing Technology in Civil, Structural and Environmental Engineering*, Civil-Comp Press, Stirlingshire, UK. DOI:10.4203/ccp.109.13.

- Dawood, T., Abouhamad, M., Shami, A., Zayed, T., and Dinh, K. (2015_c). “Progrès récents dans la cartographie de la corrosion des dalles de pont en béton.” *Proc., 22e Colloque Sur la Progression de la Recherche Québécoise Sur les Ouvrages d'art*, Quebec, QC., Canada.
- Dawood, T., Abouhamad, M., Jabri, A., Zayed, T., and Dinh, K. (2015_d). “Évaluation améliorée de la corrosivité des dalles de pont en béton.” *Proc., 22e Colloque Sur la Progression de la Recherche Québécoise Sur les Ouvrages d'art*, Quebec, QC., Canada.
- Dawood, T., Zhu, Z., and Zayed, T. (2016). “Detection and quantification of spalling distress in subway networks.” *21st International Conference on Advancement of Construction Management and Real Estate*, Hong Kong.
- Dawood, T., Zhu, Z., and Zayed, T. (2017_a). “Machine vision-based model for spalling detection and quantification in subway networks.” *Automation in Construction*, 81, 149–160.
<https://doi.org/10.1016/j.autcon.2017.06.008>.
- Dawood, T., Zhu, Z., and Zayed, T. (2017_b). “Computer vision-based model for moisture marks detection and recognition in subway networks.” *Journal of Computing in Civil Engineering*, In press. DOI: 10.1061/(ASCE)CP.1943-5487.0000728.
- Delatte, N., Chen, S., Maini, N., Parker, N., Agrawal, A., Mylonakis, G., Subramaniam, K., Kawaguchi, A., Bosela, P., McNeil, S., and Miller R. (2003). “Using NDE to evaluate the condition of subway tunnel systems.” *3rd Forensic Engineering Congress*, ASCE, San Diego, CA, USA, 329-340. [https://doi.org/10.1061/40692\(241\)33](https://doi.org/10.1061/40692(241)33).
- Derrible, S., and Kennedy, C. (2010). “Evaluating, comparing, and improving metro networks.” *Proc., Transportation Research Record*, Washington, D.C., 2146, 43-51.
 DOI: <http://dx.doi.org/10.3141/2146-06>.

- Dikmen, I., Birgonul, M., and Kiziltas, S. (2005). "Prediction of organizational effectiveness in construction companies." *Journal of Construction Engineering and Management*, 131(2), 252-261. DOI: 10.1061/(ASCE)0733-9364(2005)131:2(252).
- Dilek, U. (2006). "Nondestructive and laboratory evaluation of damage gradients in concrete structure exposed to cryogenic temperatures." *Journal of Performance of Constructed Facilities*, 20(1), 37–44. [http://dx.doi.org/10.1061/\(ASCE\)0887-3828\(2006\)20:1\(37\)](http://dx.doi.org/10.1061/(ASCE)0887-3828(2006)20:1(37)).
- Ding, L., and Goshtasby, A. (2001). "On the canny edge detector." *Pattern Recognition*, 34(3), 721 – 725. DOI: [https://doi.org/10.1016/S0031-3203\(00\)00023-6](https://doi.org/10.1016/S0031-3203(00)00023-6).
- Dinh, K. (2014). "Condition assessment of concrete bridge decks using ground penetrating radar." Ph.D. Thesis, Concordia University, Montréal, QC., Canada.
- Dinh, K., Zayed, T., Moufti, S., Shami, A., Jabri, A., Abouhamad, M., and Dawood, T. (2015). "Clustering-based threshold model for condition assessment of concrete bridge decks using ground penetrating radar." *Transportation Research Record (TRR): Journal of the Transportation Research Board (TRB)*, 2522, 81-89. DOI: 10.3141/2522-08.
- Ebrat, M., and Ghodsi, R. (2014). "Construction project risk assessment by using adaptive-network-based Fuzzy inference system: an empirical study." *KSCE J Civ Eng.*, 18(5) 1213-1227. Doi:10.1007/s12205-014-0139-5.
- Esragh, F., and Mamdani, E. H. (1981). "A general approach to linguistic approximation." *Fuzzy reasoning and its applications*, London: Academic Press.
- Farran, M. (2006). "Life cycle cost for rehabilitation of public infrastructure: application to Montréal Metro system." M.Sc. Thesis, Concordia University, Montréal, QC., Canada.
- Fryer, J. G. (2000). *Introduction in close range photogrammetry and machine vision*, Whittles Publishing, Roseleigh House, Latheronwheel, Scotland, UK.

- FHWA (1997). *Federal highway administration research and technology; coordinating, developing, and delivering highway transportation innovations*. Publication number: FHWA-RD-97-146.
- Gehrig, M. D., Morris, D. V., and Bryant J. T. (2004). "Ground penetrating radar for concrete evaluation studies." *Technical Presentation Paper for Performance Foundation Association*, 197-200.
- German, S., Brilakis, I., and DesRoches, R. (2012). "Rapid entropy-based detection and properties measurement of concrete spalling with machine vision for post-earthquake safety assessments." *Advanced Engineering Informatics*, 26(4), 846-858.
<http://dx.doi.org/10.1016/j.aei.2012.06.005>.
- Gkountis, I. and Zayed, T. (2013). "Subway station condition assessment using analytic network processes." *Proc., The Third International Conference on Soft Computing Technology in Civil, Structural and Environmental Engineering*, Civil-Comp Press, Stirlingshire, UK.
- Gonzalez, R. C., and Wintz, P. (1987). *Digital Image Processing*, Addison-Wesley Publishing Co., Massachusetts.
- Gonzalez, R. C., and Woods, R. E. (2008). *Digital image processing*, 3rd Ed., Harlow: Pearson/Prentice Hall, New Jersey.
- Gucunski, N., Kee, S-H., La, H., Basily, B., and Maher, A. (2015). "Delamination and concrete quality assessment of concrete bridge decks using a fully autonomous RABIT platform." *Structural Monitoring and Maintenance*, 2(1), 19-34.
<http://dx.doi.org/10.12989/smm.2015.2.1.019>.

- Gucunski, N., Romero, F., Imani, A. S., and Fetrat, F. (2013). "NDE-based assessment of deterioration progression in concrete bridge decks." *Proc., Transportation Research Board 92nd Annual Meeting*, No. 13-3043, Washington D.C., USA.
- Gucunski, N., Romero, F., Kruschwitz, S., Feldmann, R., Abu-Hawash, A. and Dunn, M. (2010). "Multiple complementary nondestructive evaluation technologies for condition assessment of concrete bridge decks." *Proc., Transportation Research Record*, Washington, D.C., 2201, 34-44.
- Guo, W., Soibelman, L., and Garrett, J. (2009). "Visual pattern recognition supporting defect reporting and condition assessment of wastewater collection systems." *Journal of Computing in Civil Engineering*, 23(3), 160-169. [http://dx.doi.org/10.1061/\(ASCE\)0887-3801\(2009\)23:3\(160\)](http://dx.doi.org/10.1061/(ASCE)0887-3801(2009)23:3(160)).
- Ham, S., Song, H., Oelze, M. L., and Popovics, J. S. (2017). "A contactless ultrasonic surface wave approach to characterize distributed cracking damage in concrete." *Ultrasonics*, 75, 46-57. <http://dx.doi.org/10.1016/j.ultras.2016.11.003>.
- Hammad, A., Garrett, J. H. and Karimi, H.A. (2003). "Mobile infrastructure management support system considering location and task awareness." *Towards a Vision for Information Technology in Civ. Eng. Conf.*, Nashville, Tennessee, USA. 157–166. [https://doi.org/10.1061/40704\(2003\)13](https://doi.org/10.1061/40704(2003)13).
- Hamrouche, R., Klysz, G., Balayssac, J.P., Rhazi, J. and Ballivy, G. (2011). "Numerical simulations and laboratory tests to explore the potential of ground-penetrating radar (GPR) in detecting unfilled joints in brick masonry structures." *International Journal of Architectural Heritage: Conservation, Analysis, and Restoration*, 6(6), 648-664.

- Hoegh, K., Khazanovich, L., Dai, S., and Yu, T. (2015). "Evaluating asphalt concrete air void variation via GPR antenna array data." *Case Studies in Nondestructive Testing and Evaluation*, 3, 27-33. <https://doi.org/10.1016/j.csndt.2015.03.002>.
- Hubbard, D., and Samuelson, D. (2009). *Modeling without measurements: how the decision analysis culture's lack of empiricism reduces its effectiveness*, 3rd Ed., Wiley, A John Wiley & Sons Inc. Publication, NJ, USA.
- Hugenschmidt, J., Mastrangelo, R. (2006). "GPR inspection of concrete bridges." *Cement and Concrete Composites*, 28(4), 384–392. <https://doi.org/10.1016/j.cemconcomp.2006.02.016>.
- Hutchinson, T., and Chen, Z. (2006). "Improved image analysis for evaluating concrete damage." *Journal of Computing in Civil Engineering*, 20(3), 210-216.
[http://dx.doi.org/10.1061/\(ASCE\)0887-3801\(2006\)20:3\(210\)](http://dx.doi.org/10.1061/(ASCE)0887-3801(2006)20:3(210)).
- Hwang, S. (2009). "Dynamic regression models for prediction of construction costs." *Journal of Construction Engineering and Management*, 135(5).
[http://dx.doi.org/10.1061/\(ASCE\)CO.1943-7862.0000006](http://dx.doi.org/10.1061/(ASCE)CO.1943-7862.0000006).
- ImageJ, Commercial Software for Image Analysis Version 1.50g, Online Resources.
- Iyer, S., and Sinha, S.K. (2006). "Segmentation of pipe images for crack detection in buried sewers." *Journal of Computer-Aided Civil and Infrastructure Engineering*, 21(6), 395-410.
DOI: 10.1111/j.1467-8667.2006.00445.x.
- Jahanshahi, M., and Masri, S. (2011). "A novel crack detection approach for condition assessment of structures." *International Workshop on Computing in Civil Engineering*, Miami, Florida, USA. DOI: [http://dx.doi.org/10.1061/41182\(416\)48](http://dx.doi.org/10.1061/41182(416)48).

- Jahanshahi, M., Masri, S., Padgett, C., and Sukhatme, G. (2013). “An innovative methodology for detection and quantification of cracks through incorporation of depth perception.” *Machine Vision and Applications*, 24(2), 227-241. DOI: 10.1007/s00138-011-0394-0.
- Jain, K. K., and Bhattacharjee, B. (2012). “Application of Fuzzy concepts to the visual assessment of deteriorating reinforced concrete structures.” *Journal of Construction Engineering and Management*, 138(3), pp. 399–408.
- Jang, J.-S. R. (1993). “ANFIS: adaptive-network-based Fuzzy inference system.” *IEEE Transactions on Systems, Man, and Cybernetics*, 23(3), 665 - 685. DOI: 10.1109/21.256541.
- Jang, J.-S. R. (1996). “Input selection for ANFIS learning.” *Fuzzy Systems, Proceedings of the Fifth IEEE International Conference on*, New Orleans, LA, USA. 1493-1499.
DOI: 10.1109/FUZZY.1996.552396.
- Jang, J.-S. R., Sun, C.-T., and Mizutani, E. (1997). *Neuro-Fuzzy and soft computing: a computational approach to learning and machine intelligence*, Prentice Hall, NJ, USA.
- Jobson, D. J., Rahman, Z., and Woodell, G. A. (1997). “A multiscale retinex for bridging the gap between color images and the human observation of scenes.” *IEEE Transactions on Image Processing*, 6(7), 965 – 976. DOI: 10.1109/83.597272.
- Kabir, S. (2008). “Transform-and statistical-based image analysis for assessment of deterioration in concrete infrastructure.” Ph.D. Thesis, University of Sherbrooke, QC. Canada.
- Kepaptsoglou, K., Gkountis, I., Karlaftis, M. G., Mintsis, G., and Vardaki, S. (2012). “Fuzzy analytical hierarchy process model for assessing condition and performance of metro stations.” *Proc., Transportation Research Board 91st Annual Meeting*, No. 12-2026, Washington D.C., USA.

- Kilic, G., and Unluturk, M. (2014). "Performance evaluation of the neural networks for moisture detection using GPR." *Nondestructive Testing and Evaluation*, 29(4), 283-296.
DOI:10.1080/10589759.2014.941839.
- Kim, G. H., Shin, J. M., Kim, S., and Shin, Y. (2013). "Comparison of school building construction costs estimation methods using regression analysis, neural network, and support vector machine." *Journal of Building Construction and Planning Research*, 1(1), 1-7
<http://dx.doi.org/10.4236/jbcpr.2013.11001>.
- Kim, M., Cheng, J., Sohn, H., and Chang, C. (2015). "A framework for dimensional and surface quality assessment of precast concrete elements using BIM and 3D laser scanning." *Automation in Construction*, 49, 180-194. <http://dx.doi.org/10.1016/j.autcon.2014.07.010>.
- Koch, C., and Brilakis, I. (2011). "Pothole detection in asphalt pavement images." *Advanced Engineering Informatics*, 25(3), 507–515. <http://dx.doi.org/10.1016/j.aei.2011.01.002>.
- Koo, D. H., and Ariaratnam, S. T. (2006). "Innovative method for assessment of underground sewer pipe condition." *Automation in Construction*. 15, 479 – 488.
DOI:10.1016/j.autcon.2005.06.007.
- Kutner, M., Nachtsheim, C., and Neter, J. (2003). *Applied linear regression models*, 4th Ed., McGraw-Hill Company Inc., New York, USA.
- Kutner, M., Nachtsheim, C., Neter, J., and Li, W. (2005). *Applied linear statistical models*, 5th Ed., McGraw-Hill Inc., New York, USA.
- La, H. M., Gucunski, N., Kee, S., Yi, J., Senlet, T., and Nguyen, L. (2014). "Autonomous robotic system for bridge deck data collection and analysis." *International Conference on Intelligent Robots and Systems (IROS 2014)*, Chicago, IL. DOI: 10.1109/IROS.2014.6942821.

- La, H. M., Lim, R. S., Basily, B., Gucunski, N., Yi, J., Maher, A., and Parvardeh, H. (2013). “Autonomous robotic system for high-efficiency non-destructive bridge deck inspection and evaluation.” *Automation Science and Engineering (CASE), IEEE International Conference*, Madison, WI, USA. 1053-1058. DOI: 10.1109/CoASE.2013.6653886.
- Lataste, J., Sirieix, C., Breysse, D., and Frappa, M. (2003). “Electrical resistivity measurement applied to cracking assessment on reinforced concrete structures in civil engineering.” *NDT and E International*, 36(6), 383–394. [http://dx.doi.org/10.1016/S0963-8695\(03\)00013-6](http://dx.doi.org/10.1016/S0963-8695(03)00013-6).
- Le, T., Gibb, S., Pham, N., La, H. M., Falk, L., and Berendsen, T. (2017). “Autonomous robotic system using non-destructive evaluation methods for bridge deck inspection.” *IEEE International Conference on Robotics and Automation (ICRA)*, Singapore, Singapore. DOI: 10.1109/ICRA.2017.7989421.
- Li, M., Anderson, N., Sneed, L., and Torgashov, E. (2016_a). “Condition assessment of concrete pavements using both ground penetrating radar and stress-wave based techniques.” *Journal of Applied Geophysics*, 135, 297-308. <https://doi.org/10.1016/j.jappgeo.2016.10.022>.
- Li, S., Yuan, C., Liu, D., and Cai, H. (2016_b). “Integrated processing of image and GPR data for automated pothole.” *Journal of Computing in Civil Engineering*, 30(6), [http://dx.doi.org/10.1061%2F\(ASCE\)CP.1943-5487.0000582](http://dx.doi.org/10.1061%2F(ASCE)CP.1943-5487.0000582).
- Looney, C. (1997). *Pattern recognition using neural networks*, Oxford University Press, New York, USA.
- Martino, N., Birken, R., Maser, K., and Wang, M. (2014). “Developing a deterioration threshold model for assessment of concrete bridge decks using ground penetrating radar.” *Proc., Transportation Research Board 93rd Annual Meeting*, No. 14-3861, Washington D.C., USA.

- Martino, N., Maser, K., Birken, R., and Wang, M. (2016). "Quantifying bridge deck corrosion using ground penetrating radar." *Research in Nondestructive Evaluation*, 27(2), 112-124.
<http://dx.doi.org/10.1080/09349847.2015.1067342>.
- Marzouk, M., and Abdel Aty, A. (2012). "Maintaining subway infrastructure using BIM." *Construction Research Congress*, West Lafayette, Indiana, USA. 2320-2328.
<http://ascelibrary.org/doi/abs/10.1061/9780784412329.233>.
- Mathworks. (2013). "MATLAB R2013b." The Technical Computing Computer Software.
<https://www.mathworks.com/>.
- McNeill, F. M., and Thro, E. (1994). *Fuzzy logic: a practical approach*, Ap. Professional, Boston, MA, USA.
- McRobbie, S. G. (2008). *Automated inspection of highway structures*, Published Project Report PPR 412, Transportation Research Laboratory, UK.
- Mindess, S., and Young, J. F. (1981). *Concrete*, Prentice-Hall, Englewood Cliffs, New Jersey, USA.
- Momeni, E., Nazir, R., Armaghani, D. J., and Maizir, H. (2015). "Application of artificial neural network for predicting shaft and tip resistances of concrete piles." *Earth Sciences Research Journal*, 19(1), 85-93. DOI: 10.15446/esrj.v19n1.38712.
- Montaser, A., Bakry, I., Alshibani, A., and Moselhi, O. (2012). "Estimating productivity of earthmoving operations using spatial technologies." *Canadian Journal of Civil Engineering*, 39(9), 1072-1082. <https://doi.org/10.1139/l2012-059>.
- Moselhi, O., Hegazy, T., and Fazio, P. (1991). "Neural networks as tools in construction." *J. Constr. Eng. Manage.*, 117(4), 606-625.

- MTR (2012). *Sustainability report - caring for life's journeys*.
<<http://www.mtr.com.hk/eng/sustainability/2012rpt/files/sustainabilityreport2012.pdf>> (June 15, 2017).
- NTD/FTA (2017). *The national transit database (NTD)*, Federal Transit Administration, Washington, DC., USA. <<https://www.transit.dot.gov/ntd>> (June 15, 2017).
- OSIM (2008). *Ontario structure inspection manual*, Ontario Ministry of Transportation, Toronto, Canada, <http://www.elliottlakeinquiry.ca/exhibits/pdf/05162-NL_E000013134.pdf> (Dec. 15, 2013).
- Parrillo, R., Roberts, R., and Haggan, A. (2006). "Bridge deck condition assessment using ground penetrating radar." *ECNDT Conference Proceeding*, Berlin, Germany, 25-29.
- Parvizsedghy, L., and Zayed, T. (2015). "Consequence of failure: neuro-fuzzy-based prediction model for gas pipelines." *J. Perform. Constr. Facil.*, 30(4).
[https://doi.org/10.1061/\(ASCE\)CF.1943-5509.0000817](https://doi.org/10.1061/(ASCE)CF.1943-5509.0000817).
- Patterson, D. (1996). *Artificial neural network*, Prentice-Hall, Singapore, Singapore.
- Pentala, V. (2009). "Failure Mechanisms in Concrete." In: Delatte, N. (editor), *Failure, Distress and Repair of Concrete Structures*, Woodhead Publishing Limited, Great Abington, Cambridge, UK.
- Perona, P., and Malik, J. (1990). "Scale-space and edge detection using anisotropic diffusion." *IEEE Transactions on Pattern Analysis and Machine Intelligence*, 12(7), 629-639.
DOI: 10.1109/34.56205.
- Pigeon, M., and Pleau, R. (1995). *Durability of Concrete in Cold Climates*, E & FN Spon, London, UK.

- Polikar, R. (2006). "Pattern recognition." *Wiley Encyclopedia of Biomedical Engineering*, John Wiley & Sons, Inc., DOI: 10.1002/9780471740360.ebs0904.
- Pratt, W. K. (1978). *Digital image processing*, Wiley, New York.
- Prego, F. J., Solla, M., Núñez,-N. X., and Arias, P. (2016). "Assessing the applicability of ground-penetrating radar to quality control in tunneling construction." *J. Constr. Eng. Manage.*, 142(5). DOI: 10.1061/(ASCE)CO.1943-7862.0001095.
- Public transit (2010). *At the Heart of Montréal's Economic Development*, Montréal, Quebec. www.ccmm.ca/~media/Files/News/2010/10_11_26_ccmm_etude-transport_en.pdf (Sep. 4, 2017).
- Rajani, B., Kleiner, Y., and Sadiq, R. (2006). "Translation of pipe inspection results into condition ratings using the Fuzzy synthetic evaluation technique." *International Journal of Water Supply Research and Technology: Aqua*, 55(1), 11–24.
- Rhim, H.C. (2001). "Condition monitoring of deteriorating concrete dams using radar." *Cement and Concrete Research*, 31(3), 363 - 373. [https://doi.org/10.1016/S0008-8846\(00\)00496-8](https://doi.org/10.1016/S0008-8846(00)00496-8).
- Rosenfeld, A., and Kak, A. C. (1982). *Digital picture processing*, 2nd Ed., Academic Press, New York.
- Roy, B., Present, M., and Silhol, D. (1986). "A programming method for determining which Paris Metro stations should be renovated." *European Journal of Operational Research*, 24(2), pp. 318-334.
- Russ, J. C., Woods, R. P. (1995). "The image processing handbook." *Journal of Computer Assisted Tomography*, 19(6), 979–981.

- Russel, H.A., and Gilmore, J. (1997). *Inspection policy and procedures for transit tunnels and underground structures*, Transit Cooperative Research Program Synthesis 23, National Academy Press, Washington, D.C.
- Sadeghi, N., Fayek, A., and Pedrycz, W. (2010). "Fuzzy Monte Carlo simulation and risk assessment in construction." *Computer-Aided Civil and Infrastructure Engineering*, 25, 238–252.
- Sadowski, Ł. (2015). "Non-destructive identification of pull-off adhesion between concrete layers." *Automation in Construction*, 57, 146-155.
<http://dx.doi.org/10.1016/j.autcon.2015.06.004>.
- Sarle, W.S. (1994). "Neural networks and statistical methods." *Proc. of the 19th SAS Users Group International Conference*, SAS Institute, Cary, North Carolina, USA.
- Scott, M., Rezaizadeh, A., Delahaza, A., Santos, C., Moore, M., Graybeal, B., and Washer, G. (2003). "A comparison of nondestructive evaluation methods for bridge deck assessment." *NDT and E International*, 36(4), 245–255. [http://dx.doi.org/10.1016/S0963-8695\(02\)00061-0](http://dx.doi.org/10.1016/S0963-8695(02)00061-0).
- Semaan, N. (2006). "Subway station diagnosis index (SSDI): a condition assessment model." M.Sc. Thesis, Concordia University, Montréal, QC., Canada.
- Semaan, N. (2011). "Structural performance model for subway networks." Ph.D. Thesis, Concordia University, Montréal, QC., Canada.
- Sengur, A. (2008). "Wavelet transform and adaptive neuro-Fuzzy inference system for color texture classification." *Expert Systems with Applications*, 34(3), 2120–2128.
<https://doi.org/10.1016/j.eswa.2007.02.032>.

- Senin, S. F., and Hamid, R. (2016). "Ground penetrating radar wave attenuation models for estimation of moisture and chloride content in concrete slab." *Construction and Building Materials*, 106, 659-669. <https://doi.org/10.1016/j.conbuildmat.2015.12.156>.
- Senouci, A., Elabbasy, M., Elwakil, E., Abdrabou, B., and Zayed, T. (2014). "A model for predicting failure of oil pipelines." *Structure and Infrastructure Engineering*, 10(3), 375-387, DOI: 10.1080/15732479.2012.756918.
- Shah, A., Ribakov, Y., and Zhang, C. (2013). "Efficiency and sensitivity of linear and nonlinear ultrasonics to identifying micro and macro-scale defects in concrete." *Materials & Design*, 50, 905-916. <http://dx.doi.org/10.1016/j.matdes.2013.03.079>.
- SHRP 2 (2013). *Nondestructive testing to identify concrete bridge deck deterioration*, Strategic Highway Research Program, Transportation Research Board, Washington, DC., USA.
- Sinha, S. K., and Fieguth, P. W. (2006). "Neuro-Fuzzy network for the classification of buried pipe defects." *Autom. Constr.*, 15(1), 73-83.
- Smith, A. R. (1978). "Color gamut transform pairs." *SIGGRAPH '78 Proceedings of the 5th Annual Conference on Computer Graphics and Interactive Techniques*, New York, NY, USA, 12(3), 12-19.
- Stent, S., Gherardi, R., Stenger, B., Soga, K., and Cipolla, R. (2016). "Visual change detection on tunnel linings." *Machine Vision and Applications*, 27(3), 319–330. DOI: 10.1007/s00138-014-0648-8.
- STM (2011). *CPE: Capital Expenditures Program, 2012 - 2013 – 2014*.
<<http://www.stm.info/sites/default/files/a-pti12-14.pdf>> (Dec. 2014).

- Tarussov, A., Vandry, M., and De La Haza, A. (2013). "Condition assessment of concrete structures using a new analysis method: ground-penetrating radar computer-assisted visual interpretation." *Journal of Construction and Building Materials*, 38, 1246–1254.
- Temurcan, P., Dawood, T., and Zayed, T. (2016). "Image-based versus numerical analyses of concrete bridge decks using GPR." *Proc. IBridge 2016*, Istanbul, Turkey.
http://2016.istanbulbridgeconference.org/files/2016papers/ID_044.pdf.
- TOMIE (2015). *Tunnel operations, maintenance, inspection, and evaluation manual*, U.S. Department of Transportation, Publication No. FHWA-HIF-15-005, Washington, DC., USA.
- Tsoukalas, H., and Uhrig, E. (1997). *Fuzzy and neural approaches in engineering*, Wiley, New York.
- Vaidhehi, V. (2014). "The role of dataset in training ANFIS system for course advisor." *International Journal of Innovative Research in Advanced Engineering (IJIRAE)*, 1(6). ISSN: 2349-2163. <http://ijirae.com>.
- Valença, J., Gonçalves, L.M.S., and Júlio, E. (2013). "Damage assessment on concrete surfaces using multi-spectral image analysis." *Construction and Building Materials*, 40, 971-981.
<http://dx.doi.org/10.1016/j.conbuildmat.2012.11.061>.
- Wang, J., and Hu, H. (2006). "Vibration-based fault diagnosis of pump using Fuzzy technique." *International Journal of Measurement*, 39, 176–185.
- Wang, Y., Zayed, T., and Moselhi, O. (2009). "Prediction models for annual break rates of water mains." *J. Perform. Constr. Facil.*, 23(1), 47-54. [https://doi.org/10.1061/\(ASCE\)0887-3828\(2009\)23:1\(47\)](https://doi.org/10.1061/(ASCE)0887-3828(2009)23:1(47)).

- Wang, Z., and Wang, H. (2016). "Image smoothing with generalized random walks: algorithm and applications." *Applied Soft Computing*, 46, 792-804.
<https://doi.org/10.1016/j.asoc.2016.01.003>.
- Weeks, A. R. (1996). *Fundamentals of Electronic Image Processing*, SPIE Optical Engineering Press, Bellingham, Washington.
- Westoby, M., Brasington, J., Glasser, N., Hambrey, M., and Reynolds, J. (2012). "Structure-from-motion' photogrammetry: a low-cost, effective tool for geoscience applications." *Geomorphology*, 179, 300-314. <http://dx.doi.org/10.1016/j.geomorph.2012.08.021>.
- Wiwatrojanagul, P., Sahamitmongkol, R., Tangtermsirikul, S., and Khamsemanan, N. (2017). "A new method to determine locations of rebars and estimate cover thickness of RC structures using GPR data." *Construction and Building Materials*, 140, 257-273.
<https://doi.org/10.1016/j.conbuildmat.2017.02.126>.
- WMATA (2013). *Vital signs report, a scorecard of metro's key performance indicators*, KPI2012 3rd Quarter Results.
<http://www.wmata.com/about_metro/scorecard/documents/Vital_Signs_Q3_2013_Accessible.pdf> (April, 2014).
- Xu, H., and Humar, J. (2006). "Damage detection in a girder bridge by artificial neural network technique." *Computer-Aided Civil and Infrastructure Engineering*, 21(6), 450-464.
- Yu, S., Jang, J., and Han, C. (2006). "Auto inspection system using a mobile robot for detecting concrete cracks in a tunnel." *Automation in Construction*, 16(3), 255-261.
<http://dx.doi.org/10.1016/j.autcon.2006.05.003>.

- Yu, W-d., and Skibniewski, M. J. (2010). "Integrating neuro-fuzzy system with conceptual cost estimation to discover cost-related knowledge from residential construction projects." *J. Comput. Civ. Eng.*, 24(1), 35-44.
- Yu, X., and Salari, E. (2011). "Pavement pothole detection and severity measurement using laser imaging." *IEEE International Conference*, Mankato, MN, USA.
DOI: 10.1109/EIT.2011.5978573.
- Zayed, T., and Halpin, D. (2005). "Deterministic models for assessing productivity and cost of bored piles." *Journal of Construction Management and Economics*, 23(5), 531-543.
<http://dx.doi.org/10.1080/01446190500039911>.
- Zayed, T., and Mahmoud, M. (2014). "Neurofuzzy-Based Productivity Prediction Model for Horizontal Directional Drilling." *Journal of Pipeline Systems Engineering and Practice*, 5(3).
[https://doi.org/10.1061/\(ASCE\)PS.1949-1204.0000167](https://doi.org/10.1061/(ASCE)PS.1949-1204.0000167).
- Zhu, Z. (2011). "Column recognition and defects/damage properties retrieval for rapid infrastructure assessment and rehabilitation using machine vision." Ph.D. Thesis, Georgia Institute of Technology, Atlanta, GA, USA.
- Zhu, Z., and Brilakis, I. (2010). "Machine vision-based concrete surface quality assessment." *Journal of Construction Engineering and Management*, 136(2), 210-218. DOI: 10.1061/_ASCE_CO.1943-7862.0000126.

**APPENDIX A: DATA COLLECTION AND VALIDATION IMAGES IN
MONTREAL SUBWAY NETWORK**



Figure A1 Measurements in the Tunnel Inter Frontenac and Papineau



Figure A2 Marking Scanning Paths in the Tunnel Inter Frontenac and Papineau



Figure A3 GPR Calibration



Figure A4 Scanning the Vault by GPR in the Tunnel Inter Frontenac and Papineau



Figure A5 First Captured Sign of Water Existence in the Tunnel Inter Frontenac and Papineau



Figure A6 Marking Scanning Paths on a Wall in Outremont Station

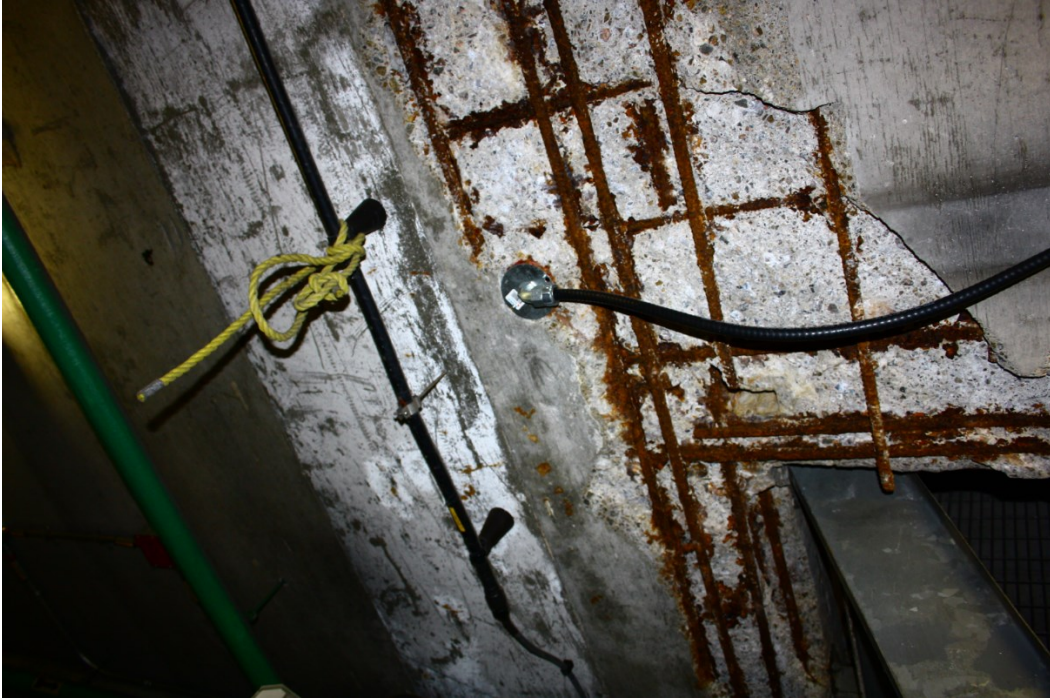


Figure A7 Corrosion and Delamination in Vendôme Station



Figure A8 Corrosion, Delamination, and Efflorescence in Outremont Station



Figure A9 Coring Rig



Figure A10 Rotary Hammer Core Bit

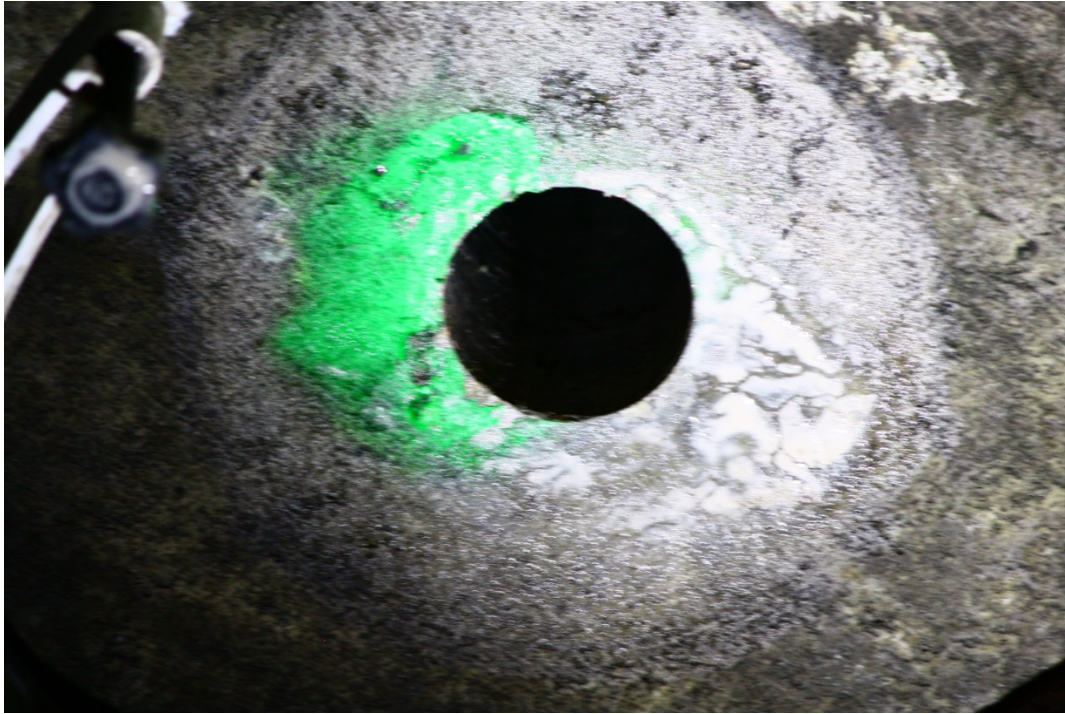


Figure A11 First Core in the Vault Inter Frontenac and Papineau Tunnel



Figure A12 Dripping Water after Coring the Vault



Figure A13 Laser Scanner for Results Validation

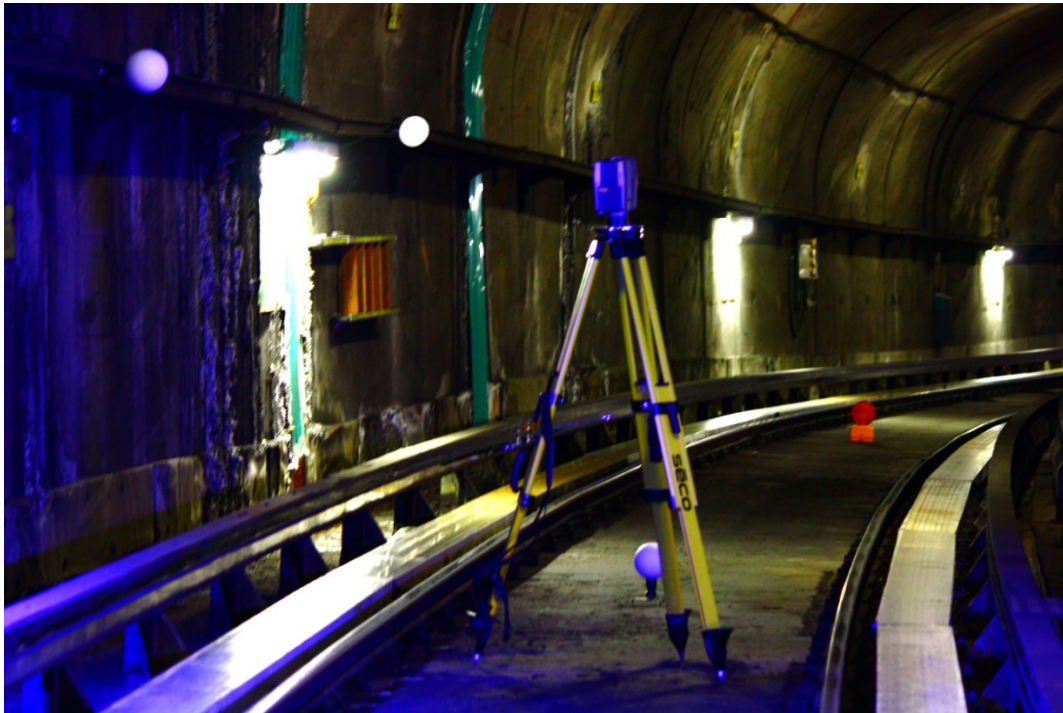


Figure A14 Laser Scanner in the Tunnel Inter Frontenac and Papineau

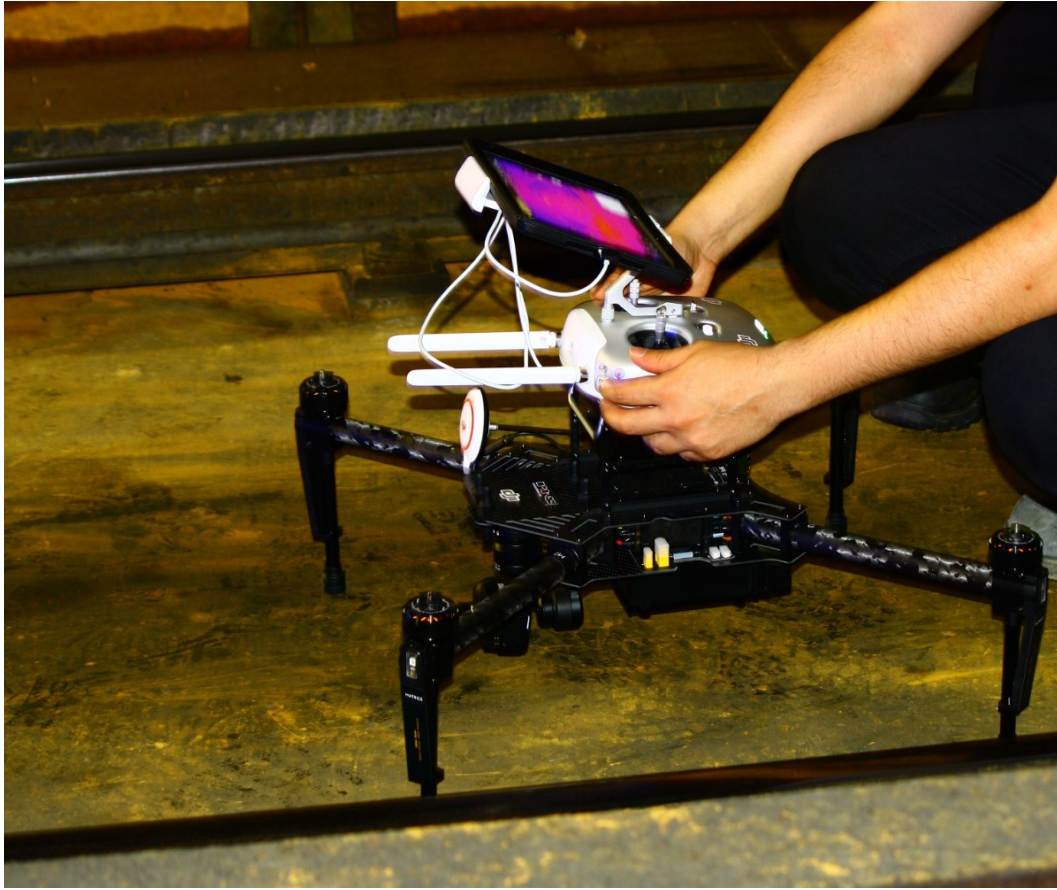


Figure A15 Drone and Infrared Camera for Results Validation

APPENDIX B: PLANS OF THE SELECTED SYSTEMS IN MONTRÉAL NETWORK

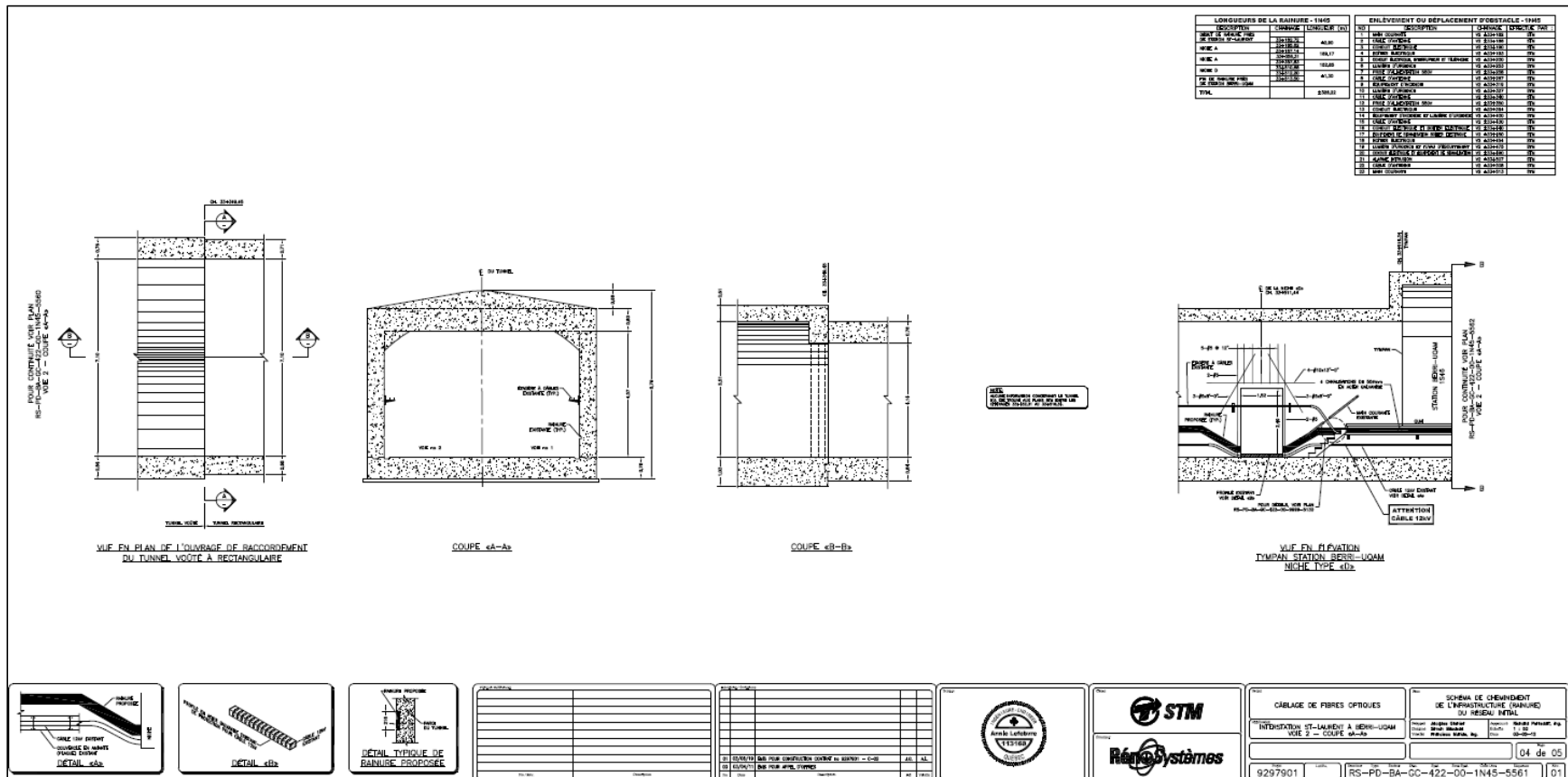


Figure B1 Plan of the Tunnel Inter St. Laurent and Place-Des-Arts

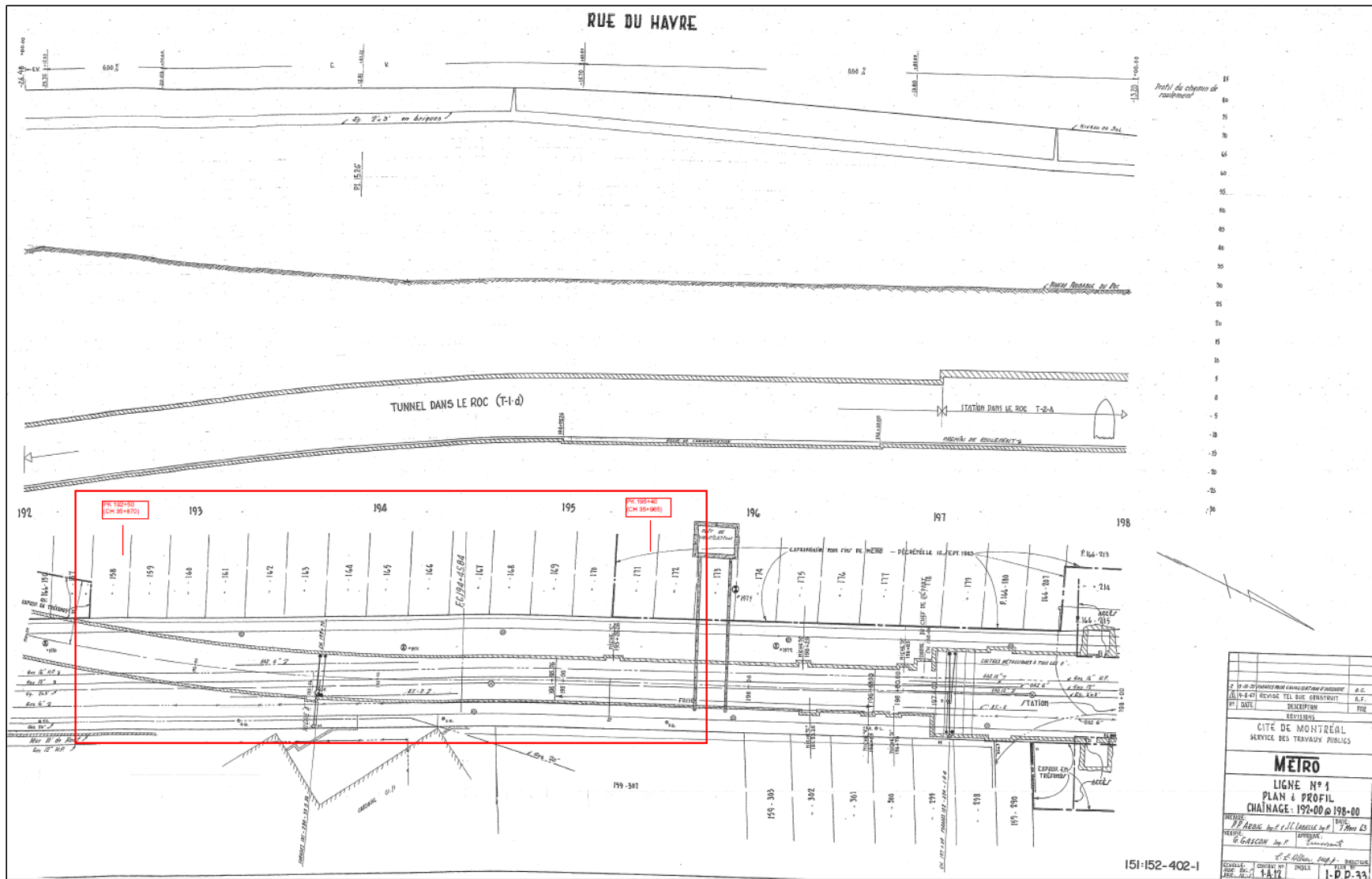


Figure B2 Plan of the Tunnel Inter Frontenac and Papineau, Showing the Studied Segment

